GEOPHYSICAL AND GEOCHEMICAL CONSTRAINTS ON SUBMARINE VOLCANIC PROCESSES

by

Meghan R. Jones

B.S., University of Miami (2014)

to the Department of Earth, Atmospheric, and Planetary Sciences

Submitted in partial fulfillment of the requirements for the degree of

Doctor of Philosophy

at the

MASSACHUSETTS INSTITUTE OF TECHNOLOGY

and the

WOODS HOLE OCEANOGRAPHIC INSTITUTION

September 2019

Signature redacted

Author.....

Joint Program in Oceanography /Applied Ocean Science & Engineering
Massachusetts Institute of Technology & Woods Hole Oceanographic Institution
June 18, 2019

Signature redacted

Certified by.....

Dr. S. Adam Soule
Associate Scientist with Tenure in Geology & Geophysics
Woods Hole Oceanographic Institution
Thesis Supervisor

Signature redacted

Accepted by.....

Dr. Daniel McCorkle
Senior Scientist in Geology & Geophysics
Woods Hole Oceanographic Institution
Chair, Joint Committee for Marine Geology & Geophysics

GEOPHYSICAL AND GEOCHEMICAL CONSTRAINTS ON SUBMARINE VOLCANIC PROCESSES

by

Meghan R. Jones

Submitted to the MIT-WHOI Joint Program in Oceanography and Applied Ocean Science and Engineering on June 18, 2019 in Partial Fulfillment of the Requirements for the Degree of Doctor of Philosophy in Geological Oceanography.

Abstract

Submarine volcanic systems form new oceanic crust, host unique chemosynthetic ecosystems, concentrate rare metals, and provide a conduit for chemical transfer from the Earth's interior to hydrosphere. Although our understanding of submarine volcanoes has been historically limited due to their relative inaccessibility, recent observations from active systems provide valuable opportunities to address key open questions in submarine volcanology. This thesis provides new insight into submarine volcanic processes using observations and samples from the 2011 Axial Seamount eruption, the 2012 Havre Volcano eruption, and the Mid-Atlantic Ridge near 14°N. In Chapter 2, I develop best practices for quantifying vesicle textures and reconstructing total CO_2 concentrations in mid-ocean ridge basalts (MORB). Based on synthetic vesicle populations, 2D and 3D measurements, and Raman spectroscopy, I show that traditional methods overestimate MORB CO_2 concentrations by as much as 50%, which has important implications for estimating ridge CO_2 flux. In Chapter 3, I apply methods from Chapter 2, along with a bubble growth model, to samples from the 2011 Axial Seamount eruption in order to evaluate magma ascent and lava flow rates. I show that the variability in ascent rates during the 2011 eruption spans the range previously proposed over the global mid-ocean ridge system. I suggest that the variability in ascent rates relates to lateral dike propagation and evolving reservoir overpressures and that ascent rates influence flow morphology. In Chapter 4, I address the origin of highly vesicular MORB that pop upon recovery from the seafloor. I show that bubble accumulation produces the high volatile concentrations in these popping rocks and demonstrate that mantle carbon concentrations are lower and less heterogeneous than previously proposed. In Chapter 5, I evaluate models for the submarine dispersal of giant pumice clasts using observations from the 2012 Havre Volcano eruption. I show that the seafloor distribution of giant pumice is controlled by conductive cooling, the advective displacement of steam by water through highly permeable pathways, and clast breakup during transport and deposition. Together, these chapters provide critical constraints on the flux of volatiles at mid-ocean ridges and the processes governing the emplacement of volcanic products on the seafloor.

Thesis Supervisor: Dr. S. Adam Soule
Title: Associate Scientist with Tenure in Geology & Geophysics
Woods Hole Oceanographic Institution

Acknowledgments

This thesis has benefited immensely from the support and contributions of many people. Foremost, I thank my thesis supervisor, Adam Soule, who made this possible. I am grateful for the support and guidance of my committee members, Mark Kurz, Veronique Le Roux, Michael Manga, Taylor Perron, and Dorsey Wanless. I am grateful to Dan Lizarralde for chairing my thesis defense, advising my second generals project, and providing many thoughtful conversations throughout my five years at WHOI. I appreciate the recommendations provided by my generals committee, including Mark Kurz, Veronique Le Roux, Dan Lizarralde, and Tim Grove.

Many field teams contributed to the collection of samples and data used in this thesis. I am grateful to the captain, crew, and science participants on the *R/V Thompson, R/V Western Flyer, R/V Atlantis*, and *R/V Revelle* and the vehicle teams of the *AUV Sentry, HOV Alvin, ROV Jason, ROV ROPOS*, and *ROV Doc Ricketts*. I am also fortunate to have worked with some excellent field teams in the collection of data not included in this thesis, particularly during expeditions in the Galapagos.

I appreciate those in the Academic Programs Office at WHOI and the Education Office at MIT who make the Joint Program function, including Meg Tivey, Jim Yoder, Delia Oppo, Julia Westwater, Christine Charette, Lea Fraser, Kris Kipp, and Martha Bridgers. I appreciate the service of JCMG&G members. I am grateful for all the WHOI administrators, security, and service staff.

There are many scientists who have improved my time in Woods Hole. I am immensely grateful to Dan and CL Fornari for all their support. I appreciate the guidance and assistance provided by Josh Curtice, Frieder Klein, Yang Liao, and Brian Monteleone. I am grateful to Debbie Smith, who recommended that I contact Adam about a JP thesis. Chris German transformed my career by inviting me to participate in a telepresence cruise in 2012, for which I will always be grateful. I also thank the many others who provided scientific opportunities during and prior to graduate school.

I thank Laura Stevens for the continuous mentorship. I am grateful to Hannah Mark for being my office mate, house mate, and friend through these transformative years. I appreciate the JP students who have served as student representatives and am grateful to the many students who have provided guidance, advice, and/or support during my time in the Joint Program. I appreciate many insightful conversations with several WHOI post-docs, including Kristen Fauria, Ayla Pamukcu, and Ross Parnell-Turner.

I am thankful for the friendship of many individuals both within and outside of the walls of MIT and WHOI. I am grateful to have an amazing family. My brothers have always been my inspirations. Lastly, I am incredibly fortunate to have Ludda and Buffy in my life.

Funding for this research was provided by a Department of Defense National Defense Science and Engineering Graduate (NDSEG) Fellowship, a Woods Hole Oceanographic Institution Ocean Ridge Initiative Fellowship and Ocean Ventures Fund Grant, an ExxonMobil Research Grant, and the National Science Foundation (NSF) Division of Ocean Sciences through grants 1333492, 1259218, 1260578, and 1357216. Sample collection was also supported by the David and Lucile Packard Foundation and the University of Washington. Additional travel support was provided by WHOI, MIT, NSF, the Deep Carbon Observation, GeoPRISMS, the Deep Submergence Science Committee, the American Geophysical Union, and the Dalio Family Foundation.

Contents

List of Figures

List of Tables

Chapter 1

Introduction

[*This introduction is written for a general audience; relevant citations can be found in the introduction sections of individual chapters]

The vast majority of volcanoes on Earth exist at the boundaries between tectonic plates. About 2/3 of the volcanic activity on Earth occurs at divergent plate boundaries, such as along the global mid-ocean ridge system. Beneath mid-ocean ridges, the Earth's mantle flows upwards and partially melts. The melts produced by the upwelling of the mantle percolate towards the center of the ridge. Most of the melt crystallizes within the oceanic crust, but a portion may erupt onto the Earth's surface. Although we think that volcanic eruptions frequently occur at mid-ocean ridges, very few of these eruptions have ever been observed due to the remote, underwater nature of most of the mid-ocean ridge system.

Most of the remaining volcanic activity on Earth occurs at subduction zones, where one tectonic plate sinks beneath another. The down-going plate releases fluids during subduction, which reduces the melting temperature of the overlying mantle. The melts produced by this process migrate through the mantle and crust, commonly forming volcanic arcs.

The magmas produced at mid-ocean ridges and volcanic arcs contain small amounts of volatiles, which are elements and compounds that easily form vapors at relatively low temperatures. Magmatic volatiles, including H_2O, CO_2, sulfur, halogens, and noble gases, can be either dissolved in the melt or exsolved in bubbles. Despite their relatively low concentrations in magmas, volatiles have a disproportionately large impact on magmatic and volcanic processes. For example, volatiles influence the melting of the mantle, the migration of melt through the mantle and crust, and the style of volcanic eruptions (e.g., effusive vs. explosive).

This thesis considers the behavior of volatiles during volcanic eruptions, and how volatiles can be used to trace magmatic and volcanic processes. Chapter 2 develops methods for quantifying the abundance of magmatic volatiles within bubbles. Chapters 3 and 4 consider the behavior of volatiles

during magmatic and volcanic processes at mid-ocean ridges. Chapter 5 considers these processes at submarine arc volcanoes. The chapters in this thesis provide insight into processes that are also relevant at mid-plate volcanic settings.

The solubility, or amount of any given volatile that can be dissolved in a melt, generally increases with pressure. The pressure dependent solubility of volatiles means that magmas deep in the Earth can contain more dissolved CO_2 and H_2O than magmas close to the surface. As magma ascends towards the Earth's surface, these volatiles begin to exsolve into bubbles according to their solubilities. CO_2 has a lower solubility than H_2O, so it begins to exsolve at greater depths than H_2O. Bubbles containing volatiles can escape from the magma, especially during storage in the crust and eruption on the surface. Due to the low solubility of CO_2 and H_2O at atmospheric pressures and the easy escape of exsolved gas, most volcanic products at subaerial volcanoes are completed degassed, meaning that they have lost all their initial CO_2 and H_2O. The shallow degassing of magmas presents a challenge for measuring volatiles and understanding their influence on volcanic processes. Scientists often use melt inclusions – tiny blobs of melt trapped in crystals – to investigate pre-eruptive volatile concentrations. In this thesis, I instead approach the problem by studying volcanic glass produced during deep ocean eruptions.

In contrast to most subaerial volcanic products, submarine lavas often retain some of their initial volatile content. During submarine eruptions, seawater rapidly quenches – or turns to glass – the outer surface of submarine lava flows. The outer glassy rind traps bubbles that might otherwise be lost to the atmosphere during subaerial eruptions and contains valuable information about the pre-eruptive chemistry of the magma. In addition, some volatiles remain dissolved in the melt during submarine eruptions due to the high pressure at the seafloor. Volatiles in mid-ocean ridge basalts – the most common type of rock produced at mid-ocean ridges – have been studied since at least the early 1970's. However, recent technological advancements in mass spectrometry and imaging have created new opportunities to investigate volcanic processes using the concentration of volatiles in mid-ocean ridge basalts.

In the second chapter of this thesis, I develop best practices for quantifying the amount and distribution of CO_2 in mid-ocean ridge basalts. I compare 2D measurements of bubbles with 3D measurements from x-ray computed tomography scans (similar to CAT scans) and synthetic bubble populations. I use the results from these comparisons, along with mass spectrometry and Raman

spectroscopy (which can measure the vibrational response of CO_2 to laser light), to provide recommendations for calculating total CO_2 concentrations in mid-ocean ridge basalts. I show that traditional methods, which use the ideal gas law and a quenching temperature of ~700°C, can overestimate the amount of CO_2 in a sample by up to 50%. Importantly, this error would propagate through calculations of the amount of carbon in the Earth's mantle and the amount of CO_2 released to the oceans by mid-ocean ridge volcanism.

Experimental solubility studies provide us with the opportunity to calculate the expected CO_2 and H_2O concentrations in mid-ocean ridge basalts. Commonly, we find that mid-ocean ridge basalts contain more dissolved CO_2 than expected at the depth (or pressure) of the seafloor. This 'super-saturation' in CO_2 partially reflects the large amount of energy required to nucleate a new bubble, which causes volatiles to mostly diffuse towards existing bubbles rather than nucleate new bubbles. Mid-ocean ridge basalts are commonly supersaturated because CO_2 diffusion is slow relative to magma ascent and lava flow rates. This disequilibrium process provides us with an opportunity to evaluate eruption rates by comparing measurements of CO_2 supersaturation in mid-ocean ridge basalts with models for CO_2 diffusion and bubble growth.

In Chapter 3 of this thesis, I constrain the rates of magma ascent and lava flow emplacement during the 2011 eruption of Axial Seamount using volatile measurements in mid-ocean ridge basalts and a diffusive bubble growth model. Axial Seamount is located ~500 km off the coast of Oregon and is one of the most active and best-studied volcanoes on the mid-ocean ridge system. I show that ascent rates varied dramatically during the 2011 eruption and suggest that the fastest ascent rates likely occurred early in the eruption. I also show that lava flows were produced by the fastest ascent rates and that the flows experienced roughly constant emplacement rates. I compare the results from this relatively new method with independent estimates based on seismicity and seafloor pressures. Similarities between our results and the seismicity-based constraints provide confidence in applying these methods elsewhere along the global mid-ocean ridge system. In contrast to other methods for evaluating magma ascent and lava flow emplacement rates, the CO_2 supersaturation method does not require instruments to be on the seafloor at the time of the eruption, which means that it can be broadly applied to both past and future mid-ocean ridge eruptions.

Most mid-ocean ridge basalts contain only a small amount of exsolved volatiles, around 1 – 4% by volume. Popping rocks are a notable exception. These mid-ocean ridge basalts are so vesicular (i.e.,

bubbly) that they pop after recovery from the seafloor due to the expansion of gases trapped in bubbles. Some scientists think that popping rocks are highly vesicular because they did not experience any gas loss during magma ascent, storage, or eruption. Based on this interpretation, popping rocks may be the most representative samples of the volatile composition of the Earth's interior. However, questions about the origin of popping rocks have lingered since their discovery over 40 years ago.

In Chapter 4 of this thesis, I address the origin of popping rocks using samples collected from the Mid-Atlantic Ridge (i.e., the mid-ocean ridge beneath the Atlantic Ocean) near 14°N. I show that the accumulation of bubbles most likely produced the high volatile concentrations in these mid-ocean ridge basalts. Therefore, I suggest that the initial concentration of volatiles was likely lower than the concentration measured in the highest vesicularity popping rocks. I discuss the possible mechanisms for bubble accumulation in popping rocks as well as the implications for mantle volatile abundances and mid-ocean ridge CO_2 flux.

One of the primary ways that volatiles affect the behavior of volcanic eruptions is by influencing the magma viscosity. More viscous magmas tend to erupt more explosively, but dissolved H_2O reduces the viscosity of magmas. During the 2012 eruption of Havre Volcano (a subduction zone volcano north of New Zealand), we think that the magma retained enough dissolved H_2O, due to the pressure at the seafloor, to erupt effusively rather than explosively. Nevertheless, there was still enough exsolved H_2O to produce highly vesicular volcanic rocks, up to 90% bubbles by volume, called pumice. The pumice clasts are initially buoyant because the bubbles are filled with magmatic volatiles (mostly steam). During the Havre eruption, the buoyant pumice clasts rose to the sea surface to form a massive pumice raft, which initially covered an area roughly twice the size of Boston. As the pumice clasts cool, seawater can infiltrate through the highly connected vesicles, which increases the density of the clasts until they eventually sink back to the seafloor.

In Chapter 5 of this thesis, I address the dispersal behavior of giant (>1 m across) pumice clasts produced during the 2012 Havre Volcano eruption. I use high resolution seafloor maps to quantify the distribution of pumice blocks on the seafloor. I compare the seafloor distribution of giant pumice with model predictions for giant pumice cooling, saturation, and dispersal. I show that the macroscale vesicle texture of giant pumice strongly influences dispersal behavior.

The chapters in this thesis are tied together by the ubiquitous importance of volatiles in magmatic and volcanic systems. In Chapters 2 – 5, I explore how volatiles, combined with other geochemical and geophysical tools, can be used to understand processes that cannot be easily observed, either because they are deep underwater or within the Earth's interior. In Chapter 6, I provide some insight into future research directions motivated by this thesis.

Chapter 2

Quantitative vesicle analyses and total CO_2 reconstruction in mid-ocean ridge basalts

This chapter is being prepared for publication as: Jones, M.R., Soule, S.A., Liao, Y., Brodsky, H., Le Roux, V., Klein, F. Quantitative vesicle analyses and total CO_2 reconstruction in mid-ocean ridge basalts

2.1 Abstract

Vesicle textures in submarine lavas have been used to calculate total (pre-eruption) volatile concentrations in mid-ocean ridge basalts (MORB), which provide constraints on upper mantle volatile concentrations and global mid-ocean ridge CO_2 flux. In this study, we evaluate vesicle size distributions (VSDs) and volatile concentrations in a suite of 20 MORB samples that span the range of vesicularities and vesicle number densities observed in MORB globally. We provide recommended best practices for quantifying vesicularity, vesicle number densities, and VSDs based on synthetic vesicle populations and comparisons between traditional 2D methods and x-ray computed micro-tomography results. For 2D measurements, we recommend analyzing multiple polished fragments with a cumulative area >100 times the area of the largest observed vesicle and including >200 vesicles in stereological VSD reconstructions. For 3D measurements, we recommend analyzing sample volumes >0.01 cm^3 at resolutions <2.0 μm/pixel for low vesicularity MORB (i.e., <4 vol.%) and sample volumes >0.1 cm^3 with resolutions <5 μm/pixel for higher vesicularity samples. Our validation of vesicularity measurements allows reconstructions of total CO_2 concentrations in MORB using dissolved volatile concentrations, vesicularities, and equations of state. We assess approaches for estimating the exsolved CO_2 concentration in MORB vesicles and find that $CO_{2(g)}$ density is ~40% lower than previously suggested, likely due to melt contraction during quenching. Based on these results, we recommend using sample eruption pressures, magmatic temperatures, and an equation of state that accounts for non-ideality at high temperatures to calculate exsolved CO_2 when independent constraints from Raman spectroscopy are unavailable. Our results suggest that some previous studies may have overestimated MORB volatile concentrations by as much as 50%, with the greatest differences in samples with the highest vesicularities. These new results imply lower CO_2/Ba of undegassed, enriched-MORB and lower integrated global ridge CO_2 flux than previously inferred.

2.2 Introduction

Mid-ocean ridge basalts (MORB) frequently experience incomplete degassing due to the hydrostatic pressure at the seafloor. As a result, MORB volatile concentrations can provide valuable insight into volatile abundances in Earth's upper mantle (e.g., Cartigny et al., 2008; Jones et al., 2019; Michael and Graham, 2015), which influence mantle melting, melt migration, and geophysical properties of the Earth's interior (e.g., Dasgupta and Hirschmann, 2010; Hirth and Kohlstedt, 1996). MORB CO_2 concentrations and vesicle textures have also been used to constrain mid-ocean ridge CO_2 flux (e.g., Chavrit et al., 2014), magma storage conditions within the oceanic crust (e.g., Aubaud et al., 2004; Dixon et al., 1988; le Roux et al., 2006; Sarda and Graham, 1990) and magma ascent and effusion rates during mid-ocean ridge eruptions (e.g., Chavrit et al., 2012; Gardner et al., 2016; Jones et al., 2018; Soule et al., 2012). Many of these studies estimate 3D vesicularities and reconstruct total CO_2 concentrations using 2D measurements on polished sections (e.g., Aubaud et al., 2004; Chavrit et al., 2014; Hekinian et al., 2000; Javoy and Pineau, 1991; Jones et al., 2018; Pineau et al., 2004; Soule et al., 2012). However, the methods for reconstructing 3D vesicle textures and total CO_2 concentrations in MORB have not yet been rigorously tested. Aubry et al. (2013) highlight the sensitivity of CO_2 reconstructions to assumptions regarding the behavior of vesicles during quenching, suggesting that improper assumptions may explain systematic differences between calculated and simulated CO_2 contents in a suite of MORB samples. Several studies compare 2D and 3D vesicularities and vesicle size distributions in subaerial samples (Baker et al., 2011; Giachetti et al., 2011; Gurioli et al., 2008; Hughes et al., 2017); however, MORB have different vesicle characteristics than most subaerial samples including low vesicularities (i.e., gas volume fractions), low vesicle number densities (i.e., number of vesicles per unit volume), and small vesicle sizes, which motivates a robust evaluation of these methods specific to MORB.

This study examines theoretical and empirical methods for quantifying vesicle populations in a suite of MORB samples and offers new insights into the validity of those methods and best practices for evaluating vesicularity, vesicle size distributions, and CO_2 concentrations in this subgroup of volcanic rocks. We use comparative 2D and 3D measurements of MORB samples along with synthetic data to provide a consistent, comprehensive evaluation of stereological corrections in MORB. We further suggest an improved method for quantifying exsolved CO_2 concentrations based on vesicularity through an evaluation of equations of state, theoretical estimates of vesicle volume change during cooling, and measurements of gas density in MORB samples.

2.3 Background

2.3.1 Stereological corrections

Stereology allows the determination of volumetric vesicle number densities and size distributions from cross-sectional measurements. The mathematical formulations and limitations of stereology are reviewed in Dehoff and Rhines (1968), Hilliard and Lawson (2003) Russ (1986), Underwood (1970) and Vander Voort (1999). Several papers have focused on the application of stereology to vesicle size distributions (e.g. Cashman and Mangan, 1994; Sahagian and Proussevitch, 1998; Shea et al., 2010) and crystal size distributions (e.g. Cashman and Marsh, 1988; Higgins, 2000; Mock and Jerram, 2005; Peterson, 1996). For example, Cashman and Mangan (1994) highlight the two main problems associated with interpreting 3D distributions from 2D imagery. Namely, a randomly placed cross-sectional plane is 1) unlikely to intersect the true diameter of an object and 2) less likely to intersect small objects than large objects. Here, we briefly review various methods proposed for overcoming these stereological problems. Each method requires the assumption that vesicle sizes vary discretely. Thus, the observed vesicle size distribution must first be binned into a finite number of size classes. The median, mean, or maximum vesicle size within a given size class is often chosen as the representative size for that class.

The earliest vesicle and crystal size distribution studies commonly used the equation presented by Wager (1961):

$$Nv_k = {Na_k}^{1.5} \tag{2.1}$$

where Nv is the 3-dimensional vesicle number density (i.e., number of vesicles per unit volume) and Na is the 2-dimensional vesicle number density (i.e., number of vesicles per unit area), each within a given size class k. Subsequent studies applied the alternate formulation presented by Cheng and Lemlich (1983) based on the methods presented by de Vries (1972):

$$Nv_k = \frac{Na_k}{D_k} \tag{2.2}$$

where D_k is the median vesicle diameter in the size class k. Mangan et al. (1993) further proposed that the entire measured size distribution should be multiplied by 1.18 based on the empirical observation that random sections through a single sphere will result in an average measured diameter 0.85 times the true diameter (Cashman and Marsh, 1988).

Saltikov (1967) proposed a different method based on the principle that the distribution of random cross-sectional areas produced by a particle can be predicted based on its shape. The method 'unfolds' the population by successively subtracting the expected cross-sectional distribution produced by larger size classes from each observed size class. The Saltikov method is applicable to particles divided into 12 or fewer class intervals. The number of particles in the kth class interval is given by:

$$Nv_k = \frac{1}{D_k}[1.6461Na_k - 0.4561Na_{k-1} - 0.1162Na_{k-2} - 0.415Na_{k-3} - 0.0173Na_{k-4} - 0.0079Na_{k-5} - 0.0038Na_{k-6} - 0.0018Na_{k-7} - 0.0010Na_{k-8} - 0.0003Na_{k-9} - 0.0002Na_{k-10} - 0.0002Na_{k-11}] \quad (2.3)$$

where the calculation for a given interval continues until the index for Na reduces to zero.

Peterson (1996) proposed an empirical calibration based on linear regressions of $ln(Na)$ on D_k. However, the method proposed by Peterson (1996) requires an assumed unimodal log-normal distribution, which is not always observed in natural samples (e.g., Giachetti et al., 2011). Sahagian and Proussevitch (1998) introduced a more general formulation based on the Saltikov (1967) method that can be easily applied to non-spherical particles, without the need for an assumed size distribution:

$$Nv_k = \frac{1}{P_1 D_k}\left(Na_k - \sum_{j=1}^{k-1} P_{j+1} D_{j+1} N_{v(k-j)}\right) \quad (2.4)$$

where P_k is the intersection probability for a given class interval, given by

$$P_k = \frac{1}{R}\left(\sqrt{R^2 - r_1^2} - \sqrt{R^2 - r_2^2}\right) \quad (2.5)$$

for spherical particles where R is the largest observed radius and r_1 and r_2 are the edges of the class interval. The intersection probabilities were derived numerically for non-spherical particles.

Equations (2.4) and (2.5) apply to vesicle size distributions binned in geometric size classes, for example with each size class $10^{-0.1}$ smaller than the last. Intersection probabilities and stereological methods for linear size classes are also presented in Sahagian and Proussevitch (1998).

Higgins (2000) further modified this stereological correction by calculating intersection probabilities based on the mean diameter rather than the largest diameter with a bin. However, the methods proposed by Cheng and Lemlich (1983) and Sahagian and Proussevitch (1998) are most commonly applied to volcanic rocks (e.g. Cashman et al., 1994; Giachetti et al., 2010; Klug et al., 2002; Klug and Cashman, 1994; Mangan et al., 1993; Shea et al., 2010; Soule et al., 2012) and are therefore chosen for this comparative study.

2.3.2 Comparisons between stereology and x-ray micro-tomography

Stereological methods allow relatively rapid and inexpensive evaluation of vesicle textures, which is particularly beneficial for large sample sets. However, the methods are usually destructive and should only be applied to convex and randomly distributed vesicles. In contrast, x-ray computed micro-tomography (μ-CT) allows non-destructive visualization and quantification of complex and anisotropic vesicle textures (e.g. Barnes et al., 2011; Brown et al., 1999; Carlson and Denison, 1992; Godel et al., 2010; Ketcham, 2005; Ketcham et al., 2005; Polacci et al., 2006, 2012; Song et al., 2001; Voltolini et al., 2011). The principles and techniques of x-ray μ-CT and its applications in geosciences are reviewed in Ketcham and Carlson (2001), Baker et al. (2012), and Cnudde and Boone (2013). Several recent studies have compared vesicle textures measured by stereology and x-ray μ-CT (e.g., Baker et al., 2011; Giachetti et al., 2011; Gurioli et al., 2008; Hughes et al., 2017). Gurioli et al. (2008) observed higher vesicle number densities using the Sahagian and Proussevitch (1998) stereological correction for two scoria bombs but did not compare vesicularities. Baker et al. (2011) found vesicularities within 10 vol.% for one basaltic scoria and one synthetic rhyolitic foam but did not convert 2D vesicle number densities to 3D. Giachetti et al. (2011) found vesicularities within 10 vol.%, but μ-CT vesicle number densities that varied from 37% to 309% of stereological values reconstructed using the Sahagian and Proussevitch (1998) method for four pyroclasts. In this study, we compare vesicularities and vesicle size distributions derived from 2D and 3D methods for 20 MORB samples that span the range of vesicularities (<1 – 20 vol.%) and vesicle number densities (10^1 – $10^{2.5}$ mm^{-3}) observed in global MORB.

3.3.3 MORB CO_2 concentrations

Total MORB CO_2 estimates require constraints on the CO_2 concentration dissolved in the melt and exsolved into vesicles. The dissolved concentration can be measured using Fourier Transform Infrared Spectrometry (e.g., Fine and Stolper, 1986) or Secondary Ion Mass Spectrometry (e.g., Hauri et al., 2002). The exsolved concentration has traditionally been inferred from vesicularity and equations of state (EOS) at the eruption conditions (e.g., Javoy and Pineau, 1991) or measured using capacitance manometry (Burnard, 1997; Moore et al., 1977). Capacitance manometry is less often employed given accuracy limitations caused by gas loss through micro-fractures formed during quenching and sample preparation (e.g., Gerlach, 1991; Moore et al., 1977). The total CO_2 concentration based on vesicularity is usually calculated as the sum of the CO_2 dissolved in the gas and the CO_2 contained in vesicles assuming ideal gas behavior at a glass transition temperature of 726°C (e.g., Aubaud et al., 2004; Chavrit et al., 2014; Hekinian et al., 2000; Javoy and Pineau, 1991; Pineau et al., 2004). In this study, we evaluate and improve methods for calculating total MORB CO_2 concentrations using 2D and 3D vesicularity measurements and CO_2 density determined using Raman spectroscopy.

2.4 Methods

2.4.1 Samples

The MORB glasses analyzed for vesicularity and vesicle size distributions were collected from Axial Seamount on the Juan de Fuca Ridge (N=8; sample descriptions in Jones et al. (2018)) and the Mid-Atlantic Ridge (N=12; sample descriptions in Jones et al. (2019)). The methods for calculating total CO_2 concentrations in MORB were evaluated using samples from the 2011 eruption of Axial Seamount on the Juan de Fuca Ridge. The published 2D vesicularity measurements and dissolved volatile concentrations for the 2011 eruption of Axial Seamount (Jones et al., 2018), combined with new gas density measurements for two samples (AX13-RC13 and AX13-RC06), make these samples ideal for evaluating methods for quantifying CO_2 concentrations in MORB. Previously published data for Axial Seamount samples include the 2D vesicularities, 2D vesicle size distributions, and 2D vesicle number densities (Jones et al., 2018). Previously published data for Mid-Atlantic Ridge samples include the 2D and 3D vesicularities, 3D vesicle size distributions, and 3D vesicle number densities (Jones et al., 2019).

2.4.2 Reflected light photomicrographs

Vesicularities and vesicle size distributions were measured using 10x magnification reflected light photomicrograph mosaics of polished glass fragments from the outer 1 cm of MORB samples, following methods described in Jones et al. (2018). Vesicles, glass, and the surrounding epoxy were digitally separated using the MATLAB image processing toolbox. Cracks and non-vesicles were cleaned using image analysis software (ImageJ) (Schindelin et al., 2012). Vesicle areas were determined using ImageJ's analyze particles tool. Only vesicles larger than 15 μm in diameter (~3x the maximum x-ray μ-CT pixel size) are considered for comparison with x-ray μ-CT results. Vesicularity (2D) was calculated as the percent fraction of the fragment area represented by vesicles. 2D data (i.e. Na and the surface area distribution of vesicles) were converted to 3D data (i.e. Nv and the volume distribution of vesicles) using the Cheng and Lemlich (1983) and Sahagian and Proussevitch (1998) stereological corrections. The measured size distributions were multiplied by 1.18 prior to applying the Cheng and Lemlich (1983) stereological correction, based on the recommendation from Mangan et al. (1993). The results reflect the average values for samples with multiple polished fragments analyzed.

2.4.3 X-ray micro-tomography

X-ray μ-CT scans were collected using a Bruker Skyscan 1272 at the Woods Hole Oceanographic Institution, using methods described by Jones et al. (2019) and acquisition/reconstruction parameters listed in Supplementary Table S.2.1. The step size for transmitted radiograph collection was between 0.15° and 0.35° over 180°, the source voltage was 65 – 100 kV, the current was 100 – 153 μA, and the pixel resolution was 0.5 – 5.0 μm. Beam hardening, ring artifact, and thermal misalignment corrections (Ketcham and Carlson, 2001) were applied during reconstruction using the Bruker NRecon software. The reconstructed data was digitally segmented using a global threshold in Bruker CTAn software. Cracks and non-vesicles were manually removed using ImageJ following identification in Bruker visualization software. CTAn, ImageJ, and MATLAB image processing tools were used to calculate individual vesicle parameters. Only vesicles larger than 15 μm in radius (~3x the maximum pixel size) are considered for comparison with stereology results.

The spatial resolution and volume of sample imaged in a μ-CT scan are commonly proportional to the distance between the x-ray source and the scanned object (Ketcham and Carlson, 2001).

Although higher scan resolutions allow the detection of smaller objects, higher resolutions also limit sample size and thus the probability of detecting the largest vesicles, which often occur with the lowest frequency. Some previous studies have conducted scans at multiple resolutions in order to capture the entire size distribution of vesicles, which often spans several orders of magnitude (e.g. Bai et al., 2011; Giachetti et al., 2011). The observed vesicle radii (3 μm – 1 mm) and vesicularity (<1 – 20 vol.%) in this study spans the range typically observed in MORB (Burnard, 1999; Chavrit et al., 2014; Gardner et al., 2016; Soule et al., 2012) and enables us to evaluate optimal sample sizes and spatial resolutions for MORB vesicle studies. Three of the 20 samples were imaged using x-ray μ-CT at varying spatial resolutions in order to evaluate the effect of sample size and resolution on observed vesicle size distributions.

2.4.4 Synthetic vesicle populations

In order to evaluate errors associated with stereological methods, synthetic vesicle populations were generated using MATLAB for the range of vesicle number densities and porosities typically observed in MORB. The vesicles are randomly distributed in space and the individual vesicle sizes were randomly selected from a pre-defined exponential distribution. The vesicles were restricted from overlapping. Synthetic 'thin sections' were created by analyzing random planes through the vesicle population. The Cheng and Lemlich (1983) and Sahagian and Proussevitch (1998) stereological corrections were applied to the synthetic thin sections and evaluated by comparing results with the known 3D distribution.

2.4.5 Confocal Raman spectroscopy

The density of CO_2 in vesicles was determined using a Horiba LabRam HR Raman spectrometer at the Woods Hole Oceanographic Institution using methods described in Jones et al. (2019), following previously established protocols (e.g., Esposito et al., 2011; Moore et al., 2015). We used a 100x long working distance objective with a numerical aperture of 0.8, a 632 nm laser, a grating with 1800 grooves/mm, a confocal hole diameter of 300 μm, and a slit size of 30 μm. Spectra were collected for three 60 s acquisitions between 1160 and 1429 cm^{-1}. The background for each spectrum was subtracted using LabSpec6 and the peaks were fit using a Gaussian function in MATLAB. The CO_2 Fermi diad splits were calibrated using the measured separation between the 1249.03 cm^{-1} and 1388.25 cm^{-1} bands for argon, which drifted by <0.05 cm^{-1} during each session. The calibration

developed by Lamadrid et al. (2017) at Virginia Tech for a 632 nm laser and 1800 grooves/mm grating was used to calculate the density of CO_2 within the vesicles based on the difference in wavenumber between the two peaks of the Fermi diad (Wright and Wang, 1973). In addition to the previous methods described for calculating CO_2 densities, lower resolution scans between 200 and 4200 cm^{-1} were collected for each bubble using three 30 s acquisitions, a 600 grooves/mm grating, a 100 μm slit size, a 500 μm confocal hole diameter, and a 632 nm laser in order to identify other gaseous species (e.g., CO_2, SO_2, CH_4, N_2, H_2, and H_2O; Frezzotti et al., 2012).

2.5 Results

2.5.1 Qualitative visual observations

The following visual observations were made based on the reflected light photomicrographs and reconstructed x-ray μ-CT scans (Figure 2-1). The visually estimated crystal concentration is <2% for all samples. The crystals are commonly clustered and often touching vesicles. All samples display similar vesicle textures. Small vesicles (<250 μm radius) appear mostly spherical while larger vesicles appear occasionally elongated (Figure 2-1c). The smallest vesicles (<20 μm radius) are often clustered near crystals (Figure 2-1d). Vesicle coalescence occurs in small proportions in most samples. Coalescence is observable in both the reflected light photomicrographs and x-ray μ-CT scans in high vesicularity (>6 vol.%) samples (Figure 2-1c), but only in the x-ray μ-CT scans in most low vesicularity samples. Vesicle-vesicle interactions, such as dimpling surfaces in larger vesicles caused by proximal, smaller vesicles, occur in the more vesicular (>6 vol.%) samples (e.g., Figure 2-1c). Although the samples display minor clustering, coalescence, and vesicle-vesicle interactions, these samples have relatively simple vesicle textures relative to subaerial basalt or pumice (Giachetti et al., 2011; Hughes et al., 2017; Polacci et al., 2006; Song et al., 2001) and therefore should be ideal candidates for evaluating stereological conversion methods.

2.5.2 Quantitative measurements from 2D and 3D methods

The quantitative parameters derived from the reflected light photomicrographs and x-ray μ-CT scans are listed in Supplementary Table S.2.2. All samples contain vesicles near the resolution limit for the applied methods (15 μm radius) while the maximum vesicle radius ranges from 50 to 1574 μm. The 2D vesicularities are within 4.6 vol.% of the 3D values, with relative errors ($\frac{|\Phi_{2D}-\Phi_{3D}|}{\Phi_{3D}}$,

where Φ is vesicularity) ranging from 0.03 to 0.46, with a mean of 0.17. Each reconstructed x-ray μ-CT scan contains ~2500 stacked 2D slices. The 2D vesicularities calculated from these individual slices provide insight into the probability of a randomly selected polished section displaying a 2D vesicularity near the bulk 3D vesicularity. Histograms of 2D vesicularities calculated from the individual x-ray μ-CT slices are commonly normally distributed with an average standard deviation 0.3 times the mean, however, several histograms display multiple peaks (e.g., Figure 2-2).

The cumulative vesicle number density calculated using the methods of Cheng and Lemlich (1983) ranges from 45 to 133% the 3D values (μ=88%) , while Nv produced using the methods of Sahagian and Proussevitch (1998) ranges from 46 to 150% those measured in 3D (μ= 91%), roughly ½ the range observed in Giachetti et al. (2011) in four subaerial pyroclasts.

The natural log of the vesicle number density ($\ln(n)$), normalized based on the width of the size class, displays a linear relationship with the vesicle diameter (L) with some deviations at large size classes in the highest vesicularity samples (Figure 2-3). These relationships between $\ln(n)$ and L are similar to observations from other subaerial and submarine basalts (Cashman et al., 1994; Chavrit et al., 2014; Klug and Cashman, 1994; Mangan et al., 1993; Sarda and Graham, 1990; Soule et al., 2012). As described in Cashman and Mangan (1994), the intercept given by the regression of $\ln(n)$ on L represents the volumetric number density of vesicle nuclei ($\ln(N_o)$) and the slope represents $-\frac{1}{G\tau}$ where G represents the mean vesicle growth rate and τ is the time scale of nucleation and growth. $G\tau$ calculated using the Cheng and Lemlich (1983) method ranges from 72 to 123% the 3D values (μ=98%), while $G\tau$ calculated using the Sahagian and Proussevitch (1998) methods ranges from 68 to 144% the 3D values (μ=99%). $\ln(N_o)$ varies from 89 to 152% the 3D values (μ=103%) using the methods of Cheng and Lemlich (1983) and from 91 to 175% the 3D values (μ=116%) using the Sahagian and Proussevitch (1998) methods. The vesicle volume distributions are observed to be lognormal with slight deviations at large size classes in some samples based on both the stereological and x-ray μ-CT measurements (e.g. Figure 2-4).

2.5.3 Comparison between scans at multiple resolutions

X-ray μ-CT scans collected at multiple resolutions for the same samples (AX13-RC02, AL4820-037, and AL4821-054) were subjected to the same analysis methods for comparison (Supplementary

Table S.2.1). The samples display log-linear vesicle size distributions and log-normal vesicle volume distributions at both resolutions (Figure 2-4). The largest vesicle size measured in the lower-resolution scans is greater than in the higher-resolution scans (Supplementary Table S.2.2). The largest size classes observed in the lower resolution scans are commonly missing in the higher resolution scans (Figure 2-4). However, higher-resolution scans capture a greater number of small vesicles and have greater total vesicle number densities. The vesicularity in the higher-resolution scan is smaller than in the lower-resolution scan for two of the three samples scanned at multiple resolutions (Supplementary Table S.2.2).

2.5.4 Results from synthetic vesicle analysis

The coefficient of determination (R^2) between the vesicle size distribution reconstructed from 2D slices and the synthetic 3D vesicle populations increases logarithmically with the number of vesicles analyzed (Figure 2-5). The average coefficient of determination between the Cheng and Lemlich (1983) and 3D population is greater than for the Sahagian and Proussevitch (1998) correction. The method for treating vesicles on the edge of the region of interest does not impact the correlation between the stereological measurements and the 3D vesicle size distribution, likely due to the low proportion of vesicles on the edge relative to the total number of vesicles.

2.5.5 Gas density determined by Raman spectroscopy

Thirteen vesicles from samples AX13-RC06 and AX13-RC13, which were chosen randomly for analysis and collected from the seafloor at similar pressures, had detectable $CO_{2(g)}$ bands in the acquired Raman spectra (Supplementary Table S.2.3). We qualitatively found that $CO_{2(g)}$ was reliably observed in spectra collected from vesicles less than ~50 μm below the polished surface, while a Gaussian function could be reliably fit to the data for vesicles less than ~30 μm below the polished surface. The average Fermi diad splitting in vesicles with detectable $CO_{2(g)}$ bands was 102.83 ± 0.02 cm^{-1} (uncertainty is 1σ), corresponding to a density of 0.05 ± 0.01 g/cm^3 (Figure 2-6, Supplementary Table 2.2.3). Four of the 13 vesicles analyzed exhibited small peaks near 1151 cm^{-1} in the coarse resolution scans, likely associated with SO_2 (Figure 2-6, Frezzotti et al., 2012). Three of the 13 vesicles analyzed showed Raman bands associated with pyrite in the coarse resolution scans (Figure 2-6), and one vesicle displayed peaks associated with a hydrous manganese sulfate mineral (Held and Bohatý, 2002). None of the 13 vesicles analyzed showed Raman bands associated with carbonate at

~1080 – 1094 cm^{-1}. The spectra commonly displayed a broad peak between ~800 and ~1100 cm^{-1}, which was likely associated with silicate glass.

2.6 Discussion

2.6.1 Optimal sample size and spatial resolution for MORB vesicularity studies

The inherent trade-off between x-ray μ-CT resolution and sample volume analyzed can impact the measured vesicularity and vesicle number density. Two of the three samples scanned at multiple resolutions demonstrate that analyzing too small of a sample volume, despite the potential for improved resolution, can produce erroneous vesicularities and vesicle size distributions. The limited sample volume likely caused the apparent truncation of the vesicle size distributions and vesicle volume distributions in the higher-resolution scans relative to the lower-resolution scans (Figure 2-4). The truncation of the largest vesicles, which comprise a large proportion of the total vesicularity, can explain the vesicularity difference between the higher- and lower-resolution scans for samples AX13-RC02 and AL4820-037. In contrast, the lower resolution scan for AL4821-054 has higher vesicularity due to more abundant small to medium sized vesicles, possibly due to improved detection of these size classes or natural variability in the distribution of vesicles (Figure 2-4). Based on these results, we suggest that sample volumes >0.01 cm^3 and resolutions <2.0 μm/pixel should allow accurate vesicularity, vesicle number density, and vesicle size distribution measurements for low vesicularity (i.e., <4 vol.%) MORB. For higher vesicularity (i.e., >4 vol.%) MORB, larger samples volumes (>0.1 cm^3) with resolutions <5.0 μm/pixel are required. The trade-off between resolution and sample volume analyzed could also be circumvented collecting x-ray μ-CT scans at multiple spatial resolutions (e.g., Giachetti et al., 2011).

2.6.2 Effectiveness of stereological corrections

Based on the comparison between the reflected light photomicrographs and x-ray μ-CT scans, 2D measurements can be used to accurately determine the vesicularity in mid-ocean ridge basalts. However, we note that sufficient fragment sizes and replicate measurements are essential for the accurate assessment of vesicularity. The variability in vesicularity between individual slices from the x-ray μ-CT reconstructions (Figure 2-2) along with the large uncertainties in vesicle size distributions at low sampling densities (Figure 2-5) demonstrate that individual cross-sections can differ substantially in both vesicularity and vesicle size distribution from the bulk population. In order to

minimize the errors associated with quantifying bulk vesicularity using 2D measurements, we recommend analyzing a total fragment area >100 times the area of the largest measured vesicle. Most MORB have maximum vesicle radii <500 μm (Chavrit et al., 2012), corresponding to a recommended total fragment area of >0.78 cm^2. Based on the observed variability in vesicularity between slices of the reconstructed x-ray μ-CT scans (Figure 2-2), we also recommend analyzing multiple fragments from each sample.

Rates of gas exsolution, used to infer eruption rates and lava flow rates from measured CO_2 supersaturation and vesicularity (Jones et al., 2018; Soule et al., 2012), are highly sensitive to the vesicle number density (Gardner et al., 2016), demonstrating the importance of employing appropriate methods for characterizing vesicle size distributions and number densities. The comparison between reflected light photomicrographs and x-ray μ-CT scans suggests that 2D methods can accurately characterize vesicle size distributions in MORB glass, given sufficient sample sizes and measurements on multiple fragments. Based on the correlation between the stereological data and synthetic 3D vesicle size distributions for each method (Figure 2-5), we slightly prefer the Cheng and Lemlich (1983) correction. However, we anticipate that either method will accurately reproduce the 3D vesicle size distribution when >200 vesicles are analyzed. In addition, we note that comparisons between multiple studies require consistency in the minimum vesicle size included in the vesicle size distribution and number density.

2.6.3 Calculating total CO_2 concentrations in MORB

The similarity between 2D and 3D vesicularity measurements validates the use of 2D measurements to evaluate the concentration of exsolved gas in MORB. Previous studies have commonly converted from glass vesicularity to exsolved CO_2 concentration using the ideal gas law, the eruption pressure, and glass transition temperature, T_g = 726°C based on experimental results from Ryan and Sammis (1981) (e.g. Aubaud et al., 2004; Chavrit et al., 2014; Hekinian et al., 2000; Javoy and Pineau, 1991; Pineau et al., 2004). For samples from the 2011 eruption of Axial Seamount, these methods would predict $CO_{2(g)}$ densities of ~0.08 g/cm^3 and exsolved CO_2 concentrations ranging from 20 – 533 ppm for 2D vesicularity measurements reported in Jones et al. (2018). However, the low gas densities determined by Raman spectroscopy for 2011 Axial Seamount eruption samples (~0.05 g/cm^3; Supplementary Table S.2.3) indicate that traditional methods may not reliably constrain the exsolved CO_2 concentration in MORB. The average gas density determined by Raman spectroscopy

yields exsolved CO_2 concentrations ranging from 12 – 309 ppm, which is ~0.65 times those given by traditional methods. This discrepancy could reflect the presence of other gas species in the vesicles, but only three of the vesicles showed Raman bands associated with SO_2. Two alternative explanations are higher glass transition temperatures (T_g) or lower internal vesicle pressures. Here, we discuss mechanisms that could cause high glass transition temperatures or low vesicle pressures and consequentially lower gas densities.

First, we evaluate the glass transition temperature for MORB with chemical compositions similar to the 2011 Axial Seamount eruption using an updated viscosity model (Hui and Zhang, 2007) and the temperature function of Carslaw and Jaeger (1986). We evaluate vesicle contraction during quenching using the momentum balance formulation presented in Arefmanesh and Advani (1991) (see Appendix A for methodology). We find that the viscosity begins to increase rapidly at ~830°C, which prevents any further vesicle contraction (Figure 2-7). Based on the conductive cooling model from Carslaw and Jaeger (1986), vesicles 1 mm below the lava surface would pass through the 830°C glass transition temperature within 3 seconds. T_g = 830°C would predict gas densities only 10% less than expected based on traditional methods (i.e. T_g = 726°C), which cannot fully explain the discrepancy with the Raman spectroscopy data. Glass transition temperatures would need to be much greater (~1200°C) in order to explain the low densities determined by Raman spectroscopy, which disagrees with calorimetric studies on the glass transition temperature (e.g. Gottsmann et al., 2002).

Alternatively, melt contraction during cooling could result in low internal vesicle pressures and lower than expected gas densities. Studies on vapor bubbles in melt inclusions have shown that melt contraction in a fixed-volume system may lead to an increase in the volume of bubbles during quenching, and consequently low gas densities (e.g., Aster et al., 2016). According to the model for melt density provided by Lange (1994), melt contraction in a fixed volume system would increase the observed vesicularity by up to 2 vol.% during cooling from 1200°C to 826°C. This maximum volume increase requires a fixed lava flow surface. Although it is unlikely that the surface of the lava flow remains completely fixed during quenching, melt contraction could partially account for the observed low gas densities in MORB vesicles.

Based on the consistently low gas density measurements in this study relative to those predicted by T_g = 726°C and the ideal gas law, we recommend using sample eruption pressures, magmatic

temperatures (~1200°C), and an equation of state that accounts for non-ideality at high temperatures (e.g., Flowers, 1979) to calculate exsolved CO_2 in MORB when independent constraints from Raman spectroscopy are unavailable. Using these methods, we obtain exsolved CO_2 concentrations (13 – 346 ppm) comparable to those calculated using gas densities determined by Raman spectroscopy (12 – 309 ppm). Further, our revised method yields relatively constant total CO_2 concentrations in samples from the 2011 Axial Seamount eruption when combined with dissolved measurements by SIMS from Jones et al. (2018) (Figure 2-8). The constant total concentration indicates closed-system degassing during magma ascent and lava emplacement and CO_2 saturation at ~2 km depth in the crust, similar to the depth of the seismically imaged magma reservoir (Arnulf et al., 2014). These recommended methods can further reproduce gas densities determined by Raman Spectroscopy in vesicles within high vesicularity popping rocks from the Mid-Atlantic Ridge (Jones et al., 2019). Lastly, our recommended methods yield relatively constant total CO_2 concentrations in samples from the 2005-06 eruption at the East Pacific Rise (Gardner et al., 2016), supporting the interpretation that closed system degassing occurred during the final stages of magma ascent and lava emplacement (Graham et al., 2018; Soule et al., 2012).

2.6.4 Implications for upper mantle carbon content and ridge CO_2 flux

Our results suggest traditional methods for calculating exsolved CO_2 concentrations in MORB, based on the ideal gas law, glass transition temperature, and eruption pressure, can overestimate total CO_2 concentrations in MORB by up to 50% (e.g. Figure 2-8). These results may partially explain the consistent difference in CO_2 concentration inferred from vesicularity and measured by gas manometry (e.g. Gerlach, 1991; Moore et al., 1977), with the remainder likely resulting from gas loss through cracks prior to measurement. The smallest differences between our recommended methods and traditional methods occur in samples with low vesicularity and high proportions of CO_2 in the dissolved phase (e.g., Michael and Graham, 2015); the two methods are equivalent for samples with no vesicles. The largest differences occur in samples with the highest vesicularities and lowest proportions of dissolved CO_2, in which case traditional methods could overestimate the total CO_2 concentration by 50%. For example, traditional methods estimate that the 'popping rock' 2πD43 contains ~13,300 ppm CO_2 (CO_2/Nb = 556 and CO_2/Ba = 76; Cartigny et al., 2008; Javoy and Pineau, 1991; Le Voyer et al., 2017), whereas our recommended method yields ~8,800 ppm CO_2 (CO_2/Nb = 376 and CO_2/Ba = 50). One recent study suggested that high vesicularity popping rocks reflect bubble accumulation, while intermediate vesicularity samples (5 – 7 vol.%) reflect

primary volatile concentrations (Jones et al., 2019). For these samples, our recommended method yields ~2,600 ppm CO_2 (CO_2/Nb = 108 and CO_2/Ba = 17), whereas traditional methods suggest that samples with 5 – 7 vol.% vesicles contain ~3,800 ppm CO_2. The difference between the recalculated CO_2/Ba ratios in popping rocks (17 – 50) and CO_2/Ba ratios in undegassed, depleted melt inclusions from the Equatorial Atlantic (97; Le Voyer et al., 2017) and Siqueiros transform fault (100; Saal et al., 2002) provides evidence for heterogeneities in the source CO_2/Ba ratio. Therefore, we suggest that primary CO_2 concentrations and ridge CO_2 flux cannot be accurately calculated by multiplying segment average trace element concentrations and magmatic production rates by a single CO_2/Ba, CO_2/Nb, or CO_2/Rb ratio (e.g., Le Voyer et al., 2019) and that these calculation methods have likely overestimated source carbon concentrations and integrated global ridge CO_2 flux.

2.7 Conclusions

We demonstrate that 2D analyses combined with stereological techniques accurately reproduce vesicularities and vesicle size distributions in MORB given sufficient sample sizes and replicate measurements. For accurate 2D results, we recommend measuring multiple fragments from each sample and analyzing a total fragment area >100 times the area of the largest measured bubble. We further recommend analyzing at least 200 vesicles for accurate vesicle size distributions using the stereological method presented by Cheng and Lemlich (1983) with the empirical adjustment from Mangan et al. (1993). Our results show that total CO_2 concentrations can be accurately calculated based on vesicularity. When possible, we recommend analyzing the gas density in vesicles <30 μm below the polished surface using Raman spectroscopy. When constraints from Raman spectroscopy are not available, we suggest that magmatic temperatures, eruption pressures, and non-ideal equations of state should be used to calculate the exsolved CO_2 concentration in MORB based on vesicularity. Our results imply lower CO_2 concentrations in MORB glasses than previously estimated, especially in samples with high vesicularity such as the 'popping rock' 2πD43 where CO_2 concentrations may have been overestimated by ~50%. Thus, our results hold important implications for mantle carbon abundances and ridge CO_2 flux.

2.8 Acknowledgments

We are thankful to the captain, crew, vehicle teams, and science participants of the R/V Thompson VISIONS'11 cruise, R/V Western Flyer Northern Expeditions cruises, and R/V Atlantis AT33-03

cruise for assistance in collecting the samples used in this study. We thank T. Grove, D. Lizarralde, and M. Kurz for insightful comments on an early version of this work. We thank R. Bodnar, G. Gaetani, H. Lamadrid, A. Pamukcu, and T. Shea for helpful conversations. M. Jones was supported by the Department of Defense (DoD) through the National Defense Science & Engineering Graduate Fellowship (NDSEG) Program. This work was supported by an ExxonMobil student research grant and NSF grants OCE-1333492, OCE-1259218, and OCE-1260578.

2.9 Figures

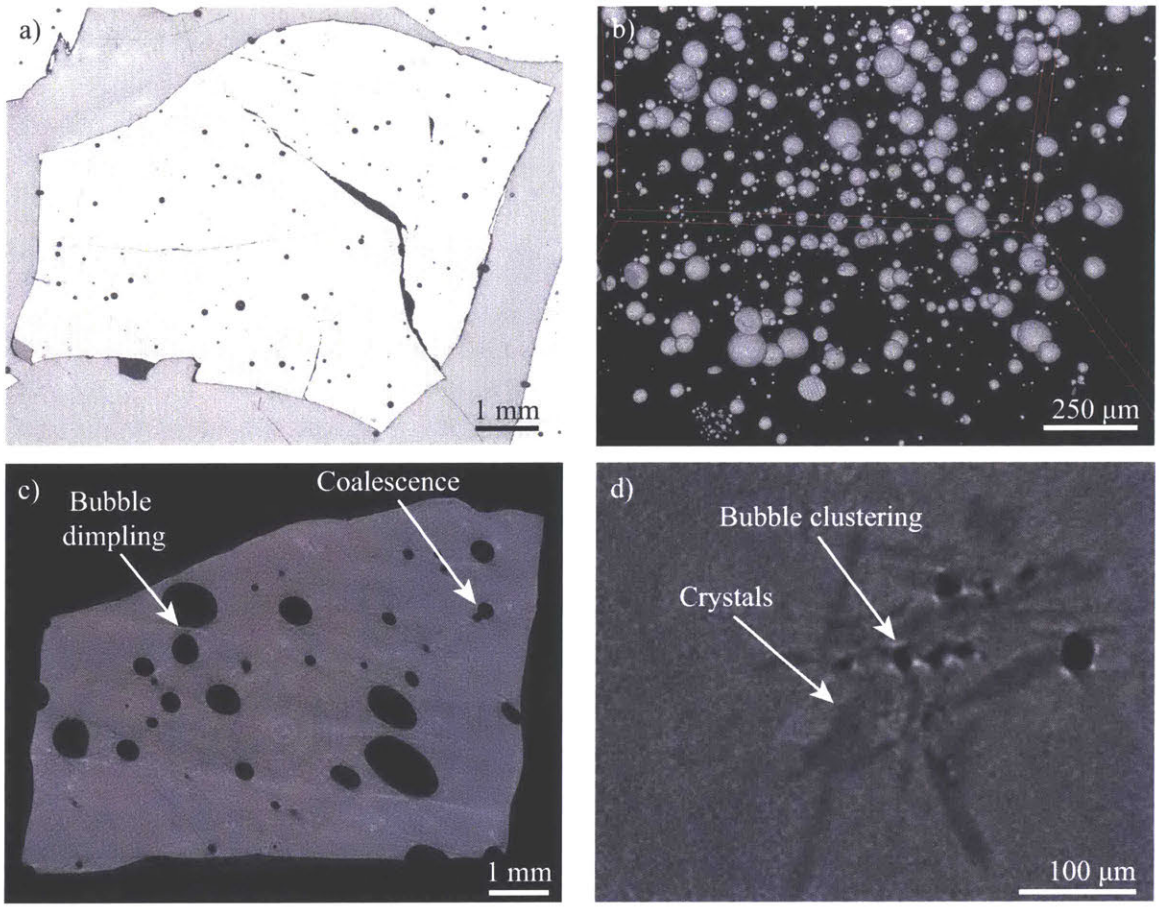

Figure 2-1. Representative (a) reflected-light photomicrograph and (b) x-ray µ-CT reconstruction. The samples display minor amounts of (c) bubble coalescence and interaction with other bubbles (e.g. dimpling surfaces) and (d) clustering near crystals but appear predominantly spherical and randomly distributed.

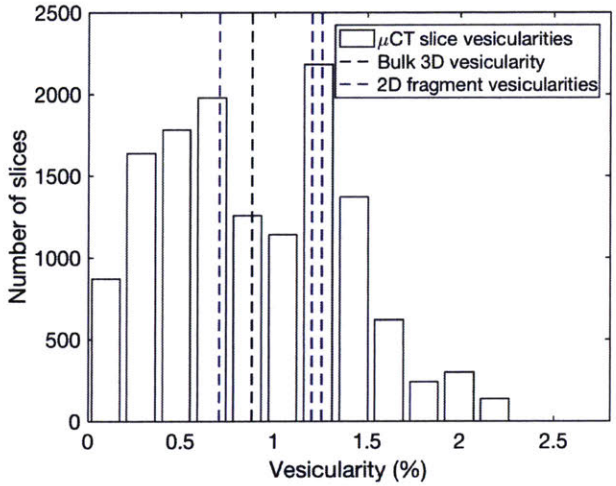

Figure 2-2. Histogram of 2D slice vesicularities from the x-ray μ-CT reconstruction for sample AX13-RC05. Histograms of individual slice vesicularities commonly display multiple peaks, demonstrating that accurate 2D vesicularity measurements require large analysis areas and/or multiple measurements.

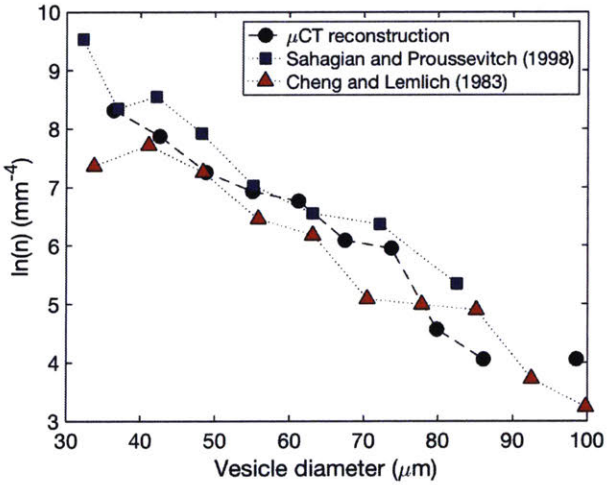

Figure 2-3. Vesicle size distribution based on stereological corrections and the x-ray μ-CT scan reconstruction for sample AX13-RC04. The vesicle size distributions are commonly log-linear and the vesicle volume distributions are commonly log-normal with slight deviations at large size classes in some samples.

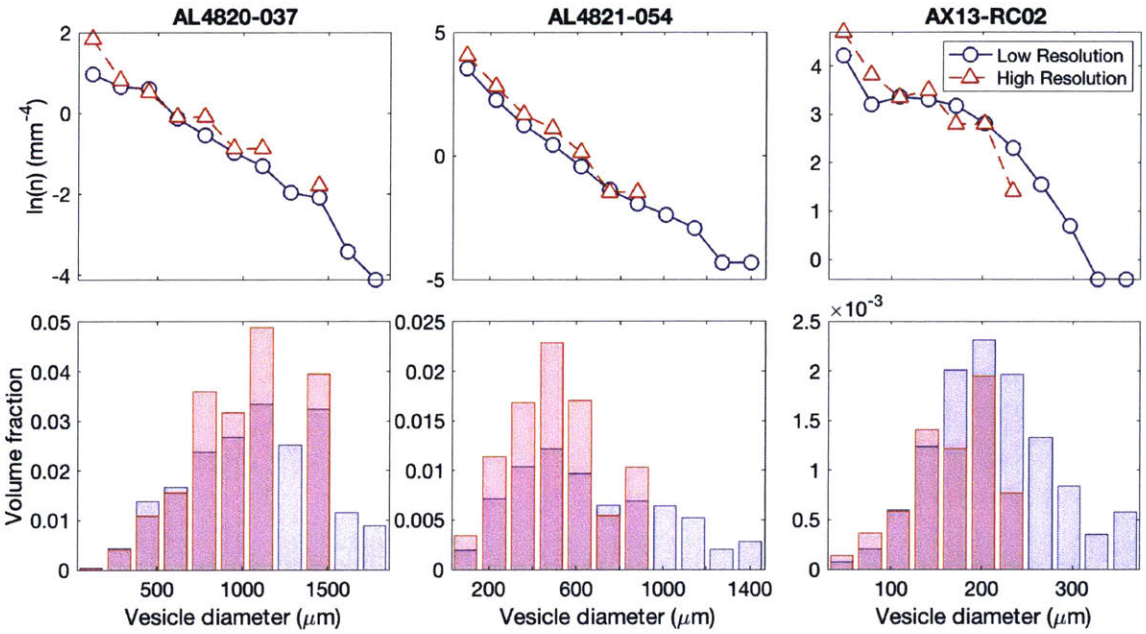

Figure 2-4. Vesicle size distributions (top) and volume distributions (bottom) for high resolution (red) and low resolution (blue) scans demonstrating that high resolution scans may produce erroneously low vesicularities by missing the largest bubbles due to the trade-off between sample volume and scan resolution.

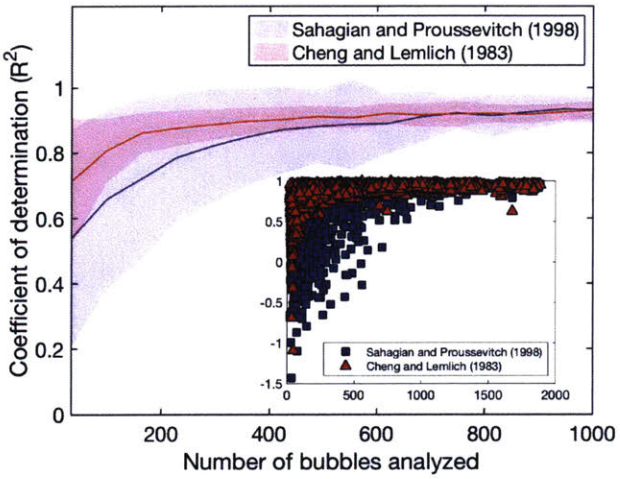

Figure 2-5. Mean coefficient of determination (R2, solid lines) ± 1σ (filled polygons) between the Cheng and Lemlich (1983) and Sahagian and Proussevitch (1998) stereological corrections and the synthetic 3D vesicle size distributions as a function of the number of bubbles analyzed. Mean and standard deviation were calculated by binning the data; inset shows the R2 for each synthetic slice analyzed.

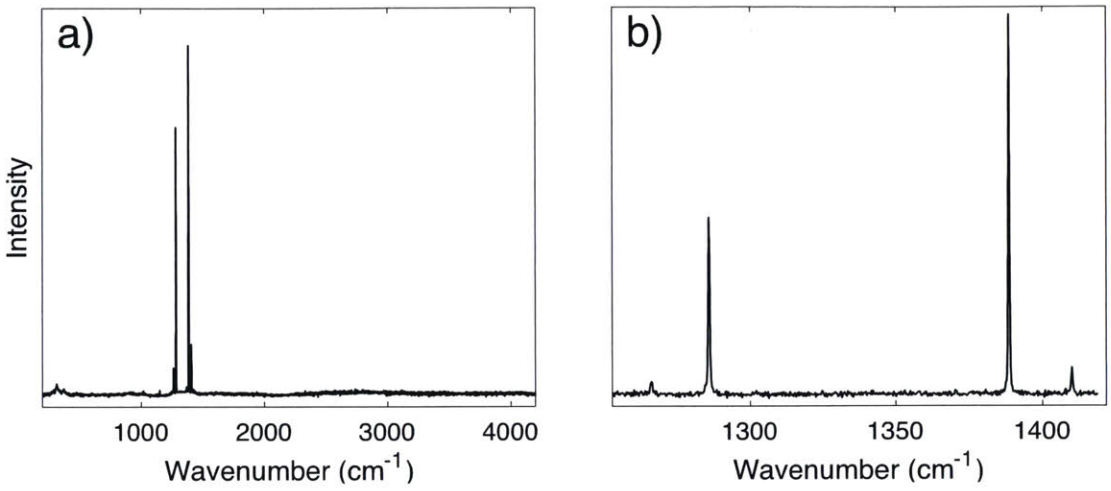

Figure 2-6. (a) Broad range Raman spectrum collected from a vesicle within sample AX13-RC06, showing that the CO2 is the primary detectable gas species with peaks at ~1249 and 1388 cm^{-1}. Small peaks associated with pyrite and SO2 are present in the Raman spectra from some of the vesicles. (b) Higher resolution Raman spectrum from the same vesicle showing the Fermi diad associated with $CO2_{(g)}$. The distance between the two primary peaks of the Fermi diad is density (pressure) dependent and is used to constrain the CO2 density in MORB bubbles.

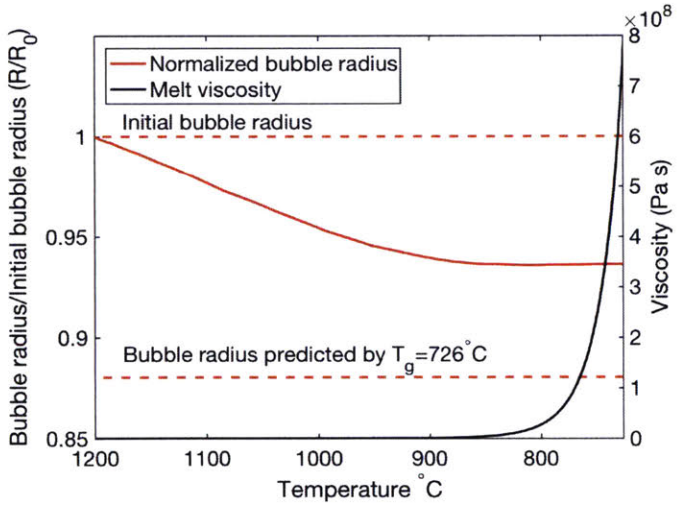

Figure 2-7. Modeled bubble size (left axis) and viscosity (right axis) as a function of temperature. The viscosity begins to increase rapidly at ~830°C, which prevents any further bubble contraction and partially explains the low gas density measured in MORB bubbles by Raman spectroscopy. The remaining difference may result from melt contraction during cooling.

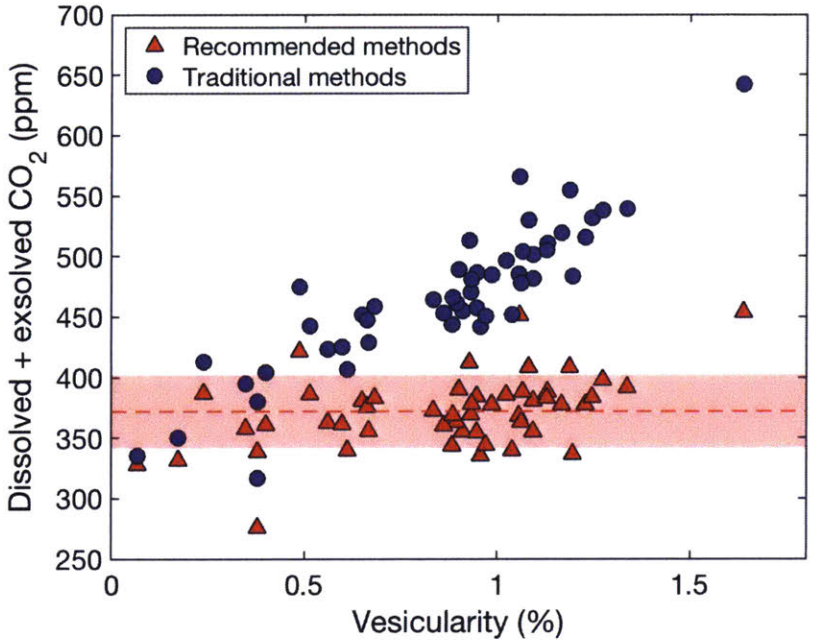

Figure 2-8. Calculated total CO_2 concentrations (measured dissolved concentrations from Jones et al. (2018) + calculated exsolved concentrations) vs. vesicularity in samples from the 2011 eruption of Axial Seamount. The blue circles show calculations using the ideal gas law, a glass transition temperature of 726°C, and the eruption pressure, while the red triangles reflect our recommended methods using a modified Redlich-Kwong equation of state (Flowers, 1979), magmatic temperatures, and the eruption pressure. The red dashed line shows the mean total CO_2 concentration using our recommended methods and the red box shows $\pm$ 1σ.

2.A Vesicle contraction during cooling

The rate of vesicle wall movement during quenching can be evaluated from a modified version of the momentum balance presented in Arefmanesh and Advani (1991), Chouet et al. (2006), and Proussevitch and Sahagian (1998):

$$\frac{dr}{dt} = \frac{r}{4\eta(t)}\left(\frac{nRT(t)}{\frac{4}{3}\pi r^3} - P_e - \frac{2\sigma}{r}\right) \tag{2.6}$$

where t is time, T is temperature, η is the viscosity, r is the vesicle radius, n is the moles of gas, R is the ideal gas constant, P_e is the eruption pressure, and σ is the surface tension. For simplicity, we consider the contraction of a single vesicle located one millimeter below the lava surface during quenching. We evaluate various initial radii and calculate n from the initial vesicle radius, ideal gas law, eruption pressure, and initial temperature (i.e. 1200°C). The surface tension is 0.32 Nm^{-1} (Proussevitch and Sahagian, 1998).

The temperature is modeled as conductive heat flow in two half-spaces with a constant temperature at the interface (Carslaw and Jaeger, 1986):

$$T(x,t) = \Delta T \,\mathrm{erf}\left(\frac{x}{2\sqrt{\kappa t}}\right) + T_s \tag{2.7}$$

where x is the distance (m) to the melt-water interface, κ is the thermal diffusivity, T_s is the seawater temperature (0°C) and ΔT is the temperature difference between the seawater and lava (initially 1200°C). We calculate the viscosity using the temperature dependent model of Hui and Zhang (2007). We evaluate the final vesicle size by numerical solving equation (1) using the temperature given by equation (2) and the viscosity given by the model of Hui and Zhang (2007). We calculate the final gas density from the initial moles of gas, molar weight, and final vesicle size.

Chapter 3

Magma ascent and lava flow emplacement rates during the 2011 Axial Seamount eruption based on CO_2 degassing

This chapter was originally published as: Jones, M.R., Soule, S.A., Gonnermann, H.M., Le Roux, V., Clague, D.A., 2018. Magma ascent and lava flow emplacement rates during the 2011 Axial Seamount eruption based on CO2 degassing. Earth Planet. Sci. Lett. 494, 32–41. 10.1016/j.epsl.2018.04.044.

3.1 Abstract

Quantitative metrics for eruption rates at mid-ocean ridges (MORs) would improve our understanding of the structure and formation of the uppermost oceanic crust and would provide a means to link volcanic processes with the conditions of the underlying magmatic system. However, these metrics remain elusive because no MOR eruptions have been directly observed. The possibility of disequilibrium degassing in mid-ocean ridge basalts (MORB), due to high eruptive depressurization rates, makes the analysis of volatile concentrations in MORB glass a promising method for evaluating eruption rates. In this study, we estimate magma ascent and lava flow emplacement rates during the 2011 eruption of Axial Seamount based on numerical modeling of diffusion-controlled bubble growth and new measurements of dissolved volatiles, vesicularity, and vesicle size distributions in erupted basalts. This dataset provides a unique view of the variability in magma ascent (~0.02–1.2 m/s) and lava flow rates (~0.1–0.7 m/s) during a submarine MOR eruption based on 50 samples collected from a >10 km long fissure system and three individual lava flow lobes. Samples from the 2011 eruption display an unprecedented range in dissolved CO_2 concentrations, nearly spanning the full range observed on the global MOR system. The variable vesicularity and dissolved CO_2 concentrations in these samples can be explained by differences in the extent of degassing, dictated by flow lengths and velocities during both vertical ascent and horizontal flow along the seafloor. Our results document, for the first time, the variability in magma ascent rates during a submarine eruption (~0.02–1.2 m/s), which spans the global range previously proposed based on CO_2 degassing. The slowest ascent rates are associated with hummocky flows while faster ascent rates produce channelized sheet flows. This study corroborates degassing-based models for eruption rates using comparisons with independent methods and documents the relationship between eruption dynamics, magma ascent rates, and the morphology of eruptive products. Globally, this approach allows interrogation of the processes that govern mid-ocean ridge eruptions and influence the formation of the oceanic crust.

3.2 Introduction

Magma ascent and effusion rates exert a strong control on basaltic eruption and emplacement styles, influencing the explosive potential of an eruption, rates of lava flow advance, formation of distributary networks, and morphology of eruptive products. Although several recent mid-ocean ridge (MOR) eruptions have been identified from repeat, high-resolution bathymetric surveys, seafloor instrumentation, post-eruption observations, and radiometric dating (Caress et al., 2012; Chadwick et al., 2016, 1991; Dziak et al., 2009; Fox et al., 2001; Rubin et al., 1994; Soule et al., 2007), no MOR eruption has been directly observed (Rubin et al., 2012). Thus, MOR eruption rates are typically estimated from indirect measures such as seismicity (Dziak et al., 2012, 2007; Tan et al., 2016) and lava flow morphology (Chadwick et al., 2013; Fundis et al., 2010; Gregg and Fink, 1995; Perfit and Chadwick, 1998; Soule et al., 2007). Although seismicity-based methods provide quantitative information about ascent rates (Dziak et al., 2012, 2007) and emplacement rates (Tan et al., 2016), these methods require nearby seafloor instrumentation during the eruption, which is rarely available. Further, lava flow morphology provides only rough estimates of effusion rates; for example, sheet flows are thought to represent higher rates than pillow lavas (e.g., Gregg and Fink, 1995). Dissolved CO_2 concentrations and vesicle characteristics in erupted basalts may provide a quantitative method for estimating magma ascent and lava flow rates in unobserved eruptions using samples that can be collected long after the eruption has concluded (e.g., Chavrit et al., 2012; Gardner et al., 2016; Soule et al., 2012).

MOR lavas contain measurable dissolved CO_2 at their eruption depth due to CO_2 solubility in basaltic melts and the hydrostatic pressure at the seafloor. Further, high decompression rates commonly lead to incomplete degassing during magma ascent and CO_2 supersaturation in mid-ocean ridge basalts (MORB) relative to expected equilibrium (Dixon et al., 1988; le Roux et al., 2006). The degree of supersaturation depends on the time available for CO_2 diffusion into bubbles, relative to the diffusion time scale, which relates to ascent and flow rates and distances (Chavrit et al., 2012; Dixon et al., 1988; Dixon and Stolper, 1995; Gardner et al., 2016; le Roux et al., 2006; Soule et al., 2012). Based on these principles, Chavrit et al. (2012) suggested that differences in the dissolved CO_2 concentrations and vesicularity characteristics between Atlantic and Pacific MORB result from shorter vertical transport distances and greater ascent rates in Pacific samples. Soule et al. (2012) and Gardner et al. (2016) further demonstrated that two lava flows produced during the 2005-06 East Pacific Rise (EPR) eruption experienced rapid ascent rates (>0.15 m/s) and lava flow

rates (0.02–0.12 m/s). Here, we seek to improve methods for interpreting submarine eruptions based on CO_2 degassing by 1) corroborating the model using comparisons with independent methods and 2) establishing the range of ascent rates experienced during a MOR eruption using dissolved CO_2 concentrations and vesicularity, which has not been accessible through other methods.

As the best-monitored submarine volcano in the world, Axial Seamount provides an ideal opportunity to explore the advantages and limitations of degassing-based models for eruption and emplacement processes through comparisons with independent constraints from seismicity and ocean bottom pressure recorders. In this study, we reconstruct magma ascent and lava flow rates (i.e., emplacement rates or flow velocities) during the 2011 Axial Seamount eruption using high-resolution bathymetry (Caress et al., 2012), numerical modeling of CO_2 degassing, and the most comprehensive suite of samples from a single MOR eruption analyzed for volatiles and vesicularity.

3.3 Axial Seamount

Axial Seamount is located ~500 km off the Oregon coast (USA) at the intersection of the Cobb hotspot and the Juan de Fuca Ridge spreading center (Figure 3-1). Robust magmatic production at Axial Seamount has resulted in one of the largest and most active, on-axis submarine volcanoes on the global MOR system. This high level of activity has motivated numerous studies about its geology (Clague et al., 2013; Dreyer et al., 2013), morphology (Caress et al., 2012; Chadwick et al., 2013), and associated magma storage (Arnulf et al., 2014; West et al., 2001). The composition of magmas erupted at the summit of Axial Seamount has been mostly bimodal during the last 1000 years, with Group 1 lavas comprising nearly aphyric transitional (T)-MORB with MgO <7.9% and Group 2 lavas comprising plagioclase phyric normal (N)-MORB with MgO >7.9% (Clague et al., 2013; Dreyer et al., 2013).

Axial Seamount has erupted three times during the past 20 years; in 1998 (Chadwick et al., 2013; Fox et al., 2001), in 2011 (Caress et al., 2012; Chadwick et al., 2012; Clague et al., 2017; Dziak et al., 2012), and most recently in 2015 (Chadwick et al., 2016; Nooner and Chadwick, 2016; Wilcock et al., 2016). Bottom pressure recorders and ocean bottom hydrophones revealed patterns in seafloor deformation and seismicity during the 2011 eruption, which were interpreted to represent the onset of diking, followed by the dike breaching the seafloor, followed by lateral, southern dike propagation

(Chadwick et al., 2012; Dziak et al., 2012). Chadwick et al. (2016) and Nooner and Chadwick (2016) suggested that diking during the three historic eruptions initiated near the same location, close to the centroid of a best-fit deformation source for the 2015 eruption and near a high-melt conduit identified in multi-channel seismic results from Arnulf et al. (2014).

The distribution of lava flows from the 2011 eruption was identified from pre- and post-eruption 1m resolution bathymetry acquired using an autonomous underwater vehicle (AUV) (Caress et al., 2012; Clague et al., 2017). The 2011 eruption produced channelized sheet flows on the east rim of the caldera, hummocky flows just south of the channelized flows on the upper south rift zone, and a large, hummocky flow on the lower south rift zone ~30 km south of the caldera (Caress et al., 2012; Clague et al., 2017). The summit lava flows erupted from a series of mostly north-south trending *en echelon* fissures (Caress et al., 2012, Figure 3-1).

3.4 Samples and methods

3.4.1 Sample descriptions

24 lava samples were collected during the VISIONS'11 cruise using the *R/V Thompson* and *ROV ROPOS*. 85 more samples were collected during MBARI's 2011 and 2013 Northern Expeditions using the *R/V Western Flyer*, *ROV Doc Ricketts*, and wax-tipped gravity corers. We analyzed 19 glassy lava samples from VISIONS'11 and 31 samples from the Northern Expeditions. The samples were collected from three large lava flow lobes and along or near the >10 km long series of north-south trending *en echelon* eruptive fissures (Figure 3-1). The samples are dominantly aphyric with glassy rinds that were analyzed for major elements, volatiles, vesicularity, and vesicle size distributions.

3.4.2 Analytical methods

Major elements were analyzed at the University of California at Davis on a 5-spectrometer Cameca SX-100 microprobe (full methods and data in supplementary material S.1). Dissolved volatile concentrations (CO_2, H_2O, F, Cl, S) within the glassy rinds were measured using the Cameca 1280 Secondary Ion Mass Spectrometer at the Northeast National Ion Microprobe Facility (NENIMF) at the Woods Hole Oceanographic Institution using the methods described by Shaw et al. (2010), based on Hauri et al. (2002) (Supplementary Table S.3.2). Analytical uncertainty ($2\sigma \sim 10\%$) has been established at NENIMF for these procedures based on repeat measurements on standard glass 519-

4-1, which agrees with repeat measurements from this study. Helium measurements were conducted on six glass samples using a magnetic sector mass spectrometer at the Isotope Geochemistry Facility at the Woods Hole Oceanographic Institution (Supplementary Table S.3.3), following methods adapted from Kurz et al. (2005) and described in Soule et al. (2012).

Vesicularities and vesicle size distributions were measured on 10x magnification reflected light photomicrographs of polished glass fragments from the outer quenched 1cm of the lava samples (Figure 3-2, full methods and data in supplementary material S.2). The vesicle number density (number of bubbles per unit volume; N_v) and the vesicle size distributions were derived from the 2D measurements using the stereological methods described in Cashman and Mangan (1994). The vesicle size distributions were interpreted using histograms of bubble density versus bubble size and cumulative bubble volume versus bubble size (Supplementary Material S.4; Shea et al., 2010). The vesicularity, vesicle number density, and vesicle size distributions derived from reflected light photomicrographs agree with those derived from 3D x-ray micro-tomography collected on a subset of the samples (Jones et al., unpublished data).

3.4.3 Bubble growth model

The numerical formulation used here was first presented for magmatic systems by Prousevitch et al. (1993) and closely follows Arefmanesh and Advani (1991). The model was adapted from single component (H_2O) to multicomponent (H_2O and CO_2) degassing by Gonnermann and Manga (2005). The model simulates gas diffusion within a melt shell, gas exsolution into a bubble, and the associated bubble growth. The model assumes that bubbles are uniformly distributed, such that each bubble can be approximated as a sphere surrounded by a spherical melt shell. The thickness of the melt shell is dictated by the bubble number density. Dissolved volatiles are initially at equilibrium with the exsolved phase and homogeneously distributed throughout the radially symmetrical melt shell. During depressurization, the reduced solubility of the volatile species induces diffusion of the gas from the surrounding melt towards the bubble-melt interface. Bubble growth occurs as dissolved volatiles pass through the bubble-melt interface into the supercritical fluid state. Initial conditions for the model include the initial bubble radius, initial volatile content in the melt, initial pressure, and bubble number density, which are all derived from observations of Axial Seamount 2011 lava samples (Section 6.1). Known parameters include diffusivity (Zhang, 2010), solubility (Dixon et al., 1995; Newman and Lowenstern, 2002), and viscosity (Hui and Zhang, 2007). The

unknown parameters are the decompression rate and the degassing timescale after decompression (i.e., while on the seafloor). We estimate decompression rates (Section 6.2) and degassing timescales after decompression (Section 6.3) by comparing model predictions for the dissolved CO_2 concentration and vesicularity with observations from the 2011 Axial samples. Because CO_2 concentrations were measured far from bubbles, we compare these to modeled concentrations at the midpoint between bubbles.

3.5 Results

3.5.1 Major Elements

Lavas emplaced in the summit caldera during the 2011 eruption are slightly enriched MORB with CaO/Al_2O_3=0.82–0.86 and K_2O/Ti_2O=0.10–0.13 (Supplementary Table S.3.1). The samples exhibit a narrow range in major elements (e.g., SiO_2=49.67–49.99 wt.%, MgO=7.26–7.56 wt.%, FeO=10.93–11.30 wt.%, Al_2O_3=14.49–14.80 wt.%, CaO=12.03–12.43 wt.%), and are similar to Group 1 lavas identified in recent eruptions at Axial Seamount (Dreyer et al., 2013).

3.5.2 Helium

Total helium concentrations (dissolved + exsolved) in the samples are relatively constant at 1.12 ± 0.16 x 10^{-5} cm^3 $^4He/g$ at standard temperature and pressure (STP) (Figure 3-3, Supplementary Material S.3). The fraction of exsolved helium, measured by crushing, correlates positively with vesicularity and inversely with dissolved CO_2 (Figure 3-3). The fraction of helium released by crushing also increases with distance along the lava flows from 0.39 near the vent to 0.66 at the distal end of the flow. Accordingly, the concentration of ^4He in the dissolved phase decreases with distance along the lava flows. The $^3He/^4He$ ratios derived from crushing and melting range from 8.12–8.33 and are consistent with the typical range of MORB values (Graham, 2002).

3.5.3 Dissolved volatile concentrations

The dissolved volatile concentrations are within the ranges typical of MORB (H_2O=0.17–0.26 wt.%, CO_2=68–339 ppm where ppm is $\mu g.g^{-1}$, F=125–177 ppm, Cl=119–196 ppm, and S=0.096–0.137 wt.%) (Supplementary Table S.3.2; Wallace et al., 2015). The minor variability in H_2O exceeds the analytical uncertainty, but does not correlate with vesicularity, distance along individual lava flows, or location along the rift zone.

Dissolved CO_2 concentrations span nearly the range of values in lava samples from the global MOR system (Le Voyer et al., 2017; Soule et al., 2012). Distinct variations in dissolved CO_2 are observed in samples collected along the eruptive fissures, with concentrations in southern samples (i.e., 45.875–45.893°N) ranging from ~70 to ~140 ppm, central samples (i.e., 45.894–45.953°N) ranging from ~120 to ~325 ppm, and northern samples (i.e., 45.954–45.961°N) ranging from ~130 to ~180 ppm (Figure 3-4c). Dissolved CO_2 concentration decreases systematically with distance along lava flows from ~325 ppm in samples proximal to the eruptive fissures to ~100 ppm in distal samples near the flow terminus (Figure 3-4d).

3.5.4 Vesicularities and vesicle size distributions

Vesicularity ranges from 0.07% to 1.64% (Supplementary Table S.3.2). Vesicularity varies systematically with location along the eruptive fissures, with the lowest vesicularities observed in the central samples, in the vicinity of the flow lobes A, B, and C (Figure 3-4a). Vesicularity also increases with distance from the eruptive fissures (Figure 3-4b) and exhibits a negative, linear correlation with dissolved CO_2 concentration and dissolved helium (e.g. Figure 3-5), but does not correlate with other volatiles.

Bubble number density (N_b) also varies systematically along the eruptive fissure and individual lava flow units. Along the eruptive fissures, the most northern and southern samples have the lowest N_b (~50-100 bubbles/mm^3), whereas central samples are more variable and have on average higher N_b, ranging from 50–325 bubbles/mm^3 (Figure 3-4e). N_b decreases with distance along individual lava flows from ~250 bubbles/mm^3 near the eruptive vents to ~20 bubbles/mm^3 near the flow terminus (Figure 3-4f).

R_{max}, defined as the mean radius of the largest bubbles comprising 80% of the total vesicularity, correlates with vesicularity. R_{max} provides a means for evaluating bubble growth independently of detection limits at small sizes. R_{max} varies along the eruptive fissures with the largest R_{max} (~200 μm) at the northern and southern ends and the smallest values (20–80 μm) in the central fissure section (Figure 3-4g). R_{max} also increases with distance along the individual lava flows from ~20 μm in samples proximal to eruptive vents to ~140 μm in distal samples (Figure 3-4h).

3.5.5 Total volatile content

Based on empirical solubility models (Dixon and Stolper, 1995), we expect that the vesicles contain >98% CO_2. Total CO_2 concentrations (exsolved + dissolved) in the 2011 samples are relatively constant at 367 ± 30 ppm (uncertainty is 1σ), based on measured dissolved concentrations and calculated exsolved concentrations using sample vesicularity, collection pressure, magmatic temperature (~1200°C), and a modified Redlich-Kwong equation of state (Flowers, 1979).

3.6 Discussion

3.6.1 Degassing during the 2011 Axial Seamount eruption

The relative similarity in total (dissolved + exsolved) ^4He and CO_2 concentrations support the assumption that degassing occurred within a closed system (Figure 3-3), because progressive bubble loss during open system degassing would produce a positive correlation between total volatile content and the degree of supersaturation. In other words, gas did not escape from the lava during ascent or flow on the seafloor. The constant total volatile concentration among the samples further suggests homogeneous volatile content in the magma prior to eruption.

Based on these observations, we model closed-system degassing of CO_2 into growing bubbles assuming a constant initial volatile content in all cases. We infer that samples with nearly 0% vesicularity experienced rapid ascent and emplacement with insufficient time for CO_2 diffusion into bubbles; therefore, the dissolved CO_2 concentration in these samples should closely approximate the initial concentration in 2011 Axial Seamount lavas. Thus, we use the volatile concentrations of these samples (0.208±0.008 wt.% H_2O and 325±9 ppm CO_2; e.g. Figure 3-5) as the initial condition for our degassing model. We assume that most of the initial CO_2 was dissolved in the melt at the onset of the eruption. Therefore, we use the saturation pressure derived from the inferred initial dissolved CO_2 and H_2O contents (~70 Pa) as an initial condition for the model (Newman and Lowenstern, 2002). Our estimated initial pressure corresponds to a depth of 2.0 km beneath the seafloor, assuming an average seawater density of 1.03 g/cm^3 and an average crustal density of 2.8 g/cm^3, which lies within the depth range of the magma reservoir inferred from multichannel seismic results (1.1–2.3 km between the seafloor and the top of the magmatic reservoir; 0.6–1 km maximum reservoir thickness; Arnulf et al., 2014).

The vesicle volume distributions (supplementary material S.4) demonstrate that small bubbles (<10 μm radius) contain only a minor fraction of the exsolved gas, implying that bubble nucleation had a

negligible impact on degassing. Instead, the positive correlation between R_{max} and vesicularity (Figure 3-4a,g) indicates that degassing instead occurred primarily through gas exsolution into growing bubbles. The predominantly linear vesicle size distributions (supplementary material S.4) suggest that the correlation between R_{max} and vesicularity results from bubble growth rather than coalescence. Therefore, we neglect bubble nucleation in our model and use measured bubble number densities as an initial condition for our model. We assume initial bubble radii of ~5 μm, based on the smallest resolvable bubble size in these samples. The assumed sphericity and uniform spacing between vesicles in our model conforms to observations of vesicles in the samples (e.g. Figure 3-2).

Solubility models for H_2O and CO_2 (Dixon et al., 1995), and the lack of correlation between vesicularity and H_2O or S suggest that CO_2 was the primary exsolving species. We interpret that the minor variability in H_2O may instead be related to pre-eruption assimilation of seawater derived brines (e.g. le Roux et al., 2006; Soule et al., 2012). Although included in the model, H_2O degassing was negligible.

The variable degree of CO_2 supersaturation, relative to ~65 ppm dissolved CO_2 expected at Axial Seamount seafloor pressures (Dixon and Stolper, 1995), in fissure samples and the progressive decrease in CO_2 supersaturation with distance from the eruptive fissures (Figure 3-4c,d) indicate that degassing occurred during both vertical magma ascent and horizontal lava flow across the seafloor. In order to evaluate magma ascent rates for near-fissure samples, we model degassing at various decompression rates and bubble number densities (Section 6.2, Figure 3-6). The decompression rate that most closely reproduces the measured dissolved CO_2 concentrations and vesicularity, given the measured bubble number density, provides an estimate for the average ascent rate between the onset of decompression and the lava quenching on the seafloor.

As lava lobe samples proximal to the eruptive vents contain high dissolved CO_2 concentrations and low vesicularities (Figure 3-4b,d), we infer that the lavas producing the flows experienced minimal degassing during vertical ascent. In order to evaluate lava flow rates for samples collected from flow lobes A–C, we therefore model degassing at a constant pressure of 15 MPa (equivalent to the hydrostatic pressure at the seafloor) from initial dissolved concentrations of 325 ppm CO_2 and 0.208 wt.% H_2O for the range of measured bubble number densities (Figure 3-7). The amount of time available for degassing was estimated by comparing measured dissolved CO_2 concentrations and vesicularity with model results using the observed bubble number densities. The average lava flow

rates were calculated from the modeled timescale for degassing and measured flow distance (Section 6.3).

3.6.2 Degassing during magma ascent

The ascent rates that produce the observed vesicularities and dissolved CO_2 range from ~0.02–1.2 m/s (Figure 3-8a), which spans the global range previously proposed based on CO_2 degassing (Chavrit et al., 2012). These ascent rates represent minimum values because the samples probably experienced some degassing while on the seafloor. The high vesicularities, low dissolved CO_2 concentrations, and large bubble radii in samples from the most northern and southern parts of the fissure (Figure 3-4b,d,h) suggest that they ascended slower (<0.2 m/s) than samples erupted along the central parts (<1.2 m/s) (Figure 3-8a). The greater variability in vesicularity and dissolved CO_2 concentrations in samples from the central parts of the fissure system could reflect complexities in the emplacement dynamics (e.g., pooling in lava ponds) or changes in eruption rate over time, perhaps due to changing pressure conditions within the storage reservoir (Harris et al., 2000; Rivalta, 2010).

Seismicity- and deformation-based methods provide an estimate for initial magma ascent rates during dike propagation, based on the time difference between the initiation of magma ascent, inferred from a pre-eruption earthquake swarm, and the dike breaching the seafloor, inferred from the onset of seafloor deflation (~0.16–0.21 m/s, Dziak et al., 2012). Those estimates are within the range of our modeled ascent rates (~0.02–1.2 m/s); our estimates are slightly more variable because CO_2 degassing records the variability in ascent rates throughout the eruption.

Bottom pressure inflation/deflation records suggest that the dike breached the surface near the north end of the eruptive vents and propagated southward (Chadwick et al., 2012). Based on our study, the lavas emplaced near where the dike first reached the surface (~45.94°N) experienced the fastest ascent rates, possibly due to high driving overpressures early in the eruption. Slower ascent rates for the northern and southern samples are consistent with lateral dike propagation resulting in longer paths to the seafloor and decreased driving pressure (Figure 3-9). The fastest ascent rates also occur near the summit channelized sheet flows while slower ascent rates occur near hummocky flows on the upper south rift zone, supporting a link between effusion rate and lava flow morphology (e.g., Gregg and Fink, 1995).

The agreement between degassing-based and seismicity- and deformation-based models of magma ascent at Axial Seamount provides confidence in applying these methods more broadly to MOR eruptions. The results from these two methods are similarly consistent for the 2005-06 East Pacific Rise (EPR) eruption (Dziak et al., 2009; Gardner et al., 2016; Tolstoy et al., 2006).

3.6.3 Degassing during lava flow emplacement

The time required to produce the observed vesicularities and dissolved CO_2 concentrations during degassing at seafloor pressures of 15.1 MPa ranges from 0.5 to 4.5 hours (Figure 3-7). The flow rates, calculated from the ratio of the distance between the fissure and sample location and modeled degassing time, range from ~0.1 to 0.7 m/s for samples greater than 500 meters from the eruptive vents (Figure 3-8b). We do not consider samples within 500 meters from the eruptive vents due to potential complexities in the transport pathways and emplacement dynamics (e.g., lava ponding) relative to the total distance flowed. The flow rates do not vary systematically with distance, which contrasts with results from the 2005-2006 EPR eruption where flow rates were inferred to peak at 3 times the average rate early in the eruption (Gardner et al., 2016; Soule et al., 2012). During the 2011 Axial Seamount eruption, samples from the distal ends of the lava flows may have not recorded the period of waning effusion rates.

The volume of the channelized flows near the summit along the upper south rift is 28.7 x 10^6 m^3 (3.5 x 10^6 m^3 per km of fissure) based on pre- and post-eruption high-resolution AUV bathymetry (Caress et al., 2012; updated in Clague et al., 2017). The modeled emplacement times (4.5 hours for samples near flow lobe C terminus; Figure 3-7b) and calculated summit channelized flow volumes yield an average volumetric effusion rate of 0.22 m^3/s per 1-m length of eruptive fissure. This average effusion rate is similar to the average effusion rate of 0.21 m^3/s per 1-m length of eruptive fissure estimated from data recorded by a trapped bottom pressure recorder (BPR) during the 1998 Axial Seamount eruption in the same area of the summit (Fox et al., 2001).

3.7 Conclusions

Magma ascent and eruption rates reflect the conditions in the underlying magmatic system (e.g., Rivalta, 2010) and influence the style and mechanisms of volcanic deposition (e.g., Harris et al., 2000; Gregg and Fink, 1995). In this study, we provide the first quantitative estimates of the variability in magma ascent rates during a single MOR eruption. These ascent rates are sensitive to

assumptions regarding the pre-eruptive volatile content and the size distribution of bubbles; however, the result that some samples ascended slow enough for near-equilibrium degassing while others ascended fast enough for minimal vesiculation does not depend on model parameters and holds important implications for our understanding of mid-ocean ridge eruptions. For example, these results, combined with the observation that the fastest ascent rates occur where the dike is thought to have first breached the seafloor, provide the first direct evidence for time-dependent effusion rates during submarine eruptions, similar to that observed during subaerial eruptions (e.g. Harris et al., 2000). In addition, the correspondence between the fastest ascent rates for the 2011 eruption, site of dike nucleation for the 2011 and 2015 eruptions (Chadwick et al., 2016), centroid of the best-fit deformation source for the 2015 eruption (Nooner and Chadwick, 2016), and location of a high-melt nearly vertical conduit in multi-channel seismic data (Arnulf et al., 2014) supports the interpretation that historic, and likely future, eruptions at Axial Seamount initiate near 45.94°N on the east caldera rim (Clague et al., 2017).

This study further supports the relationship between eruption rate and lava flow morphology. The fastest ascent rates (~1.2 m/s), associated with the greatest CO_2 supersaturation, produced channelized flows with sheet morphology from the central fissure section while slower ascent rates are estimated for the southern fissure sections, near hummocky flows and pillow ridges. The ability to evaluate conduit processes in MOR eruptions also holds promise for understanding mechanisms leading to MOR pyroclastic deposits, such as those produced during some Axial Seamount eruptions (Chadwick et al., 2016; Helo et al., 2011).

Our study corroborates degassing-based models for magma ascent and lava flow rates using comparisons with independent estimates from seismicity and caldera deformation. We suggest that degassing-based methods can be applied elsewhere on the MOR system in order to determine global variability in ascent and flow rates and evaluate the processes that control them. Importantly, this method for tracking magma ascent rates relies only on CO_2 supersaturation, which occurs in most MORB (Chavrit et al., 2012), and provides a complementary approach to other diffusion-based chronometers of eruptive processes developed for terrestrial volcanoes (e.g. Lloyd et al., 2014). The observed variability in CO_2 supersaturation within a single eruption demonstrates that sample locations (e.g., relative to eruptive vents) must be well constrained in order to effectively quantify eruption rates using volatile concentrations. With limited direct observations of active eruptions in the deep sea, degassing-based chronometers provide an ideal opportunity to evaluate the archive of

eruption dynamics recorded in seafloor volcanic deposits. Our study demonstrates how CO_2 degassing records the physical processes involved in mid-ocean ridge volcanism, including melt storage in the shallow crust, melt extraction during eruptions, and volcanic deposition on the seafloor.

3.8 Acknowledgments

We are thankful to the captain and crew of the *R/V Thompson* and *R/V Western Flyer* and the *ROV ROPOS* and *ROV Doc Ricketts* teams for assistance in collecting the samples used in this study. We thank J. Delaney, A. Fundis, and D. Kelley for sample acquisition, B. Dreyer and B. Boulahanis for assistance with sample preparation and processing, D. Wanless and B. Monteleone for assistance with ion probe measurements, M. Kurz and J. Curtice for conducting helium measurements, and N. Botto for conducting microprobe analyses. We thank D. Fornari, T. Grove, D. Lizarralde, M. Kurz, W. Chadwick, and an anonymous reviewer for insightful comments on earlier versions of this manuscript and T. Mather for editorial handling. M. Jones was supported by the Department of Defense (DoD) through the National Defense Science & Engineering Graduate Fellowship (NDSEG) Program. The *ROV Doc Ricketts* sampling and microprobe analysis were supported by a grant from the David and Lucile Packard Foundation to MBARI and the *ROV ROPOS* sampling was supported by the National Science Foundation and the University of Washington. This work was supported by NSF grant OCE-1333492 to A. Soule.

3.9 Figures

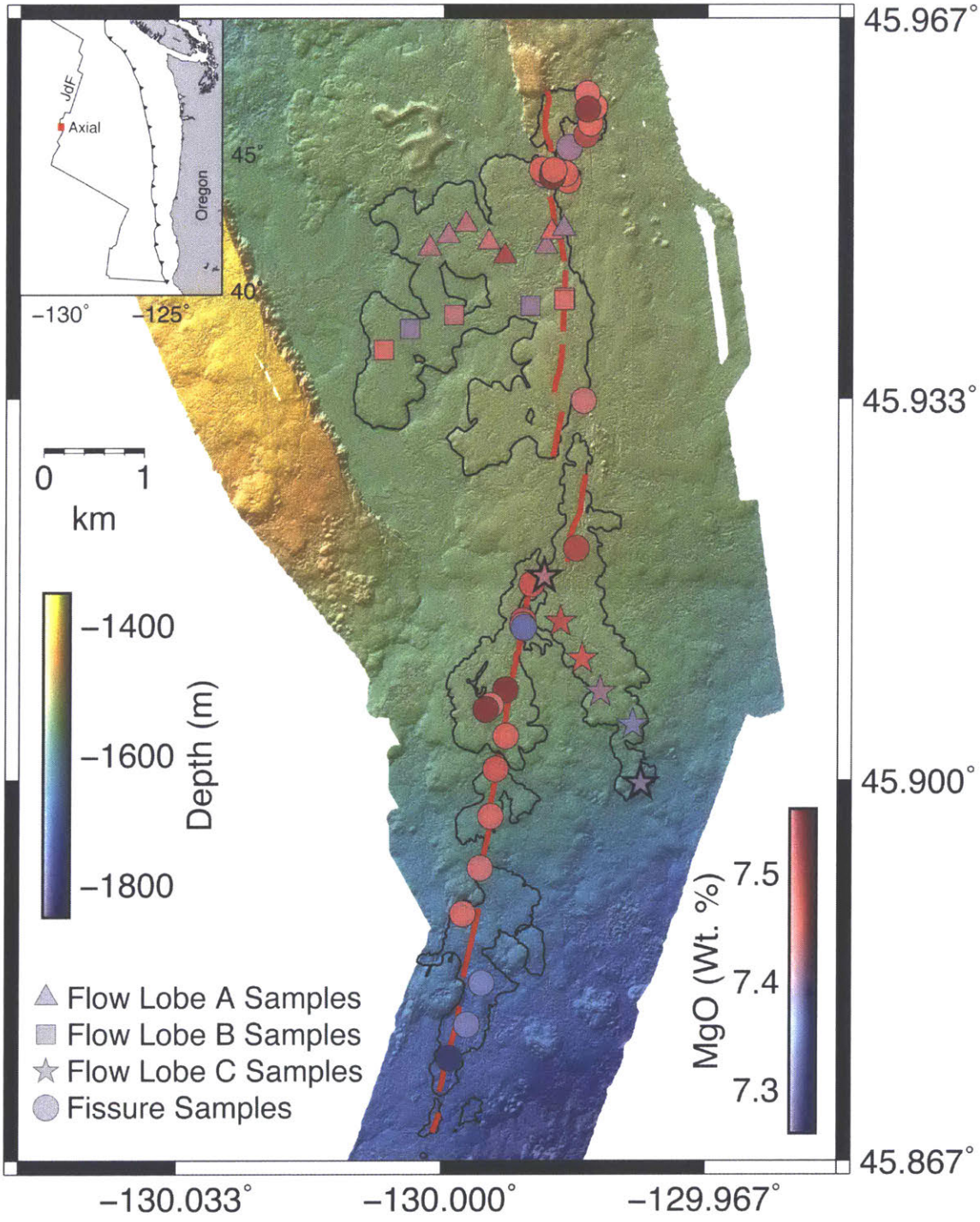
JdF
Axial
Oregon
45°
40°
−130°
−125°
0
1
km
−1400
−1600
−1800
Depth (m)
Flow Lobe A Samples
Flow Lobe B Samples
Flow Lobe C Samples
Fissure Samples
7.5
7.4
7.3
MgO (Wt. %)
45.967°
45.933°
45.900°
45.867°
−130.033°
−130.000°
−129.967°

Figure 3-1. Map of lava flows emplaced during the 2011 eruption (black outlines, based on Caress et al., 2012 and updated in Clague et al., 2017) showing eruptive fissures (red lines) and lava samples collected from near eruptive fissures (circles) and from individual lava flow lobes extending away from the fissures (Flow Lobe A–triangles, Flow Lobe B–squares, and Flow Lobe C–stars; the flow lobe names are assigned from north to south and do not correspond to a known time progression). Samples are colored according to their MgO content. AUV high-resolution bathymetry is from Clague et al. (2017). Clague et al. (2017) present detailed morphological analyses based on AUV bathymetry and seafloor observations and show that hummocky flows dominate on the upper south rift zone (~45.87°N) while channelized flows dominate from ~45.90°N–45.95°N. Reflected light photomicrographs from two flow lobe C samples, outlined in bold, are shown in Figure 3-2. Inset shows the location of Axial Seamount on the Juan de Fuca Ridge (JdF) offshore Oregon. Red box shows the region presented in the main map.

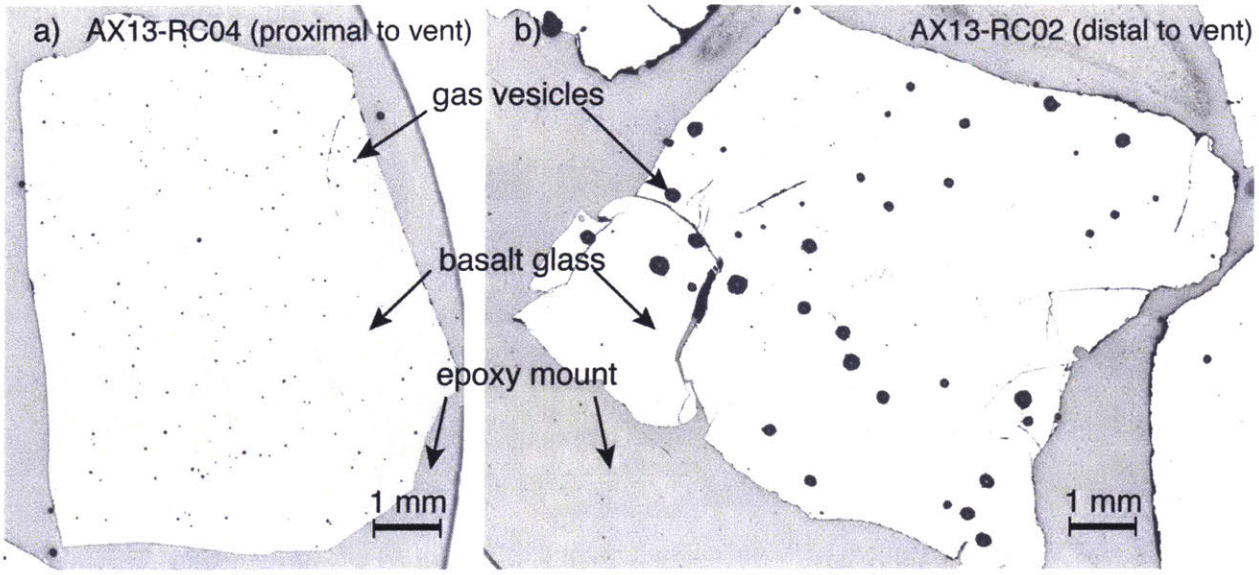

Figure 3-2. Reflected-light photomicrographs collected at 10x magnification from samples (a) proximal to eruptive fissures and (b) distal near one flow front terminus from the 2011 eruption. a) Vesicularity in sample AX13-RC04 is 0.51%. b) Vesicularity in sample AX13-RC02 is 1.64%. The outlines for these two samples, collected from flow lobe C, are shown in bold in Figure 3-1.

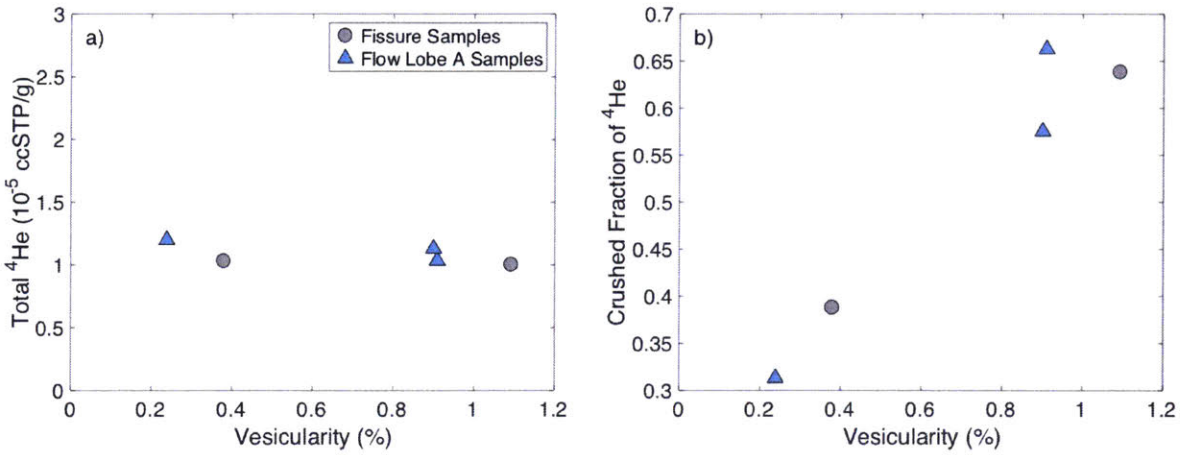

Figure 3-3. (a) Total ^{4}He concentration (melting + crushing) versus vesicularity. The limits on the y-axis reflect the ranges typically observed in MORB (e.g., Sarda and Graham, 1990). (b) Fraction of ^{4}He released by crushing versus vesicularity. The correlation between crushed fraction of ^{4}He and vesicularity and the relatively constant total ^{4}He concentration suggests that closed system degassing occurred during the 2011 eruption.

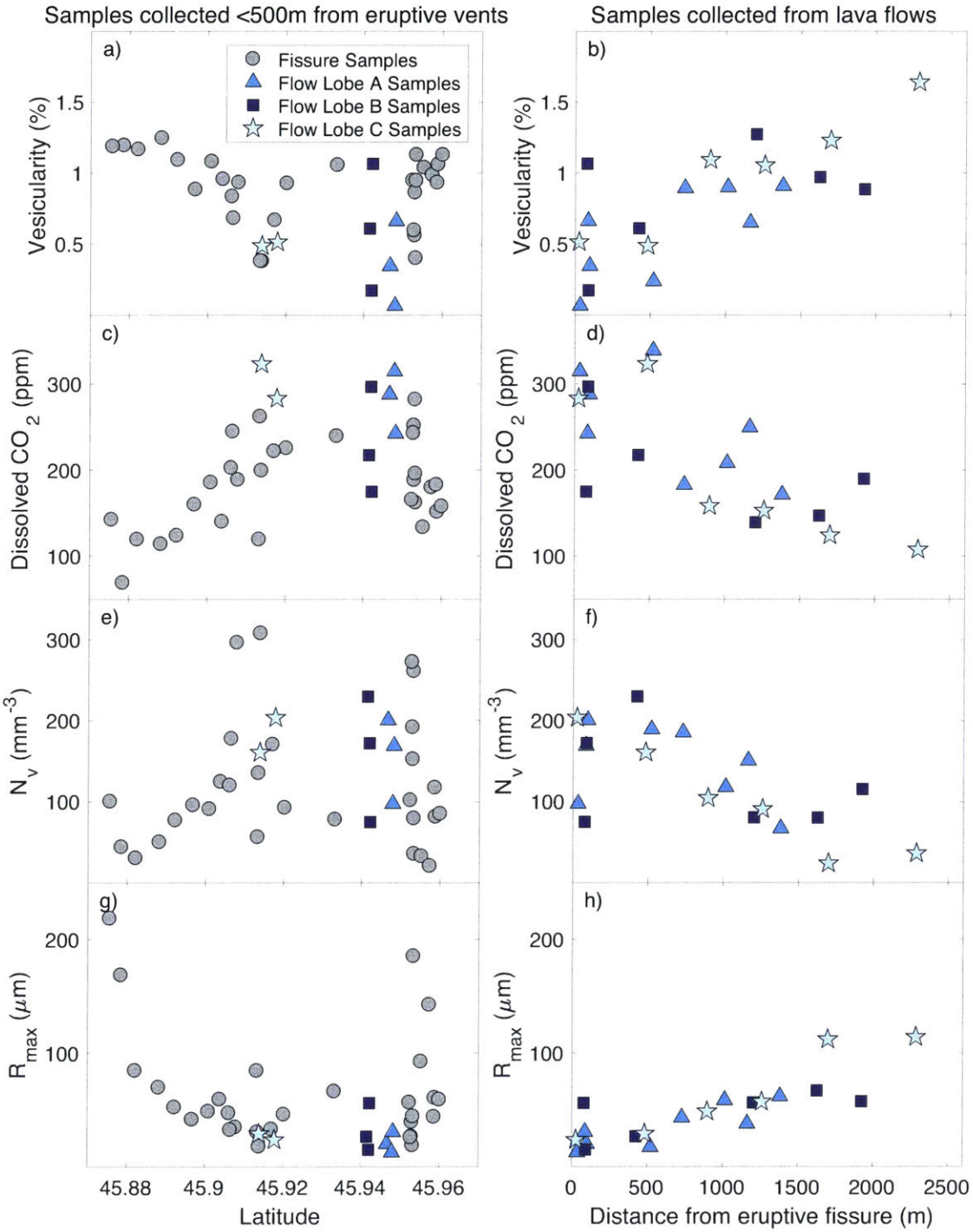
Samples collected <500m from eruptive vents
Samples collected from lava flows
a)
b)
c)
d)
e)
f)
g)
h)
Fissure Samples
Flow Lobe A Samples
Flow Lobe B Samples
Flow Lobe C Samples
Vesicularity (%)
Dissolved CO 2 (ppm)
N v (mm -3)
R max (μm)
Latitude
Distance from eruptive fissure (m)
45.88
45.9
45.92
45.94
45.96
0
500
1000
1500
2000
2500

Figure 3-4. Vesicularity (a,b), dissolved CO_2 concentrations (c,d), bubble number densities (N_v) (e,f), and characteristic bubble radii (R_{max}) (g,h) in samples from the 2011 eruption of Axial Seamount. Samples collected <500 m from eruptive fissures are plotted versus latitude (left column). Samples collected from individual lava flow lobes are plotted versus distance from the eruptive fissures (right column). Samples from the central fissure section (i.e., 45.894–45.953°N) display lower average vesicularities, higher average dissolved CO_2, higher average N_v, and lower average R_{max} than samples from the southern and northern fissure sections. Vesicularity and R_{max} in samples collected from individual lava flow lobes increases linearly with distance from the fissures, while N_v and dissolved CO_2 decreases linearly with distance from eruptive fissures.

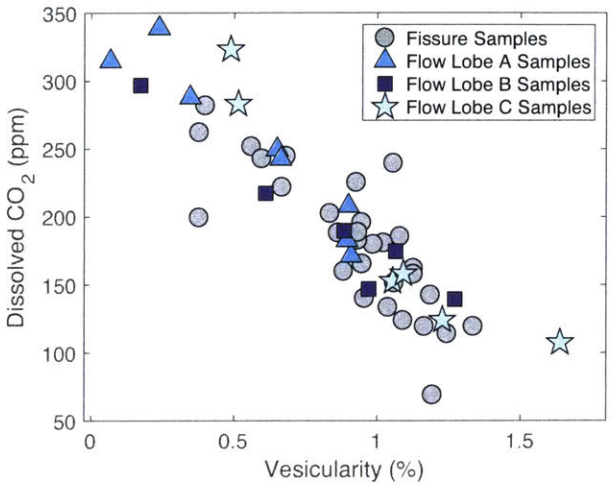

Figure 3-5. Dissolved CO_2 concentration versus vesicularity. The inverse correlation suggests that progressive CO_2 degassing due to diffusion leads to the observed variability in dissolved CO_2 concentration and vesicularity. The initial CO_2 concentration for our model was determined as the y-intercept of a linear least-squares regression of the dissolved CO_2 concentration on vesicularity.

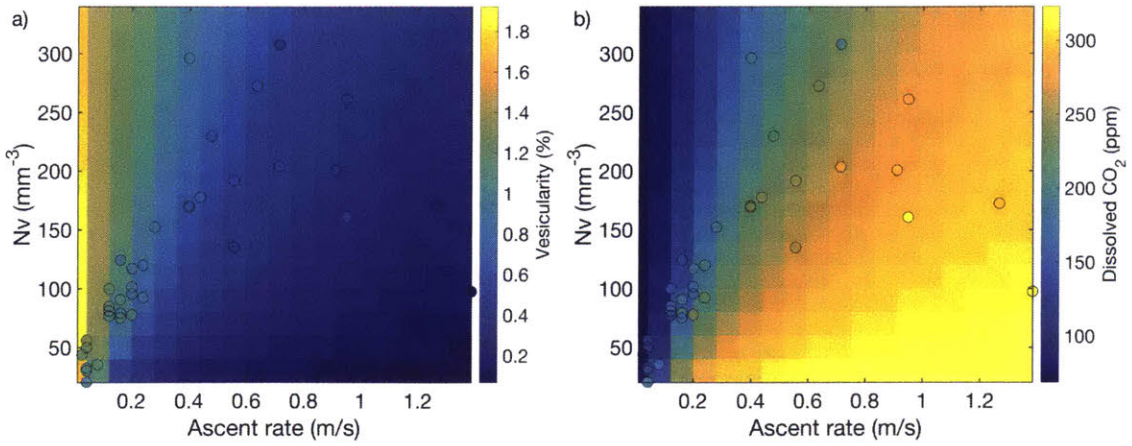

Figure 3-6. Results from numerical modeling of diffusive bubble growth during depressurization. (a) Modeled vesicularity and (b) modeled dissolved CO_2 concentration for various bubble number densities (N_v) and depressurization rates. The circles show modeled ascent rates (x-axis), measured N_v (y-axis), measured vesicularity (symbol color on left panel), and measured dissolved CO_2 content (symbol color on right panel) for samples collected <500 m from the fissures. The ascent rates were estimated from the average of the best-fit results for measured dissolved CO_2 concentration and vesicularity.

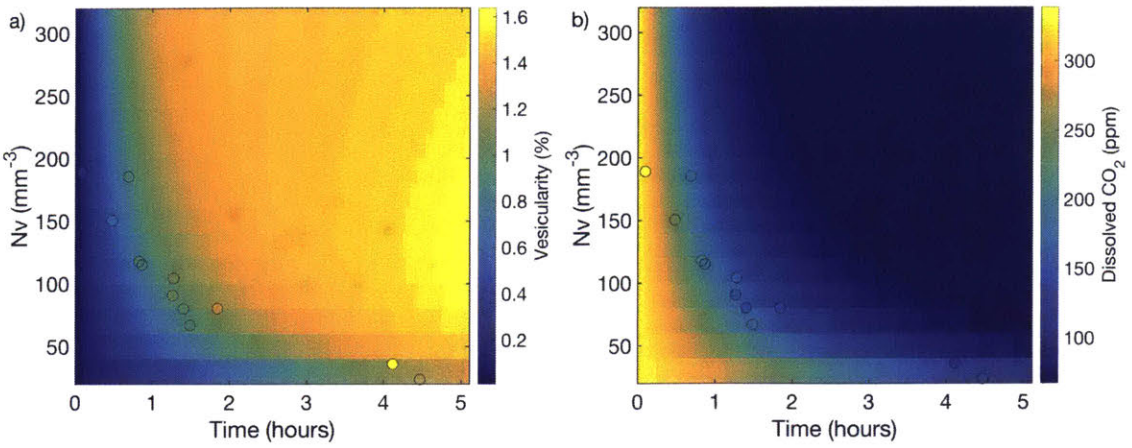

Figure 3-7. Results from numerical modeling of diffusive bubble growth during lava flow emplacement. (a) Modeled vesicularity and (b) dissolved CO_2 concentration for various bubble number densities (N_v) and emplacement times. The circles show modeled flow emplacement times (x-axis), measured N_v (y-axis), measured vesicularity (symbol color on left panel), and measured dissolved CO_2 content (symbol color on right panel) for samples collected >500 m from the fissures. The flow emplacement times were estimated from the average of the best-fit results for measured dissolved CO_2 concentration and vesicularity. The flow emplacement rates are estimated from the distance traveled along the seafloor and the amount of time necessary to produce the observed vesicularities and dissolved CO_2 concentrations.

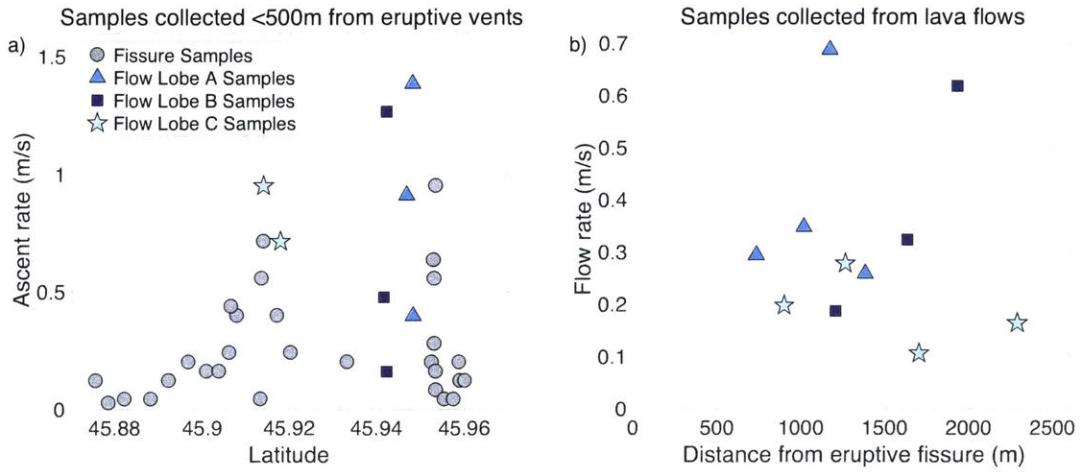

Figure 3-8. (a) Magma ascent rates for samples <500 m from eruptive fissures and (b) lava flow emplacement rates for samples >500 m from eruptive fissures based on comparisons between measured CO_2 concentrations, vesicularities and model results.

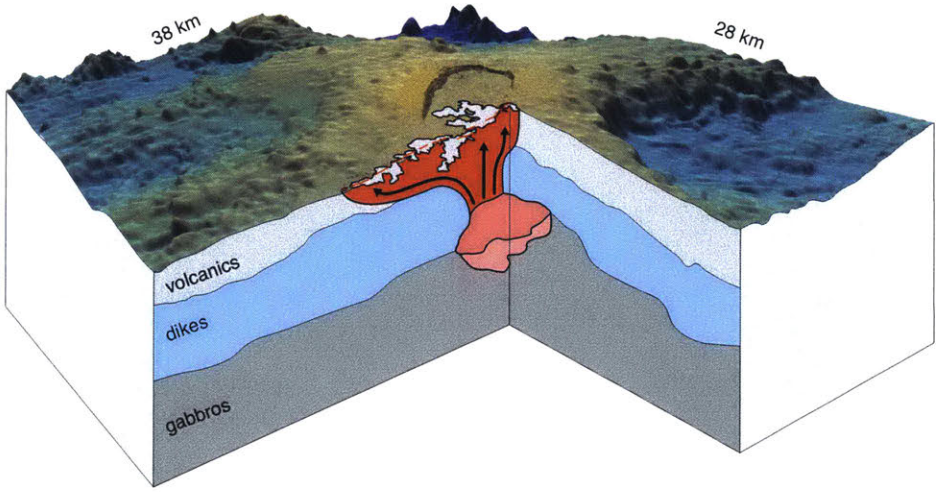

Figure 3-9. Schematic representation of the summit portion of the 2011 Axial Seamount eruption based on CO_2 degassing, caldera deformation (Chadwick et al., 2012; Chadwick et al., 2016) and seismicity (Dziak et al., 2012). Lava flow boundaries (black outlines) are based on Caress et al. (2012) and Clague et al. (2017). The subsurface structure is based on Arnulf et al. (2014). High driving overpressures caused rapid decompression rates and minimal degassing in samples from the central portion of the eruption, located above site of dike nucleation for the 2011 and 2015 eruptions (Chadwick et al., 2016), the centroid of the best-fit deformation source for the 2015 eruption (Nooner and Chadwick, 2016), and a high-melt region based on multichannel seismic data (Arnulf et al., 2014). Lateral dike propagation and reduced overpressures produced slower decompression rates, longer ascent paths, and more degassing at the northern and southern ends of the eruptive fissures. Samples collected from lava flows proximal to the vents experienced minimal degassing, based on high dissolved CO_2 concentrations and low vesicularity, indicating the channelized flows are produced by rapid ascent rates. Degassing during flow along the seafloor produced much (~200 ppm) lower dissolved CO_2 concentration in lava flow samples collected near the distal ends of lava flow lobes.

Chapter 4

New constraints on mantle carbon from Mid-Atlantic Ridge popping rocks

This chapter was originally published as: Jones, M.R., Wanless, V.D., Soule, S.A., Kurz, M.D., Mittelstaedt, E., Fornari, D.J., Curtice, J., Klein, F., Le Roux, V., Brodsky, H., Péron, S., Schwartz, D.M., 2019. New constraints on mantle carbon from Mid-Atlantic Ridge popping rocks. Earth Planet. Sci. Lett. 511, 67–75. 10.1016/j.epsl.2019.01.019. Used with permission as granted in the original copyright agreement.

4.1 Abstract

Despite the influence of mantle carbon on melt formation and migration, global volatile budgets, and volcanic eruption styles, the carbon concentration in Earth's upper mantle remains highly debated, with estimates varying by more than an order of magnitude. The relationship between carbon and incompatible trace element (e.g., Nb, Ba) concentrations in rare, undegassed mid-ocean ridge basalts and melt inclusions provide primary constraints on upper mantle carbon content. Here we investigate whether the most volatile rich mid-ocean ridge basalts, termed 'popping rocks', represent undegassed magmas from the upper mantle and provide insight into upper mantle carbon inventory. We show that fourteen new popping rocks, collected *in situ* from the Mid-Atlantic Ridge rift valley near 14°N, contain highly variable CO_2/Nb and CO_2/Ba ratios despite similar mantle sources and extents of melting. We revise the original model for popping rock formation using seafloor observations, high-resolution bathymetry, vesicle size distributions, major and trace element geochemistry, and noble gas geochemistry. Highly variable volatile concentrations despite relatively homogeneous trace element ratios and low $^{4}He/^{40}Ar^{*}$ suggest that bubble accumulation affected these popping rocks. These results provide evidence for heterogeneity in the CO_2/Ba ratio of the depleted mantle and indicate that mantle carbon concentrations are lower and less heterogeneous than previously estimated, which influences models for mantle melting and CO_2 flux at mid-ocean ridges.

4.2 Introduction

Volatiles in Earth's mantle strongly impact melt formation and migration (Dasgupta and Hirschmann, 2010), geophysical properties of the Earth's interior (Hirth and Kohlstedt, 1996), the behavior of volcanic eruptions (Wallace et al., 2015), and long-term atmospheric evolution (Huybers and Langmuir, 2009). Thus, knowledge of volatile species in the upper mantle is crucial to understanding Earth's formation and evolution. However, shallow degassing makes estimating pre-eruptive magmatic volatile concentrations notoriously difficult, resulting in several decades of debate about the carbon concentration of the upper mantle (Burnard et al., 2014; Cartigny et al., 2008; Chavrit et al., 2014; Dasgupta et al., 2013; Javoy and Pineau, 1991; Le Voyer et al., 2017; Marty and Tolstikhin, 1998; Michael and Graham, 2015; Rosenthal et al., 2015; Saal et al., 2002). The most common approach for estimating upper mantle carbon content and mid-ocean ridge (MOR) CO_2 flux relies on incompatible elements that behave in a similar manner to carbon during melting and crystallization, such as Nb or Ba, and inferences about these ratios from rare, undegassed melts. Volatile undersaturated olivine-hosted melt inclusions from the Siqueiros Transform Fault (Saal et al., 2002) and global ultra-depleted MOR basalts (MORB) (Michael and Graham, 2015) yield average CO_2/Nb ratios of 239 – 283 (Figure 4-1), corresponding to an average mantle source CO_2 concentration of 72 – 85 ppm. In contrast, undegassed melt inclusions (Le Voyer et al., 2017) from the Mid-Atlantic Ridge (MAR) yield much higher CO_2/Nb ratios of 556 – 557 (Figure 4-1). One recent study suggested that the difference between these estimates for undegassed CO_2/Nb reflects heterogeneity in upper mantle ratios, implying that mantle carbon content varies by nearly two orders of magnitude when combined with estimated depleted MORB mantle (DMM) Nb concentrations (Le Voyer et al., 2017). Another study proposed that differences in these ratios reflects partial degassing and magma mixing, implying constant CO_2/incompatible trace element ratios and less heterogeneity in mantle carbon abundances (Matthews et al., 2017). Additional observational constraints are essential for establishing the abundance and heterogeneity of carbon in Earth's mantle.

The only volatile saturated MORB that has been used to directly constrain mantle volatile concentrations was dredged in 1985 near 14°N on the MAR by the *R/V Akademik Boris Petrov* (Bougault et al., 1988). Upon recovery, the dredged '2πD43' samples began popping on the ship's deck due to their removal from seafloor pressures and the consequential release of trapped volatiles from vesicles. Due to their high volatile abundances, simple vesicle size distributions, and unique

rare gas ratios, the 2πD43 popping rocks have been interpreted as the most representative samples of undegassed magmas sourced from the upper mantle (Burnard, 1997; Cartigny et al., 2008; Javoy and Pineau, 1991; Moreira et al., 1998; Sarda and Graham, 1990). The CO_2 and incompatible trace element concentrations in the 2πD43 samples are enriched relative to undegassed, undersaturated MORB and melt inclusions, and thus provide a unique constraint on these ratios and potentially mantle carbon concentrations (Figure 4-1). However, the lack of geologic context for these samples, recovered by dredging on poorly mapped seafloor, has prompted debate about their origins and the implications for mantle carbon (Cartigny et al., 2008; Chavrit et al., 2014; Le Voyer et al., 2017; Sarda and Graham, 1990). Here, we report the CO_2 concentrations, geochemistry, vesicle size distributions, and geologic setting for fourteen new popping rock samples collected from the same ridge segment as dredge 2πD43 during a 2016 *R/V Atlantis* cruise (AT33-03). Our results provide new constraints on the formation of popping rocks and yield insight into heterogeneities in mantle carbon concentrations and eruptive processes at magma-poor ridge segments.

4.3 Methods

4.3.1 Major and trace elements

Major element concentrations were measured using the Cameca SXFive electron microprobe at Boise State University. Sample preparation techniques are described in Schwartz et al. (2017). Analyses were conducted using an accelerating voltage of 15 kV, a beam current of 10 nA, and a beam diameter of 10 μm. Al, K, and Mg were measured for 50 s, Si and Ca were measured for 40 s, Ti, Na, Fe, and P were counted for 30 s, and Mn was counted for 20 s. Five spots were measured on glass chips and averaged. Basalt standard VG-2s and internal standard 2392-9 (Perfit et al., 2012) were run approximately every 5 samples to account for instrument drift. Repeat analyses of standard glasses indicate that the analytical precision of most major elements is <1% to 3%, with the exception of MnO and P_2O_5, which have higher relative errors (5 – 25%) due to low concentrations.

Trace element concentrations were determined using a ThermoElectron X-Series II Quadrupole Inductively Coupled Plasma Mass Spectrometer (ICP-MS) at Boise State University. Samples were dissolved and analyzed following methods outlined in Schwartz et al. (2017). Each solution was measured three times; averages and standard deviations are provided in Supplementary Table S.4.1.

Standards were measured before and after each run and standard JB-3 was analyzed approximately every 10 samples to account for instrument drift.

4.3.2 Volatile elements

Volatile (H_2O, CO_2, S, F, and Cl) analyses were carried out at the Northeast National Ion Microprobe Facility (NENIMF) at the Woods Hole Oceanographic Institution (WHOI) using high mass resolution secondary ion mass spectrometry (CAMECA IMS 1280), using sample preparation and measurement techniques developed by Hauri et al. (2002) and described in Schwartz et al. (2017). Each sample was measured multiple times; averages are provided in Supplementary Table S.4.2. Calibration curves were established using nine standard glasses and drift was assessed using repeat measurements on standard glass ALV519-4-1 (Hauri et al., 2002). Analytical uncertainty ($2\sigma \sim$ 10%) has been established for these procedures at NENIMF based on repeat measurements on standard glass 519-4-1.

4.3.3 Noble gas abundances and ratios

Helium, neon, and argon abundances and isotope compositions were analyzed using a MAP 215-50 mass spectrometer in the WHOI Isotope Geochemistry Facility, as described by Kurz et al. (2005). The helium standard has a $^3He/^4He$ ratio of 8.35 times atmospheric (Ra) and is typically 5×10^{-9} cc STP ^4He. Air was used as the neon and argon standard ($\sim 1.5 \times10^{-10}$ cc STP neon and 9×10^{-8} cc STP argon). Noble gases are purified using three different SAES getters, operated between room temperature and 600°C, and separated with two cryogenic cold traps (one charcoal and one stainless-steel "nude" trap). Crushing blanks are typically 1×10^{-11} cm^3 STP ^4He and 2×10^{-12} cm^3 STP ^{20}Ne and are insignificant relative to the gas quantities measured. Argon isotopes were measured using a dedicated Quadrupole Mass Spectrometer (Hiden). All measurements were made by crushing in vacuo, using well established procedures (e.g. Kurz et al., 2009). The quantities of gas introduced into the extraction line and mass spectrometers were controlled by capacitance manometry, followed by a pre-measurement with a quadrupole mass spectrometer and volumetric splitting prior to inlet to the mass spectrometer.

4.3.4 Vesicularity, vesicle size distributions, and exsolved volatile concentrations

X-ray computed microtomography (μ-CT) scans were collected using a table-top Bruker Skyscan 1272 at the Woods Hole Oceanographic Institution. Transmitted radiographs were collected at steps ranging from 0.15° to 0.35° over 180°. The source voltage ranged between 80 and 100 kV with a current between 100 and 125 μA. Filters and exposure times were selected based on the intensity of the transmitted x-rays, which principally varied based on sample size. The pixel resolution ranged between 3.4 and 5.0 μm. The scans were reconstructed using Bruker NRecon software with corrections applied for beam hardening, ring artifacts, and thermal misalignment. The 3D dataset was segmented using a global threshold in Bruker CTAn software. Cracks and non-vesicles were identified using Bruker visualization software and manually removed using ImageJ. Vesicularity and individual vesicle parameters were calculated using a combination of CTAn, ImageJ, and MATLAB image processing tools. Only vesicles larger than 15 μm in radius (~3x the minimum pixel resolution) were considered. Additional vesicularity measurements were acquired on 10x magnification reflected light photomicrographs of polished glass fragments from the outer quenched rind of the lava samples. The vesicularity measurements based on 2D and 3D techniques are similar; small differences likely reflect a combination of measurement uncertainties and natural variability between fragments.

The exsolved CO_2 concentrations were calculated from the vesicularity and average measured density of CO_2 in the vesicles. The density of CO_2 in the vesicles was determined at the Woods Hole Oceanographic Institution using a Horiba LabRam HR Raman spectrometer with a focal length of 800 mm. The instrument is equipped with a thermoelectrically cooled (−70 °C) Synapse® 1024x256 pixel open electrode CCD detector. Measurements were conducted following previously established protocols (Aster et al., 2016; Esposito et al., 2011; Lamadrid et al., 2017; Moore et al., 2015). All analyses were conducted with a 100x long working distance objective with a numerical aperture (NA) of 0.8 and a confocal hole diameter set to 300 μm. We used a 632 nm laser, a grating with 1800 grooves per mm, and a slit size of 30 μm. Spectra were collected for five 30 s accumulations between 1160 and 1429 cm^{-1}. The background for each sample was corrected for noise in LabSpec6 and the peaks were fit using a Gaussian function in MATLAB. The CO_2 Fermi diad splits were calibrated using the measured separation between the 1249.03 cm^{-1} and 1388.25 cm^{-1} bands for argon, using spectra collected at the beginning and end of the session. The measured separations between argon bands drifted by <0.05 cm^{-1}. The density of CO_2 within the vesicles was calculated based on the difference in wavenumber between the two peaks of the Fermi diad (Wright and

Wang, 1973) according to the calibration developed by Lamadrid et al. (2017) at Virginia Tech for similar acquisition parameters (632 nm laser; 1800 grooves/mm grating). The variability between the density measurements provides an estimate of the uncertainties associated with this method of reconstructing total CO_2 concentrations (standard error is 0.01 g/cm^3).

4.4 Results

Fourteen new popping rocks were recovered *in situ* from the MAR axial valley at the 2πD43 dredge site, ~7 km west of the hanging-wall cutoff for the 13°48'N oceanic core complex (Figure 4-2). These samples, as well as 43 non-popping rocks recovered within the rift valley near 13°46'N, were analyzed for major and trace elements and volatile concentrations (Supplementary Table S.4.1 – S.4.2). Three popping rocks and three proximal, non-popping samples were analyzed for helium and argon abundances and isotopic compositions (Supplementary Table S.4.3). *AUV Sentry* near-bottom multibeam bathymetry and *HOV Alvin* sampling and seafloor observations reveal that the popping rocks are primarily restricted to a north-south trending, heavily sedimented pillow ridge and proximal pillow mounds, which we refer to as 'Popping Rock Ridge' (Figure 4-2; seafloor observations in Figure 4-3). The popping rocks are remarkably homogeneous in major and trace element concentrations and ratios (e.g., $[La/Sm]_N$ = 1.76 – 1.84; Figure 4-2; Figure 4-4), indicating similar mantle sources and extents of melting. The trace element ratios and rare earth element (REE) patterns in popping rocks are indistinguishable from eight proximal basalt samples that were not identified as popping rocks on the ship, many of which have notably lower vesicularities (Figure 4-2; Figure 4-4). The popping rocks (diamonds in Figure 4-2) and eight proximal, non-popping rocks with similar REE patterns (triangles in Figure 4-2) are geochemically distinct from all other lavas recovered from the region based on major and trace element compositions (circles in Figure 4-2; Figure 4-4; Supplementary Table S.4.1).

The dissolved volatile concentrations (CO_2, H_2O, Cl, F, S) in the popping and non-popping samples are within the range commonly observed in MORB (Wallace et al., 2015; Supplementary Table S.4.2). In contrast, the exsolved volatile concentrations in these popping rocks are amongst the highest ever recorded for submarine MORB, especially those outside the influence of mantle plumes (Chavrit et al., 2014; Supplementary Table S.4.2). The vesicularity in the popping rocks ranges from 5 – 24 vol.% based on reflected light photomicrographs and x-ray micro-computed tomography scans (Figure 4-5; Figure 4-6; Table 4-1). Based on the measured vesicularity, measured dissolved

CO_2 concentrations, and the average CO_2 density within vesicles measured by Raman spectroscopy (Supplementary Table S.4.4), the CO_2 concentration in these popping rocks varies from 3,100 – 16,200 ppm, where ppm is μg/g (Figure 4-1; Table 4-1; Supplementary Table S.4.2). The eight non-popping rocks that are geochemically similar overlap this range in vesicularity and total CO_2 concentration, but are on average lower (0.18 – 8.24 vol.%; 360 – 4,550 ppm CO_2; Figure 4-1; Figure 4-2). We rely on the CO_2 concentrations estimated from vesicularity rather than measured by capacitance manometry during crushing for helium and argon analyses because the latter method does not account for gas loss through cracks prior to analysis.

The vesicle size distributions of moderate vesicularity samples (Figure 4-5a-c) are distinct relative to high vesicularity popping rocks (Figure 4-5d-f). Moderate vesicularity popping rocks (i.e., 5 – 7 vol.%) display simple log-linear vesicle size distributions (Figure 4-5; Figure 4-6). The vesicle size distributions of higher vesicularity samples deviate from log-linear relationships, with more abundant large vesicles (>1.5 mm diameter) than expected based on a simple continuous bubble nucleation and growth model (Cashman and Mangan, 1994) (Figure 4-5; Figure 4-6). The new popping rocks exhibit relatively homogeneous $^4He/^{40}Ar^*$ (1.05 – 1.09), where $^{40}Ar^*$ is the ^{40}Ar concentration corrected for atmospheric contamination ($^{40}Ar^* = {}^{36}Ar_{sample} (^{40}Ar/^{36}Ar_{sample} - {}^{40}Ar/^{36}Ar_{air})$; e.g., Sarda and Moreira, 2002). The $^4He/^{40}Ar^*$ in three popping rocks and one geochemically similar, non-popping rock are slightly lower than the putative mantle production ratio of 3 ± 1 (Marty and Tolstikhin, 1998), while proximal, geochemically distinct non-popping samples exhibit elevated $^4He/^{40}Ar^*$ consistent with estimates for degassed MORB (Tucker et al., 2018) (Figure 4-7). The popping rocks display $^3He/^4He$ ratios of 8.07 – 8.30 R_A and $CO_2/^3He$ ratios of 2.97 x 10^9 – 3.11 x 10^9. Proximal, non-popping rocks have $^3He/^4He$ ratios of 7.63– 8.33 R_A and $CO_2/^3He$ ratios of 1.79 x 10^9 – 2.53 x 10^9.

4.5 Discussion

4.5.1 Origin of the high volatile concentrations in popping rocks

The most striking and novel observation from this study is that the new popping rock lavas display highly variable total CO_2 concentrations despite similar geochemistry and eruptive morphology (Table 4-1; Figure 4-1 – Figure 4-4). The similar trace element ratios and REE patterns in the fourteen newly recovered popping rocks and eight proximal non-popping samples (Figure 4-2;

Figure 4-4) indicate that these lavas erupted from geochemically similar mantle sources, possibly during a series of closely timed eruptions based on their restricted locations along a pillow ridge. These geochemical similarities also suggest that the variable CO_2 contents cannot be explained by dilution during progressive mantle melting, enrichment during fractional crystallization, or magma mixing, because these processes would produce comparable systematics in trace elements that behave similarly to carbon (e.g., Nb, Ba, Rb). Thus, a subset of these samples must have experienced either gas accumulation or gas loss in order to produce variable CO_2 concentrations despite homogeneous trace element ratios and REE patterns.

Vesicle size distributions and $^4He/^{40}Ar^*$ are influenced by gas accumulation and gas loss, and thus have the potential to provide insight into the processes controlling volatile concentrations in popping rocks (Cashman and Mangan, 1994; Marty and Tolstikhin, 1998; Moreira and Kurz, 2013; Sarda and Graham, 1990; Tucker et al., 2018). Progressive equilibrium degassing (i.e., gas loss from the magma) would be expected to produce enriched $^4He/^{40}Ar^*$ ratios in the lowest vesicularity samples due to the greater solubility of ^4He relative to ^{40}Ar (Burnard et al., 2004; Paonita and Martelli, 2007; Sarda and Moreira, 2002). However, the newly recovered popping rocks display consistently low $^4He/^{40}Ar^*$ ratios relative to the mantle production ratio (Marty and Tolstikhin, 1998) (Figure 4-7), which indicates that the variable volatile concentrations in these samples does not reflect open-system, equilibrium (i.e., solubility controlled) degassing (Moreira and Kurz, 2013). Disequilibrium (i.e., diffusion controlled) degassing can fractionate noble gases in the opposite sense due to the lower diffusivity of ^{40}Ar relative to ^4He, which counteracts the lower solubility of ^{40}Ar. In the case of instantaneous, continuous gas loss (i.e., Rayleigh distillation), disequilibrium degassing would still produce slightly elevated $^4He/^{40}Ar^*$ ratios in samples with 20 – 50% of the initial gas content retained based on the average degree of disequilibrium necessary to produce MORB noble gas systematics (Tucker et al., 2018). Although discrete episodes of syn-eruptive, open-system, disequilibrium gas loss could produce low $^4He/^{40}Ar^*$ ratios in degassed samples (Gonnermann and Mukhopadhyay, 2007), shallow disequilibrium degassing would also likely produce dissolved CO_2 concentrations greater than experimentally determined solubilities at the eruption depths based on similar C and Ar diffusivities (Paonita and Martelli, 2006), which is not observed in the newly recovered popping rocks. There are uncertainties in the mantle $^4He/^{40}Ar^*$ production ratio, related to K, U, and Th abundances and mantle residence time, which hinders interpretation of the small difference between the new popping rocks data presented here and the putative mantle production

ratio of 3 ± 1 (Marty and Tolstikhin, 1998). Our results show that the popping rocks have consistently low $^{4}He/^{40}Ar^{*}$ despite highly variable total volatile concentrations. These results are consistent with a bubble accumulation model, but could potentially reflect more complex degassing, such as discrete multi-stage episodes of gas loss and addition at various pressures.

Vesicle size distributions in erupted basalts also provide insight into magma storage and transport histories because volatile exsolution (i.e., bubble formation and growth) depends on depressurization rates and timescales (Cashman and Mangan, 1994). During steady ascent from depth, magmas are expected to experience continuous vesicle nucleation and growth, leading to linear relationships between the natural log of the number of vesicles per unit volume (N_v) and the binned vesicle size (Sarda and Graham, 1990). The non-linear vesicle size distributions in high vesicularity popping rocks, marked by increased vesicle densities in the largest size classes, are likely caused by coalescence and/or accumulation (Chavrit et al., 2014; Sarda and Graham, 1990; Shea et al., 2010) (Figure 4-5; Figure 4-6). Although the x-ray μ-CT scans and reflected light photomicrographs show active bubble coalescence in the high vesicularity popping rocks (e.g., Figure 4-5), coalescence alone cannot explain both the vesicle size distributions and the highly variable volatile concentrations (Figure 4-1; Figure 4-5; Figure 4-6; Table S.4.1). Therefore, we suggest that bubble accumulation also influenced a subset of the popping rocks. Bubble accumulation was previously suggested for popping rock 2πD43 based on an empirical model for primary CO_2 concentrations derived from K_2O/TiO_2 ratios, axial valley depths, and spreading rates (Chavrit et al., 2014). Although some amount of degassing may still have affected the lowest vesicularity samples, the $^{4}He/^{40}Ar^{*}$ ratios, vesicle size distributions, and variable total volatile concentrations in these samples are consistent with gas accumulation as the mechanism to produce high vesicularity popping rocks at 13°46'N on the MAR. Our interpretation that gas accumulation influences the volatile concentrations in popping rocks implies that these samples may not reflect primary mantle-derived carbon concentrations.

4.5.2 Mechanisms for popping rock formation

Degassing during magma storage and transport affects volatile concentrations in most MORB based on total glass CO_2 concentrations consistent with equilibration at pressures associated with known magma storage reservoirs (e.g., Jones et al., 2018; Soule et al., 2012), greater CO_2 abundances in phenocryst hosted melt inclusions than in the carrier magmas (e.g., Helo et al., 2011), and higher $^{4}He/^{40}Ar^{*}$ in vesicles than predicted from the mantle production ratio (e.g., Marty and Tolstikhin,

1998). Only a few high-vesicularity popping rocks have been recovered from the global MOR system (e.g., 36°N MAR (Hekinian et al., 1973), Equatorial MAR (Le Voyer et al., 2015), Mathematician Ridge on the East Pacific Rise (Batiza and Vanko, 1985)), which shows that processes leading to gas accumulation are atypical. We hypothesize that the Popping Rock Ridge samples experienced gas accumulation during storage at crustal depths (Figure 4-8). Magma storage within a compressional regime associated with bending of the 13°48'N OCC subsurface footwall (e.g., Parnell-Turner et al., 2017) may have prevented gas loss through the top of the magma reservoir and facilitated the accumulation of volatiles contained within the reservoir. Other mechanisms to decrease the permeability of the magma reservoir boundaries are also possible, including increasing lithospheric pressure with greater depths of storage (Figure 4-8).

4.5.3 Implications for undegassed MORB and mantle carbon estimates

Volatile accumulation increases CO_2 concentrations relative to similarly incompatible elements. Based on the interpretation that the unusually high volatile concentrations in popping rocks reflects bubble accumulation, the highest CO_2/Nb or CO_2/Ba ratio from the Popping Rock Ridge samples does not represent a primitive, undegassed magma. Although it is difficult to constrain the pre-accumulation volatile concentration, we suggest that intermediate vesicularity samples from Popping Rock Ridge (5 – 7 vol.%; 2,450 – 3,450 ppm CO_2) provide the closest approximation based on their simple, log-linear vesicle size distributions (Figure 4-5; Figure 4-6) and $^4He/^{40}Ar^*$ ratios near the production ratio (e.g., 1.31 ± 0.06; Figure 4-7). Our estimated pre-accumulation vesicularity and CO_2 concentration agrees with predictions from an empirical model derived from global K_2O/TiO_2 ratios, spreading rates, and axial valley depths (Chavrit et al., 2014). Popping rocks with 5 – 7% vesicularity have lower CO_2/Nb (98 – 137) and CO_2/Ba (16 – 22) ratios than all previous estimates for undegassed melts (Le Voyer et al., 2015; Michael and Graham, 2015; Saal et al., 2002) except three undersaturated MORB glasses from Gakkel Ridge in the Arctic Ocean (Michael and Graham, 2015). While it is possible that complex degassing processes influenced the intermediate vesicularity popping rocks without affecting $^4He/^{40}Ar^*$ ratios or vesicle size distributions, we explore the implications of the simple bubble accumulation model, in which popping rocks with 5 – 7% vesicularity reflect primary volatile concentrations, for carbon concentrations in the upper mantle and ridge CO_2 flux.

The inferred pre-accumulation volatile concentration in popping rocks implies that there are large heterogeneities in the CO_2/incompatible trace element ratio of the depleted MORB mantle (DMM). Further, CO_2/Ba and CO_2/Nb ratios from pre-accumulation popping rocks are less than ratios in most undegassed ultra-depleted and depleted MORB (Fig 1.; Le Voyer et al., 2017; Michael and Graham, 2015; Saal et al., 2002), and indicate that these ratios do not scale with trace element enrichment. The lack of a positive correlation between incompatible trace element and CO_2 enrichment in DMM implies that mantle carbon concentrations are lower and less heterogeneous than inferred from the post-accumulation CO_2/Nb ratio (556) of popping rock 2πD43, which has been used to suggest that mantle carbon concentrations vary by almost two orders of magnitude globally (Le Voyer et al., 2017). In addition, heterogeneities in primary CO_2/incompatible trace element ratios indicate that annual ridge CO_2 flux cannot necessarily be accurately calculated using a single CO_2/Nb or CO_2/Ba ratio, the estimated DMM Nb or Ba concentration, and the estimated annual volume of basaltic magma produced along the MOR system. These implications are based on the interpretation that gas accumulation produced the high-vesicularity popping rocks and that intermediate vesicularity samples reflect primary volatile concentrations. If the vesicle size distributions, low $^4He/^{40}Ar^*$ ratios, and highly variable volatile concentrations instead reflect extreme degrees of disequilibrium during degassing, the highest vesicularity samples could reflect primary volatile concentrations, indicating primary CO_2/Nb = 500 – 650 for popping rocks (Table 4-1) and large variability in mantle carbon concentrations (e.g., Le Voyer et al., 2017). Multiple discrete episodes of gas loss and addition could potentially produce these observations, which would complicate the interpretation of mantle volatile concentrations based on popping rocks because the primary concentration would likely not correspond with either the highest or lowest vesicularity.

4.6 Conclusions

Carbon strongly influences the viscosity and oxidation state of the mantle, melt formation and migration, long-term climate cycling, and volcanic processes. Rare, undegassed MORB and melt inclusions provide important constraints on the carbon content of the upper mantle. A suite of newly recovered *in situ* popping rocks from the Mid-Atlantic Ridge near 14°N contain highly variable vesicularities (5 – 24 vol.%) and total volatile concentrations (3,100 – 16,200 ppm CO_2) despite relatively homogeneous major and trace element geochemistry (e.g., $[La/Sm]_N$ = 1.76 – 1.84) and consistently low $^4He/^{40}Ar^*$ ratios (1.05 – 1.09). Vesicle size distributions are log-linear with slight deviations in large size classes in the highest vesicularity samples, possibly reflecting coalescence or

accumulation. Bubble accumulation is consistent with all of our observations, whereas coalescence can explain the deviations observed in the vesicle size distributions but not the variable total volatile concentrations. We suggest that popping rocks, which are the only volatile-saturated MORB previously inferred to represent 'undegassed' magmas, are not representative of primary mantle volatile concentrations and are instead influenced by gas accumulation. The results imply lower CO_2/Nb or CO_2/Ba than previously inferred based on undegassed MORB and lower and less heterogeneous mantle carbon concentrations.

4.7 Acknowledgments

We gratefully acknowledge the captain, operations teams, marine technicians, and crew of the *R/V Atlantis*, the operations teams of the *AUV Sentry* and *HOV Alvin*, and the entire scientific party onboard AT33-03. We appreciate the analytical assistance provided by B. Monteleone, S. Bendana, and M. Lytle. We thank M. Hirschmann and an anonymous reviewer for insightful comments on an earlier version of this manuscript and T. Mather for editorial handling. Seagoing and analytical efforts were supported by National Science Foundation grants OCE-1259218 and OCE-1260578 to M. Kurz and E. Mittelstaedt. M. Jones acknowledges support provided by the Department of Defense (DoD) through the National Defense Science & Engineering Graduate Fellowship (NDSEG) Program.

4.8 Figures and tables

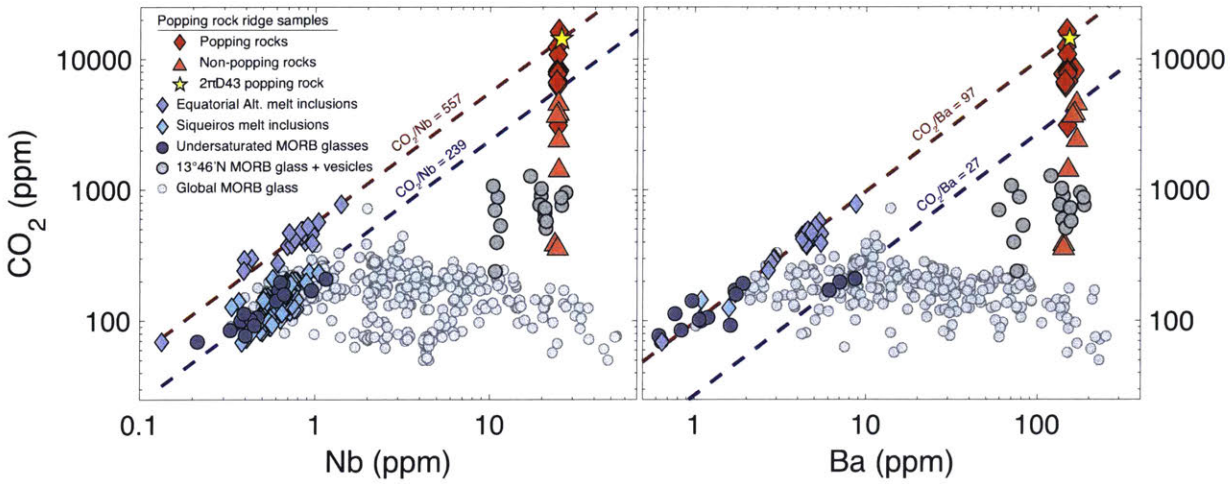

Figure 4-1. Variation in CO_2 concentration as a function of Nb and Ba concentration. Red diamonds represent the fourteen new popping rocks collected from the Mid-Atlantic Ridge near 13°46'N while orange triangles represent proximal non-popping rocks with indistinguishable REE patterns and trace elements ratios. CO_2 concentrations presented in this study were reconstructed from the dissolved concentrations, vesicularity, and measured CO_2 density within bubbles. Data sources: 2πD43 popping rock: Sarda and Graham (1990), Bougault et al. (1988), and Cartigny et al. (2008); Equatorial Atlantic melt inclusions: Le Voyer et al. (2017); Siqueiros melt inclusions: Saal et al. (2002); Undersaturated MORB glasses: Michael and Graham (2015); global MORB glass compilation from PetDB.

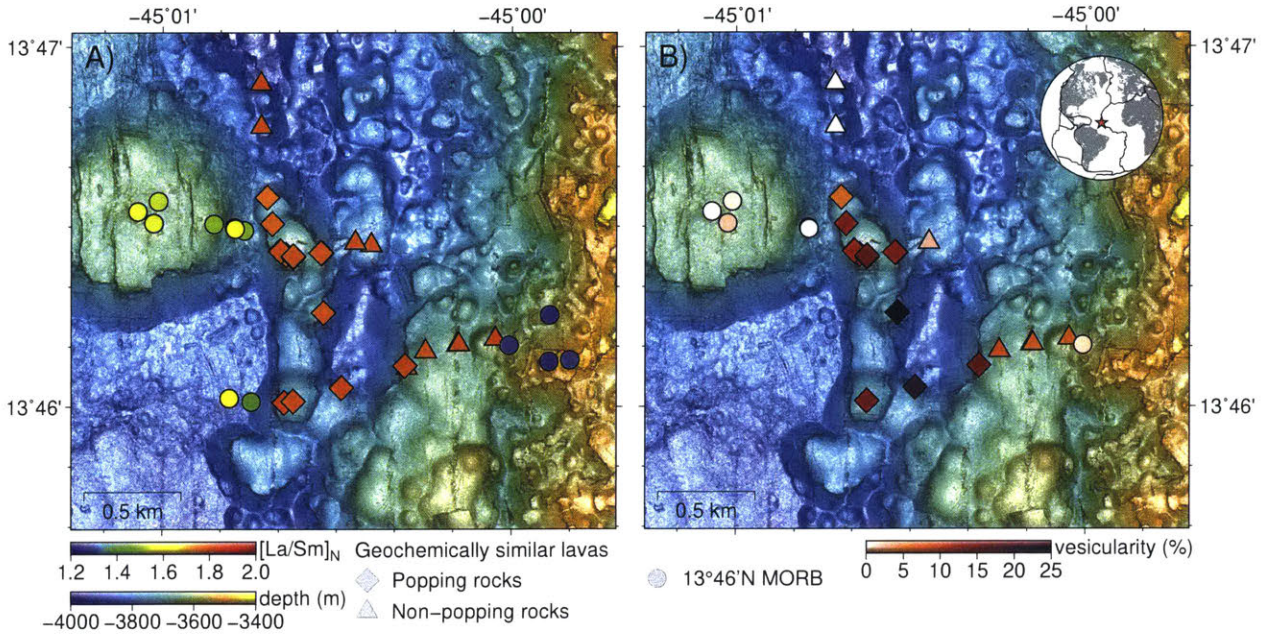

Figure 4-2. 1 m resolution bathymetric maps showing the distribution of newly recovered popping rocks (diamonds). The bathymetry reveals that popping rocks are primarily restricted to a north-south trending pillow ridge and proximal pillow mounds. (A) Symbols are colored by $[La/Sm]_N$. (B) Symbols are colored by vesicularity. Despite relatively homogeneous trace element ratios, the vesicularity and total CO_2 concentrations in popping rocks varies dramatically (5 – 24 vol.% vesicles; 3,100 – 16,200 ppm CO_2). Several proximal, non-popping rocks (triangles) are geochemically similar to popping rocks but have notably lower vesicularities (<1 – 8 vol.% vesicles; 360 – 4,550 ppm CO_2). Inset map shows the location of the popping rocks on the Mid-Atlantic Ridge as a red star.

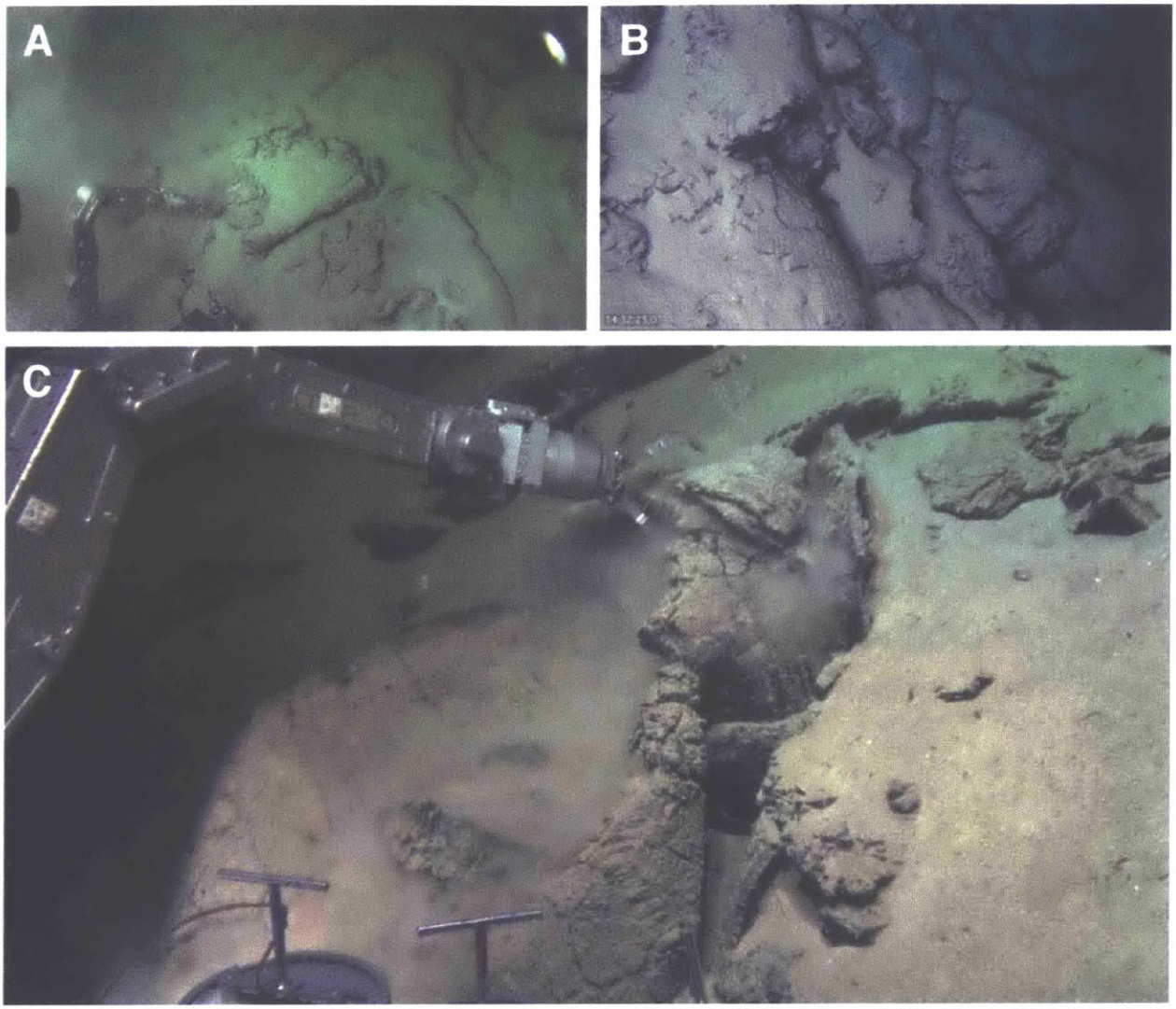

Figure 4-3. Seafloor observations from Alvin dives AL4818 and AL4821, which traversed Popping Rock Ridge. (A) Popping rock AL4818-003, the first recovered *in situ*, collected from a sedimented, collapsed pillow lava. (B) Elongated pillows from the northern edge of Popping Rock Ridge. (C) Popping rock AL4821-057, collected from the outer crust of a collapsed pillow basalt.

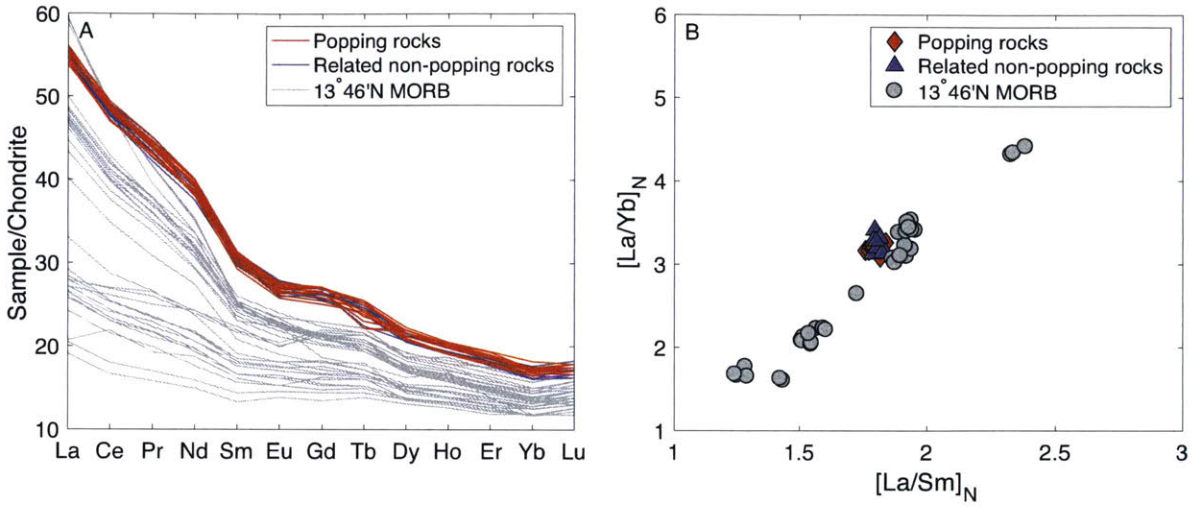

Figure 4-4. (A) Rare earth element diagrams and (B) La/Yb vs. La/Sm comparing popping rocks (red; diamonds in Figure 4-2), geochemically similar non-popping rocks (blue; triangles in Figure 4-2), and geochemically distinct samples at 13°46'N (grey; circles in Figure 4-2). Elements are normalized to CI carbonaceous chondrites (McDonough and Sun, 1995).

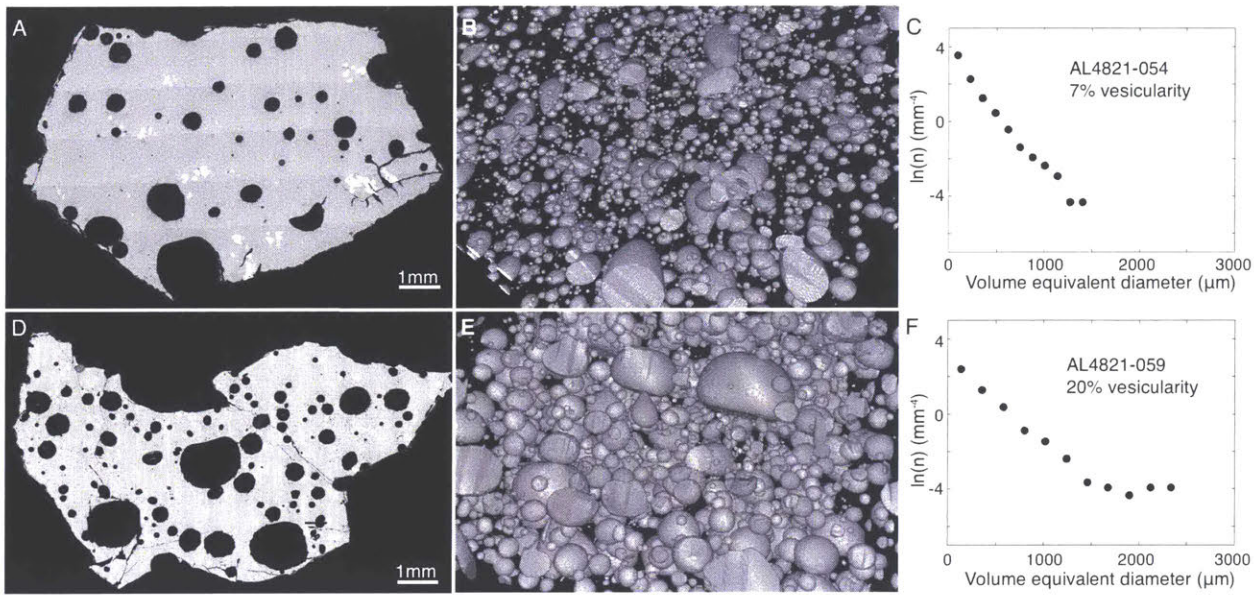

Figure 4-5. Polished section images (A,D), x-ray micro-computed tomography scans (B,E), and vesicle size distributions based on the x-ray μ-CT scans (C,F) for an intermediate vesicularity (AL4821-054; top) and high vesicularity (AL4821-059; bottom) popping rock. The high vesicularity popping rocks show deviations from a simple log-linear vesicle size distribution at the largest size classes, likely due to bubble coalescence and/or accumulation.

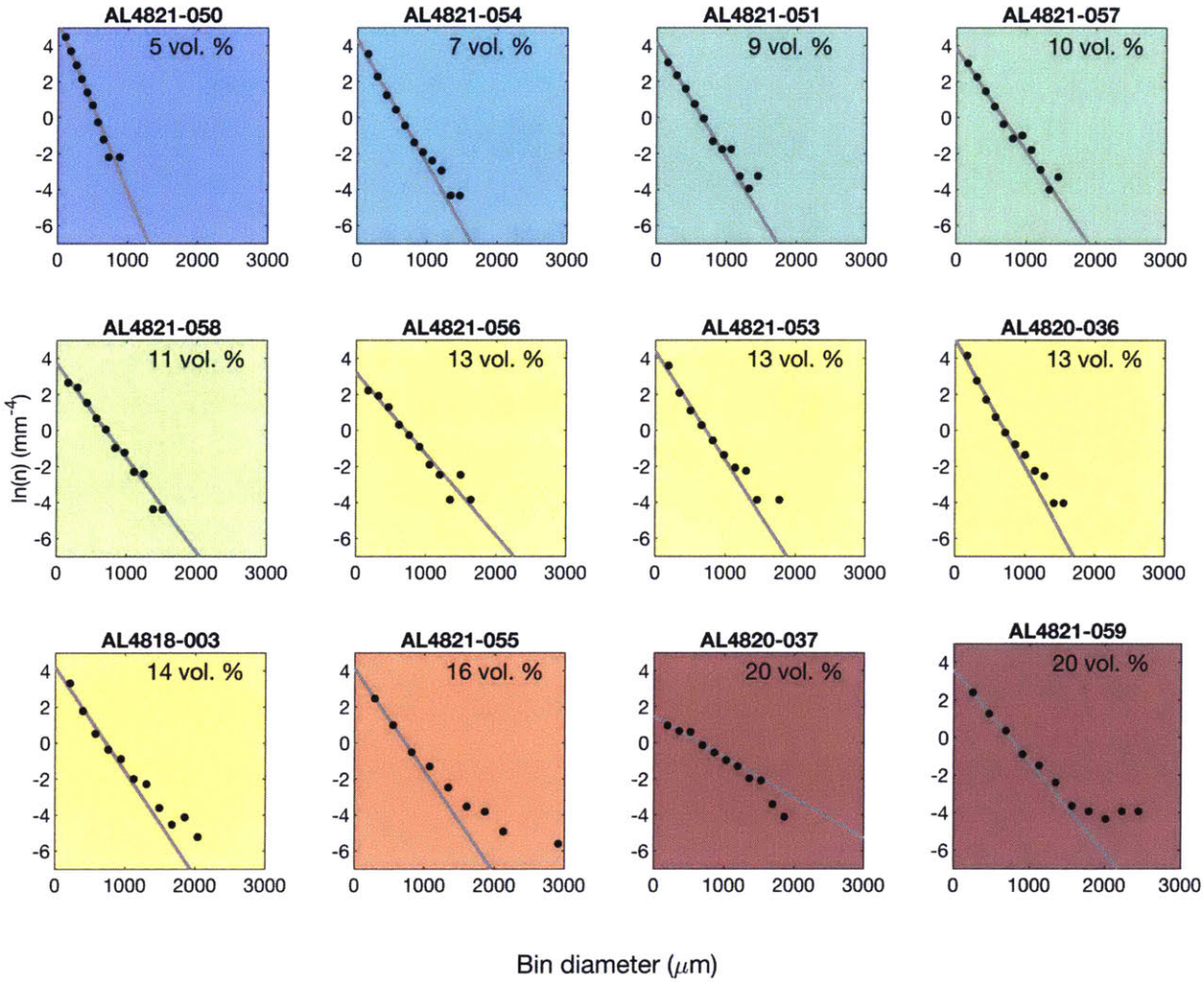

Figure 4-6. Vesicle size distributions, shown as the natural log of the volumetric number density of bubbles normalized to the width of the bin as a function of the bin diameter, for 12 newly recovered popping rocks based on x-ray microtomography scans. The vesicle size distributions from high vesicularity popping rocks (>10%) are often distinct relative to low vesicularity (5 – 7%) popping rocks, including more large bubbles (>1.5 mm diameter) than expected based on a simple bubble nucleation and growth model. Log-linear reference lines, based on least-squares regressions of ln(n) on size classes <1 mm, are shown in order to highlight deviations at large size classes in some high vesicularity samples.

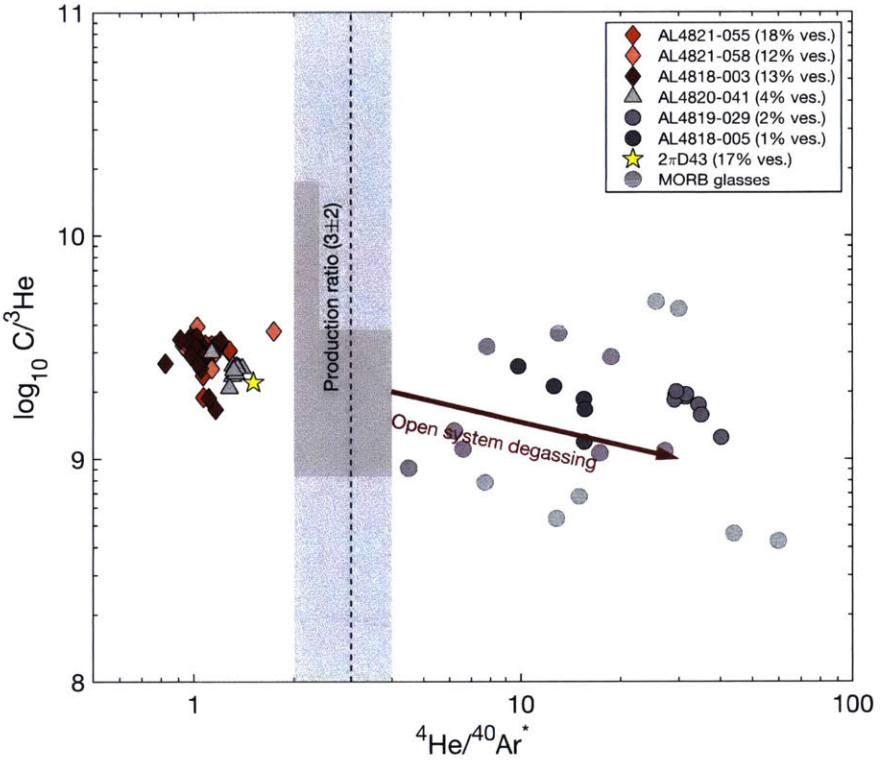

Figure 4-7. $C/^3He$ vs. $^4He/^{40}Ar^*$ for three popping rock samples (diamonds), one geochemically similar, non-popping sample (AL4820-041), and two geochemically distinct samples (AL4818-005 and AL4819-029) relative to typical MORB (Marty and Tolstikhin, 1998). The popping rocks and proximal, geochemically similar non-popping rock (AL4820-041) display $^4He/^{40}Ar$ ratios similar to the mantle production ratio of 3 ± 1 (grey bar; Marty and Tolstikhin, 1998), demonstrating that gas loss did not produce the variable volatile concentrations in these samples. Data sources: 2πD43 popping rock: Moreira et al. (1998); MORB glasses: Marty and Tolstikhin (1998).

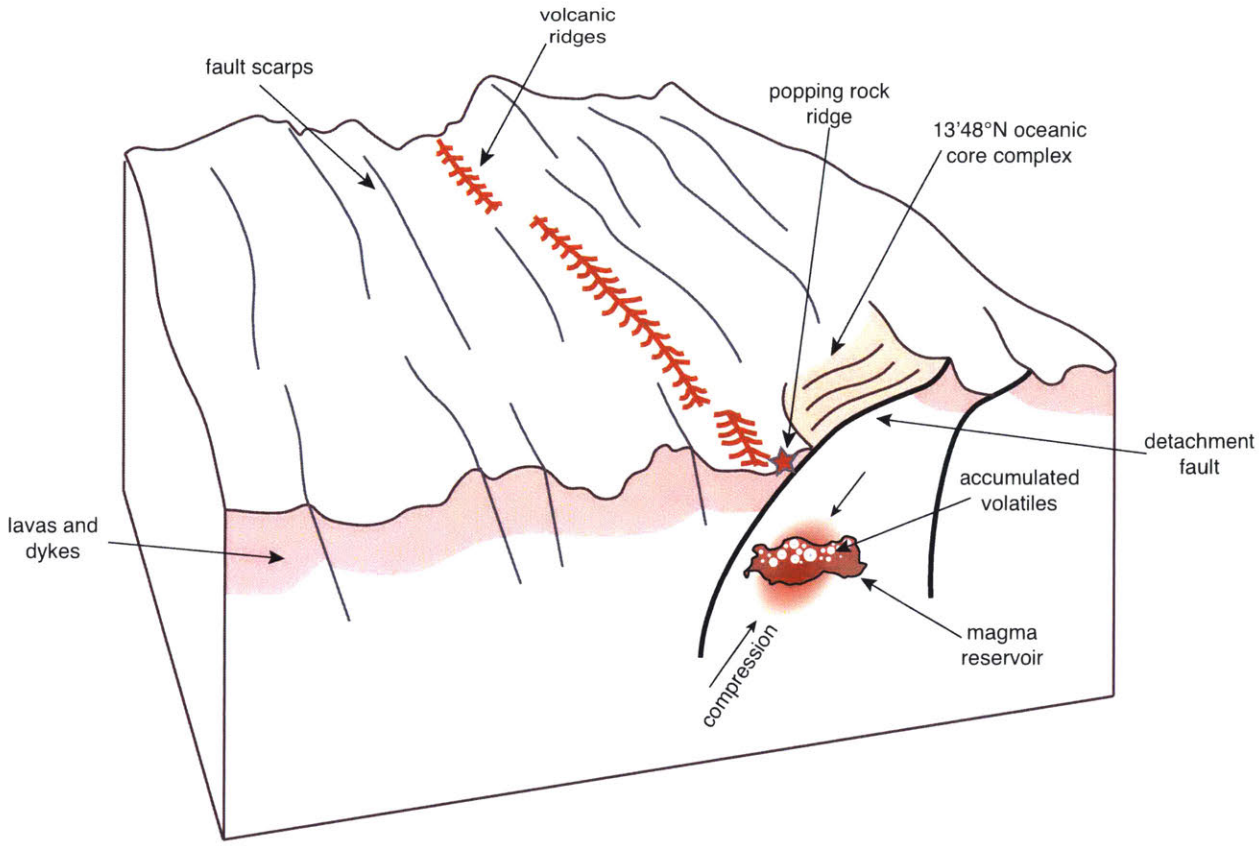

Figure 4-8. Schematic representation showing the geologic setting and a possible formation mechanism for popping rocks near 13°46'N. Seafloor features are based on bathymetry presented in Smith et al. (2008) and the ridge structure is adapted from Escartin and Canales (2011). The popping rocks were found ~7 km west of the 13°48'N OCC, near the boundary between 'tectonic' and 'magmatic' ridge segments. The volatile concentrations, major and trace element geochemistry, and noble gas geochemistry in these samples are consistent with bubble accumulation as a formation mechanism. In contrast to 'typical' MORB, popping rocks may have experienced volatile accumulation rather than loss due to storage within a compressional regime associated with the 13°48'N OCC (e.g., Parnell-Turner et al., 2017) or the sealing of cracks that would typically allow gas loss due to storage at high-pressures.

Table 4-1. Nb, Ba, vesicularity (3D and 2D), and total CO_2 concentrations (based on dissolved CO_2 concentrations, 2D vesicularity measurements, and the average CO_2 density in bubbles) for newly recovered *in situ* popping rocks.

Sample	Nb	Ba	Ves. (3D)	Ves. (2D)	total CO_2
	(ppm)	(ppm)	(%)	(%)	(ppm)
AL4818-003	24.34	149.61	13.6	13.3	7633
AL4820-035	24.05	141.06			
AL4820-036	24.21	139.43	13.2	13.3	7663
AL4820-037	24.16	145.61	19.7	20.0	12368
AL4820-039	24.98	163.49		14.1	8178
AL4821-050	24.53	148.37	5.2	5.7	3112
AL4821-051	24.65	149.88	9.1	11.9	6731
AL4821-053	24.41	149.18	12.9	14.2	8270
AL4821-054	24.37	144.38	7.1	11.2	6345
AL4821-055	24.49	147.36	15.6	17.9	10823
AL4821-056	24.20	147.24	12.8	13.8	7993
AL4821-057	24.38	148.27	9.8	13.4	7731
AL4821-058	24.21	143.32	11.3	11.7	6643
AL4821-059	24.80	146.70	20.1	24.8	16231

Chapter 5

Giant pumice dispersal during the 2012 eruption of Havre Volcano

This chapter is being prepared for publication as: Jones, M.R., Fauria, K.E., Soule, S.A., Woods, A.W., Giant pumice dispersal during the 2012 eruption of Havre Volcano

5.1 Abstract

Submarine silicic eruptions commonly produce giant pumice blocks that can rise to the sea surface to form massive, long-lived pumice rafts or sink rapidly back to the seafloor. While conceptual and quantitative models have been developed to predict the behavior of giant pumice produced by submarine eruptions, these models have not yet been robustly tested using observations from seafloor deposits. The 2012 Havre Volcano eruption produced ~1.3 km^3 of rhyolitic pumice, including a 1.2 km^3 pumice raft and >0.1 km^3 seafloor deposit. Here we quantify the seafloor distribution of giant pumice and compare our observations with model predictions for pumice dispersal. We observe a broad range of clast sizes at all distances from the vent, including clasts >5 m across within 2 km and clasts <0.5 m across greater than 5 km from the vent. We find a weak relationship between the size of individual clasts and distance from the vent, but observe that the number of large clasts per unit area strongly correlates with distance. Models for pumice cooling and saturation predict that saturation rates scale inversely with clast size, such that large clasts should travel farther from the vent than small clasts and the characteristic size of deposited clasts should increase with distance from the vent. These predictions agree with the observation that the abundance of large clasts increases with distance from the source vent for the 2012 Havre Volcano eruption. We suggest that deviations from the model predictions can be explained by advective displacement of steam by water through highly permeable pathways, which allows large clasts to settle quickly, and clast breakup, which allows small clasts to settle far from the source. These processes are strongly influenced by the macroscale vesicle structure in giant pumice clasts.

5.2 Introduction

Submarine volcanic eruptions represent roughly 70% of Earth's volcanic output (Crisp, 1984). Although submarine arc volcanoes remain less well understood than their subaerial counterparts, modern improvements in our ability to detect eruptions and collect observations have provided new insight into the effect of the overlying water column on eruption behavior (e.g., Barker et al., 2012; Carey et al., 2018; Chadwick et al., 2008; Manga et al., 2018; Resing et al., 2011; Rotella et al., 2015, 2013). In particular, recent studies have demonstrated that submarine eruption styles range from explosive activity producing fine ash and lapilli (e.g., Allen and McPhie, 2009) to intermediate behavior producing highly vesicular pumice clasts that float in water (e.g., Rotella et al., 2013) to effusive behavior forming lava flows and domes (e.g., Fiske et al., 2001). Intermediate style eruptions commonly produce meter-scale giant pumice clasts, which can float to the sea surface to form massive, long-lived rafts (e.g., Bryan et al., 2012, 2004). How environmental processes and material properties influence the dispersal and deposition of pyroclasts produced by intermediate and explosive eruptions remains a central open question in submarine volcanology (National Academies of Sciences, 2017). Recent studies suggest that the vast majority of the total erupted volume produced by intermediate regime eruptions may be transported far away from the volcano (Carey et al., 2018; Jutzeler et al., 2014; Manga et al., 2018a), which presents challenges for reconstructing the size and intensity of past submarine silicic eruptions. As most studies of modern and ancient submarine eruptions involve samples collected near the volcanic edifice, improved constraints on the processes that control pyroclast dispersal and partitioning between proximal and distal seafloor deposits would improve our ability to interpret the geologic record.

Several recent studies have proposed and developed models for the cooling, saturation, and dispersal of giant pumice produced by submarine eruptions (e.g., Allen et al., 2008; Fauria and Manga, 2018; Manga et al., 2018a; Rotella et al., 2013). These models predict that large, highly vesicular pumice should rise quickly to the surface and remain buoyant for long periods of time. In particular, Fauria and Manga (2018) demonstrate that the saturation of steam-filled pumice is paced by conductive cooling, whereby cooling allows steam condensation and water ingestion. Large pumice clasts cool – and therefore saturate – relatively slowly because the characteristic timescale for conductive cooling increases with size. The relationship between clast size and cooling rate further implies that larger clasts spend more time in the water column and are more strongly affected by ocean currents (Allen et al., 2008; Kano et al., 1996). Provided that ocean current directions are relatively constant, the size

of pumice clasts on the seafloor should therefore increase with distance from the source vent. However, models for giant pumice dispersal have not yet been robustly tested using detailed observations from a submarine eruption. The 2012 eruption of Havre Volcano provides an ideal opportunity to test models of submarine pyroclast dispersal due to the established eruption properties (e.g., water depth, eruption rate, vent locations; Carey et al., 2018; Manga et al., 2018a, 2018b; Mitchell et al., 2018) and the availability of detailed seafloor observations and high-resolution bathymetric maps collected shortly after the eruption (Carey et al., 2018). In this study, we compare the seafloor distribution of giant pumice produced by the 2012 Havre Volcano eruption with model predictions and provide new insight into the processes that control pyroclast dispersal in the submarine environment.

5.3 The 2012 Havre Volcano eruption

Moderate-Resolution Imaging Spectroradiometer (MODIS) images revealed that a large pumice raft originated above Havre Volcano in the Kermadec Arc on July 18, 2012 (Carey et al., 2014; Jutzeler et al., 2014). The production of the pumice raft lasted roughly ~21 hours and was associated with an earthquake swarm of 18 events M > 3.5. The raft covered ~400 km^2 immediately after the eruption and drifted away from the volcano at ~0.1 m/s (Jutzeler et al., 2014). Differences between pre- and post-eruption bathymetry collected by the *R/V Tangaroa* revealed several new domes on Havre Volcano (Carey et al., 2014). Seafloor observations and high-resolution bathymetry revealed that the eruption produced new lava flows and domes from 14 vents at water depths ranging from 900 – 1200 m (Carey et al., 2018; Figure 5-1). The high-resolution bathymetric maps and seafloor observations further revealed that large (1 – 9 m across) pumice blocks blanket the volcanic edifice and comprise at least 5% of the total erupted volume (Carey et al., 2018). Based on similar axes of dispersal, compositions, and microtextures, the seafloor giant pumices and raft pumices are thought to share a common origin from a single vent source (Carey et al., 2018; Manga et al., 2018; Mitchell et al., in press). Manga et al. (2018) suggest that the seafloor and raft pumice were produced effusively based on a conduit model for magma ascent, indicating that giant pumices fragmented above the vent, possibly through cooling joint propagation. Flotation experiments, x-ray computed tomography scans, and helium pycnometry measurements indicate that gas trapping through isolated porosity or air infiltration affects a portion of the Havre pumices, allowing long flotation times (Fauria et al., 2017; Manga et al., 2018; Mitchell et al., in press).

5.4 Methods

5.4.1 Seafloor mapping, observations, and sampling

The seafloor deposits from the 2012 Havre eruption were investigated during a 2015 research cruise aboard the *R/V Revelle* (Carey et al., 2018). During the cruise, the autonomous underwater vehicle (AUV) *Sentry* conducted 10 multibeam bathymetry surveys at ~60 m altitude, covering the caldera floor and rim (Figure 5-2). The remotely operated vehicle (ROV) *Jason* collected videos, down-looking images, and seafloor samples during 12 dives. The distribution of the giant pumice blocks based on the down-looking imagery is described by Carey et al. (2018). One giant pumice (~1 m^3) was recovered from the seafloor in its entirety (HVR290).

5.4.2 Quantifying the distribution of giant pumice using Sentry bathymetry

We quantified the locations, sizes, and number density of giant pumice clasts on the seafloor using the *AUV Sentry* high-resolution multibeam bathymetry published in Carey et al. (2018). Data processing steps included corrections for sound speed velocity, tides, and vehicle position and filtering based on beam angle and range (Carey et al., 2018). Despite these corrections, persistent navigational offsets between adjacent swaths and reduced quality in the outer beams result in parallel, smooth, evenly spaced bands in the 1 m resolution bathymetric map (Figure 5-2; Carey et al., 2018), which precludes giant pumice quantification in the gridded, merged dataset. Instead, we analyzed giant pumice blocks using the inner beams (within ~50 m from the center beam) from individual swaths acquired by *Sentry*. Specifically, we selected 162 roughly evenly spaced locations on the seafloor for detailed analysis, avoiding domes, block falls on the caldera floor, and the caldera walls. For each location, we gridded an area ~100 m x 100 m at 0.5 m horizontal resolution. The gridded data was detrended by subtracting the value of a planar fit to the surface at each grid cell and subsequently high-pass filtered with a 15 m cutoff using 2DSpecTools (Figure 5-3; Perron et al., 2008).

We identified pumice blocks in the gridded, detrended, and filtered bathymetry using a closed-contouring basal outlining routine (Bohnenstiehl et al., 2012). The basal outlining routine contours the data at 0.1 m intervals from a defined start level (0.5 m in this study) to the maximum value of the input grid. We selected parameters for the basal outlining routine based on the characteristics of giant pumice blocks observed in the Jason video, along with trial and error comparisons between the

contouring results and Jason observations. For a contour to be retained for analysis, it must be closed, include at least 8 points, and contain >2 contour levels within it. The maximum distance between any 2 points on the closed contour must be ≤12 m. An elliptical fit to the closed contour must have a misfit <0.15 and the ratio between the long and short axis dimensions must be ≤5. The tangent of the height-to-basal radius ratio must fall between 3 and 60. Following the application of these thresholds, the routine eliminates closed contours that lie within another contour. The remainder of the closed contours define the pumice blocks identified in the bathymetry (Figure 5-3).

5.4.3 Tomographic imaging of giant pumice

X-ray computed tomography was used to assess the internal structure of the single giant pumice that was retrieved from the seafloor in its entirety (HVR290), with methods and qualitative descriptions presented in Mitchell et al. (in press). Specifically, the NSI scanner at the University of Texas was used to image a ~0.8 x 0.4 x 0.4 m fragment of HVR290 at 0.165 mm/voxel. We manually digitized the outlines of vesicles with diameters >1 cm in five 2D slices from the tomography scan. For each slice, we calculated the minimum 2D distance between each pixel and either the nearest vesicle >1 cm in diameter or the outer edge of the pumice clast. The results from these analyses were used to interpret the distance between pathways through which liquid water could efficiently infiltrate the pumice clast.

5.5 Results

5.5.1 Distribution and size of pumice clasts in the high-resolution bathymetry

The closed contouring routine identified 7,429 pumice clasts in the 162 analyzed regions (over a total area of ~1.3×10^6 m^2). The effective diameters of the identified clasts, calculated based on the area enclosed by the contours, range from <1 – 8 m and exhibit a skewed normal distribution with a median of 2 m and a heavy right-side tail (Figure 5-4). The effective diameter of the pumice blocks does not show a strong linear relationship with distance or bearing from the source vent (e.g., Figure 5-4; $R^2 << 0.1$). The data show a broad range in pumice clast sizes at all distances.

The number density of identified pumices within each region varies from 0 to ~0.02 m^{-2} (Figure 5-5), with the highest density regions overlying the dispersal axis identified by Carey et al. (2018). The percent area covered by the identified pumice varies from 0 to 10% and increases linearly with the

pumice number density in the region (R^2=0.96). For regions along the primary dispersal zone (<500 m from the dispersal axis; Figure 5-5), we used a linear regression model with binned size classes (1.5 – 2.5 m; 2.5 – 3.5 m; 3.5 – 4.5 m; >4.5 m) as a categorical interaction term to interrogate the effect of size and dispersal distance on pumice density. The linear model fit the data well (P<0.001; R-Squared = 0.9), with significant differences between the regression slopes of density on distance for different size classes (Figure 5-5). The number density of large pumice blocks on the seafloor increases with distance from the vent. The slope relating seafloor number density to distance from the vent is larger for smaller size classes of giant pumice (Figure 5-5). For example, the number density of pumices 1.5 – 2.5 m in diameter increases from ~0.002 pumices/m^2 near the vent to ~0.015 pumices/m^2 at ~6 km from the vent, whereas pumices 2.5 – 3.5 m in diameter increase in number density from ~0.002 to ~0.005 pumices/m^2.

5.5.2 Comparison with results from Jason down-looking imagery

Similar to the Sentry results, clast diameters based on the down-looking Jason imagery (presented in Carey et al., 2018) display a skewed normal distribution with a heavy right-side tail, but with a smaller median clast size (1.2 m; Figure 5-4) The Jason results also show a broad range in clast diameters at all distances and a weak relationship between effective diameter and distance from the source vent (R^2<0.05; Figure 5-4). The Jason imagery does not allow quantification of the seafloor number density of pumices because the area observed in each image is only ~3 m x 5 m, such that >85% of the images include <=2 digitized pumices.

5.5.3 Macroscale vesicle structure in giant pumice

As described by Mitchell et al. (in press), the x-ray computed tomography scan reveals high vesicularity regions that may extend throughout the pumice clast. We quantified the distance between the vesicular pathways by analyzing five 2D slices from the x-ray computed tomography scan. We found that roughly 90% of the pixels were <6 cm from the nearest large vesicle or the outer edge of the clast (e.g., Figure 5-6). The greatest observed distance between a pixel in the pumice clast and either the nearest large vesicle or the outer surface was 11.4 cm.

5.6 Discussion

Here we discuss the processes that can explain the observed seafloor distribution of giant pumice after the 2012 eruption of Havre Volcano. In Section 5.1, we discuss observational biases that may influence the distribution of giant pumice inferred from the Sentry bathymetry and Jason down-looking imagery. In Section 5.2, we compare our observations with predictions from pumice cooling and saturation models. The comparisons suggest that conductive cooling may dominantly control pumice saturation and dispersal distances, but additional processes modify the transport distances of many clasts relative to those predicted by conductive cooling models. In Section 5.3, we suggest that deviations from the model predictions are likely due to clast breakup during transport and deposition and rapid saturation of large clasts caused by advective displacement of steam by water through highly permeable pathways. Lastly, in Section 5.4 we discuss the implications of these results for interpreting modern and ancient silicic submarine eruptions.

5.6.1 Observational biases

The primary observational biases associated with the bathymetric analysis of giant pumice distribution are 1) the potential to overlook small clasts and 2) the potential to misidentify multiple, stacked clasts as a single, larger clast. Small clasts can be overlooked in the bathymetric analysis because pumice must protrude at least ~0.8 m above the mean height of the detrended, filtered bathymetry in order to be identified by the closed contouring routine. This bias likely causes the low areal percent coverage of identified pumice ($\leq$10%) relative to the observed maximum percent coverage of pumice in the *Jason* seafloor observations (100%). Rather than representing the true percent coverage of pumice, this variable likely represents the percent coverage of the largest pumice clasts, which are most likely to protrude above the surrounding bathymetry. Similarly, the number density of extracted pumice likely represents the number density of the largest pumice clasts. The measured and actual areal percent coverage and number densities are likely most similar in regions with pumice clasts sparsely distributed over relatively smooth seafloor. The closed contouring routine can also overestimate the size of pumice clasts by aggregating multiple stacked pumices into a single contour. Unfortunately, there is no available validation dataset to test the proportion of closed contours that represent multiple pumice clasts. However, a few of the large pumices identified in the Sentry bathymetry are also recognizable in the Jason video observations. In these instances, we confirmed that the closed contours represent individual pumice clasts.

The primary observational biases associated with the Jason imagery analysis are the exclusion of 1) pumices that appear to be <1 m in diameter and 2) pumices that extend beyond the image frame (Carey et al., 2018). Large clasts are more likely to extend beyond the image frame than small clasts, which explains the decrease in the number of identified pumices with increasing size for clasts >1.2 m across (Figure 5-4E). The imagery analysis can also segment individual pumices into multiple clasts if there are fractures or irregular shapes in the pumice surface, which contrasts with the potential for the bathymetry analysis to artificially aggregate multiple pumices into a single clast.

Although the bathymetry and imagery analyses have different observation biases, both methods show a wide range in clast sizes at all distances and a weak relationship between individual clast size and distance from the vent. The observed increase in the seafloor number density of pumices with distance from the vent based on the bathymetric analysis is relatively insensitive to the biases associated with the method, which are expected to primarily influence the quantification of small clasts. Therefore, we suggest that the primary observations that 1) a wide range in clasts sizes exists on the seafloor at all distances and 2) the seafloor abundance of large clasts increases with distance from the vent are valid despite potential observational biases.

5.6.2 Comparisons between seafloor observations and model predictions

In this section we compare the seafloor distribution of giant pumice with predictions from three models for pumice cooling and saturation in water. Namely, we consider a constant heat flux model (Manga et al., 2018a), a Stefan model with and without advection (Fauria and Manga, 2018), and a heat conduction model (Recktenwald, 2006). All three models assume that clasts are spherical, cool by thermal conduction, and are initially 850°C. The models also assume that the heat flux on the surface is uniform, such that the temperature within the clast depends only on the radius and time. The constant heat flux model assumes that clasts lose thermal energy at a constant rate that depends on the clast surface area and an experimentally determined average heat flux (7.5 W/cm^2). The heat conduction model assumes that the heat flux is controlled by the temperature difference between the clast surface and the surrounding water. The Stefan model is similar to the heat conduction model, but includes a balance between latent heat production and thermal conduction at the phase change interface. All three models assume that the radial position of the 100°C isotherm (the phase change temperature at 0.1 MPa) dictates the volume fraction of liquid in the clast.

We use these models to calculate the time-dependent buoyancy of the clasts, which can be used to predict a final position relative to the source vent when coupled with background current speeds. The vertical velocity in the water column (U) is given by the clast density (ρ_c), water density (ρ_w), clast radius (R), and drag coefficient (C_D~0.3; Batchelor and Young, 1968; Manga et al., 2018a):

$$U = \sqrt{\frac{8\,(\rho_w - \rho_c)gR}{3\rho_w C_D}} \tag{5.1}$$

where the clast density depends on the porosity (ϕ), the densities of rock, water, and steam (ρ_r, ρ_w, and ρ_s, respectively), and fraction of the pore space filled with water vapor (f), according to:

$$\rho_c = \rho_r(1-\phi) + \rho_s\phi f + \rho_w\phi(1-f) \tag{5.2}$$

The depth of the pumice (Z) in the water column is given by:

$$Z = W - \int U dt, \tag{5.3}$$

where W is the height of the water column. We use a constant water column height of 1 km, based on the depth of the source vent. We do not allow pumice to rise above the sea surface (i.e., $Z \geq 0$ for all t). The lateral distance from the source is calculated assuming a constant current velocity and direction (0.1 m/s; Jutzeler et al., 2014). The dispersal distance is the lateral distance at which the pumice returns to the initial depth in the water column (1 km). We do not consider interactions between the pumice and atmosphere. In reality, clasts that breach the sea surface may remain afloat longer than predicted by these models due to air trapping (Fauria et al., 2017), which would increase transport distances. However, the assumed thickness of the pumice raft (~5 m; Carey et al., 2018) suggests that a large fraction of the clasts remained submerged.

Figure 5-7A shows the predicted transport distance for various clast sizes based on the different conductive cooling models. The constant heat flux model predicts that all clasts <5.5 m in diameter should be deposited <2 km from the source vent (Figure 5-7A). However, we observe that the seafloor number density of large clasts (>1.5 m diameter) continues to increase until at least 6 km from the source vent (Figure 5-5), which is the limit of seafloor observations at Havre Volcano. Our results indicate that the constant heat flux model does not accurately predict the behavior of large pumice clasts. The discrepancies between the seafloor observations and model predictions suggest

that the empirically determined average heat flux for clasts <10 cm across (7.5 W/cm^2; Fauria and Manga, 2018) should not be extrapolated to larger pumices. Assuming that temperature gradients, and consequently heat flux, decrease with increasing clast size, the discrepancy between the observed and predicted transport distances is expected to be greatest for the largest clasts.

The Stefan model and heat conduction model predict much greater transport distances than the constant heat flux model (Figure 5-7A). The Stefan model with advection predicts that only clasts <1.75 m should settle within 6 km from the vent. The Stefan model without advection predicts slightly larger transport distances and suggests that only clasts <1.25 m in diameter should settle within 6 km. The heat conduction model predicts the largest transport distances, suggesting than only clasts <0.8 m in diameter should settle within 6 km. The presence of large clasts (>2 m across) at distances 1 – 6 km from the vent (Figure 5-4 – Figure 5-5) indicates that these models underestimate cooling rates and overestimate transport distances for at least a portion of the clasts. Conductive cooling may still dominantly control giant pumice saturation and dispersal distances, provided that additional processes cause variability in the transport distances for clasts of a given size. As an example, we can evaluate the seafloor number density predicted by the Stefan and heat conduction models by assuming a Gaussian error distribution around the predicted transport distances, a constant width of the deposition region (1000 m), and an equal distribution of total pumice volume between each of the analyzed size classes. We assume that the total volume of the seafloor deposit is 80% of the estimated raft volume (9.6 x 10^8 m^3; Carey et al., 2018), based on the difference between the assumed initial raft thickness (5 m; Carey et al., 2018) and the observed thickness three weeks after the eruption (70 cm; Jutzeler et al., 2014), allowing for some raft spreading. If the standard deviation in transport distance scales as 0.3 times the mean, all of the models predict that a small fraction of clasts 1.5 – 5.5 m in diameter will settle within 6 km of the vent (Figure 5-7B–D). Similar to our observations, the model results predict that the seafloor number density within each of the size classes increases with distance from the vent, with the rate of increase being greatest for pumices 1.5 – 2.5 in diameter (Figure 5-5; Figure 5-7B – D).

The poorly constrained assumptions involved in estimating seafloor number densities from the model results prevent evaluation of the accuracy of the different conductive cooling models. However, the comparison demonstrates that the observations from the 2012 Havre Volcano eruption, including the broad range in clast sizes at all distances and the increase in the seafloor number density of large clasts with distance, are consistent with conductive cooling and water

saturation primarily controlling the dispersal distance of giant pumice in the submarine environment. More information about the peak dispersal distance for smaller clasts (<1.5 m across) could help further evaluate pumice cooling and saturation models. However, the distribution of small clasts may be strongly affected by clast breakup (e.g. Figure 5-4B), which would overprint the distribution caused by scale dependent cooling and saturation rates. Additional information about the abundance of large clasts (>2 m across) far (>6 km) from the source vent would provide the best opportunity to further test models for giant pumice cooling, saturation, and transport.

5.6.3 Influence of macroscale vesicle structure on giant pumice dispersal

The broad range of clasts sizes at distances 1 – 6 km from the source vent requires additional processes that shorten transport distances for large clasts and lengthen transport distances for small clasts relative to those predicted by conductive cooling models. The large vesicles observed in the x-ray computed tomography scan (e.g., Figure 5-6; Mitchell et al., in press) may allow rapid water saturation and pumice sinking. Similar mechanisms have been proposed for subaqueous giant pumice from Taupo Volcano and Shin-Iwojima Volcano (e.g., Allen et al., 2008; Kano, 2013; Manville et al., 1998; von Lichtan et al., 2016). Centimeter-scale cores from Havre Volcano giant pumice have permeabilities up to 10^{-9} m^2 (Mitchell et al., in press). As the vesicles in the x-ray computed tomography scan are significantly larger than those in cm-scale cores, we suggest that the large, vesicular pathways in the computed tomography scan likely have permeabilities exceeding 10^{-8} m^2. The rate of water infiltration (u) scales with the permeability (k), water density (ρ_w), water viscosity (μ_w), and vesicularity (ϕ) according to

$$u = \frac{k\rho_w g}{\mu_w \phi} \tag{5.4}$$

Thus, water can infiltrate 1 m through these vesicular, highly permeable pathways within 15 s. The rapid infiltration of water through these permeable pathways could effectively reduce the length scale for conductive cooling. As such, the distance between permeable pathways, rather than the diameter of the clast, would control conductive cooling length scales. The distance to the nearest vesicle >1 cm in diameter was <6 cm for most of HVR290 (Figure 5-6), which can explain the presence of this large clast (>1 m in diameter) less than 2 km from the source vent. We suggest that advective displacement of steam by liquid water through highly permeable pathways allows large clasts to settle close to the vent (Figure 5-8). Based on this explanation for the presence of large

clasts close to the vent, we would expect the characteristic distance between high permeability pathways in pumices to increase with distance from the vent. Quantitative information about the continuity of the large vesicles in the x-ray computed tomography scan would help further establish whether the macroscale vesicle structure of giant pumice strongly influences dispersal distances.

The macroscale vesicle structure may also influence the breakup of large giant pumice clasts into smaller clasts during transport and deposition, which can explain the presence of small clasts far from the vent. Cracks and vesicles can influence the fragmentation behavior of giant pumice by reducing their cohesive strength (e.g., van Otterloo et al., 2015). Seafloor observations of fragmented clasts (e.g., Figure 5-4B) and textural observations from individual giant pumices (Mitchell et al., 2019) support the interpretation that post-eruption clast breakup influenced the size of deposited clasts (Figure 5-8).

Alternatively, gas trapping in vesicles can increase transport distances, leading to the deposition of small clasts far from the vent (Fauria et al., 2017). In this instance, the timescale (τ) for pumice sinking depends on the diffusion of trapped gas out of the pumice clast, according to the scaling relationship $\tau \propto \frac{R^2}{D\theta^2}$ where D is the gas-water diffusion coefficient, R is the clast radius, and θ is the vesicularity (Fauria et al., 2017). This scaling relationship suggests that relatively small pumices (10^2 cm^3) with a vesicularity ~80% should float for ~100 days, using a diffusion coefficient of 2 x 10^{-5} cm^2/s. Therefore, gas trapping is more likely to have affected the dispersal of clasts deposited much farther than 6 km from the source vent. As a result, we suggest that clast breakup is the most likely explanation for the presence of small (<0.5 m in diameter) clasts up to 6 km from the vent during the 2012 Havre Volcano eruption.

5.6.4 Implications for interpreting silicic submarine eruptions

Our results suggest that giant pumice clasts deposited proximal to submarine vents should consistently contain high permeability pathways. These characteristics may be used to constrain vent locations for ancient eruptions and guide sampling in modern eruptions. The large vesicles may result from the generation of void space during folding, which has been inferred to occur in obsidian flows (Castro et al., 2002; Castro and Cashman, 1999). The bands of large vesicles could also reflect processes that promote vesicle shearing and coalescence within the conduit. Large vesicles, although not nearly at the scale observed in HVR290, have been documented in laboratory experiments of

deforming rhyolitic magmas due to shear and brittle failure (Okumura et al., 2010; Shields et al., 2014). While conduit processes may be responsible for the large vesicles and permeable pathways observed in giant pumice from Havre Volcano, these processes are unlikely to be recorded in subaerial volcanic products because continued water exsolution would likely lead to explosive fragmentation (Manga et al., 2018a). As such, giant pumice from submarine eruptions may provide a unique window into vesiculation and conduit processes (e.g., Mitchell et al., in press).

The increase in seafloor number density of large pumice clasts with distance for at least 6 km supports the interpretation that non-explosive submarine volcanism can produce widespread seafloor deposits (e.g., Carey et al., 2018; Rotella et al., 2013). Although giant pumice comprise the majority of the material erupted during the 2012 eruption of Havre Volcano (Carey et al., 2018), the giant pumice deposit would not have been identifiable without either satellite observations of the raft or high-resolution seafloor bathymetry. Therefore, improved observational methods are necessary in order to fully understand the nature and prevalence of intermediate regime submarine eruptions.

5.7 Conclusions

The distribution of seafloor pumice produced by large submarine eruptions may be controlled by conductive cooling, the advective displacement of steam by water through highly permeable pathways, and clast breakup during transport and deposition. Pumice with large vesicles and highly permeable pathways will water-log quickly and settle to the seafloor near the volcanic edifice (Figure 5-8). Giant pumice without these high permeability pathways will be partitioned into the floating pumice raft and will be dispersed farther from the source (Figure 5-8). Smaller clasts may break off giant pumice during transport and deposition, leading to the presence of small clasts far from the source location. As the dispersal distances are strongly influenced by macroscale vesicle textures, vesicle characteristics in giant pumice may provide insight into source vent locations for ancient submarine eruptions.

5.8 Acknowledgments

We gratefully acknowledge the captain and crew of the R/V Roger Revelle, the ROV *Jason* and AUV *Sentry* teams, and all science and support members during cruise RR1506. We thank F. Ikegami for providing helpful instructions for Blender imagery, M. Jutzeler for providing MODIS imagery, C.

Weare for digitizing giant pumice blocks, and R. Carey, S. Ludwig, M. Manga, and J.T. Perron for helpful discussions. This work was supported by NSF grant OCE1357216 to S.A. Soule and a National Defense Science and Engineering Graduate Fellowship to M. Jones.

5.9 Figures

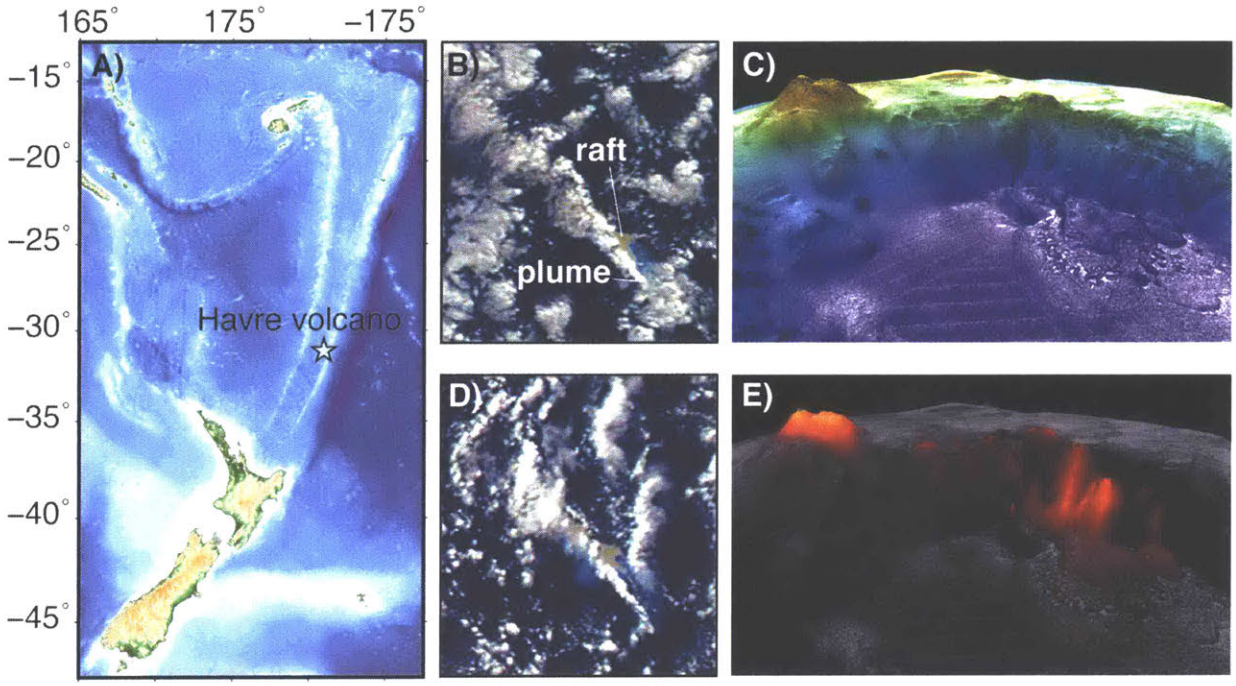

Figure 5-1. (A) Location of Havre Volcano (grey star) in the Kermadec Arc. MODIS imagery showing the pumice raft and steam plume (B) ~21 hours and (D) ~25 hours after the onset of the raft formation. Perspective view looking SW of Havre Volcano (C) colored by bathymetric depth and (E) illuminated by pre- vs. post-eruption bathymetric change.

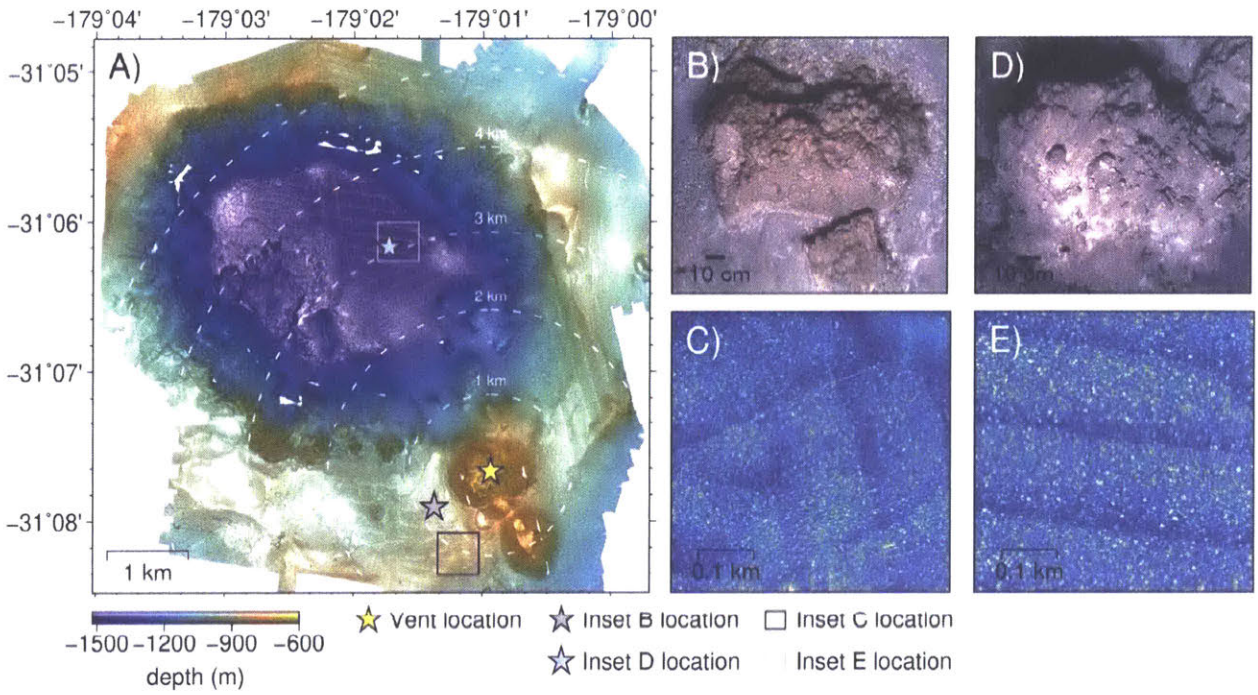

Figure 5-2. (A) 1 m resolution bathymetric map of Havre Volcano from Carey et al. (2018). The yellow star denotes the inferred source vent location for the giant pumice unit. (B) and (D) show seafloor giant pumices located roughly (B) 1km and (D) 3km from the source vent. (C) and (E) show seafloor roughness maps for regions (C) 1 km and (E) 3 km from the source vent. Seafloor observations collected by the *ROV Jason* suggest that individual pumice blocks contribute to the observed seafloor roughness.

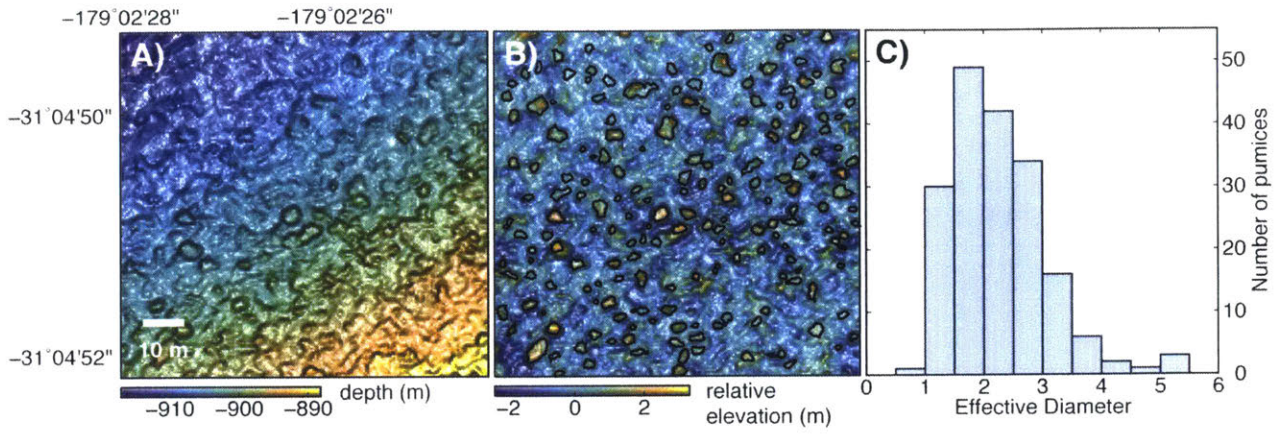

Figure 5-3. Pumice extraction methods. (A) Caldera floor bathymetry gridded at 0.5 m. (B) Detrended and high-pass filtered bathymetry with identified pumice blocks outlined in black. (C) Histogram of extracted pumice sizes. The pumices were quantified using the detrended and filtered bathymetry and the closed-contour basal outlining routine from Bohnenstiehl et al. (2012).

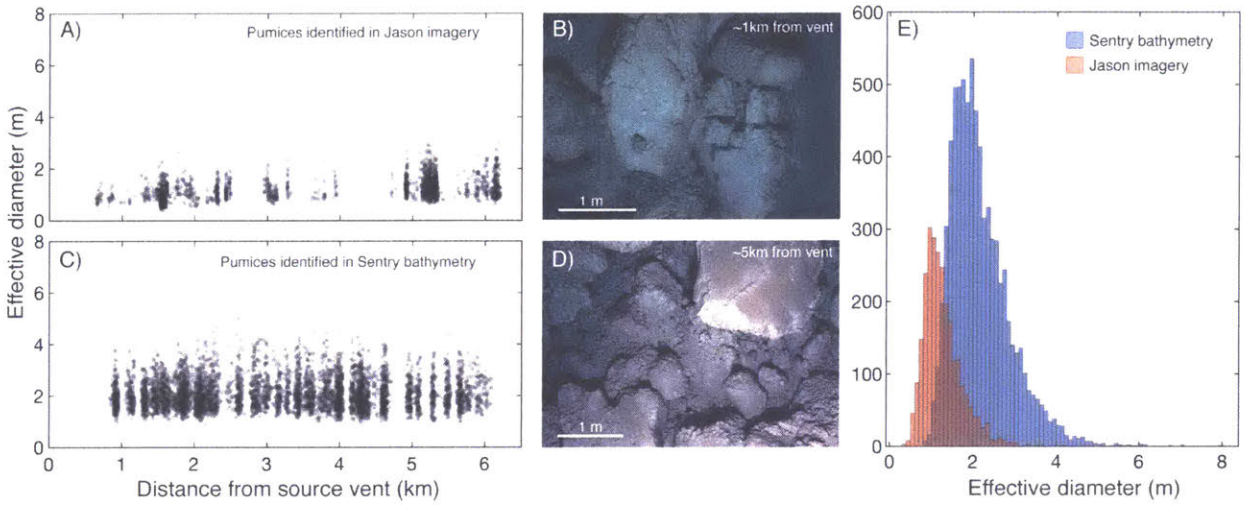

Figure 5-4. The effective diameter of identified pumice clasts plotted as a function of radial distance from the source vent for (A) *Jason* imagery and (C) *Sentry* bathymetry. There is a weak relationship between transport distance and the size of identified pumice blocks. Seafloor images show a broad range of clast sizes at both (B) 1 km and (D) 5 km from the vent. (E) Histograms comparing the pumice size distributions derived from *Jason* imagery and *Sentry* bathymetry. The differences between these size distributions likely reflects biases in the methods, with the imagery analysis preferentially missing the largest pumice blocks (>2 – 3 m diameter) and the bathymetry analysis failing to capture pumice blocks <1.5 m diameter. Neither method captures the distribution of pumice blocks <1 m diameter.

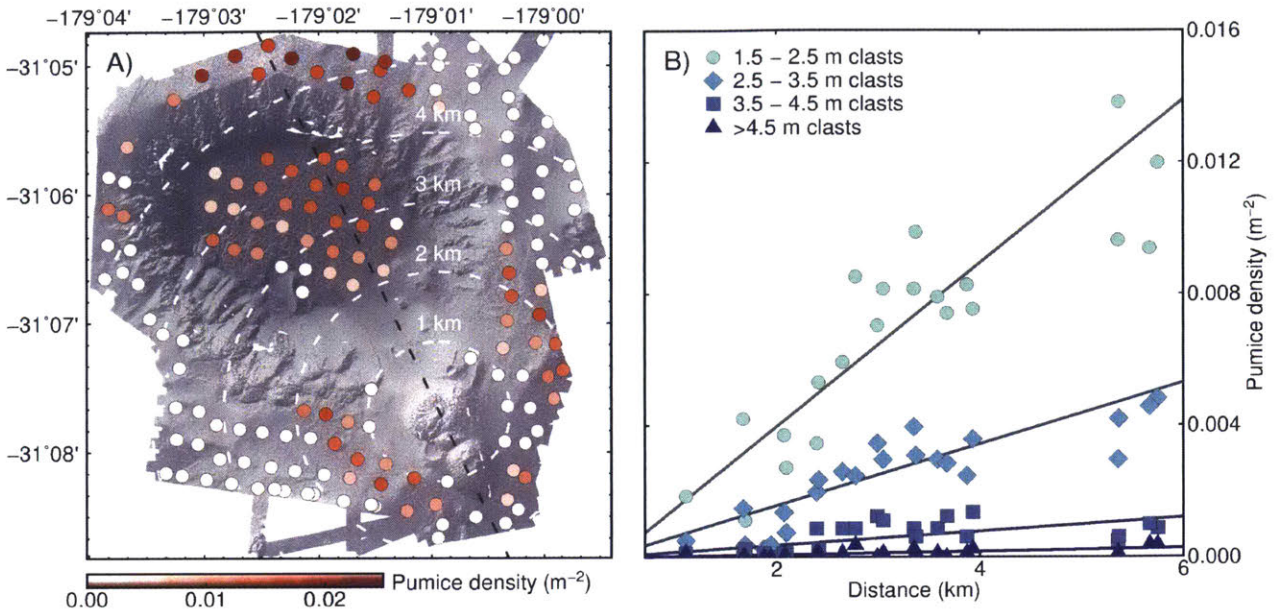

Figure 5-5. (A) Number density of identified pumice in each analyzed bathymetric region (N = 162). (B) Seafloor number density of pumices within four binned size classes as a function of transport distance, for sub-regions <500 m from the dispersal axis (black dashed line in Panel A). Although the distance from the source vent cannot predict the size of extracted clasts (e.g., Figure 5-4), distance from the vent strongly influences the abundance of large pumice clasts.

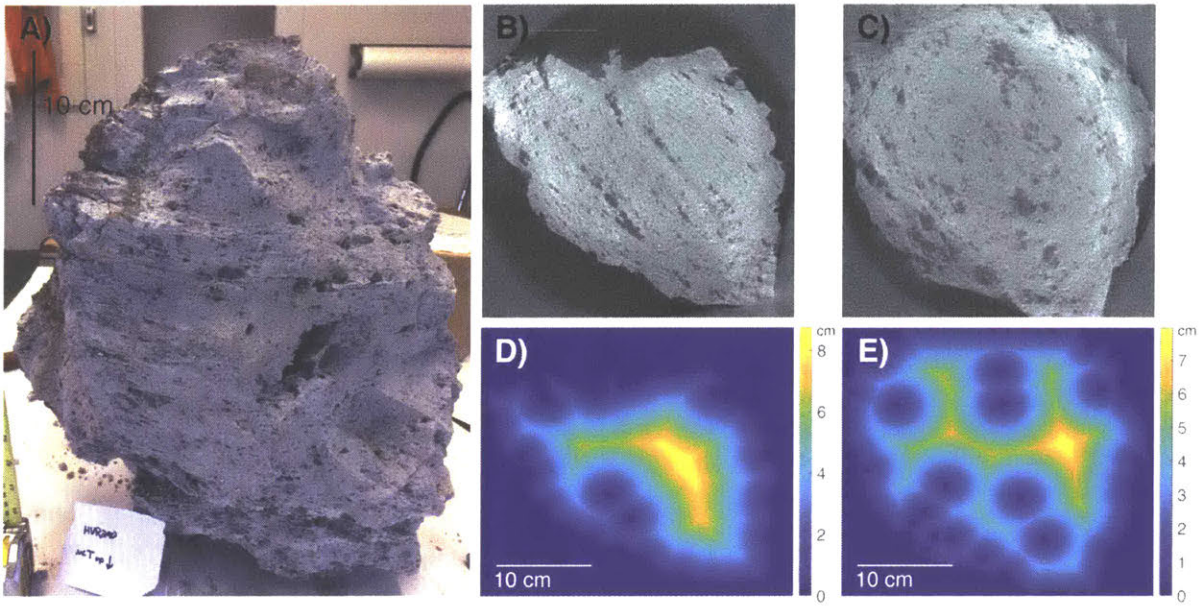

Figure 5-6. (A) Pumice clast (HVR290) imaged using x-ray computed tomography. Individual slices from the scan (B – C) show abundant vesicles >1 cm in diameter. D) and E) show the distance from each pixel in the slice to either the nearest vesicle >1 cm in diameter or the outer surface of the clast. The large vesicles may serve as highly permeable pathways that allow water to displace steam and reduce the length scale for conductive cooling.

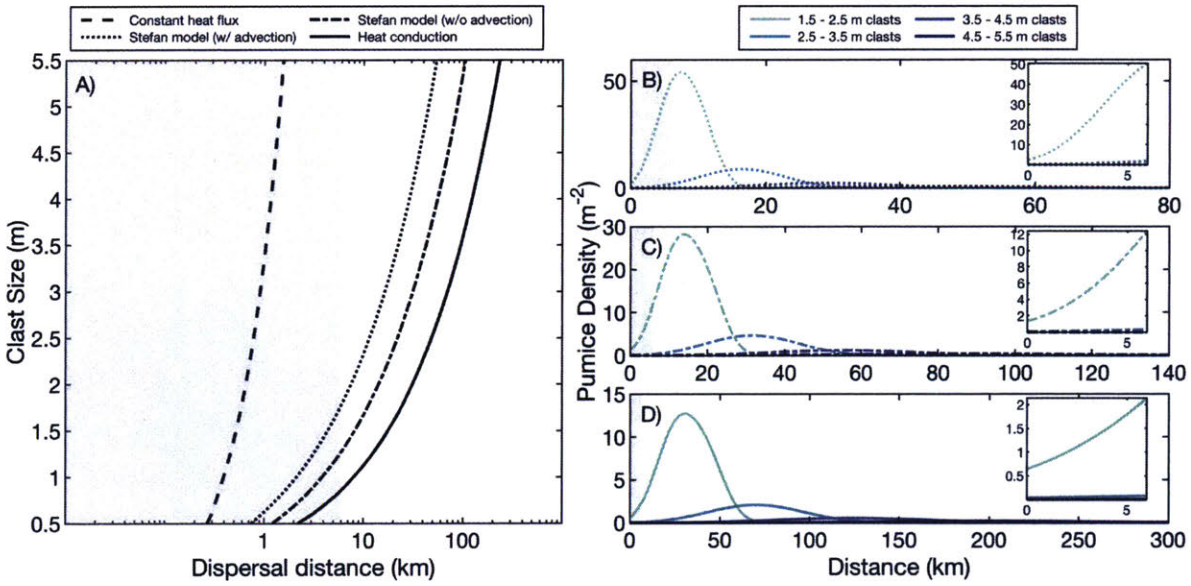

Figure 5-7. (A) Predicted clast size as a function of dispersal distance based on empirical and theoretical models for pumice cooling and saturation (Fauria and Manga, 2018; Manga et al., 2018; Recktenwald, 2006). (B, C, D) Predicted seafloor number density of pumices for four discrete size classes (1.5 – 2.5 m; 2.5 – 3.5 m; 3.5 – 4.5 m; 4.5 – 5.5 m) as a function of distance from the source vent based on a B) Stefan model with advection, C) Stefan model without advection, and D) heat conduction model, along with assumptions about the error distributions around predicted transport distances, the width of the depositional zone, the current velocity, and the total volume of pumice within each size class. The grey bar in each panel shows the limit of seafloor observations at Havre Volcano.

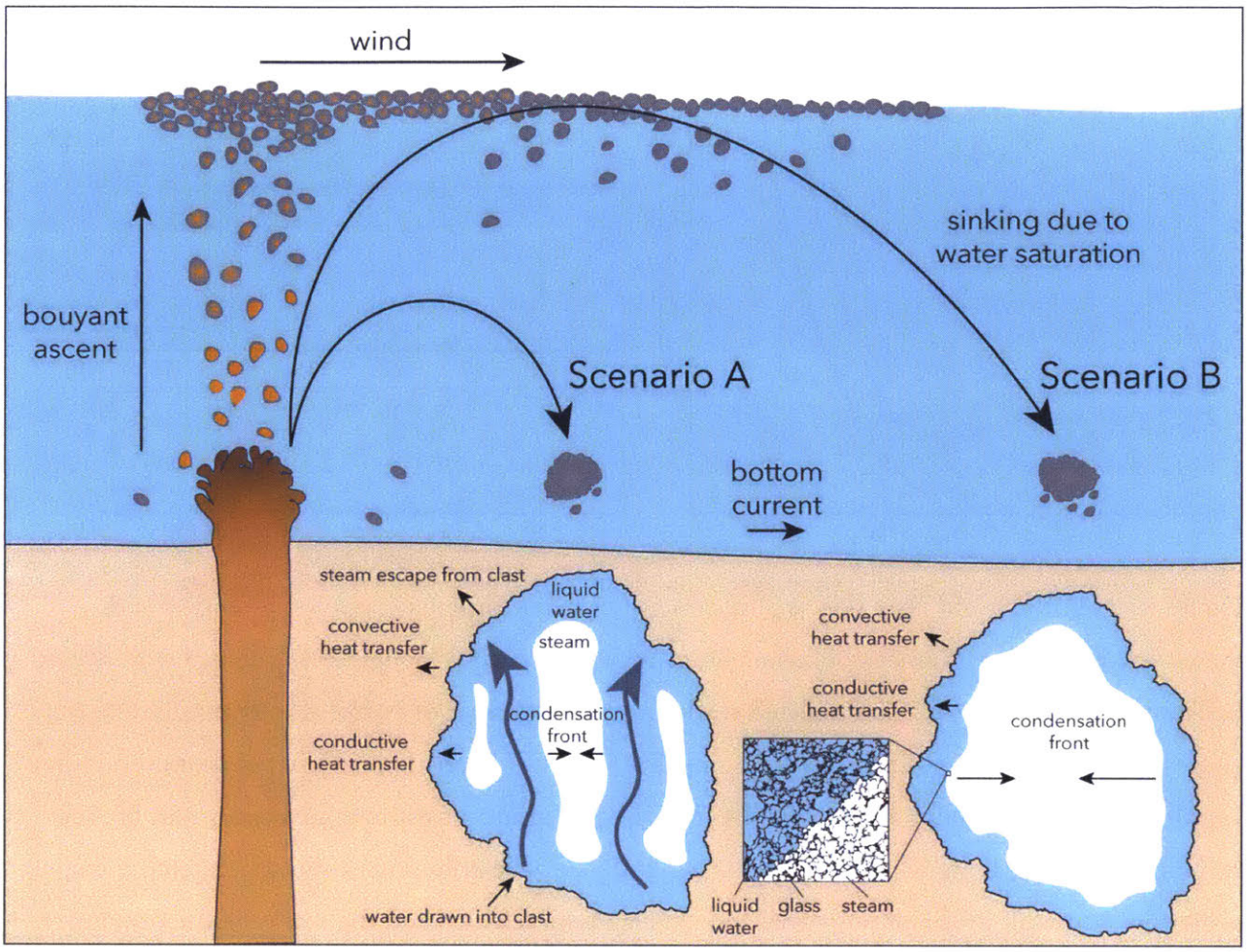

Figure 5-8. Schematic representation showing that pumices with high permeability (i.e., 10^{-7} – 10^{-9} m^2) pathways (scenario A) will saturate with water faster and sink to the seafloor closer to the vent than pumices with a homogeneous, low permeability internal structure (scenario B). The macroscale vesicle structure may also influence clast breakup, which can produce small clasts far from the source vent.

Chapter 6

Conclusions and future directions

This thesis provides new insight into volcanic processes using observations and samples from the 2011 Axial Seamount eruption, the 2012 Havre Volcano eruption, and the Mid-Atlantic Ridge near 14°N. In Chapter 2, I provided recommendations for accurately quantifying vesicle characteristics and total CO_2 concentrations in mid-ocean ridge basalts (MORB). I showed that 2D analyses combined with stereological techniques can accurately reproduce vesicularities and vesicle size distributions in MORB. I suggested that CO_2 densities in MORB bubbles are lower than expected based on traditional methods due to melt contraction during quenching. Future research could experimentally evaluate melt contraction in MORB by measuring the volume change in vesicles during relatively rapid heating and/or cooling. The high-resolution x-ray microtomography scans evaluated in Chapter 2 could also provide future insight into heterogeneous nucleation or the effects of bubbles on flow rheology, using the subset of vesicles that are clustered and/or sheared.

In Chapter 3, I documented the variability in magma ascent and lava flow emplacement rates during the 2011 eruption of Axial Seamount. I showed that some samples ascended slow enough for near-equilibrium degassing while others ascended fast enough for minimal vesiculation and gas exsolution. Based on a model for diffusion-controlled bubble growth, I suggested that the ascent rates during the 2011 eruption spanned the range previously proposed for the global mid-ocean ridge system. I explained that the results of the bubble growth model were highly dependent on the vesicle number density in these samples (Gardner et al. 2016). Most bubble growth and conduit models assume uniform vesicle sizes, despite observations that vesicle size distributions are often log-linear (e.g., Chapters 2 – 4). These models also commonly assume that the bubble number density does not change throughout the eruption. Improved conceptual or experimental constraints on bubble nucleation and the influence of vesicles of different sizes on gas exsolution would therefore improve our ability to interpret observations using numerical models.

I suggested in Chapter 3 that variable magma ascent rates during the 2011 Axial eruption may relate to evolving overpressures within the magmatic reservoir. Previous studies have suggested that the

eruption recurrence interval at Axial Seamount is controlled by a critical level of magmatic pressure (e.g., Nooner and Chadwick, 2016). Therefore, it would be insightful to compare the results from Chapter 3 with a similar study on precisely located samples from the 2015 Axial Seamount eruption.

In Chapter 4, I showed that the high volatile concentrations in popping rocks from the Mid-Atlantic Ridge reflect bubble accumulation. I suggested that bubbles may have accumulated during storage at high pressures due to the sealing of cracks that would typically allow gas loss. Future studies could evaluate whether the concentration of volatiles varies systematically with location or morphology, which would provide insight into whether emplacement processes influence exsolved volatile concentrations. Additionally, future studies could investigate whether popping rocks found elsewhere on the mid-ocean ridge system are associated with core complexes or non-transform discontinuities, which would inform whether the tectonic environment influences bubble accumulation. It would also be insightful to use a multi-component bubble growth model to evaluate whether disequilibrium degassing influenced the noble gas abundance ratios of popping rocks from the Mid-Atlantic Ridge. Finally, research conducted synchronously with Chapter 4 (Parnell-Turner et al., 2018) suggests that the volatile concentrations in mid-ocean ridge basalts may provide a valuable tool for evaluating vertical motions caused by fault slip and/or seafloor subsidence, which offers a promising avenue for future research.

In Chapter 5, I showed that the seafloor distribution of giant pumice produced by silicic submarine eruptions is likely controlled by conductive cooling, the advective displacement of steam by water through highly permeable pathways, and clast breakup during transport and deposition. I suggested that heat flux increases with clast size, which could be tested using experiments on large clasts (e.g., Fauria and Manga, 2018). I also suggested that giant pumice <6 km from the vent at Havre Volcano comprise a small portion of the total seafloor deposit, which could be further tested using seafloor observations farther from the source vent. In addition, seafloor photo surveys would provide an immensely valuable validation dataset for the methods used in Chapter 5 to identify giant pumice clasts in the high-resolution bathymetry. Finally, this research likely would not have been possible without pre-eruption bathymetry, which highlights the benefits of pro-actively mapping the seafloor.

Together, the chapters in this thesis provide new insight into the behavior of volatiles during magmatic processes, the concentration of CO_2 in the Earth's mantle, and the processes influencing the emplacement of volcanic products on the seafloor.

References

Allen, S.R., Fiske, R.S., Cashman, K.V., 2008. Quenching of steam-charged pumice: Implications for submarine pyroclastic volcanism. Earth Planet. Sci. Lett. 274, 40–49. https://doi.org/10.1016/j.epsl.2008.06.050

Allen, S.R., McPhie, J., 2009. Products of neptunian eruptions. Geology 37, 639–642. https://doi.org/10.1130/G30007A.1

Arefmanesh, A., Advani, S., 1991. Diffusion-Induced Growth of a Gas Bubble in a Viscoelastic Fluid. Rheol. Acta 30, 274–283. https://doi.org/10.1007/BF00366641

Arnulf, A.F., Harding, A.J., Kent, G.M., Carbotte, S.M., Canales, J.P., Nedimovic, M.R., 2014. Anatomy of an active submarine volcano. Geology 42, 655–658. https://doi.org/10.1130/G35629.1

Aster, E.M., Wallace, P.J., Moore, L.R., Watkins, J., Gazel, E., Bodnar, R.J., 2016. Reconstructing CO2 concentrations in basaltic melt inclusions using Raman analysis of vapor bubbles. J. Volcanol. Geotherm. Res. 323, 148–162. https://doi.org/10.1016/j.jvolgeores.2016.04.028

Aubaud, C., Pineau, F., Jambon, A., Javoy, M., 2004. Kinetic disequilibrium of C, He, Ar and carbon isotopes during degassing of mid-ocean ridge basalts. Earth Planet. Sci. Lett. 222, 391–406. https://doi.org/10.1016/j.epsl.2004.03.001

Aubry, G.J., Sator, N., Guillot, B., 2013. Vesicularity, bubble formation and noble gas fractionation during MORB degassing. Chem. Geol. 343, 85–98. https://doi.org/10.1016/j.chemgeo.2013.02.006

Bai, L., Baker, D.R., Polacci, M., Hill, R.J., 2011. In-situ degassing study on crystal-bearing Stromboli basaltic magmas: Implications for Stromboli explosions. Geophys. Res. Lett. 38, n/a-n/a. https://doi.org/10.1029/2011GL048540

Baker, D.R., Mancini, L., Polacci, M., Higgins, M.D., Gualda, G.A.R., Hill, R.J., Rivers, M.L., 2012. An introduction to the application of X-ray microtomography to the three-dimensional study of igneous rocks. Lithos 148, 262–276. https://doi.org/10.1016/j.lithos.2012.06.008

Baker, D.R., Polacci, M., LaRue, A., 2011. A study on the reproducibility of counting vesicles in volcanic rocks. Geosphere 7, 70–78. https://doi.org/10.1130/GES00553.1

Barker, S.J., Rotella, M.D., Wilson, C.J.N., Wright, I.C., Wysoczanski, R.J., 2012. Contrasting pyroclast density spectra from subaerial and submarine silicic eruptions in the Kermadec arc: implications for eruption processes and dredge sampling. Bull. Volcanol. 74, 1425–1443. https://doi.org/10.1007/s00445-012-0604-2

Barnes, S.J., Osborne, G.A., Cook, D., Barnes, L., Maier, W.D., Godel, B., 2011. The Santa Rita Nickel Sulfide Deposit in the Fazenda Mirabela Intrusion, Bahia, Brazil: Geology, Sulfide Geochemistry, and Genesis. Econ. Geol. 106, 1083–1110. https://doi.org/10.2113/econgeo.106.7.1083

Batchelor, G.K., Young, A.D., 1968. An Introduction to Fluid Mechanics. J. Appl. Mech. 35, 624. https://doi.org/10.1115/1.3601282

Batiza, R., Vanko, D.A., 1985. Petrologic Evolution of Large Failed Rifts in the Eastern Pacific: Petrology of Volcanic and Plutonic Rocks from the Mathematician Ridge Area and the Guadalupe Trough. J. Petrol. 26, 564–602. https://doi.org/10.1093/petrology/26.3.564

Bohnenstiehl, D.R., Howell, J.K., White, S.M., Hey, R.N., 2012. A modified basal outlining algorithm for identifying topographic highs from gridded elevation data, Part 1: Motivation and methods. Comput. Geosci. 49, 308–314. https://doi.org/10.1016/j.cageo.2012.04.023

Bougault, H., Dmitriev, L., Schilling, J.G., Sobolev, A., Joron, J.L., Needham, H.D., 1988. Mantle heterogeneity from trace elements: MAR triple junction near 14°N. Earth Planet. Sci. Lett. 88, 27–36. https://doi.org/10.1016/0012-821X(88)90043-X

Bryan, S.E., Cook, A., Evans, J.P., Colls, P.W., Wells, M.G., Lawrence, M.G., Jell, J.S., Greig, A., Leslie, R., 2004. Pumice rafting and faunal dispersion during 2001–2002 in the Southwest Pacific: record of a dacitic submarine explosive eruption from Tonga. Earth Planet. Sci. Lett. 227, 135–154. https://doi.org/10.1016/j.epsl.2004.08.009

Bryan, S.E., Cook, A.G., Evans, J.P., Hebden, K., Hurrey, L., Colls, P., Jell, J.S., Weatherley, D., Firn, J., 2012. Rapid, Long-Distance Dispersal by Pumice Rafting. PLOS ONE 7, e40583. https://doi.org/10.1371/journal.pone.0040583

Brown, M.A., Brown, M., Carlson, W.D., Denison, C., 1999. Topology of syntectonic melt-flow networks in the deep crust; inferences from three-dimensional images of leucosome geometry in migmatites. Am. Mineral. 84, 1793–1818. https://doi.org/10.2138/am-1999-11-1208

Burnard, P., 1999. Eruption dynamics of "'popping rock"' from vesicle morphologies. J. Volcanol. Geotherm. Res. 92, 247–258. https://doi.org/10.1016/S0377-0273(99)00057-8

Burnard, P., 1997. Vesicle-Specific Noble Gas Analyses of "Popping Rock": Implications for Primordial Noble Gases in Earth. Science 276, 568–571. https://doi.org/10.1126/science.276.5312.568

Burnard, P., Graham, D., Farley, K., 2004. Fractionation of noble gases (He, Ar) during MORB mantle melting: a case study on the Southeast Indian Ridge. Earth Planet. Sci. Lett. 227, 457–472. https://doi.org/10.1016/j.epsl.2004.08.021

Burnard, P., Reisberg, L., Colin, A., 2014. An observed link between lithophile compositions and degassing of volatiles (He, Ar, CO2) in MORBs with implications for Re volatility and the mantle C/Nb ratio. Earth Planet. Sci. Lett. 395, 159–167. https://doi.org/10.1016/j.epsl.2014.03.045

Caress, D.W., Clague, D.A., Paduan, J.B., Martin, J.F., Dreyer, B.M., Chadwick, W.W., Denny, A., Kelley, D.S., 2012. Repeat bathymetric surveys at 1-metre resolution of lava flows erupted at Axial Seamount in April 2011. Nat. Geosci. 5, 483–488. https://doi.org/10.1038/ngeo1496

Carey, R., Soule, S.A., Manga, M., White, J.D.L., McPhie, J., Wysoczanski, R., Jutzeler, M., Tani, K., Yoerger, D., Fornari, D., Caratori-Tontini, F., Houghton, B., Mitchell, S., Ikegami, F., Conway, C., Murch, A., Fauria, K., Jones, M., Cahalan, R., McKenzie, W., 2018. The largest deep-ocean silicic volcanic eruption of the past century. Sci. Adv. 4, e1701121. https://doi.org/10.1126/sciadv.1701121

Carey, R.J., Wysoczanski, R., Wunderman, R., Jutzeler, M., 2014. Discovery of the Largest Historic Silicic Submarine Eruption. Eos Trans. Am. Geophys. Union 95, 157–159. https://doi.org/10.1002/2014EO190001

Carlson, W.D., Denison, C., 1992. Mechanisms of porphyroblast crystallization: Results from high-resolution computed X-ray tomography. Science 257, 1236–1239. https://doi.org/10.1126/science.257.5074.1236

Carslaw, H.S., Jaeger, J.C., 1986. Conduction of Heat in Solids. Clarendon Press.

Cartigny, P., Pineau, F., Aubaud, C., Javoy, M., 2008. Towards a consistent mantle carbon flux estimate: Insights from volatile systematics (H2O/Ce, δD, CO2/Nb) in the North Atlantic mantle (14°N and 34°N). Earth Planet. Sci. Lett. 265, 672–685. https://doi.org/10.1016/j.epsl.2007.11.011

Cashman, K.V., Mangan, M.T., 1994. Physical aspects of magmatic degassing II. Rev. Mineral. Geochem. 30, 447–478.

Cashman, K.V., Mangan, M.T., Newman, S., 1994. Surface degassing and modifications to vesicle size distributions in active basalt flows. J. Volcanol. Geotherm. Res. 61, 45–68. https://doi.org/10.1016/0377-0273(94)00015-8

Cashman, K.V., Marsh, B.D., 1988. Crystal size distribution (CSD) in rocks and the kinetics and dynamics of crystallization II: Makaopuhi lava lake. Contrib. Mineral. Petrol. 99, 292–305. https://doi.org/10.1007/BF00375363

Castro, J., Cashman, K., Joslin, N., Olmsted, B., 2002. Structural origin of large gas cavities in the Big Obsidian Flow, Newberry Volcano. J. Volcanol. Geotherm. Res. 114, 313–330. https://doi.org/10.1016/S0377-0273(01)00296-7

Castro, J., Cashman, K.V., 1999. Constraints on rheology of obsidian lavas based on mesoscopic folds. J. Struct. Geol. 21, 807–819. https://doi.org/10.1016/S0191-8141(99)00070-X

Chadwick, W.W., Clague, D.A., Embley, R.W., Perfit, M.R., Butterfield, D.A., Caress, D.W., Paduan, J.B., Martin, J.F., Sasnett, P., Merle, S.G., Bobbitt, A.M., 2013. The 1998 eruption of Axial Seamount: New insights on submarine lava flow emplacement from high-resolution mapping. Geochem. Geophys. Geosystems 14, 3939–3968. https://doi.org/10.1002/ggge.20202

Chadwick, W.W., Embley, R.W., Fox, C.G., 1991. Evidence for volcanic eruption on the southern Juan de Fuca ridge between 1981 and 1987. Nature 350, 416–418. https://doi.org/10.1038/350416a0

Chadwick, W.W., Nooner, S.L., Butterfield, D.A., Lilley, M.D., 2012. Seafloor deformation and forecasts of the April 2011 eruption at Axial Seamount. Nat. Geosci. 5, 474–477. https://doi.org/10.1038/ngeo1464

Chadwick, W.W., Paduan, J.B., Clague, D.A., Dreyer, B.M., Merle, S.G., Bobbitt, A.M., Caress, D.W., Philip, B.T., Kelley, D.S., Nooner, S.L., 2016. Voluminous eruption from a zoned magma body after an increase in supply rate at Axial Seamount. Geophys. Res. Lett. 43, 12063–12070. https://doi.org/10.1002/2016GL071327

Chadwick, W.W., Cashman, K.V., Embley, R.W., Matsumoto, H., Dziak, R.P., Ronde, C.E.J. de, Lau, T.K., Deardorff, N.D., Merle, S.G., 2008. Direct video and hydrophone observations of submarine explosive eruptions at NW Rota-1 volcano, Mariana arc. J. Geophys. Res. Solid Earth 113. https://doi.org/10.1029/2007JB005215

Chavrit, D., Humler, E., Morizet, Y., Laporte, D., 2012. Influence of magma ascent rate on carbon dioxide degassing at oceanic ridges: Message in a bubble. Earth Planet. Sci. Lett. 357–358, 376–385. https://doi.org/10.1016/j.epsl.2012.09.042

Chavrit, D., Humler, E., Grasset, O., 2014. Mapping modern CO2 fluxes and mantle carbon content all along the mid-ocean ridge system. Earth Planet. Sci. Lett. 387, 229–239. https://doi.org/10.1016/j.epsl.2013.11.036

Cheng, H.C., Lemlich, R., 1983. Errors in the measurement of bubble size distribution in foam. Ind. Eng. Chem. Fundam. 22, 105–109. https://doi.org/10.1021/i100009a018

Chouet, B., Dawson, P., Nakano, M., 2006. Dynamics of diffusive bubble growth and pressure recovery in a bubbly rhyolitic melt embedded in an elastic solid. J. Geophys. Res. Solid Earth 111, B07310. https://doi.org/10.1029/2005JB004174

Clague, D., Paduan, J., Caress, D., Chadwick, W., Le Saout, M., Dreyer, B., Portner, R., 2017. High-Resolution AUV Mapping and Targeted ROV Observations of Three Historical Lava Flows at Axial Seamount. Oceanography 30. https://doi.org/10.5670/oceanog.2017.426

Clague, D.A., Dreyer, B.M., Paduan, J.B., Martin, J.F., Chadwick, W.W., Caress, D.W., Portner, R.A., Guilderson, T.P., McGann, M.L., Thomas, H., Butterfield, D.A., Embley, R.W., 2013. Geologic history of the summit of Axial Seamount, Juan de Fuca Ridge. Geochem. Geophys. Geosystems 14, 4403–4443. https://doi.org/10.1002/ggge.20240

Cnudde, V., Boone, M.N., 2013. High-resolution X-ray computed tomography in geosciences: A review of the current technology and applications. Earth-Sci. Rev. 123, 1–17. https://doi.org/10.1016/j.earscirev.2013.04.003

Crisp, J.A., 1984. Rates of magma emplacement and volcanic output. J. Volcanol. Geotherm. Res. 20, 177–211. https://doi.org/10.1016/0377-0273(84)90039-8

Dasgupta, R., Hirschmann, M.M., 2010. The deep carbon cycle and melting in Earth's interior. Earth Planet. Sci. Lett. 298, 1–13. https://doi.org/10.1016/j.epsl.2010.06.039

Dasgupta, R., Mallik, A., Tsuno, K., Withers, A.C., Hirth, G., Hirschmann, M.M., 2013. Carbon-dioxide-rich silicate melt in the Earth's upper mantle. Nature 493, 211–215. https://doi.org/10.1038/nature11731

de Vries, A.J., 1972. Chapter 2: Morphology, Coalescence, and Size Distribution of Foam Bubbles. Adsorpt. Bubble Sep. Tech. 7–31. https://doi.org/10.1016/B978-0-12-443350-2.50007-1

Dehoff, R.T., Rhines, F.N., 1968. Method of estimating size of discrete objects, in: DeHoff, R.T., Rhines, Frederick N. (Eds.), Quantitative Microscopy. New York: Mcgraw-Hill, pp. 75–102.

Dixon, J.E., Stolper, E., Delaney, J.R., 1988. Infrared spectroscopic measurements of CO2 and H2O in Juan de Fuca Ridge basaltic glasses. Earth Planet. Sci. Lett. 90, 87–104. https://doi.org/10.1016/0012-821X(88)90114-8

Dixon, J.E., Stolper, E.M., 1995. An Experimental Study of Water and Carbon Dioxide Solubilities in Mid-Ocean Ridge Basaltic Liquids. Part II: Applications to Degassing. J. Petrol. 36, 1633–1646. https://doi.org/10.1093/oxfordjournals.petrology.a037268

Dixon, J.E., Stolper, E.M., Holloway, J.R., 1995. An Experimental Study of Water and Carbon Dioxide Solubilities in Mid-Ocean Ridge Basaltic Liquids. Part I: Calibration and Solubility Models. J. Petrol. 36, 1607–1631. https://doi.org/10.1093/oxfordjournals.petrology.a037267

Dreyer, B.M., Clague, D.A., Gill, J.B., 2013. Petrological variability of recent magmatism at Axial Seamount summit, Juan de Fuca Ridge. Geochem. Geophys. Geosystems 14, 4306–4333. https://doi.org/10.1002/ggge.20239

Dziak, R.P., Bohnenstiehl, D.R., Cowen, J.P., Baker, E.T., Rubin, K.H., Haxel, J.H., Fowler, M.J., 2007. Rapid dike emplacement leads to eruptions and hydrothermal plume release during seafloor spreading events. Geology 35, 579–582. https://doi.org/10.1130/G23476A.1

Dziak, R.P., Bohnenstiehl, D.R., Matsumoto, H., Fowler, M.J., Haxel, J.H., Tolstoy, M., Waldhauser, F., 2009. January 2006 seafloor-spreading event at 9°50'N, East Pacific Rise: Ridge dike intrusion and transform fault interactions from regional hydroacoustic data. Geochem. Geophys. Geosystems 10, Q06T06. https://doi.org/10.1029/2009GC002388

Dziak, R.P., Haxel, J.H., Bohnenstiehl, D.R., Chadwick, W.W., Nooner, S.L., Fowler, M.J., Matsumoto, H., Butterfield, D.A., 2012. Seismic precursors and magma ascent before the April 2011 eruption at Axial Seamount. Nat. Geosci. 5, 478–482. https://doi.org/10.1038/ngeo1490

Escartín, J., Canales, J.P., 2011. Detachments in Oceanic Lithosphere: Deformation, Magmatism, Fluid Flow, and Ecosystems. Eos Trans. Am. Geophys. Union 92, 31–31. https://doi.org/10.1029/2011EO040003

Esposito, R., Bodnar, R.J., Danyushevsky, L.V., De Vivo, B., Fedele, L., Hunter, J., Lima, A., Shimizu, N., 2011. Volatile Evolution of Magma Associated with the Solchiaro Eruption in the Phlegrean Volcanic District (Italy). J. Petrol. 52, 2431–2460. https://doi.org/10.1093/petrology/egr051

Fauria, K.E., Manga, M., 2018. Pyroclast cooling and saturation in water. J. Volcanol. Geotherm. Res. 362, 17–31. https://doi.org/10.1016/j.jvolgeores.2018.07.002

Fauria, K.E., Manga, M., Wei, Z., 2017. Trapped bubbles keep pumice afloat and gas diffusion makes pumice sink. Earth Planet. Sci. Lett. 460, 50–59. https://doi.org/10.1016/j.epsl.2016.11.055

Fiske, R.S., Naka, J., Iizasa, K., Yuasa, M., Klaus, A., 2001. Submarine silicic caldera at the front of the Izu-Bonin arc, Japan: Voluminous seafloor eruptions of rhyolite pumice. Geol. Soc. Am. Bull. 113, 813–824. https://doi.org/10.1130/0016-7606(2001)113<0813:SSCATF>2.0.CO;2

Fine, G., Stolper, E., 1986. Dissolved carbon dioxide in basaltic glasses: concentrations and speciation. Earth Planet. Sci. Lett. 76, 263–278. https://doi.org/10.1016/0012-821X(86)90078-6

Flowers, G.C., 1979. Correction of Holloway's (1977) adaptation of the modified Redlich-Kwong equation of state for calculation of the fugacities of molecular species in supercritical fluids of geologic interest. Contrib. Mineral. Petrol. 69, 315–318. https://doi.org/10.1007/BF00372333

Fox, C.G., Chadwick, W.W., Embley, R.W., 2001. Direct observation of a submarine volcanic eruption from a sea-floor instrument caught in a lava flow. Nature 412, 727–729. https://doi.org/10.1038/35089066

Frezzotti, M.L., Tecce, F., Casagli, A., 2012. Raman spectroscopy for fluid inclusion analysis. J. Geochem. Explor. 112, 1–20. https://doi.org/10.1016/j.gexplo.2011.09.009

Fundis, A.T., Soule, S.A., Fornari, D.J., Perfit, M.R., 2010. Paving the seafloor: Volcanic emplacement processes during the 2005-2006 eruptions at the fast spreading East Pacific Rise, 9°50'N. Geochem. Geophys. Geosystems 11, Q08024. https://doi.org/10.1029/2010GC003058

Gardner, J.E., Jackson, B.A., Gonnermann, H., Soule, S.A., 2016. Rapid ascent and emplacement of basaltic lava during the 2005–06 eruption of the East Pacific Rise at ca. 9°51'N as inferred from CO2 contents. Earth Planet. Sci. Lett. 453, 152–160. https://doi.org/10.1016/j.epsl.2016.08.007

Gerlach, T.M., 1991. Comment on "Mid-ocean ridge popping rocks: implications for degassing at ridge crests" by P. Sarda and D. Graham. Earth Planet. Sci. Lett. 105, 566–567. https://doi.org/10.1016/0012-821X(91)90193-L

Giachetti, T., Burgisser, A., Arbaret, L., Druitt, T.H., Kelfoun, K., 2011. Quantitative textural analysis of Vulcanian pyroclasts (Montserrat) using multi-scale X-ray computed microtomography: comparison with results from 2D image analysis. Bull. Volcanol. 73, 1295–1309. https://doi.org/10.1007/s00445-011-0472-1

Giachetti, T., Druitt, T.H., Burgisser, A., Arbaret, L., Galven, C., 2010. Bubble nucleation, growth and coalescence during the 1997 Vulcanian explosions of Soufrière Hills Volcano, Montserrat. J. Volcanol. Geotherm. Res. 193, 215–231. https://doi.org/10.1016/j.jvolgeores.2010.04.001

Godel, B., Barnes, S.J., Barnes, S.-J., Maier, W.D., 2010. Platinum ore in three dimensions: Insights from high-resolution X-ray computed tomography. Geology 38, 1127–1130. https://doi.org/10.1130/G31265.1

Gonnermann, H.M., Manga, M., 2005. Nonequilibrium magma degassing: Results from modeling of the ca. 1340 A.D. eruption of Mono Craters, California. Earth Planet. Sci. Lett. 238, 1–16. https://doi.org/10.1016/j.epsl.2005.07.021

Gonnermann, H.M., Mukhopadhyay, S., 2007. Non-equilibrium degassing and a primordial source for helium in ocean-island volcanism. Nature 449, 1037–1040. https://doi.org/10.1038/nature06240

Gottsmann, J., Giordano, D., Dingwell, D.B., 2002. Predicting shear viscosity during volcanic processes at the glass transition: a calorimetric calibration. Earth Planet. Sci. Lett. 198, 417–427. https://doi.org/10.1016/S0012-821X(02)00522-8

Graham, D.W., 2002. Noble Gas Isotope Geochemistry of Mid-Ocean Ridge and Ocean Island Basalts: Characterization of Mantle Source Reservoirs. Rev. Mineral. Geochem. 47, 247–317. https://doi.org/10.2138/rmg.2002.47.8

Graham, D.W., Michael, P.J., Rubin, K.H., 2018. An investigation of mid-ocean ridge degassing using He, CO2, and δ13C variations during the 2005–06 eruption at 9°50'N on the East Pacific Rise. Earth Planet. Sci. Lett. 504, 84–93. https://doi.org/10.1016/j.epsl.2018.09.040

Gregg, T.K.P., Fink, J.H., 1995. Quantification of submarine lava-flow morphology through analog experiments. Geology 23, 73–76. https://doi.org/10.1130/0091-7613(1995)023<0073:QOSLFM>2.3.CO;2

Gurioli, L., Harris, A.J.L., Houghton, B.F., Polacci, M., Ripepe, M., 2008. Textural and geophysical characterization of explosive basaltic activity at Villarrica volcano. J. Geophys. Res. Solid Earth 113, B08206. https://doi.org/10.1029/2007JB005328

Harris, A.J.L., Murray, J.B., Aries, S.E., Davies, M.A., Flynn, L.P., Wooster, M.J., Wright, R., Rothery, D.A., 2000. Effusion rate trends at Etna and Krafla and their implications for eruptive mechanisms. J. Volcanol. Geotherm. Res. 102, 237–269. https://doi.org/10.1016/S0377-0273(00)00190-6

Hauri, E., Wang, J., Dixon, J.E., King, P.L., Mandeville, C., Newman, S., 2002. SIMS analysis of volatiles in silicate glasses: 1. Calibration, matrix effects and comparisons with FTIR. Chem. Geol., Melt Inclusions at the Millennium: Toward a Deeper Understanding of Magmatic Processes 183, 99–114. https://doi.org/10.1016/S0009-2541(01)00375-8

Hekinian, R., Chaigneau, M., Cheminee, J.L., 1973. Popping Rocks and Lava Tubes from the Mid-Atlantic Rift Valley at 36° N. Nature 245, 371–373. https://doi.org/10.1038/245371a0

Hekinian, R., Pineau, F., Shilobreeva, S., Bideau, D., Gracia, E., Javoy, M., 2000. Deep sea explosive activity on the Mid-Atlantic Ridge near 34°50'N: Magma composition, vesicularity and volatile content. J. Volcanol. Geotherm. Res. 98, 49–77. https://doi.org/10.1016/S0377-0273(99)00190-0

Held, P., Bohatý, L., 2002. Manganese(II) sulfate tetrahydrate (ilesite). Acta Crystallogr. Sect. E Struct. Rep. Online 58, i121–i123. https://doi.org/10.1107/S1600536802020962

Helo, C., Longpre, M.-A., Shimizu, N., Clague, D.A., Stix, J., 2011. Explosive eruptions at mid-ocean ridges driven by CO2-rich magmas. Nat. Geosci. 4, 260–263. https://doi.org/10.1038/NGEO1104

Higgins, M.D., 2000. Measurement of crystal size distributions. Am. Mineral. 85, 1105–1116. https://doi.org/10.2138/am-2000-8-901

Hilliard, J.E., Lawson, L., 2003. Stereology and Stochastic Geometry. Springer Science & Business Media.

Hirth, G., Kohlstedt, D.L., 1996. Water in the oceanic upper mantle: implications for rheology, melt extraction and the evolution of the lithosphere. Earth Planet. Sci. Lett. 144, 93–108. https://doi.org/10.1016/0012-821X(96)00154-9

Hughes, E.C., Neave, D.A., Dobson, K.J., Withers, P.J., Edmonds, M., 2017. How to fragment peralkaline rhyolites: Observations on pumice using combined multi-scale 2D and 3D imaging. J. Volcanol. Geotherm. Res. 336, 179–191. https://doi.org/10.1016/j.jvolgeores.2017.02.020

Hui, H., Zhang, Y., 2007. Toward a general viscosity equation for natural anhydrous and hydrous silicate melts. Geochim. Cosmochim. Acta 71, 403–416. https://doi.org/10.1016/j.gca.2006.09.003

Huybers, P., Langmuir, C., 2009. Feedback between deglaciation, volcanism, and atmospheric CO2. Earth Planet. Sci. Lett. 286, 479–491. https://doi.org/10.1016/j.epsl.2009.07.014
Javoy, M., Pineau, F., 1991. The volatiles record of a "popping" rock from the Mid-Atlantic Ridge at 14°N: chemical and isotopic composition of gas trapped in the vesicles. Earth Planet. Sci. Lett. 107, 598–611.
Jones, M.R., Soule, S.A., Gonnermann, H.M., Le Roux, V., Clague, D.A., 2018. Magma ascent and lava flow emplacement rates during the 2011 Axial Seamount eruption based on CO2 degassing. Earth Planet. Sci. Lett. 494, 32–41. https://doi.org/10.1016/j.epsl.2018.04.044
Jones, M.R., Wanless, V.D., Soule, S.A., Kurz, M.D., Mittelstaedt, E., Fornari, D.J., Curtice, J., Klein, F., Le Roux, V., Brodsky, H., Péron, S., Schwartz, D.M., 2019. New constraints on mantle carbon from Mid-Atlantic Ridge popping rocks. Earth Planet. Sci. Lett. 511, 67–75. https://doi.org/10.1016/j.epsl.2019.01.019
Jutzeler, M., Marsh, R., Carey, R.J., White, J.D.L., Talling, P.J., Karlstrom, L., 2014. On the fate of pumice rafts formed during the 2012 Havre submarine eruption. Nat. Commun. 5. https://doi.org/10.1038/ncomms4660
Kano, K., 2013. Subaqueous Pumice Eruptions and Their Products: A Review, in: Explosive Subaqueous Volcanism. American Geophysical Union (AGU). https://doi.org/10.1029/140GM14
Kano, K., Yamamoto, T., Ono, K., 1996. Subaqueous eruption and emplacement of the Shinjima Pumice, Shinjima (Moeshima) Island, Kagoshima Bay, SW Japan. J. Volcanol. Geotherm. Res. 71, 187–206. https://doi.org/10.1016/0377-0273(95)00077-1
Ketcham, R.A., 2005. Computational methods for quantitative analysis of three-dimensional features in geological specimens. Geosphere 1, 32–41. https://doi.org/10.1130/GES00001.1
Ketcham, R.A., Carlson, W.D., 2001. Acquisition, Optimization and Interpretation of X-ray Computed Tomographic Imagery: Applications to the Geosciences. Comput Geosci 27, 381–400. https://doi.org/10.1016/S0098-3004(00)00116-3
Ketcham, R.A., Meth, C., Hirsch, D.M., Carlson, W.D., 2005. Improved methods for quantitative analysis of three-dimensional porphyroblastic textures. Geosphere 1, 42. https://doi.org/10.1130/GES00002.1
Klug, C., Cashman, K., Bacon, C., 2002. Structure and physical characteristics of pumice from the climactic eruption of Mount Mazama (Crater Lake), Oregon. Bull. Volcanol. 64, 486–501. https://doi.org/10.1007/s00445-002-0230-5
Klug, C., Cashman, K.V., 1994. Vesiculation of May 18, 1980, Mount St. Helens magma. Geology 22, 468–472. https://doi.org/10.1130/0091-7613(1994)022<0468:VOMMSH>2.3.CO;2
Kurz, M.D., Curtice, J., Fornari, D., Geist, D., Moreira, M., 2009. Primitive neon from the center of the Galápagos hotspot. Earth Planet. Sci. Lett. 286, 23–34. https://doi.org/10.1016/j.epsl.2009.06.008
Kurz, M.D., Moreira, M., Curtice, J., Lott III, D.E., Mahoney, J.J., Sinton, J.M., 2005. Correlated helium, neon, and melt production on the super-fast spreading East Pacific Rise near 17°S. Earth Planet. Sci. Lett. 232, 125–142. https://doi.org/10.1016/j.epsl.2005.01.005
Lamadrid, H.M., Moore, L.R., Moncada, D., Rimstidt, J.D., Burruss, R.C., Bodnar, R.J., 2017. Reassessment of the Raman CO2 densimeter. Chem. Geol. 450, 210–222. https://doi.org/10.1016/j.chemgeo.2016.12.034
Lange, R., 1994. The Effect of H2O, CO2 and F on the Density and Viscosity of Silicate Melts, in: Carroll, M.R., Holloway, J.R. (Eds.), Volatiles in Magmas. Mineralogical Soc Amer, Chantilly, pp. 331–369.
Le Roux, P., Shirey, S., Hauri, E., Perfit, M., Bender, J., 2006. The effects of variable sources, processes and contaminants on the composition of northern EPR MORB (8–10°N and 12–

14°N): Evidence from volatiles (H2O, CO2, S) and halogens (F, Cl). Earth Planet. Sci. Lett. 251, 209–231. https://doi.org/10.1016/j.epsl.2006.09.012
Le Voyer, M., Cottrell, E., Kelley, K.A., Brounce, M., Hauri, E.H., 2015. The effect of primary versus secondary processes on the volatile content of MORB glasses: An example from the equatorial Mid-Atlantic Ridge (5°N-3°S). J. Geophys. Res. Solid Earth 120, 125–144. https://doi.org/10.1002/2014JB011160
Le Voyer, M., Hauri, E.H., Cottrell, E., Kelley, K.A., Salters, V.J.M., Langmuir, C.H., Hilton, D.R., Barry, P.H., Füri, E., 2019. Carbon Fluxes and Primary Magma CO2 Contents Along the Global Mid-Ocean Ridge System. Geochem. Geophys. Geosystems 20, 1387–1424. https://doi.org/10.1029/2018GC007630
Le Voyer, M., Kelley, K.A., Cottrell, E., Hauri, E.H., 2017. Heterogeneity in mantle carbon content from CO2-undersaturated basalts. Nat. Commun. 8, 14062. https://doi.org/10.1038/ncomms14062
Lloyd, A.S., Ruprecht, P., Hauri, E.H., Rose, W., Gonnermann, H.M., Plank, T., 2014. NanoSIMS results from olivine-hosted melt embayments: Magma ascent rate during explosive basaltic eruptions. J. Volcanol. Geotherm. Res. 283, 1–18. https://doi.org/10.1016/j.jvolgeores.2014.06.002
Manga, M., Fauria, K.E., Lin, C., Mitchell, S.J., Jones, M., Conway, C.E., Degruyter, W., Hosseini, B., Carey, R., Cahalan, R., Houghton, B.F., White, J.D.L., Jutzeler, M., Soule, S.A., Tani, K., 2018a. The pumice raft-forming 2012 Havre submarine eruption was effusive. Earth Planet. Sci. Lett. 489, 49–58. https://doi.org/10.1016/j.epsl.2018.02.025
Manga, M., Mitchell, S.J., Degruyter, W., Carey, R.J., 2018b. Transition of eruptive style: Pumice raft to dome-forming eruption at the Havre submarine volcano, southwest Pacific Ocean. Geology 46, 1075–1078. https://doi.org/10.1130/G45436.1
Mangan, M.T., Cashman, K.V., Newman, S., 1993. Vesiculation of basaltic magma during eruption. Geology 21, 157–160.
Manville, V., White, J.D.L., Houghton, B.F., Wilson, C.J.N., 1998. The saturation behaviour of pumice and some sedimentological implications. Sediment. Geol. 119, 5–16. https://doi.org/10.1016/S0037-0738(98)00057-8
Marty, B., Tolstikhin, I.N., 1998. CO2 fluxes from mid-ocean ridges, arcs and plumes. Chem. Geol. 145, 233–248. https://doi.org/10.1016/S0009-2541(97)00145-9
Matthews, S., Shorttle, O., Rudge, J.F., Maclennan, J., 2017. Constraining mantle carbon: CO2-trace element systematics in basalts and the roles of magma mixing and degassing. Earth Planet. Sci. Lett. 480, 1–14. https://doi.org/10.1016/j.epsl.2017.09.047
McDonough, W.F., Sun, S., 1995. The composition of the Earth. Chem. Geol., Chemical Evolution of the Mantle 120, 223–253. https://doi.org/10.1016/0009-2541(94)00140-4
Michael, P.J., Graham, D.W., 2015. The behavior and concentration of CO2 in the suboceanic mantle: Inferences from undegassed ocean ridge and ocean island basalts. Lithos 236–237, 338–351. https://doi.org/10.1016/j.lithos.2015.08.020
Mitchell, S.J., McIntosh, I.M., Houghton, B.F., Carey, R.J., Shea, T., 2018. Dynamics of a powerful deep submarine eruption recorded in H2O contents and speciation in rhyolitic glass: The 2012 Havre eruption. Earth Planet. Sci. Lett. 494, 135–147. https://doi.org/10.1016/j.epsl.2018.04.053
Mock, A., Jerram, D.A., 2005. Crystal Size Distributions (CSD) in Three Dimensions: Insights from the 3D Reconstruction of a Highly Porphyritic Rhyolite. J. Petrol. 46, 1525–1541. https://doi.org/10.1093/petrology/egi024
Moore, J.G., Batchelder, J.N., Cunningham, C.G., 1977. CO2-filled vesicles in mid-ocean basalt. J. Volcanol. Geotherm. Res. 2, 309–327. https://doi.org/10.1016/0377-0273(77)90018-X

Moore, L.R., Gazel, E., Tuohy, R., Lloyd, A.S., Esposito, R., Steele-MacInnis, M., Hauri, E.H., Wallace, P.J., Plank, T., Bodnar, R.J., 2015. Bubbles matter: An assessment of the contribution of vapor bubbles to melt inclusion volatile budgets. Am. Mineral. 100, 806–823. https://doi.org/10.2138/am-2015-5036

Moreira, M., Kunz, J., Allegre, C., 1998. Rare Gas Systematics in Popping Rock: Isotopic and Elemental Compositions in the Upper Mantle. Science 279, 1178–1181. https://doi.org/10.1126/science.279.5354.1178

Moreira, M.A., Kurz, M.D., 2013. Noble Gases as Tracers of Mantle Processes and Magmatic Degassing, in: The Noble Gases as Geochemical Tracers, Advances in Isotope Geochemistry. Springer, Berlin, Heidelberg, pp. 371–391. https://doi.org/10.1007/978-3-642-28836-4_12

National Academies of Sciences, E., 2017. Volcanic Eruptions and Their Repose, Unrest, Precursors, and Timing. https://doi.org/10.17226/24650

Newman, S., Lowenstern, J.B., 2002. VolatileCalc: a silicate melt–H2O–CO2 solution model written in Visual Basic for excel. Comput. Geosci. 28, 597–604. https://doi.org/10.1016/S0098-3004(01)00081-4

Nooner, S.L., Chadwick, W.W., 2016. Inflation-predictable behavior and co-eruption deformation at Axial Seamount. Science 354, 1399–1403. https://doi.org/10.1126/science.aah4666

Okumura, S., Nakamura, M., Nakano, T., Uesugi, K., Tsuchiyama, A., 2010. Shear deformation experiments on vesicular rhyolite: Implications for brittle fracturing, degassing, and compaction of magmas in volcanic conduits. J. Geophys. Res. Solid Earth 115. https://doi.org/10.1029/2009JB006904

Paonita, A., Martelli, M., 2007. A new view of the He–Ar–CO2 degassing at mid-ocean ridges: Homogeneous composition of magmas from the upper mantle. Geochim. Cosmochim. Acta 71, 1747–1763. https://doi.org/10.1016/j.gca.2006.12.019

Paonita, A., Martelli, M., 2006. Magma dynamics at mid-ocean ridges by noble gas kinetic fractionation: Assessment of magmatic ascent rates. Earth Planet. Sci. Lett. 241, 138–158. https://doi.org/10.1016/j.epsl.2005.10.018

Parnell-Turner, R., Sohn, R.A., Peirce, C., Reston, T.J., MacLeod, C.J., Searle, R.C., Simão, N.M., 2017. Oceanic detachment faults generate compression in extension. Geology 45, 923–926. https://doi.org/10.1130/G39232.1

Perfit, M.R., Chadwick, W.W., 1998. Magmatism at Mid-Ocean Ridges: Constraints from Volcanological and Geochemical Investigations, in: Buck, W.R., Delaney, P.T., Karson, J.A., Lagabrielle, Y. (Eds.), Faulting and Magmatism at Mid-Ocean Ridges. American Geophysical Union, pp. 59–115.

Perfit, M., Wanless, V.D., Ridley, W.I., Klein, E., Smith, M., Goss, A., Hinds, J., Kutza, S., Fornari, D., 2012. Lava Geochemistry as a Probe into Crustal Formation at the East Pacific Rise. Oceanography 25, 89–93. https://doi.org/10.5670/oceanog.2012.06

Perron, J.T., Kirchner, J.W., Dietrich, W.E., 2008. Spectral signatures of characteristic spatial scales and nonfractal structure in landscapes. J. Geophys. Res. Earth Surf. 113, F04003. https://doi.org/10.1029/2007JF000866

Peterson, T.D., 1996. A refined technique for measuring crystal size distributions in thin section. Contrib. Mineral. Petrol. 124, 395–405. https://doi.org/10.1007/s004100050199

Pineau, F., Shilobreeva, S., Hekinian, R., Bideau, D., Javoy, M., 2004. Deep-sea explosive activity on the Mid-Atlantic Ridge near 34°50'N: a stable isotope (C, H, O) study. Chem. Geol. 211, 159–175. https://doi.org/10.1016/j.chemgeo.2004.06.029

Polacci, M., Baker, D.R., La Rue, A., Mancini, L., Allard, P., 2012. Degassing behaviour of vesiculated basaltic magmas: an example from Ambrym volcano, Vanuatu Arc. J. Volcanol. Geotherm. Res. 233–234, 55–64. https://doi.org/10.1016/j.jvolgeores.2012.04.019

Polacci, M., Baker, D.R., Mancini, L., Tromba, G., Zanini, F., 2006. Three-dimensional investigation of volcanic textures by X-ray microtomography and implications for conduit processes. Geophys. Res. Lett. 33. https://doi.org/10.1029/2006GL026241

Proussevitch, A.A., Sahagian, D.L., 1998. Dynamics and energetics of bubble growth in magmas: Analytical formulation and numerical modeling. J. Geophys. Res. Solid Earth 103, 18223–18251. https://doi.org/10.1029/98JB00906

Prousevitch, A., Sahagian, D., Anderson, A., 1993. Dynamics of Diffusive Bubble-Growth in Magmas - Isothermal Case. J. Geophys. Res.-Solid Earth 98, 22283–22307. https://doi.org/10.1029/93JB02027

Recktenwald, G., 2006. Transient, One-Dimensional Heat Conduction in a Convectively Cooled Sphere. MATLAB Code. http://web.cecs.pdx.edu/~gerry/epub/pdf/transientConductionSphere.pdf

Resing, J.A., Rubin, K.H., Embley, R.W., Lupton, J.E., Baker, E.T., Dziak, R.P., Baumberger, T., Lilley, M.D., Huber, J.A., Shank, T.M., Butterfield, D.A., Clague, D.A., Keller, N.S., Merle, S.G., Buck, N.J., Michael, P.J., Soule, A., Caress, D.W., Walker, S.L., Davis, R., Cowen, J.P., Reysenbach, A.-L., Thomas, H., 2011. Active submarine eruption of boninite in the northeastern Lau Basin. Nat. Geosci. 4, 799–806. https://doi.org/10.1038/ngeo1275

Rivalta, E., 2010. Evidence that coupling to magma chambers controls the volume history and velocity of laterally propagating intrusions. J. Geophys. Res. 115. https://doi.org/10.1029/2009JB006922

Rosenthal, A., Hauri, E.H., Hirschmann, M.M., 2015. Experimental determination of C, F, and H partitioning between mantle minerals and carbonated basalt, CO2/Ba and CO2/Nb systematics of partial melting, and the CO2 contents of basaltic source regions. Earth Planet. Sci. Lett. 412, 77–87. https://doi.org/10.1016/j.epsl.2014.11.044

Rotella, M.D., Wilson, C.J.N., Barker, S.J., Ian Schipper, C., Wright, I.C., Wysoczanski, R.J., 2015. Dynamics of deep submarine silicic explosive eruptions in the Kermadec arc, as reflected in pumice vesicularity textures. J. Volcanol. Geotherm. Res. 301, 314–332. https://doi.org/10.1016/j.jvolgeores.2015.05.021

Rotella, M.D., Wilson, C.J.N., Barker, S.J., Wright, I.C., 2013. Highly vesicular pumice generated by buoyant detachment of magma in subaqueous volcanism. Nat. Geosci. 6, 129–132. https://doi.org/10.1038/ngeo1709

Rubin, K., Soule, S.A., Chadwick, W., Fornari, D., Clague, D., Embley, R., Baker, E., Perfit, M., Caress, D., Dziak, R., 2012. Volcanic Eruptions in the Deep Sea. Oceanography 25, 142–157. https://doi.org/10.5670/oceanog.2012.12

Rubin, K.H., Macdougall, J.D., Perfit, M.R., 1994. 210Po–210Pb dating of recent volcanic eruptions on the sea floor. Nature 368, 841–844. https://doi.org/10.1038/368841a0

Russ, J.C., 1986. Practical stereology. New York : Plenum Press, [1986].

Ryan, M.P., Sammis, C.G., 1981. The glass transition in basalt. J. Geophys. Res. Solid Earth 86, 9519–9535. https://doi.org/10.1029/JB086iB10p09519

Saal, A.E., Hauri, E.H., Langmuir, C.H., Perfit, M.R., 2002. Vapour undersaturation in primitive mid-ocean-ridge basalt and the volatile content of Earth's upper mantle. Nature 419, 451–455. https://doi.org/10.1038/nature01073

Sahagian, D.L., Proussevitch, A.A., 1998. 3D particle size distributions from 2D observations: stereology for natural applications. J. Volcanol. Geotherm. Res. 84, 173–196. https://doi.org/10.1016/S0377-0273(98)00043-2

Saltikov, S., 1967. The determination of the size distribution of particles in an opaque material from a measurement of the size distribution of their sections, in: Stereology: Proceeding of the Second International Congress for Stereology. pp. 163–173.

Sarda, P., Graham, D., 1990. Mid-ocean ridge popping rocks: implications for degassing at ridge crests. Earth Planet. Sci. Lett. 97, 268–289. https://doi.org/10.1016/0012-821X(90)90047-2

Sarda, P., Moreira, M., 2002. Vesiculation and vesicle loss in mid-ocean ridge basalt glasses: He, Ne, Ar elemental fractionation and pressure influence. Geochim. Cosmochim. Acta 66, 1449–1458. https://doi.org/10.1016/S0016-7037(01)00863-8

Schindelin, J., Arganda-Carreras, I., Frise, E., Kaynig, V., Longair, M., Pietzsch, T., Preibisch, S., Rueden, C., Saalfeld, S., Schmid, B., Tinevez, J.-Y., White, D.J., Hartenstein, V., Eliceiri, K., Tomancak, P., Cardona, A., 2012. Fiji: an open-source platform for biological-image analysis. Nat. Methods 9, 676–682. https://doi.org/10.1038/nmeth.2019

Shea, T., Houghton, B.F., Gurioli, L., Cashman, K.V., Hammer, J.E., Hobden, B.J., 2010. Textural studies of vesicles in volcanic rocks: An integrated methodology. J. Volcanol. Geotherm. Res. 190, 271–289. https://doi.org/10.1016/j.jvolgeores.2009.12.003

Shields, J.K., Mader, H.M., Pistone, M., Caricchi, L., Floess, D., Putlitz, B., 2014. Strain-induced outgassing of three-phase magmas during simple shear. J. Geophys. Res. Solid Earth 119, 6936–6957. https://doi.org/10.1002/2014JB011111

Schwartz, D.M., Wanless, V.D., Berg, R., Jones, M., Fornari, D.J., Soule, S.A., Lytle, M.L., Carey, S., 2017. Petrogenesis of Alkalic Seamounts on the Galápagos Platform. Deep Sea Res. Part II Top. Stud. Oceanogr. https://doi.org/10.1016/j.dsr2.2017.09.019

Shaw, A.M., Behn, M.D., Humphris, S.E., Sohn, R.A., Gregg, P.M., 2010. Deep pooling of low degree melts and volatile fluxes at the 85°E segment of the Gakkel Ridge: Evidence from olivine-hosted melt inclusions and glasses. Earth Planet. Sci. Lett. 289, 311–322. https://doi.org/10.1016/j.epsl.2009.11.018

Shea, T., Houghton, B.F., Gurioli, L., Cashman, K.V., Hammer, J.E., Hobden, B.J., 2010. Textural studies of vesicles in volcanic rocks: An integrated methodology. J. Volcanol. Geotherm. Res. 190, 271–289. https://doi.org/10.1016/j.jvolgeores.2009.12.003

Smith, D.K., Escartín, J., Schouten, H., Cann, J.R., 2008. Fault rotation and core complex formation: Significant processes in seafloor formation at slow-spreading mid-ocean ridges (Mid-Atlantic Ridge, 13°-15°N). Geochem. Geophys. Geosystems 9, n/a-n/a. https://doi.org/10.1029/2007GC001699

Song, S.-R., Jones, K.W., Lindquist, B.W., Dowd, B.A., Sahagian, D.L., 2001. Synchrotron X-ray computed microtomography: studies on vesiculated basaltic rocks. Bull. Volcanol. 63, 252–263. https://doi.org/10.1007/s004450100141

Soule, S.A., Fornari, D.J., Perfit, M.R., Rubin, K.H., 2007. New insights into mid-ocean ridge volcanic processes from the 2005-2006 eruption of the East Pacific Rise, 9°46'N-9°56'N. Geology 35, 1079–1082. https://doi.org/10.1130/G23924A.1

Soule, S.A., Nakata, D.S., Fornari, D.J., Fundis, A.T., Perfit, M.R., Kurz, M.D., 2012. CO2 variability in mid-ocean ridge basalts from syn-emplacement degassing: Constraints on eruption dynamics. Earth Planet. Sci. Lett. 327–328, 39–49. https://doi.org/10.1016/j.epsl.2012.01.034

Tan, Y.J., Tolstoy, M., Waldhauser, F., Wilcock, W.S.D., 2016. Dynamics of a seafloor-spreading episode at the East Pacific Rise. Nature 540, 261–265. https://doi.org/10.1038/nature20116

Tolstoy, M., Cowen, J.P., Baker, E.T., Fornari, D.J., Rubin, K.H., Shank, T.M., Waldhauser, F., Bohnenstiehl, D.R., Forsyth, D.W., Holmes, R.C., Love, B., Perfit, M.R., Weekly, R.T., Soule, S.A., Glazer, B., 2006. A Sea-Floor Spreading Event Captured by Seismometers. Science 314, 1920–1922. https://doi.org/10.1126/science.1133950

Tucker, J.M., Mukhopadhyay, S., Gonnermann, H.M., 2018. Reconstructing mantle carbon and noble gas contents from degassed mid-ocean ridge basalts. Earth Planet. Sci. Lett. 496, 108–119. https://doi.org/10.1016/j.epsl.2018.05.024

Underwood, E.E., 1970. Quantitative stereology, Addison-Wesley series in metallurgy and materials. Reading, Mass., Addison-Wesley Pub. Co. [1970].

van Otterloo, J., Cas, R.A.F., Scutter, C.R., 2015. The fracture behaviour of volcanic glass and relevance to quench fragmentation during formation of hyaloclastite and phreatomagmatism. Earth-Sci. Rev. 151, 79–116. https://doi.org/10.1016/j.earscirev.2015.10.003

Vander Voort, G.F., 1999. Metallography, principles and practice. [electronic resource]. Materials Park, OH : ASM International, c1999.

Voltolini, M., Zandomeneghi, D., Mancini, L., Polacci, M., 2011. Texture analysis of volcanic rock samples: Quantitative study of crystals and vesicles shape preferred orientation from X-ray microtomography data. J. Volcanol. Geotherm. Res. 202, 83–95. https://doi.org/10.1016/j.jvolgeores.2011.02.003

von Lichtan, I.J., White, J.D.L., Manville, V., Ohneiser, C., 2016. Giant rafted pumice blocks from the most recent eruption of Taupo volcano, New Zealand: Insights from palaeomagnetic and textural data. J. Volcanol. Geotherm. Res. 318, 73–88. https://doi.org/10.1016/j.jvolgeores.2016.04.003

Wager, L.R., 1961. A note on the origin of ophitic texture in the chilled olivine gabbro of the Skaergaard intrusion. Geol. Mag. 98, 353–366.

Wallace, P.J., Plank, T., Edmonds, M., Hauri, E.H., 2015. Volatiles in Magmas, in: Sigurdsson, H. (Ed.), The Encyclopedia of Volcanoes (Second Edition). Academic Press, Amsterdam, pp. 163–183. https://doi.org/10.1016/B978-0-12-385938-9.00007-9

West, M., Menke, W., Tolstoy, M., Webb, S., Sohn, R., 2001. Magma storage beneath Axial volcano on the Juan de Fuca mid-ocean ridge. Nature 413, 833–836. https://doi.org/10.1038/35101581

Wilcock, W.S.D., Tolstoy, M., Waldhauser, F., Garcia, C., Tan, Y.J., Bohnenstiehl, D.R., Caplan-Auerbach, J., Dziak, R.P., Arnulf, A.F., Mann, M.E., 2016. Seismic constraints on caldera dynamics from the 2015 Axial Seamount eruption. Science 354, 1395–1399. https://doi.org/10.1126/science.aah5563

Wright, R.B., Wang, C.H., 1973. Density effect on the Fermi resonance in gaseous CO2 by Raman scattering. J. Chem. Phys. 58, 2893–2895. https://doi.org/10.1063/1.1679594

Supplementary Material

S.2 Supplementary material accompanying Chapter 2

Table S.2.1 Acquisition and processing parameters for x-ray computed micro-tomography scans

§ denotes x-ray computed tomography scans published in Jones et al. (2019)

Sample	Image Pixel Size	Volume Analyzed	Source Voltage	Source Current	Exposure	Rotation Step
	(um)	(um3)	(kV)	(uA)	(ms)	(deg)
AX13-RC02 (high res)	0.70	7.8E+09	80	125	9275	0.35
AX13-RC02 (low res)	2.30	4.8E+10	80	125	6300	0.25
AX13-RC03	1.50	1.6E+10	80	125	9275	0.3
AX13-RC04	0.88	8.4E+09	80	125	9275	0.3
AX13-RC05	0.60	1.7E+09	65	153	5800	0.25
AX13-RC06	0.70	8.5E+09	80	125	9700	0.35
AX13-RC07	2.00	3.5E+10	80	125	9275	0.3
AX13-RC13	0.50	2.1E+09	70	142	7900	0.35
AX13-RC15	0.70	1.2E+10	70	142	8200	0.35
AL4818-003	5.00	1.0E+12	100	100	5800	0.2
AL4820-036	4.57	8.2E+11	100	100	5800	0.2
AL4820-037 (high res)	1.65	7.2E+10	80	125	11000	0.15
AL4820-037 (low res)§	4.75	7.3E+11	100	100	5900	0.25
AL4821-050§	4.00	3.5E+11	100	100	4593	0.25
AL4821-051§	3.35	4.0E+11	90	111	4462	0.25
AL4821-053§	3.50	3.0E+11	100	100	5900	0.25
AL4821-054 (low res)§	4.37	3.4E+10	90	111	4462	0.25
AL4821-054 (high res)	1.60	5.8E+11	90	111	11250	0.35
AL4821-055§	4.75	1.0E+12	100	100	5400	0.25
AL4821-056§	3.63	3.2E+11	90	111	4462	0.25
AL4821-057§	4.10	4.2E+11	90	111	4462	0.3
AL4821-058§	4.00	5.9E+11	90	111	4462	0.25
AL4821-059§	4.15	7.0E+11	90	111	4462	0.25

Table S.2.1 (cont.)

Sample	Filter	Frame averaging	Post-alignment	Smoothing	Ring artifact correction	Beam hardening correction
AX13-RC02 (high res)	1 mm Al	8	-37	5	7	41
AX13-RC02 (low res)	1 mm Al	6	-55.5	7	15	64
AX13-RC03	1 mm Al	5	-13.5	2	23	35
AX13-RC04	1 mm Al	5	-36.5	7	13	43
AX13-RC05	0.25 mm Al	9	-59.5	6	20	64
AX13-RC06	1 mm Al	8	-55	7	30	51
AX13-RC07	1 mm Al	5	-11	6	30	39
AX13-RC13	0.5 mm Al	8	-67	7	28	35
AX13-RC15	0.5 mm Al	8	-60	7	38	57
AL4818-003	0.11 mm Cu	6	-47	7	15	43
AL4820-036	0.11 mm Cu	6	-24.5	4	15	35
AL4820-037 (high res)	1 mm Al	8	-36.5	7	30	41
AL4820-037 (low res)[§]	0.11 mm Cu	7	-17	4	6	40
AL4821-050[§]	0.11 mm Cu	8	-27	6	10	36
AL4821-051[§]	0.5 mm Al + 0.038 mm Cu	8	-20	6	12	40
AL4821-053[§]	0.11 mm Cu	6	-19	6	9	30
AL4821-054 (low res)[§]	0.5 mm Al + 0.038 mm Cu	6	-19	3	18	41
AL4821-054 (high res)	0.5 mm Al + 0.038 mm Cu	6	-12.5	5	9	31
AL4821-055[§]	0.11 mm Cu	6	-19.5	4	10	30
AL4821-056[§]	0.5 mm Al + 0.038 mm Cu	8	-15.5	6	7	44
AL4821-057[§]	0.5 mm Al + 0.038 mm Cu	6	-27	5	10	44
AL4821-058[§]	0.5 mm Al + 0.038 mm Cu	8	-20	5	7	41
AL4821-059[§]	0.5 mm Al + 0.038 mm Cu	6	-22.5	4	13	35

Table S.2.2 Vesicularity, vesicle number density, and vesicle characteristics based on 2D reflected light photomicrographs combined with stereological corrections and 3D x-ray computed micro-tomography scans

*C&L refers to Cheng and Lemlich (1983)

*S&P refers to Sahagian and Proussevitch (1998)

† denotes data published in Jones et al. (2018)

§ denotes data published in Jones et al. (2019)

Sample	2D area analyzed	3D Vesicularity	2D Vesicularity	3D Minimum Radius	2D Minimum Radius	3D Maximum Radius
	(um^2)	(Vol. %)	(Vol. %)	(um)	(um)	(um)
AX13-RC02 (high res)	1.2E+08	0.7	1.6†	15	15	113
AX13-RC02 (low res)	1.20E+08	1.2	1.6†	15	15	187
AX13-RC03	8.8E+07	1.1	1.2†	15	16	147
AX13-RC04	1.1E+08	0.4	0.5†	15	15	49
AX13-RC05	1.5E+08	0.9	1.1†	16	15	56
AX13-RC06	1.5E+08	0.9	1.1†	15	15	73
AX13-RC07	1.0E+08	0.5	0.5†	15	15	57
AX13-RC13	1.3E+08	0.7	0.7†	15	15	59
AX13-RC15	1.2E+08	0.2	0.2†	15	15	49
AL4818-003	4.4E+08	13.6§	13.3§	15	15	1019
AL4820-036	2.9E+08	13.2§	13.3§	15	15	778
AL4820-037 (high res)	4.2E+08	18.7	20.0§	15	20	710
AL4820-037 (low res)§	4.2E+08	19.7§	20.0§	15	20	930
AL4821-050§	1.4E+08	5.2§	5.7§	15	15	443
AL4821-051§	2.7E+08	9.1§	11.9§	15	15	723
AL4821-053§	2.2E+08	12.9§	14.2§	15	15	884
AL4821-054 (high res)	1.2E+08	8.7	11.2§	15	15	436
AL4821-054 (low res)§	1.2E+08	7.1§	11.2§	15	15	773
AL4821-055§	6.0E+08	15.6§	17.9§	15	15	1456
AL4821-056§	1.3E+08	12.8§	13.8§	15	19	820
AL4821-057§	8.8E+07	9.8§	13.4§	15	15	731
AL4821-058§	1.4E+08	11.3§	11.7§	15	15	759
AL4821-059§	1.5E+08	20.1§	24.8§	15	15	1225

Table S.2.2 (cont.)

Sample	2D Maximum Radius	3D Mean Radius	2D Mean Radius	3D Nv	2D Nv (C & L)*	2D Nv (S & P)*
	(um)	(um)	(um)	(bubbles/ mm^3)	(bubbles/mm^3)	(bubbles/mm^3)
AX13-RC02 (high res)	189	44	67	7.9	8.0†	9.1
AX13-RC02 (low res)	189	57	67	6.5	8.0†	9.1
AX13-RC03	236	50	56	9.9	8.9†	7.1
AX13-RC04	44	22	21	68.9	50.5†	74.9
AX13-RC05	89	30	37	53.3	28.5†	31.5
AX13-RC06	101	32	34	42.3	35.4†	33.0
AX13-RC07	51	22	24	85.0	38.2†	50.9
AX13-RC13	88	25	26	69.7	41.3†	42.5
AX13-RC15	33	19	19	32.3	20.5†	35.2
AL4818-003	903	84	127	6.7§	7.0	5.3
AL4820-036	720	74	112	12.2§	11.0	8.0
AL4820-037 (high res)	775	152	260	2.2§	1.9	1.5
AL4820-037 (low res)§	775	206	260	1.5§	1.9	1.5
AL4821-050§	293	64	89	12.8§	11.4	9.7
AL4821-051§	708	98	135	5.3§	6.1	4.3
AL4821-053§	1028	82	147	7.8§	5.2	3.6
AL4821-054 (high res)	623	75	112	10.9§	8.7	7.7
AL4821-054 (low res)§	623	76	112	6.5§	8.7	7.7
AL4821-055§	962	103	180	4.1§	4.1	6.1
AL4821-056§	624	132	187	3.3§	3.1	2.6
AL4821-057§	618	97	165	4.9§	4.3	5.8
AL4821-058§	617	118	165	4.5§	3.6	4.7
AL4821-059§	1272	116	211	3.7§	3.1	3.9

Table S.2.3 CO_2 density in bubbles determined by Raman spectroscopy. The CO_2 density was calculated from the Fermi diad splitting using the calibration developed with a 632 nm laser and 1800 grooves/mm grating by Lamadrid et al. (2017)

Sample	Vesicle ID	Fermi diad shift	CO2 density
		(cm^{-1})	(g/cm^3)
AX13-RC06	63	102.84	0.06
AX13-RC06	77	102.83	0.05
AX13-RC06	78	102.84	0.06
AX13-RC06	79	102.82	0.05
AX13-RC06	80	102.83	0.05
AX13-RC06	81	102.84	0.06
AX13-RC06	82	102.83	0.05
AX13-RC13	83	102.86	0.06
AX13-RC13	84	102.81	0.05
AX13-RC13	85	102.78	0.04
AX13-RC13	86	102.85	0.06
AX13-RC13	87	102.85	0.06
AX13-RC13	88	102.81	0.05

S.3 Supplementary material accompanying Chapter 3

S.3.1 Sample locations and major element concentrations

The glass rinds were chipped, cleaned in an ultrasonic bath, hand-picked, mounted on 8-hole polished sections, and analyzed at the University of California at Davis on a 5-spectrometer Cameca SX-100 microprobe (Supplementary Table S.1). Si, Al, Fe, Mg, Ca, and Na were standardized against Smithsonian glass VG2 (with an MgO value of 7.07 wt.%), Ti against rutile, Mn against rhodonite, K against potassium feldspar, P against apatite, S against pyrrhotite, and Cl against scapolite. The reported values consist of an average of five analyses, each using a 10x10 μm raster area and off-peak backgrounds. The major oxides are normalized on a volatile-free basis.

Table S.3.1 Sample locations and major element concentrations

Sample	Longitute	Latitude	Depth	Flow Distance	SiO2	TiO2	Al2O3
	(deg)	(deg)	(m)	(m)	(Wt. %)	(Wt. %)	(Wt. %)
AX13_RC01	-129.9831	45.9203	1523	75	49.86	1.56	14.63
AX13_RC02	-129.9749	45.8997	1589	2286	49.76	1.57	14.53
AX13_RC03	-129.9759	45.9048	1557	1702	49.96	1.54	14.49
AX13_RC04	-129.9871	45.9178	1525	26	49.89	1.55	14.49
AX13_RC05	-129.9800	45.9077	1544	1261	49.83	1.54	14.73
AX13_RC06	-129.9823	45.9106	1537	897	49.93	1.51	14.75
AX13_RC07	-129.9850	45.9138	1530	483	49.80	1.53	14.55
AX13_RC08	-129.9938	45.8968	1577	22	49.79	1.57	14.77
AX13_RC09	-129.9949	45.8822	1678	159	49.76	1.54	14.75
AX13_RC10	-129.9973	45.8883	1639	71	49.67	1.56	14.61
AX13_RC12	-130.0017	45.9465	1530	1383	49.82	1.52	14.78
AX13_RC13	-129.9993	45.9476	1530	1164	49.90	1.53	14.57
AX13_RC15	-129.9922	45.9459	1529	521	49.84	1.52	14.55
AX13_RC16	-129.9971	45.9486	1529	1015	49.89	1.53	14.51
AX13_RC17	-129.9942	45.9471	1525	729	49.88	1.57	14.52
AX13_RC22	-129.9951	45.8923	1604	11	49.84	1.54	14.69
AX13_RC23	-129.9931	45.9009	1561	19	49.71	1.53	14.68
AX13_RC25	-129.9919	45.9038	1548	20	49.75	1.53	14.71
AX13_RC26	-129.9887	45.9171	1526	20	49.73	1.53	14.68
AX13_RC37	-129.9967	45.8786	1696	90	49.97	1.59	14.51
D522_R03	-129.9870	45.9467	1521	98	49.80	1.54	14.80
D522_R04	-129.9863	45.9479	1521	34	49.85	1.48	14.56
D522_R05	-129.9848	45.9483	1519	87	49.82	1.55	14.52
D522_R08	-129.9873	45.9530	1506	68	49.91	1.54	14.53
D522_R09	-129.9876	45.9534	1513	84	49.93	1.57	14.55
D522_R12	-129.9862	45.9533	1505	19	49.78	1.54	14.76
D522_R13	-129.9841	45.9554	1502	257	49.79	1.55	14.50
D522_R14	-129.9820	45.9565	1513	507	49.72	1.52	14.69
D522_R15	-129.9814	45.9575	1514	460	49.92	1.51	14.52
D522_R16	-129.9809	45.9589	1509	456	49.86	1.53	14.53
D522_SB08	-129.9819	45.9601	1507	316	49.83	1.53	14.72
R1467_R01	-129.9843	45.9525	1509	196	49.79	1.52	14.65
R1467_R02	-129.9846	45.9531	1507	146	49.80	1.53	14.69
R1467_R04	-129.9863	45.9528	1506	9	49.74	1.49	14.69
R1467_R05	-129.9860	45.9534	1506	34	49.99	1.51	14.60
R1467_R08	-129.9846	45.9422	1512	79	49.74	1.54	14.59
R1469_R01	-129.9818	45.9587	1512	386	49.75	1.51	14.63
R1469_R02	-129.9890	45.9415	1522	424	49.90	1.52	14.55
R1469_R03	-129.9986	45.9407	1532	1203	49.85	1.55	14.58
R1469_R04	-130.0041	45.9395	1532	1630	49.78	1.51	14.62
R1469_R05	-130.0074	45.9376	1532	1925	49.67	1.52	14.63
R1470_S05	-129.9822	45.9332	1513	42	49.77	1.52	14.62
R1472_R01	-129.9847	45.9420	1514	89	49.84	1.54	14.58
R1472_R02	-129.9898	45.9139	1531	13	49.90	1.50	14.70
R1472_R03	-129.9898	45.9135	1531	14	49.82	1.53	14.55
R1472_R04	-129.9897	45.9133	1536	14	49.88	1.50	14.74
R1472_R05	-129.9919	45.9079	1537	48	49.80	1.51	14.77
R1472_R06	-129.9938	45.9065	1540	178	49.77	1.51	14.63
R1472_R07	-129.9944	45.9062	1541	242	49.84	1.50	14.73
R1473_R02	-129.9989	45.8756	1699	24	49.77	1.59	14.50

Table S.3.1 (cont.)

Sample	FeO	MnO	MgO	CaO	Na2O	K2O	P2O5	ISGN
	(Wt. %)	(Wt. %)	(Wt. %)	(Wt. %)	(Wt. %)	(Wt. %)	(Wt. %)	
AX13_RC01	10.97	0.22	7.50	12.23	2.73	0.17	0.13	IEAMB0009
AX13_RC02	11.21	0.22	7.40	12.22	2.77	0.18	0.14	IEAMB000A
AX13_RC03	11.09	0.19	7.38	12.32	2.73	0.17	0.13	IEAMB000B
AX13_RC04	11.10	0.20	7.43	12.34	2.68	0.17	0.15	IEAMB000E
AX13_RC05	11.02	0.21	7.41	12.20	2.75	0.17	0.13	IEAMB000C
AX13_RC06	10.93	0.21	7.48	12.15	2.71	0.17	0.16	IEAMB000G
AX13_RC07	11.05	0.18	7.49	12.43	2.68	0.18	0.12	IEAMB000F
AX13_RC08	11.01	0.20	7.45	12.14	2.75	0.19	0.14	IEAMB003B
AX13_RC09	11.11	0.17	7.37	12.26	2.72	0.17	0.15	IEAMB005C
AX13_RC10	11.10	0.20	7.45	12.29	2.80	0.18	0.15	IEAMB005O
AX13_RC12	10.94	0.17	7.43	12.30	2.72	0.18	0.14	IEAMB000S
AX13_RC13	11.02	0.18	7.43	12.34	2.69	0.18	0.17	IEAMB000R
AX13_RC15	11.17	0.18	7.50	12.25	2.68	0.17	0.14	IEAMB002P
AX13_RC16	11.03	0.17	7.44	12.39	2.71	0.18	0.15	IEAMB000T
AX13_RC17	11.04	0.18	7.44	12.35	2.70	0.17	0.16	IEAMB002O
AX13_RC22	11.09	0.19	7.44	12.18	2.75	0.18	0.11	IEAMB005B
AX13_RC23	11.00	0.21	7.48	12.36	2.73	0.17	0.14	IEAMB003A
AX13_RC25	11.05	0.18	7.46	12.26	2.73	0.16	0.16	IEAMB003C
AX13_RC26	11.05	0.19	7.48	12.27	2.74	0.18	0.15	IEAMB005A
AX13_RC37	11.06	0.19	7.38	12.23	2.79	0.17	0.11	IEAMB005P
D522_R03	10.93	0.21	7.41	12.27	2.71	0.17	0.16	IEAMB0027
D522_R04	11.06	0.19	7.46	12.39	2.66	0.18	0.16	IEAMB0028
D522_R05	11.09	0.19	7.41	12.41	2.68	0.18	0.15	IEAMB0029
D522_R08	11.00	0.19	7.42	12.38	2.72	0.18	0.15	IEAMB002C
D522_R09	10.95	0.19	7.47	12.34	2.70	0.17	0.14	IEAMB002D
D522_R12	11.01	0.19	7.45	12.22	2.73	0.17	0.15	IEAMB002G
D522_R13	11.11	0.18	7.41	12.41	2.71	0.18	0.16	IEAMB002H
D522_R14	11.03	0.18	7.50	12.28	2.75	0.17	0.16	IEAMB002I
D522_R15	11.04	0.18	7.46	12.37	2.71	0.17	0.13	IEAMB002J
D522_R16	11.13	0.20	7.46	12.28	2.72	0.17	0.12	IEAMB002K
D522_SB08	11.01	0.19	7.45	12.24	2.74	0.17	0.12	
R1467_R01	11.00	0.20	7.48	12.32	2.74	0.17	0.14	IER140001
R1467_R02	11.01	0.19	7.47	12.24	2.76	0.17	0.14	IER140002
R1467_R04	11.04	0.19	7.56	12.23	2.74	0.18	0.15	IER140003
R1467_R05	10.93	0.19	7.47	12.27	2.73	0.18	0.14	IER140004
R1467_R08	11.07	0.19	7.45	12.36	2.75	0.17	0.14	IER140005
R1469_R01	11.01	0.19	7.54	12.28	2.76	0.17	0.15	IER140006
R1469_R02	11.08	0.19	7.40	12.30	2.74	0.17	0.15	IER140007
R1469_R03	11.09	0.19	7.44	12.24	2.74	0.17	0.14	IER140008
R1469_R04	11.17	0.19	7.40	12.30	2.73	0.16	0.14	IER140009
R1469_R05	11.17	0.19	7.45	12.32	2.75	0.17	0.14	IER14000A
R1470_S05	11.01	0.20	7.44	12.37	2.75	0.17	0.15	IER14000B
R1472_R01	11.07	0.20	7.45	12.27	2.75	0.17	0.14	IER14000C
R1472_R02	10.95	0.17	7.49	12.22	2.76	0.17	0.14	IER14000D
R1472_R03	11.02	0.20	7.46	12.33	2.78	0.16	0.14	IER14000E
R1472_R04	11.03	0.19	7.34	12.20	2.80	0.19	0.14	IER14000F
R1472_R05	11.06	0.20	7.54	12.04	2.74	0.17	0.16	IER14000G
R1472_R06	11.03	0.19	7.45	12.34	2.77	0.17	0.15	IER14000H
R1472_R07	10.93	0.21	7.54	12.14	2.78	0.18	0.16	IER14000I
R1473_R02	11.30	0.21	7.26	12.24	2.80	0.18	0.14	IER14000J

S.3.2 Volatile concentrations and vesicularity characteristics

Vesicularities and vesicle size distributions were measured on 10x magnification reflected light photomicrographs of polished glass fragments from the outer quenched 1cm of the lava samples (Figure 3-2, Supplementary Table S.2). The epoxy, glass, and vesicles were extracted from the surrounding glass using the MATLAB image processing toolbox. The resulting images of vesicles and basalt were reviewed and, if necessary, manually cleaned using image analysis software (ImageJ) to remove non-vesicles and cracks (Schindelin et al., 2012). Vesicle areas were determined using ImageJ's analyze particles tool, which determines regions of contiguous black pixels. These areas were converted to effective radii assuming perfect circularity. Only vesicles with radii greater than 5 μm (2-6 pixels) were retained for analysis. Vesicularity (2D) was calculated as the percent fraction of the fragment area represented by vesicles. The data represent averages of at least three polished fragments.

In order to infer vesicle sizes and distributions from 2D data, two stereological corrections were applied (e.g. Cashman and Mangan, 1994; Sahagian and Proussevitch, 1998; Shea et al., 2010). First, the number of bubbles in a given size class was divided by the average diameter of that size class to account for the higher probability for 2D slices to intersect large bubbles than small bubbles (Cheng and Lemlich, 1983). Second, vesicle radii were multiplied by a scaling factor (1.176) to account for the probability that a random plane will not intersect the largest cross section of a sphere (Mangan et al., 1993). The bubble density for each size interval was calculated by dividing the number per unit volume by the interval size. The vesicle size distributions were interpreted using histograms of bubble density versus bubble size and cumulative bubble volume versus bubble size (Shea et al., 2010).

Table S.3.2 Volatile concentrations and vesicularity characteristics

Sample	CO_2	H_2O	F	Cl	S	Vesicularity	Rmax	Nv
	ppm	(wt.%)	ppm	ppm	(wt.%)	(%)	(μm)	(mm^{-3})
AX13_RC01	225	0.18	157	170	0.13	0.93	46	92
AX13_RC02	107	0.20	169	182	0.13	1.64	114	36
AX13_RC03	124	0.21	165	174	0.13	1.23	112	24
AX13_RC04	283	0.22	165	180	0.13	0.51	24	203
AX13_RC05	153	0.17	152	167	0.12	1.06	57	91
AX13_RC06	158	0.17	159	175	0.13	1.09	49	104
AX13_RC07	323	0.19	161	175	0.13	0.49	29	161
AX13_RC08	160	0.23	163	186	0.13	0.88	42	95
AX13_RC09	119	0.22	168	176	0.13	1.17	85	30
AX13_RC10	114	0.20	158	182	0.13	1.25	70	50
AX13_RC12	171	0.18	163	173	0.13	0.91	62	67
AX13_RC13	250	0.19	162	176	0.13	0.65	38	150
AX13_RC15	339	0.22	167	181	0.13	0.24	17	189
AX13_RC16	208	0.17	164	174	0.13	0.90	59	118
AX13_RC17	183	0.18	160	175	0.13	0.89	43	185
AX13_RC22	124	0.21	160	184	0.13	1.09	52	77
AX13_RC23	185	0.18	161	175	0.13	1.08	49	91
AX13_RC25	140	0.18	155	178	0.13	0.96	59	124
AX13_RC26	222	0.21	158	180	0.13	0.67	33	170
AX13_RC37	69	0.22	165	188	0.13	1.19	168	44
D522_R03	288	0.19	165	170	0.13	0.35	20	201
D522_R04	315	0.21	161	183	0.13	0.07	13	97
D522_R05	243	0.21	163	177	0.13	0.66	31	169
D522_R08	252	0.23	163	182	0.13	0.56	27	192
D522_R09	162	0.21	160	171	0.13	1.13	185	35
D522_R12	282	0.21	171	181	0.13	0.40	19	261
D522_R13	133	0.22	162	181	0.13	1.04	93	32
D522_R14	181	0.18	157	167	0.12	1.02	71	93
D522_R15	180	0.19	153	182	0.13	0.99	142	20
D522_R16	151	0.21	154	187	0.13	1.06	61	81
D522_SB08	158	0.21	159	179	0.13	1.13	59	85
R1467_R01	165	0.24	178	197	0.14	0.95	57	102
R1467_R02	188	0.19	164	182	0.13	0.86	39	152
R1467_R04	243	0.20	146	164	0.12	0.60	26	272
R1467_R05	196	0.24	164	183	0.13	0.95	44	79
R1467_R08	175	0.22	127	125	0.10	1.07	56	75
R1469_R01	183	0.21	165	187	0.13	0.93	44	117
R1469_R02	217	0.18	163	176	0.13	0.61	27	230
R1469_R03	139	0.21	167	182	0.13	1.27	56	80
R1469_R04	147	0.19	164	177	0.13	0.97	67	80

Table S.3.2 (cont.)

Sample	CO_2	H_2O	F	Cl	S	Vesicularity	Rmax	Nv
	ppm	(wt.%)	ppm	ppm	(wt.%)	(%)	(μm)	(mm^{-3})
R1469_R05	190	0.19	163	174	0.13	0.88	57	115
R1470_S05	239	0.21	174	180	0.13	1.06	66	78
R1472_R01	297	0.21	162	182	0.13	0.17	15	172
R1472_R02	199	0.25	167	191	0.13	0.38	18	308
R1472_R03	262	0.23	165	178	0.13	0.38	30	135
R1472_R04	119	0.20	159	175	0.13	1.34	84	56
R1472_R05	189	0.20	146	165	0.12	0.93	35	296
R1472_R06	245	0.19	155	162	0.12	0.68	32	177
R1472_R07	202	0.17	136	147	0.11	0.83	47	120
R1473_R02	142	0.22	125	119	0.10	1.19	218	100

S.3.3 Helium ratios and concentrations

Table S.3.3 Helium ratios and concentrations

Sample	$^3He/^4He$ vesicles	$^3He/^4He$ glass	^4He vesicles	^4He glass	Total ^4He
	(R/Ra)	(R/Ra)	(10^{-5} cc STP/g)	(10^{-5} cc STP/g)	(10^{-5} cc STP/g)
AX13_RC12	8.386	8.155	0.638	0.329	0.967
AX13_RC15	8.388	8.247	0.364	0.777	1.141
AX13_RC16	8.374	8.277	0.605	0.453	1.058
AX13_RC22	8.200	8.171	0.620	0.342	0.962
R1472_R03	8.145	8.165	0.387	0.595	0.982
AX13_RC13	8.0494	8.2139	0.580	0.474	1.055

S.3.4 Vesicle size distributions and volume distributions for each sample

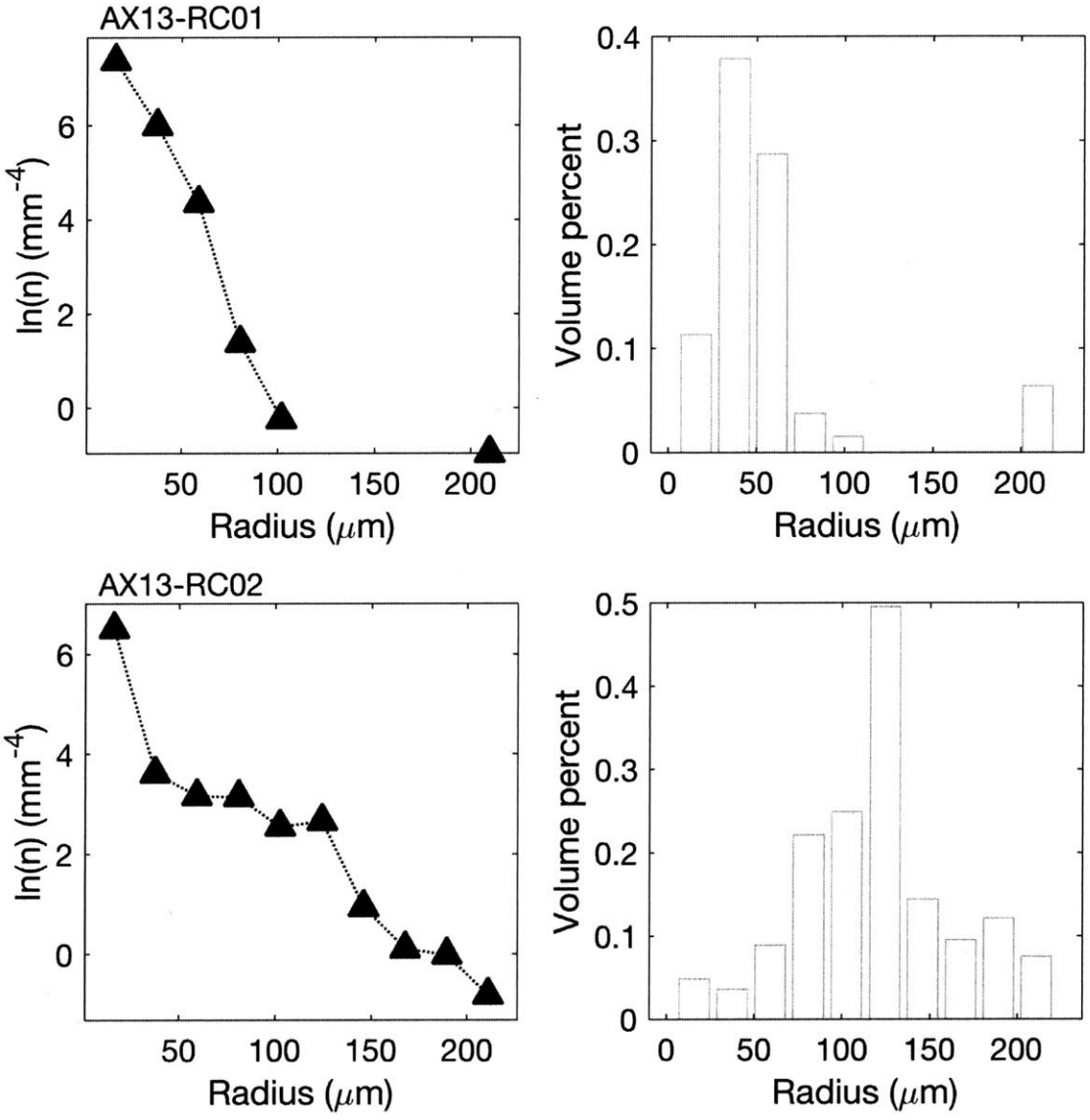

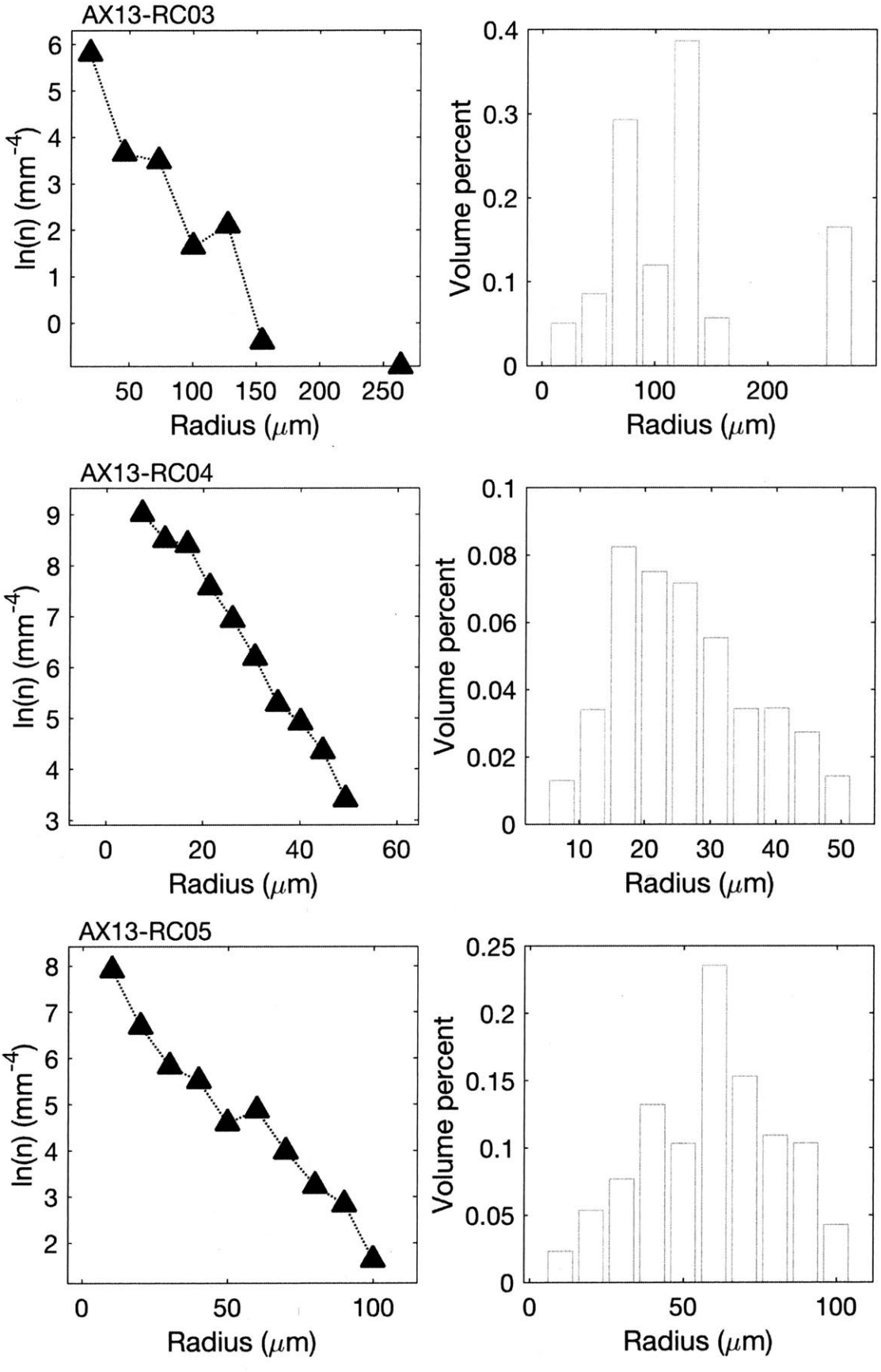
AX13-RC03
ln(n) (mm^{-4})
Radius (μm)
Volume percent
Radius (μm)
AX13-RC04
ln(n) (mm^{-4})
Radius (μm)
Volume percent
Radius (μm)
AX13-RC05
ln(n) (mm^{-4})
Radius (μm)
Volume percent
Radius (μm)

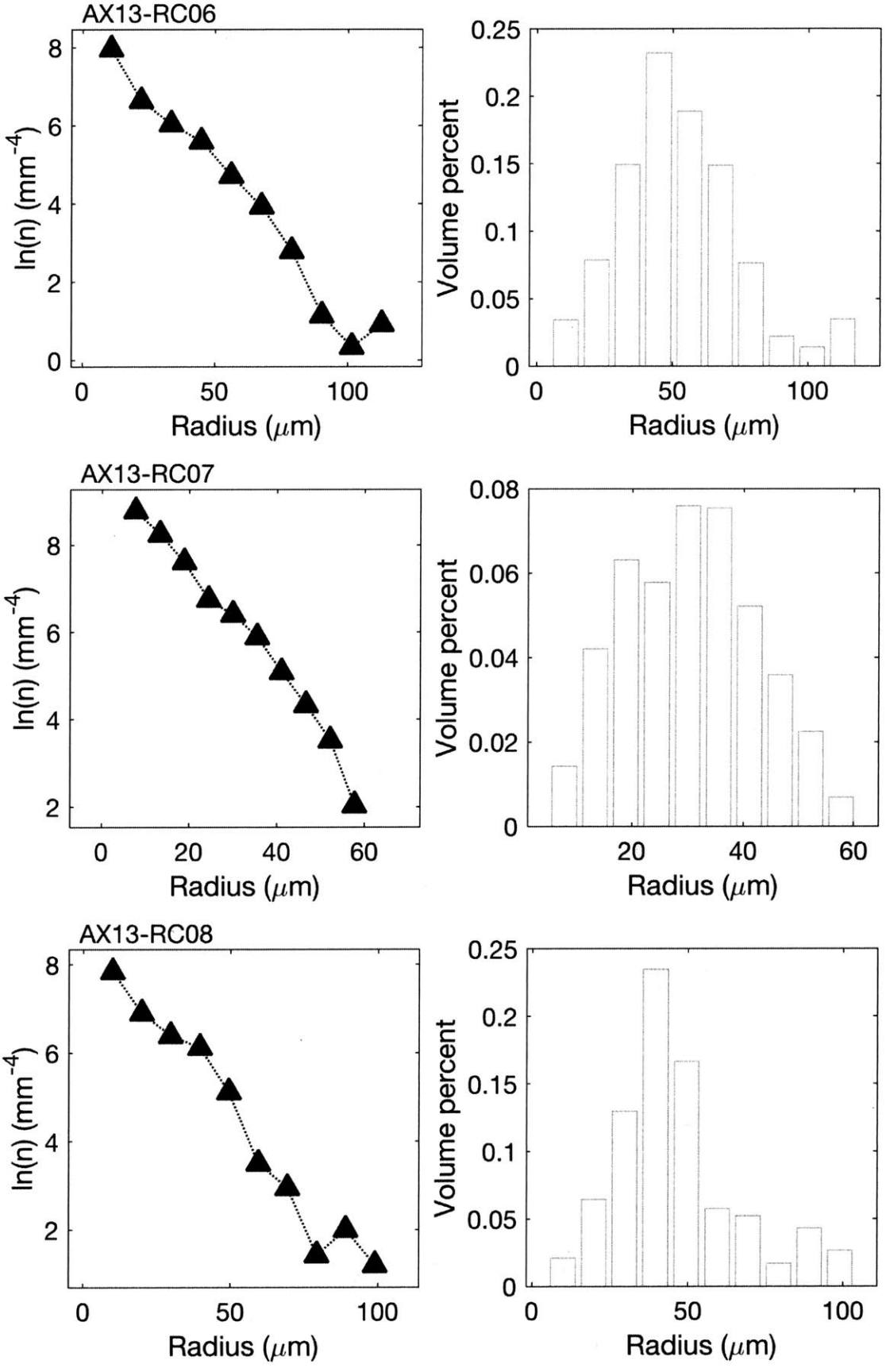
AX13-RC06
ln(n) (mm^{-4})
Radius (μm)
Volume percent
Radius (μm)
AX13-RC07
ln(n) (mm^{-4})
Radius (μm)
Volume percent
Radius (μm)
AX13-RC08
ln(n) (mm^{-4})
Radius (μm)
Volume percent
Radius (μm)

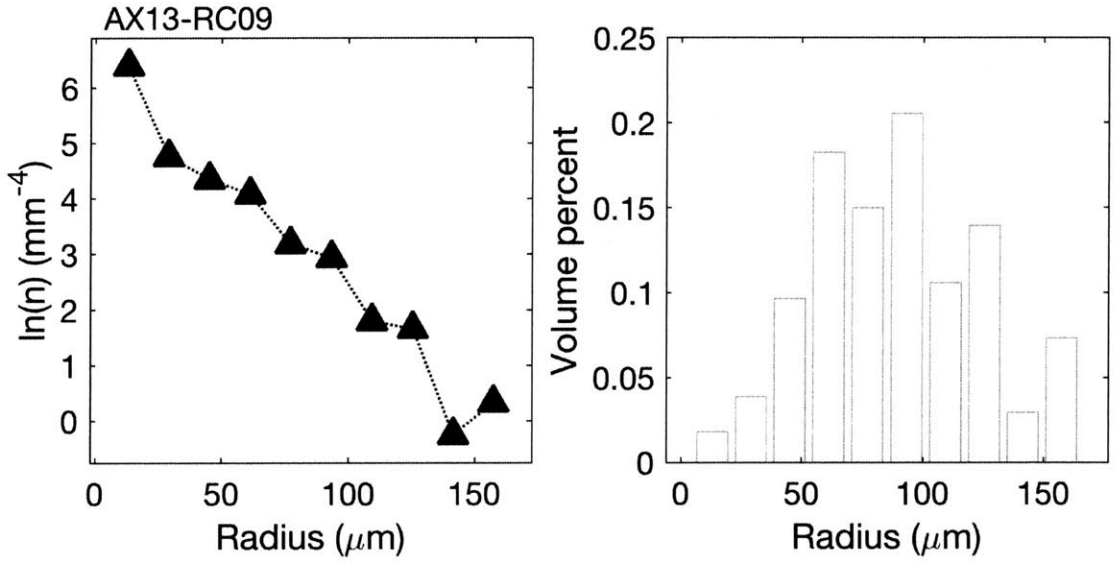
AX13-RC09
ln(n) (mm^{-4})
Radius (μm)
Volume percent
Radius (μm)

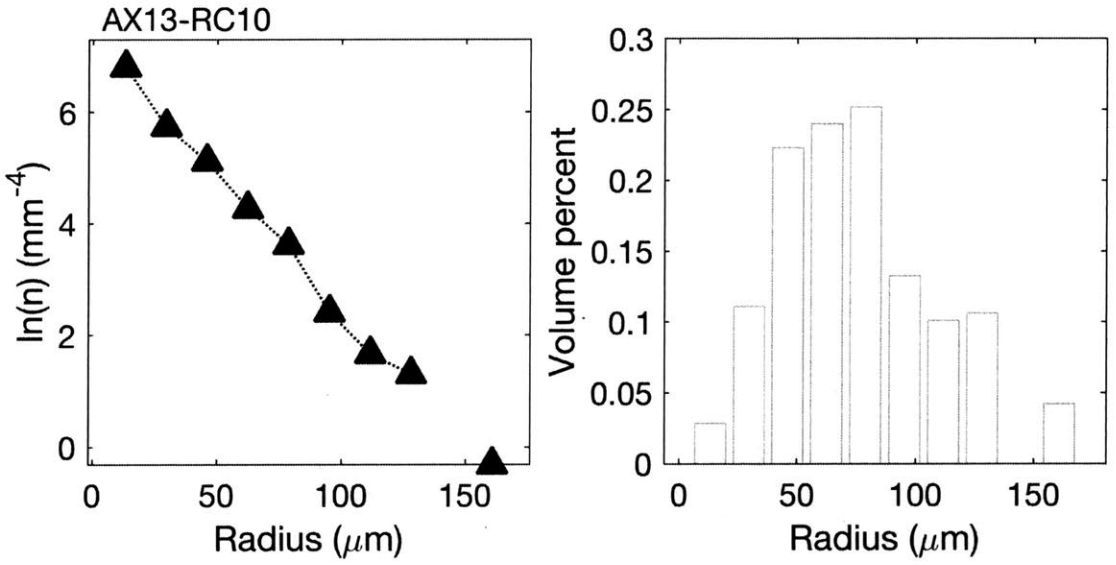
AX13-RC10
ln(n) (mm^{-4})
Radius (μm)
Volume percent
Radius (μm)

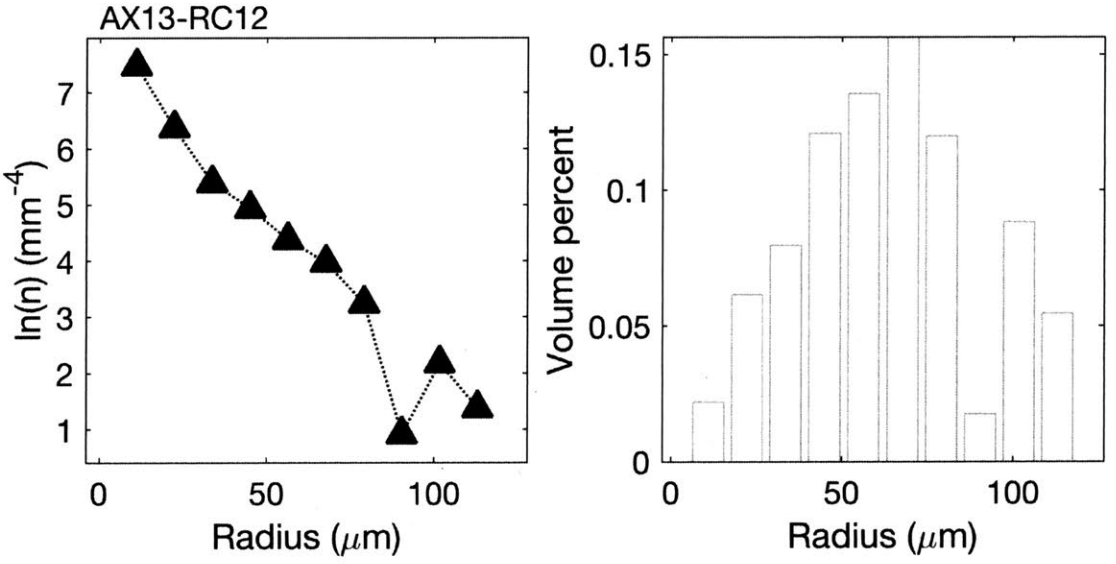
AX13-RC12
ln(n) (mm^{-4})
Radius (μm)
Volume percent
Radius (μm)

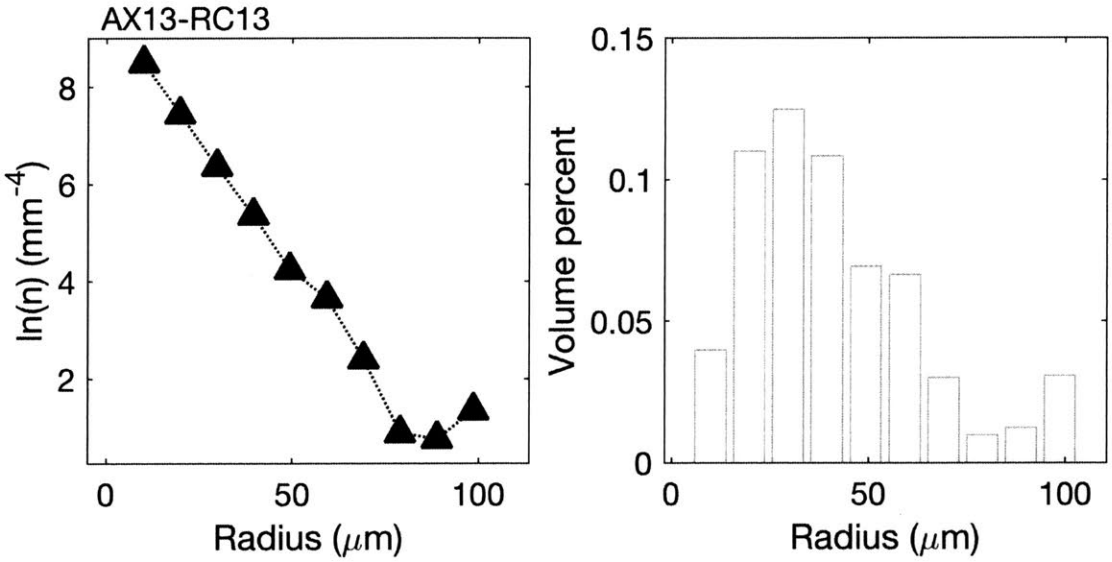
AX13-RC13
ln(n) (mm^{-4})
Radius (μm)
Volume percent
Radius (μm)

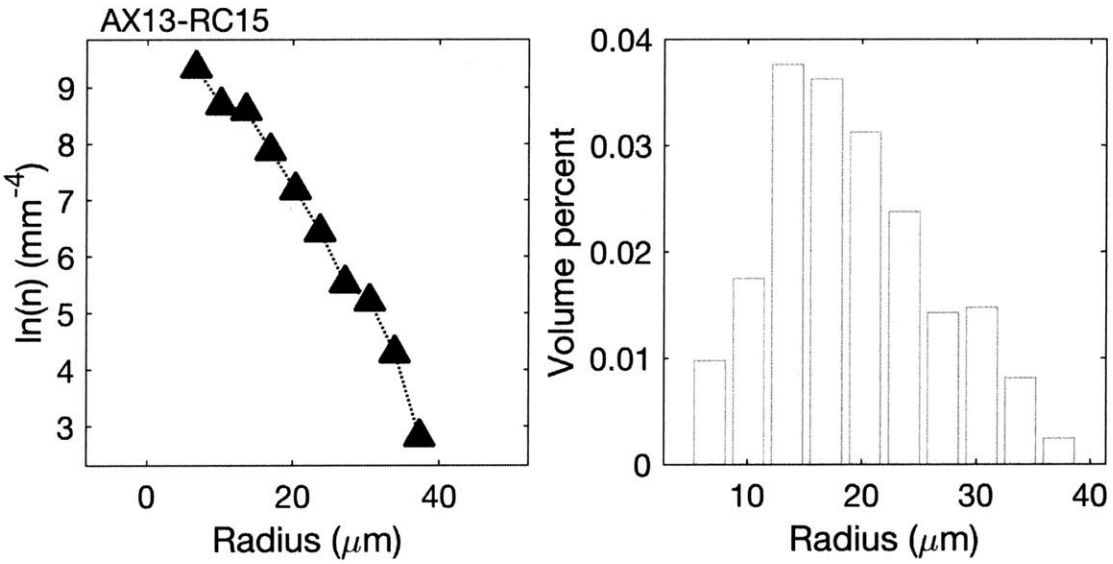
AX13-RC15
ln(n) (mm^{-4})
Radius (μm)
Volume percent
Radius (μm)

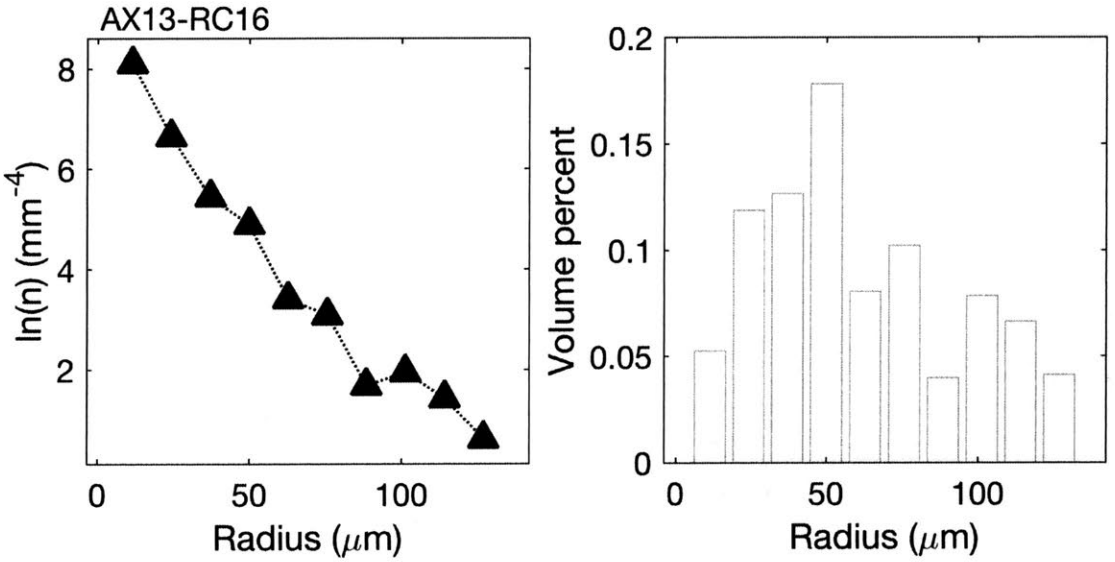
AX13-RC16
ln(n) (mm^{-4})
Radius (μm)
Volume percent
Radius (μm)

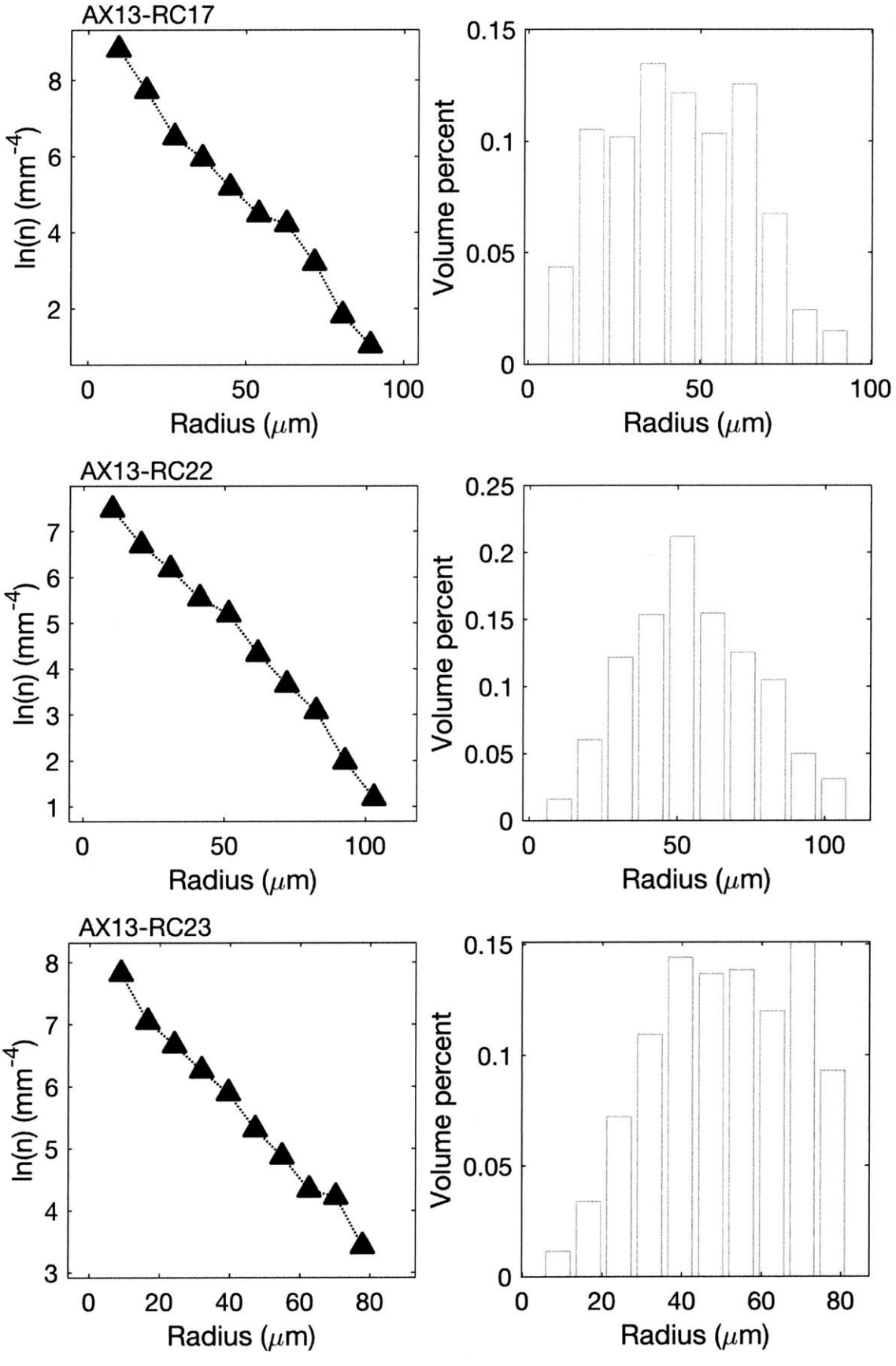
AX13-RC17
ln(n) (mm^{-4})
Radius (μm)
Volume percent
Radius (μm)
AX13-RC22
ln(n) (mm^{-4})
Radius (μm)
Volume percent
Radius (μm)
AX13-RC23
ln(n) (mm^{-4})
Radius (μm)
Volume percent
Radius (μm)

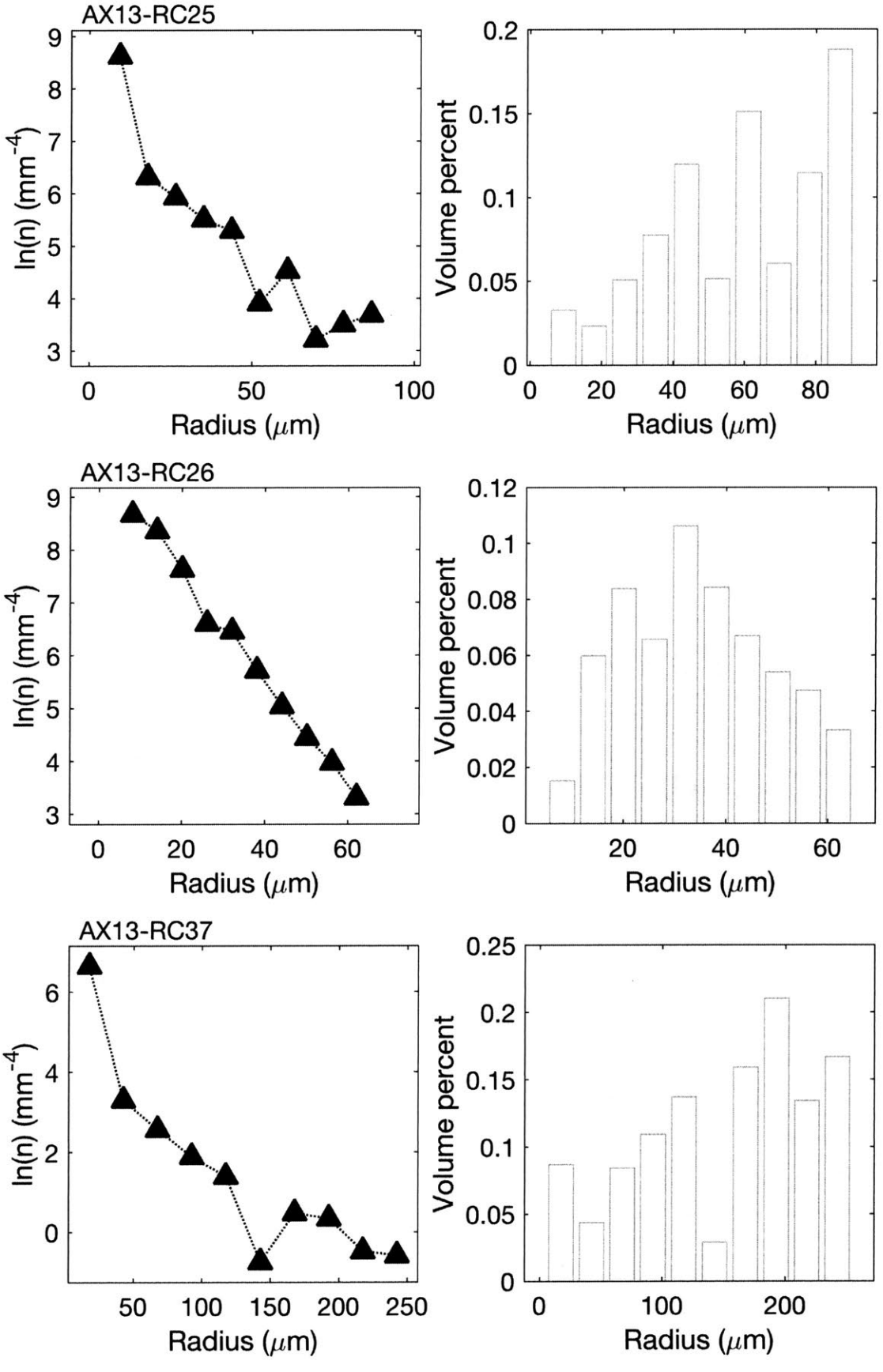
AX13-RC25
ln(n) (mm^{-4})
Radius (μm)
Volume percent
Radius (μm)
AX13-RC26
ln(n) (mm^{-4})
Radius (μm)
Volume percent
Radius (μm)
AX13-RC37
ln(n) (mm^{-4})
Radius (μm)
Volume percent
Radius (μm)

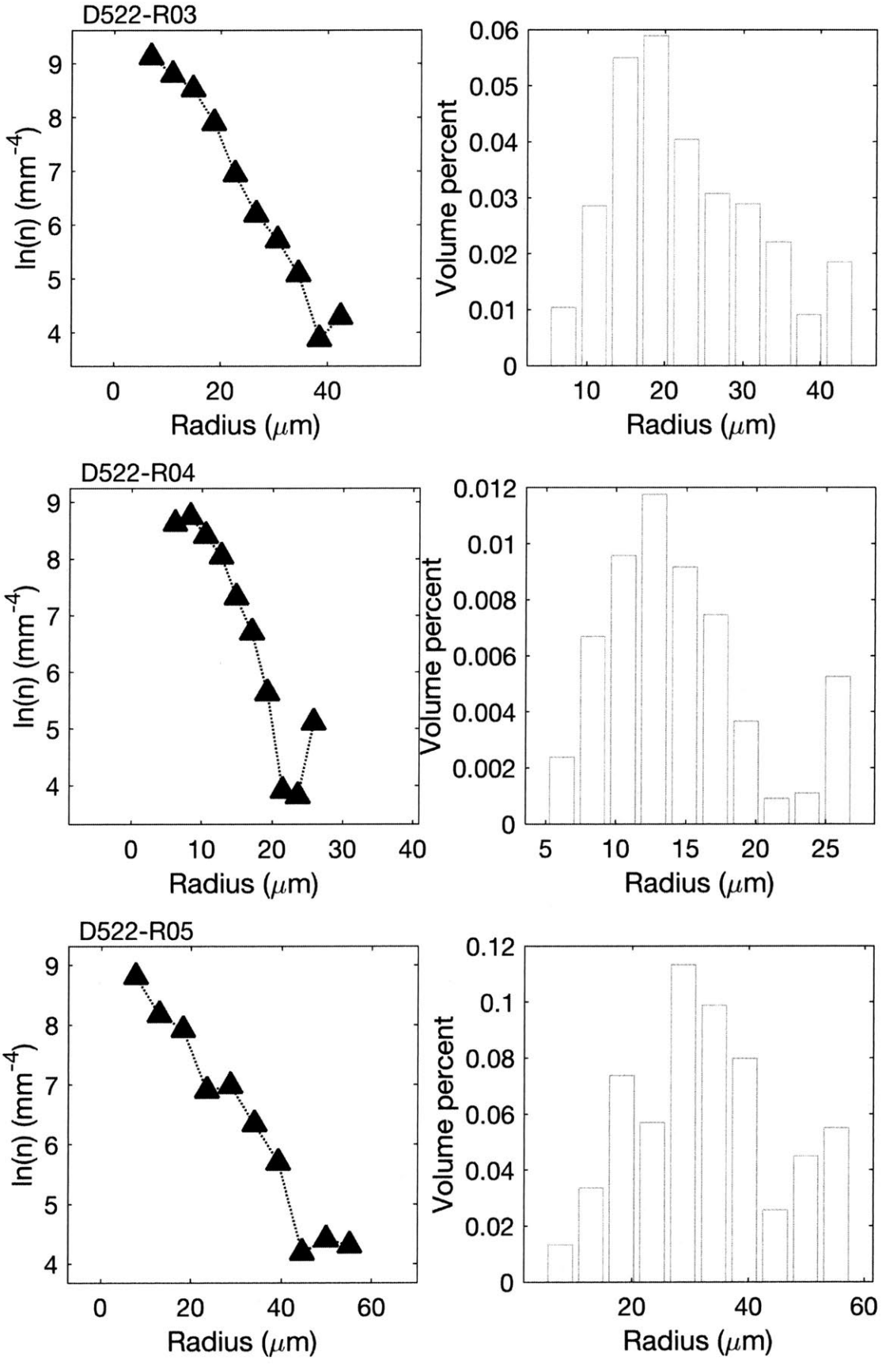
D522-R03
ln(n) (mm^{-4})
Radius (μm)
Volume percent
Radius (μm)
D522-R04
ln(n) (mm^{-4})
Radius (μm)
Volume percent
Radius (μm)
D522-R05
ln(n) (mm^{-4})
Radius (μm)
Volume percent
Radius (μm)

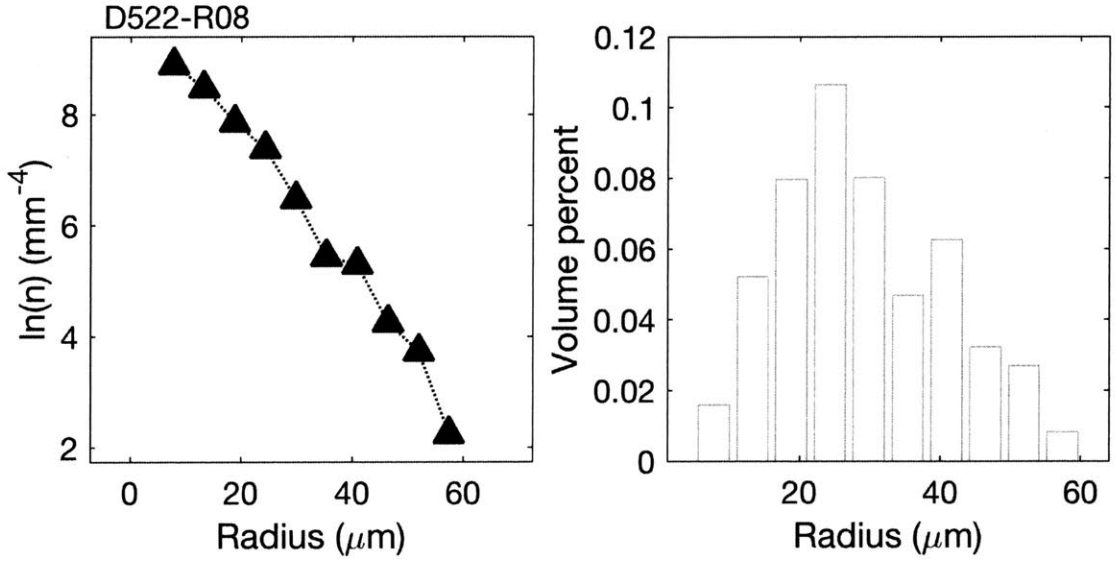
D522-R08
ln(n) (mm^{-4})
Radius (μm)
Volume percent
Radius (μm)

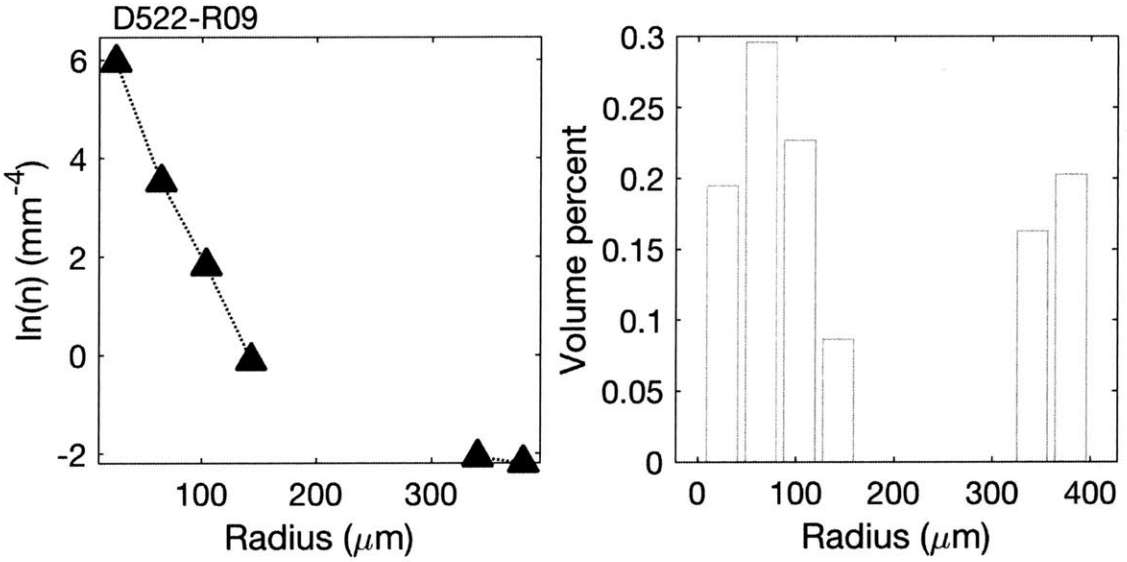
D522-R09
ln(n) (mm^{-4})
Radius (μm)
Volume percent
Radius (μm)

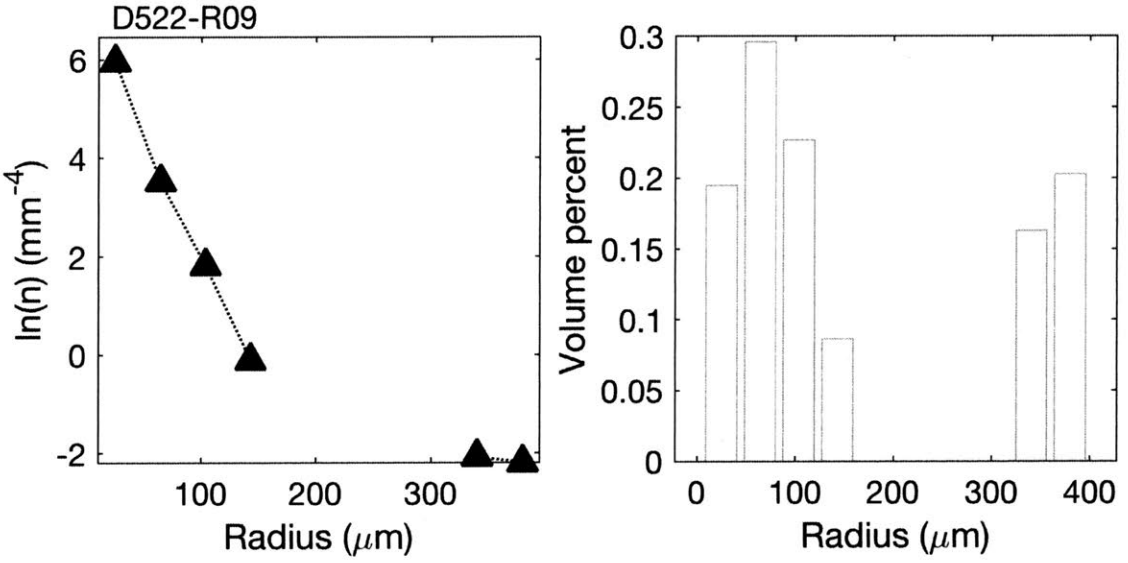
D522-R09
ln(n) (mm^{-4})
Radius (μm)
Volume percent
Radius (μm)

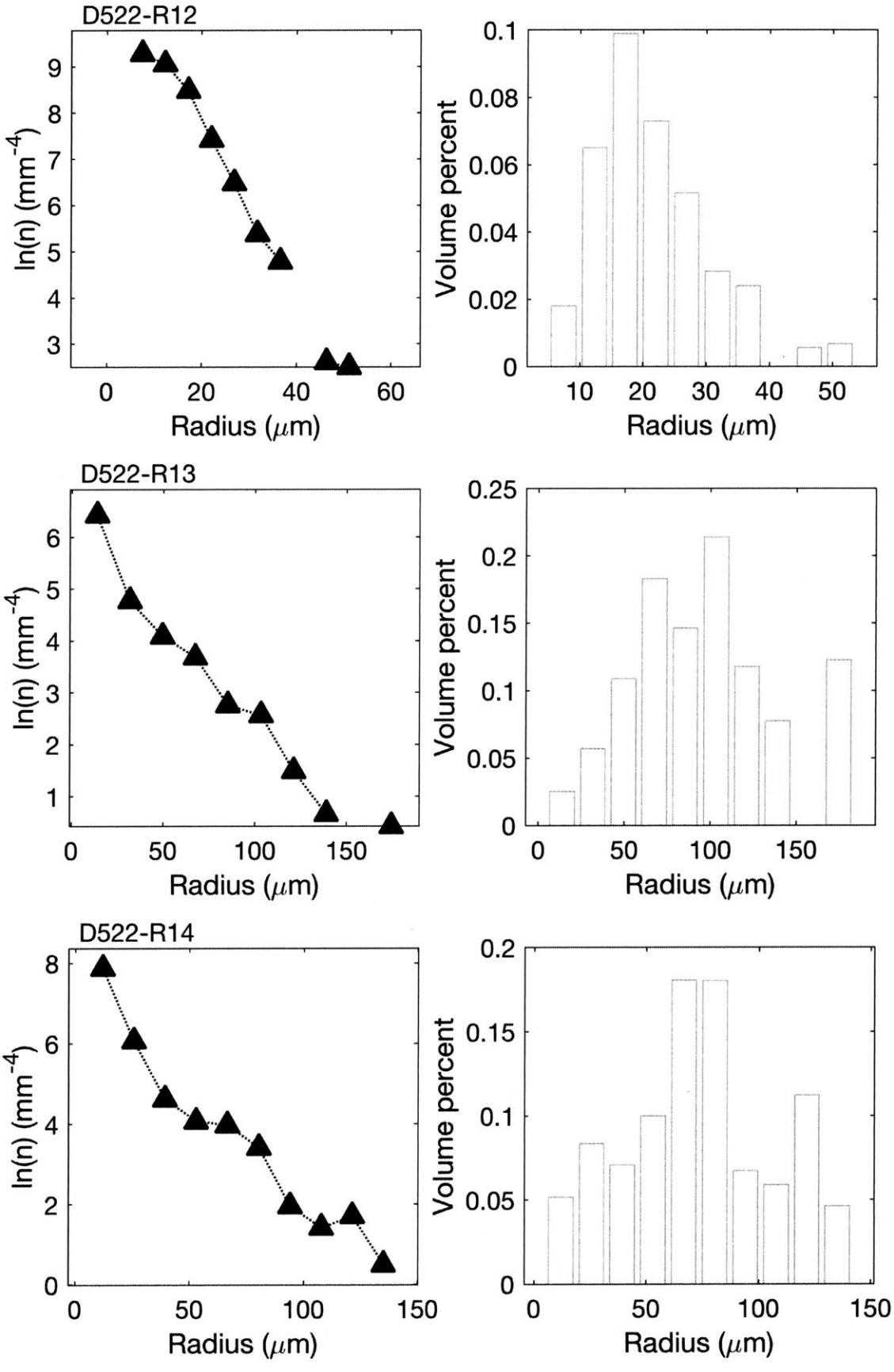
D522-R12
ln(n) (mm^{-4})
Radius (μm)
Volume percent
Radius (μm)
D522-R13
ln(n) (mm^{-4})
Radius (μm)
Volume percent
Radius (μm)
D522-R14
ln(n) (mm^{-4})
Radius (μm)
Volume percent
Radius (μm)

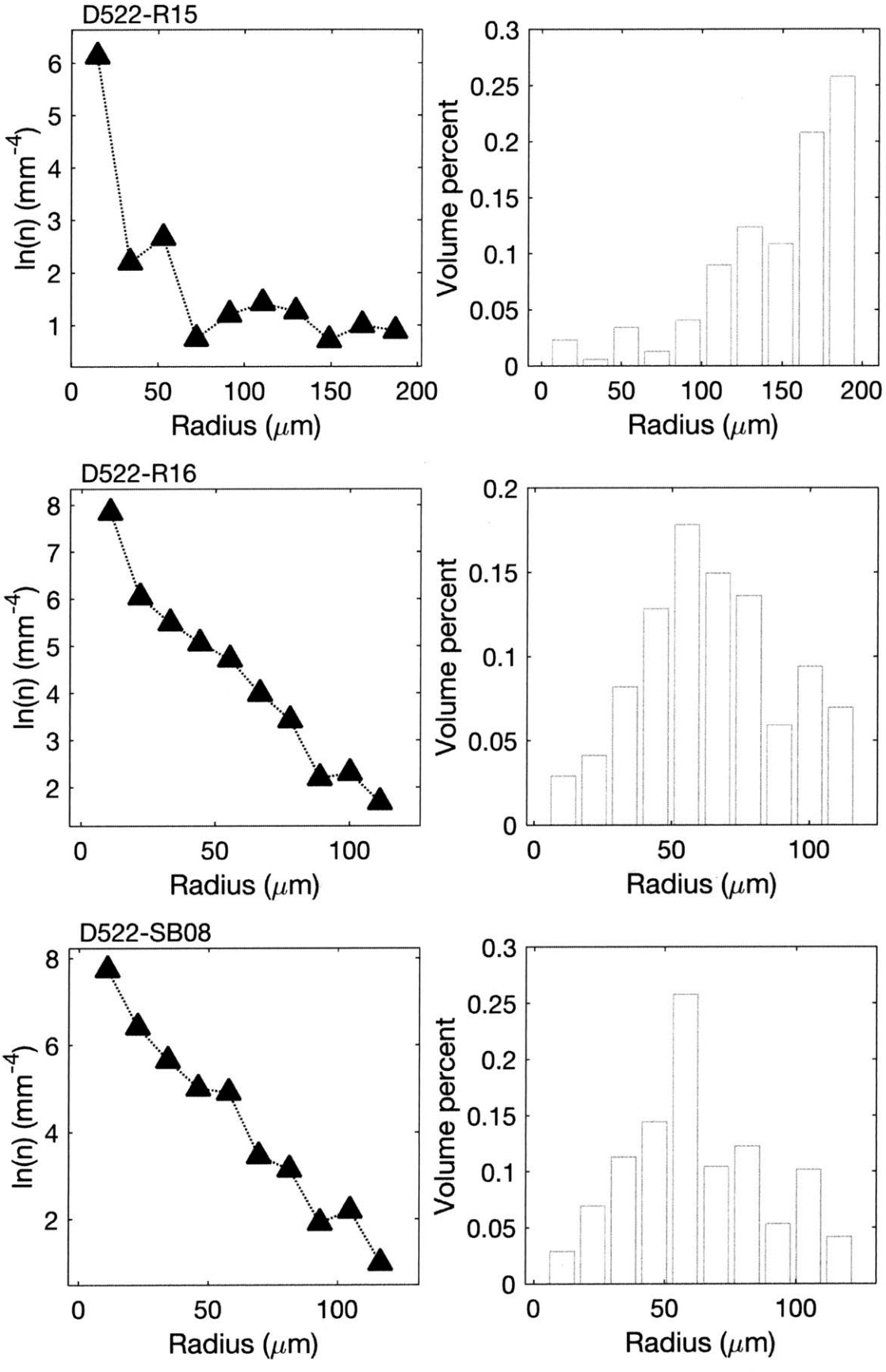
D522-R15
ln(n) (mm^{-4})
Radius (μm)
Volume percent
Radius (μm)
D522-R16
ln(n) (mm^{-4})
Radius (μm)
Volume percent
Radius (μm)
D522-SB08
ln(n) (mm^{-4})
Radius (μm)
Volume percent
Radius (μm)

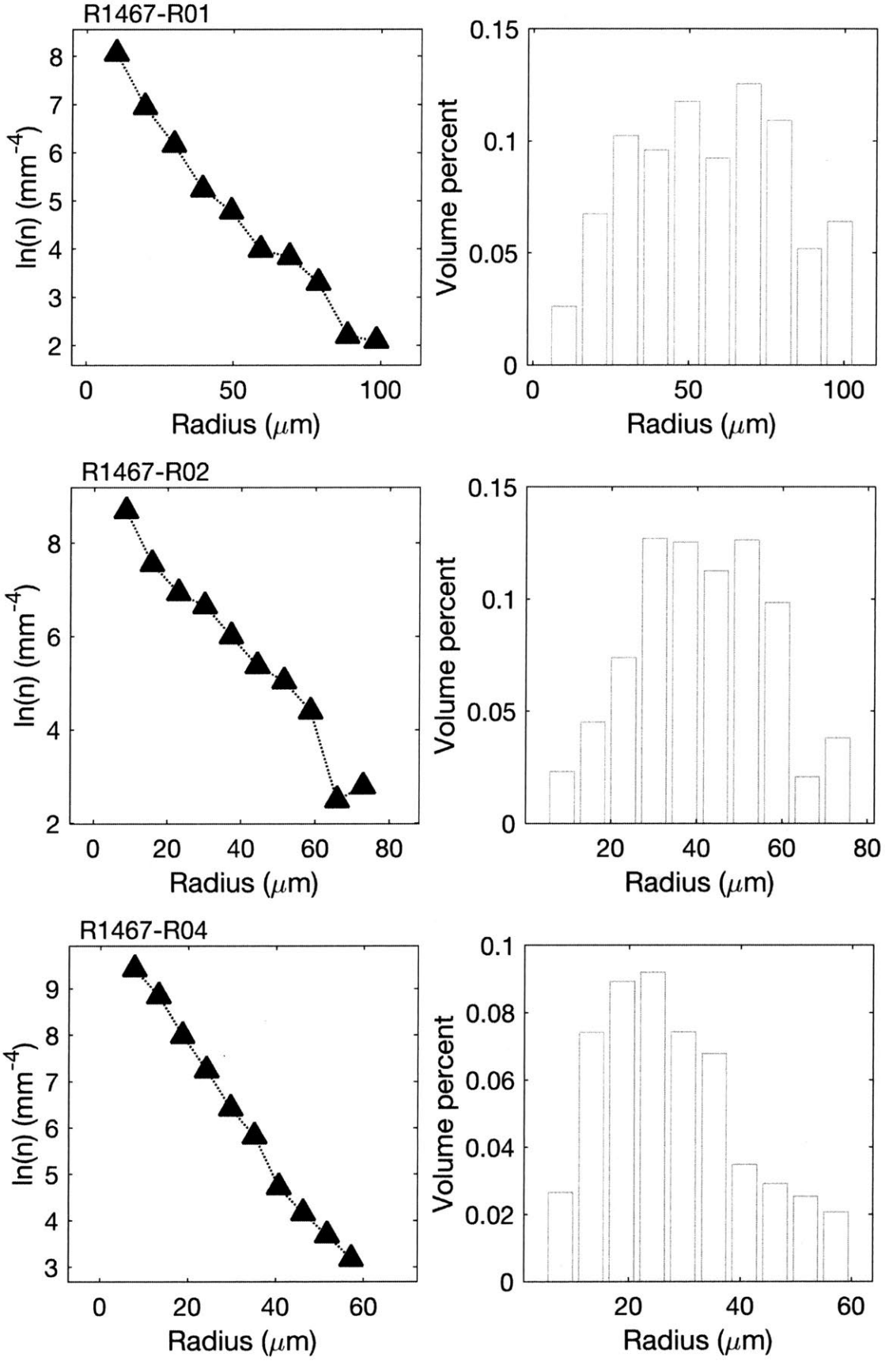
R1467-R01
ln(n) (mm^{-4})
Radius (μm)
Volume percent
R1467-R02
R1467-R04

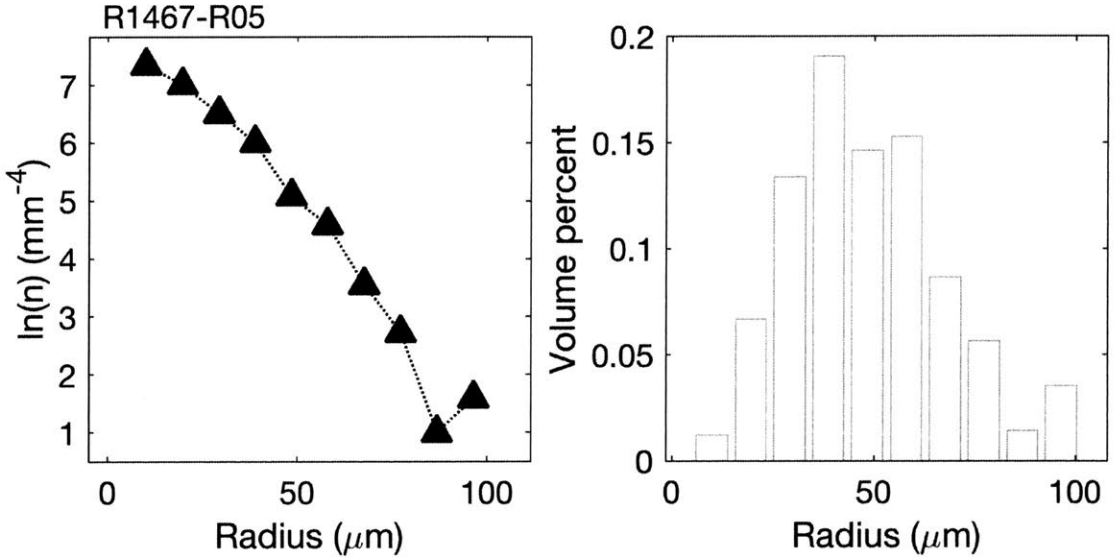
R1467-R05
ln(n) (mm^{-4})
Radius (μm)
Volume percent
Radius (μm)

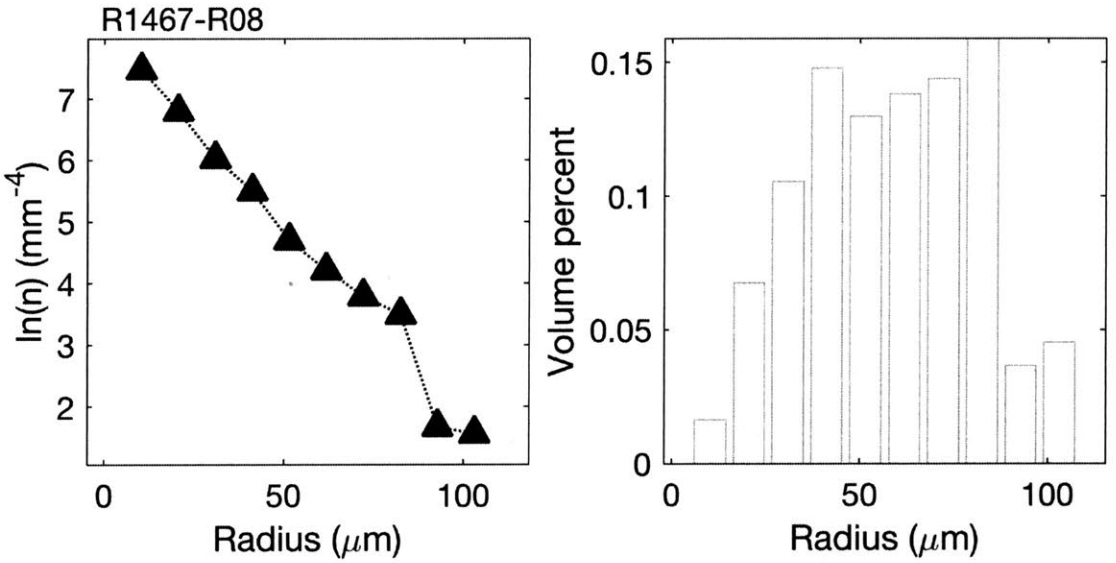
R1467-R08
ln(n) (mm^{-4})
Radius (μm)
Volume percent
Radius (μm)

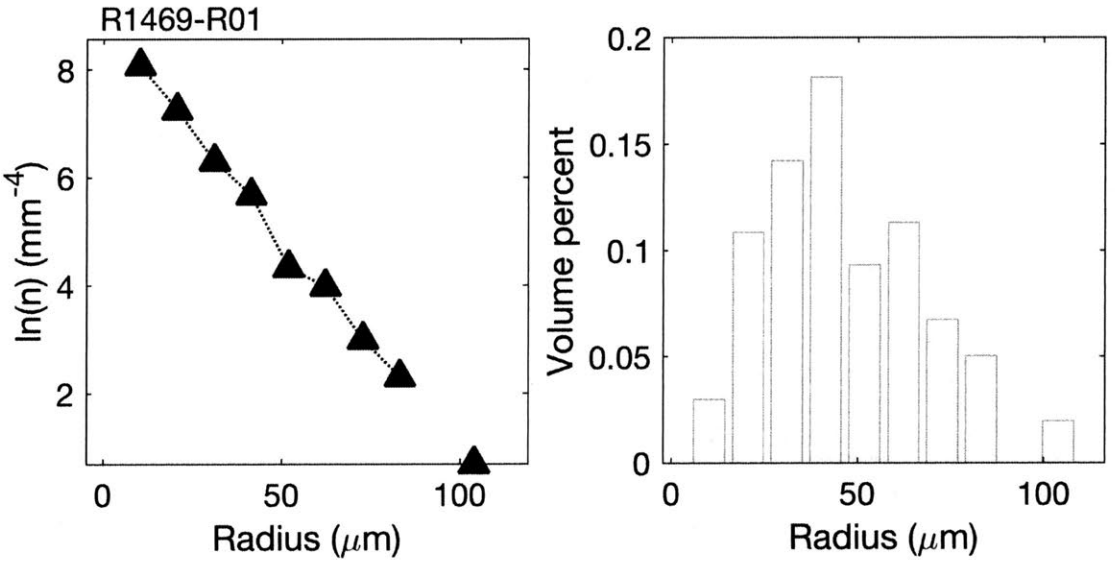
R1469-R01
ln(n) (mm^{-4})
Radius (μm)
Volume percent
Radius (μm)

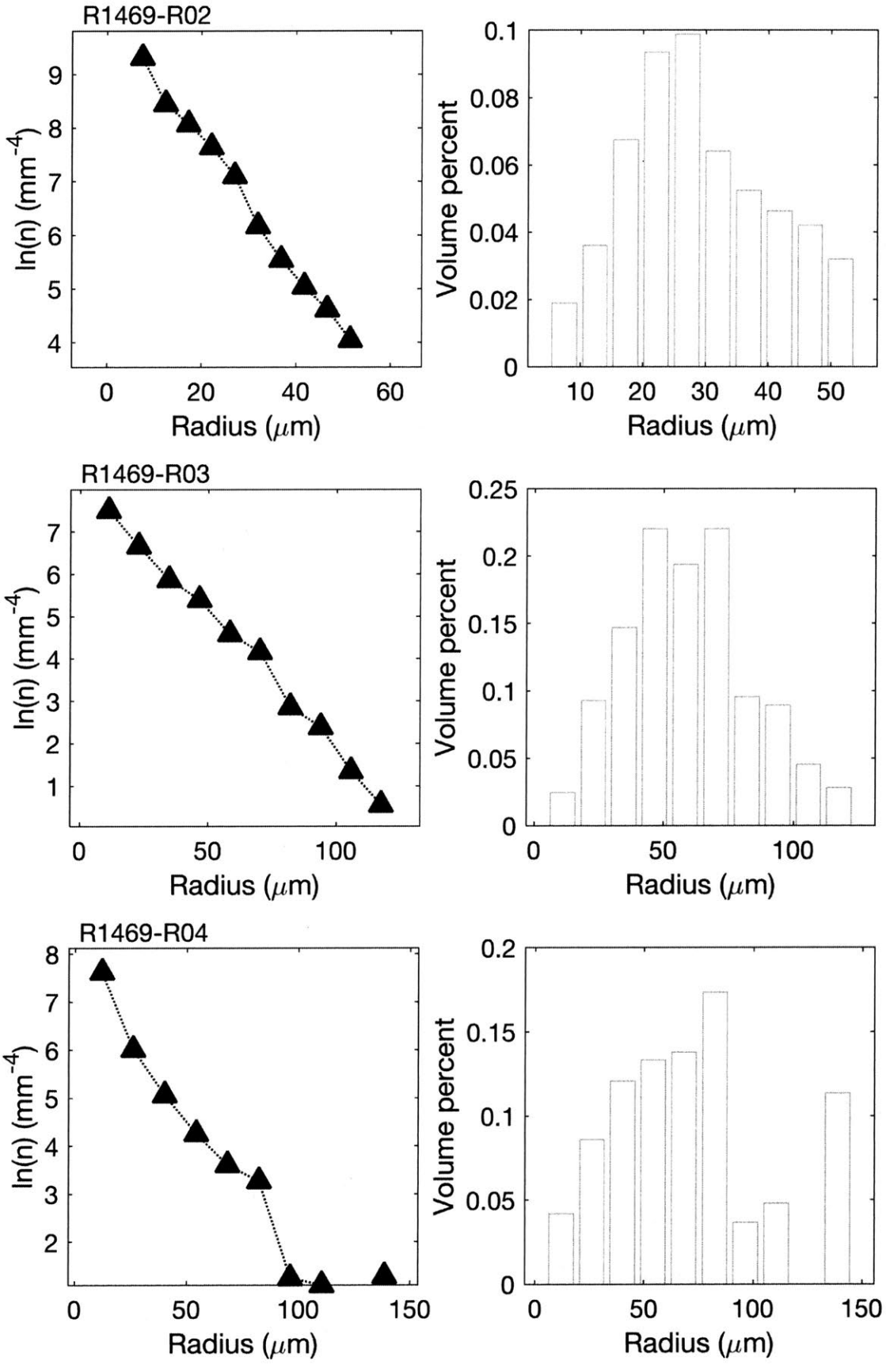
R1469-R02
ln(n) (mm^{-4})
Radius (μm)
Volume percent
Radius (μm)
R1469-R03
ln(n) (mm^{-4})
Radius (μm)
Volume percent
Radius (μm)
R1469-R04
ln(n) (mm^{-4})
Radius (μm)
Volume percent
Radius (μm)

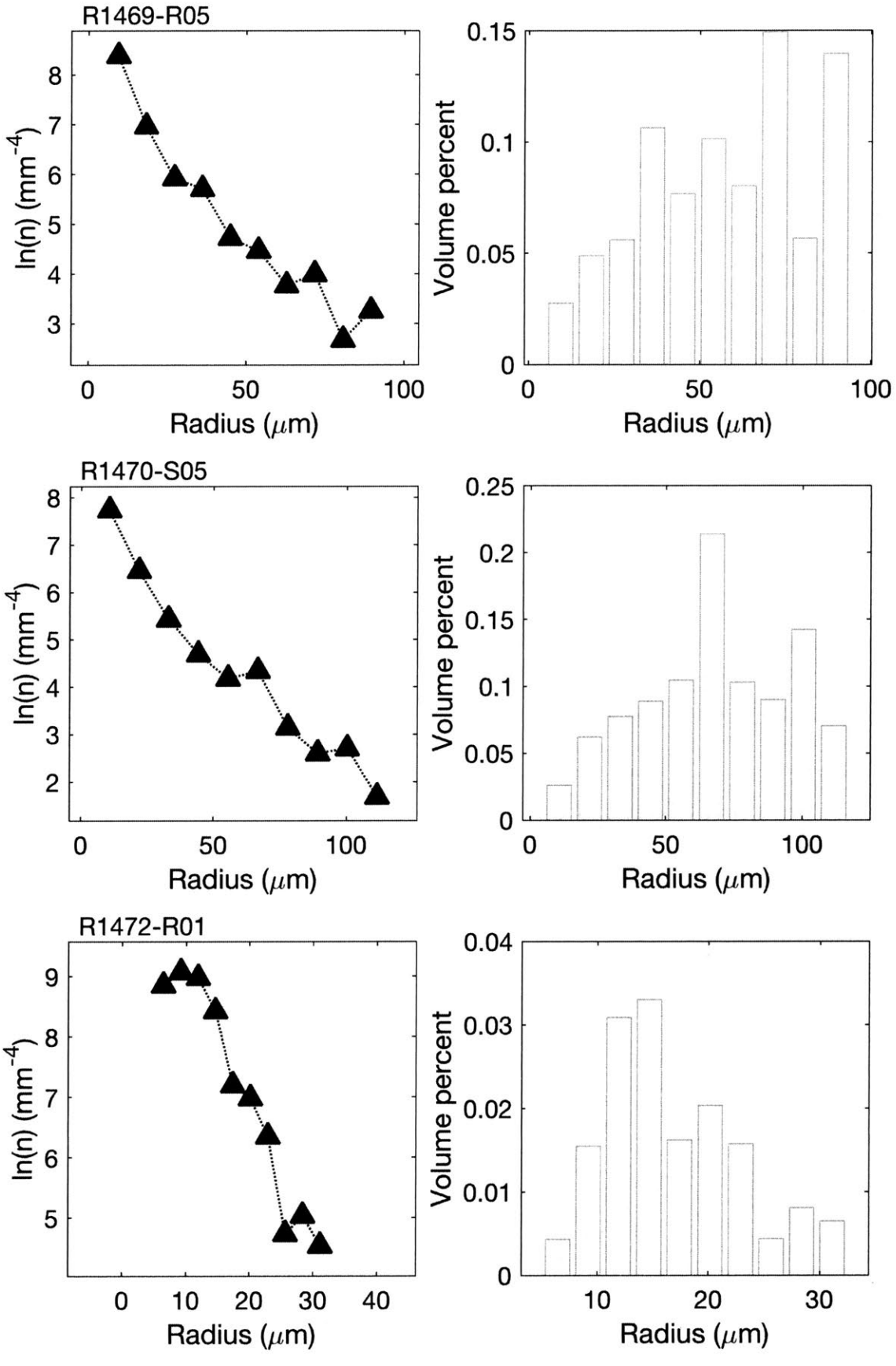
R1469-R05
ln(n) (mm^{-4})
Radius (μm)
Volume percent
R1470-S05
ln(n) (mm^{-4})
Radius (μm)
Volume percent
R1472-R01
ln(n) (mm^{-4})
Radius (μm)
Volume percent

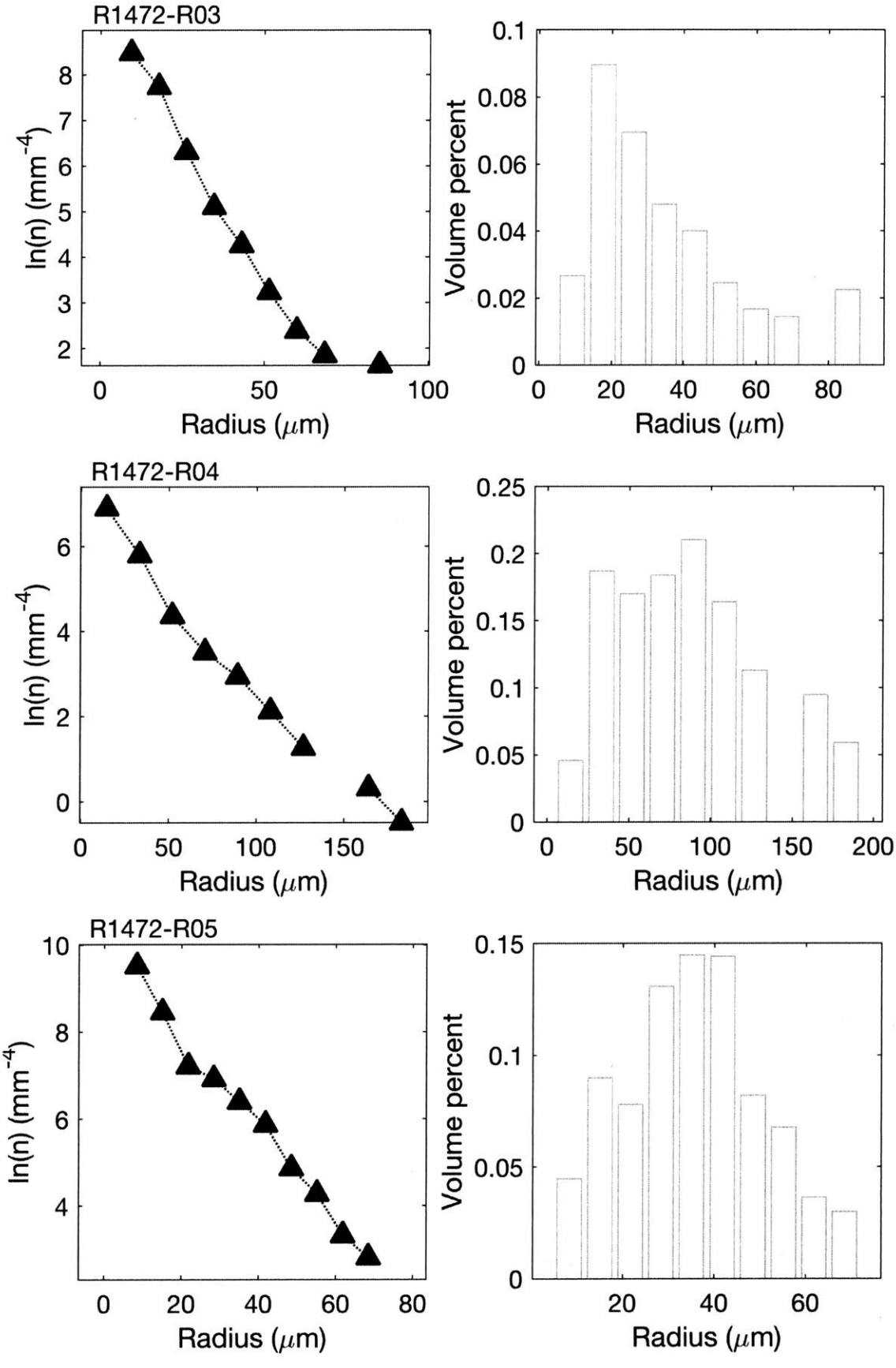
R1472-R03
ln(n) (mm^{-4})
Radius (μm)
Volume percent
Radius (μm)
R1472-R04
ln(n) (mm^{-4})
Radius (μm)
Volume percent
Radius (μm)
R1472-R05
ln(n) (mm^{-4})
Radius (μm)
Volume percent
Radius (μm)

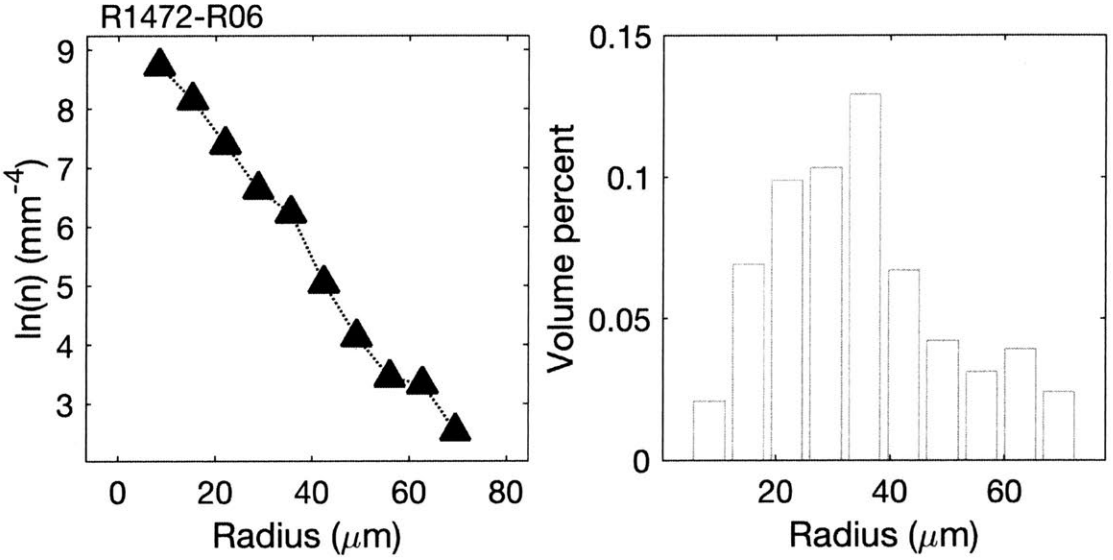
R1472-R06
ln(n) (mm^{-4})
Radius (μm)
Volume percent
Radius (μm)

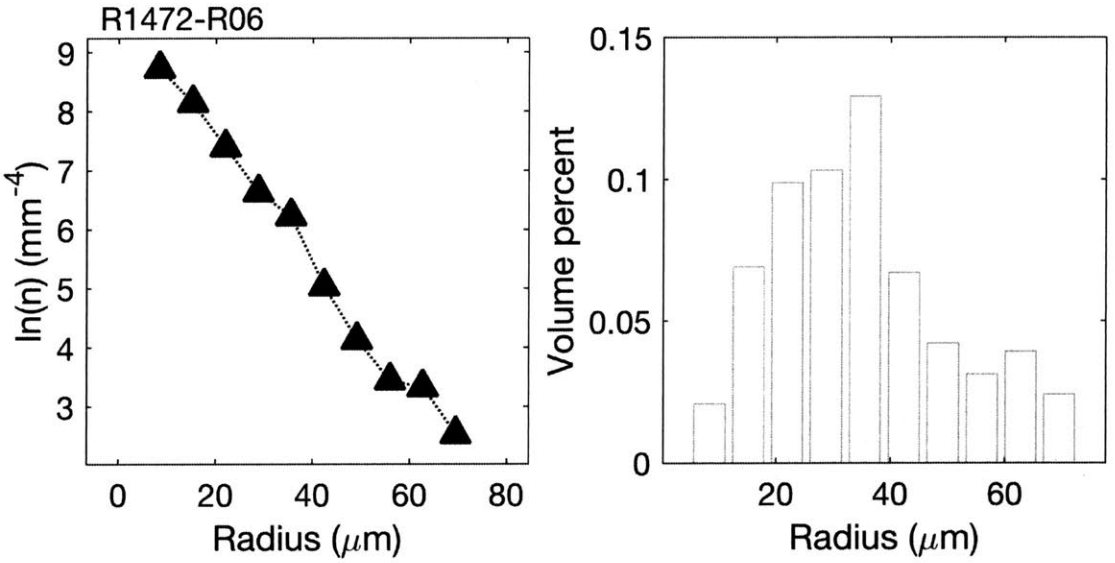
R1472-R06
ln(n) (mm^{-4})
Radius (μm)
Volume percent
Radius (μm)

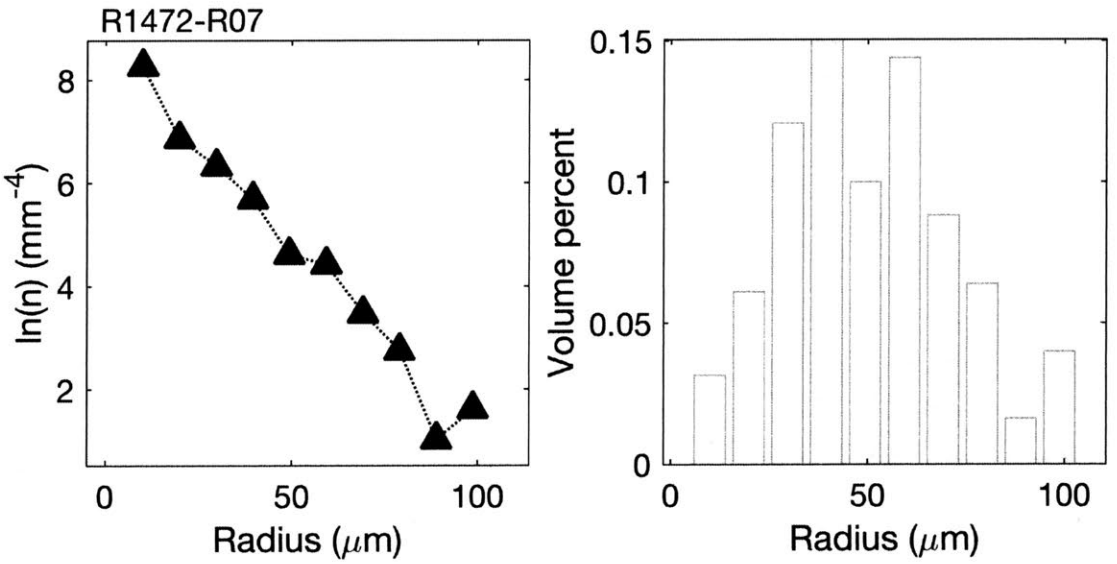
R1472-R07
ln(n) (mm^{-4})
Radius (μm)
Volume percent
Radius (μm)

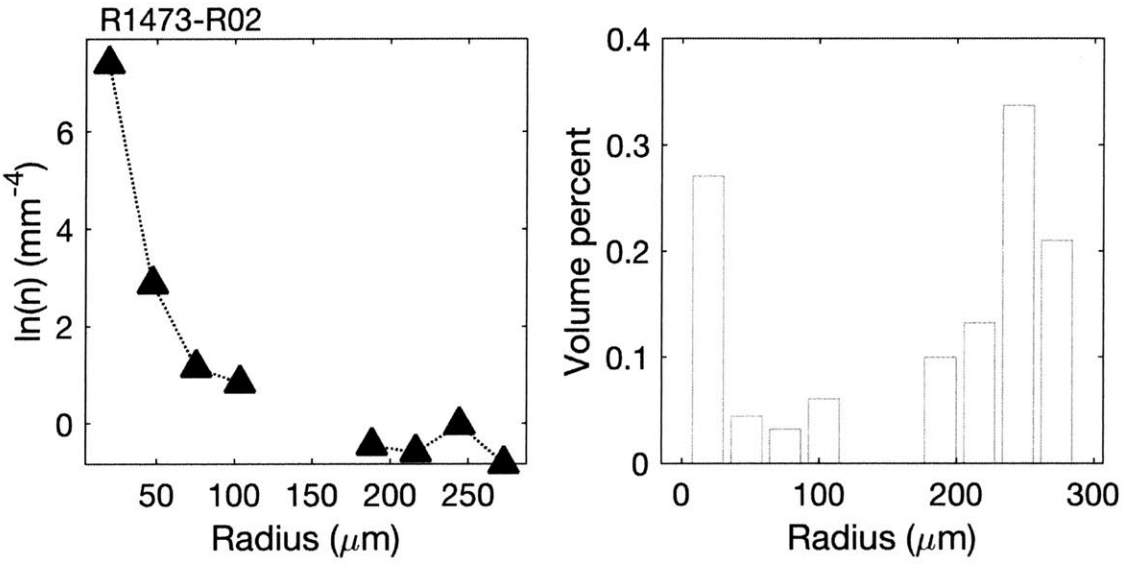
R1473-R02
ln(n) (mm^{-4})
6
4
2
0
50
100
150
200
250
Radius (μm)
Volume percent
0.4
0.3
0.2
0.1
0
0
100
200
300
Radius (μm)

S.4 Supplementary material accompanying Chapter 4

Table S.4.1 Sample locations and major and trace element concentrations.

Sample	Longitude	Latitude	Depth	SiO2	TiO2	Al2O3	FeO	MnO	MgO
	(deg)	(deg)	(m)	(wt. %)	(wt. %)	(wt. %)	(wt. %)	(wt. %)	(wt. %)
AL4818-001	-45.00669	13.77414	3773	49.78	1.87	14.84	9.94	0.15	7.65
AL4818-002	-45.00744	13.77425	3761	49.93	1.84	14.89	9.99	0.17	7.61
AL4818-003	-45.01077	13.77368	3672	50.52	1.83	14.95	10.01	0.19	7.30
AL4818-004	-45.01276	13.77481	3718	49.93	1.21	15.64	9.72	0.19	7.77
AL4818-005	-45.01323	13.77494	3697	49.59	1.13	15.81	9.70	0.19	7.95
AL4818-006	-45.01320	13.77489	3697	49.40	1.12	15.82	9.61	0.18	7.94
AL4818-007	-45.01419	13.77511	3623	50.05	1.22	15.69	9.61	0.16	7.89
AL4818-008	-45.01707	13.77515	3628	49.82	1.12	15.38	10.18	0.17	7.86
AL4818-009	-45.01782	13.77569	3617	50.02	1.13	15.46	10.18	0.18	7.87
AL4818-010	-45.01685	13.77616	3624	49.20	1.13	15.72	9.65	0.17	7.88
AL4818-011	-45.02543	13.77381	3687	50.33	1.56	14.89	10.44	0.19	6.52
AL4818-012	-45.02555	13.77390	3666	50.85	1.58	14.79	10.47	0.17	6.49
AL4819-014	-45.03108	13.78167	3575	50.80	1.56	14.96	10.29	0.19	6.55
AL4819-015	-45.03145	13.78093	3530	50.91	1.61	14.85	10.43	0.20	6.37
AL4819-016	-45.03213	13.77922	3560	49.64	1.47	14.93	10.28	0.19	6.67
AL4819-017	-45.03348	13.77841	3586	50.40	1.47	14.93	10.32	0.19	6.71
AL4819-018	-45.03463	13.77810	3579	50.71	1.55	14.99	10.06	0.16	6.31
AL4819-019	-45.03478	13.77781	3562	50.10	1.59	15.05	10.28	0.19	6.17
AL4819-020	-45.03571	13.77744	3579	50.49	1.62	14.92	10.29	0.17	6.08
AL4819-021	-45.03596	13.77718	3570	50.71	1.61	15.05	10.37	0.19	6.08
AL4819-022	-45.03850	13.77812	3586	50.50	1.66	14.79	10.21	0.16	6.44
AL4819-023	-45.03854	13.77812	3585	51.04	1.65	14.83	10.24	0.19	6.38
AL4819-024	-45.04049	13.77890	3511	51.28	1.67	14.79	10.20	0.16	6.39
AL4819-025	-45.04376	13.77922	3500	50.61	1.52	15.03	9.97	0.17	6.76
AL4819-026	-45.04690	13.77732	3539	50.60	1.66	14.82	10.26	0.18	6.35
AL4819-027	-45.04900	13.77628	3640	50.66	1.67	14.76	10.37	0.19	6.29
AL4819-028	-45.04900	13.77619	3640	50.33	1.67	14.88	10.47	0.19	6.14
AL4819-029	-45.04988	13.77552	3566	50.37	1.32	15.71	8.77	0.16	7.82
AL4819-030	-45.05251	13.77397	3476	50.83	1.14	15.46	9.38	0.16	8.17
AL4819-031	-45.05347	13.77393	3411	50.25	1.30	15.22	9.49	0.15	7.49
AL4819-032	-45.01347	13.76704	3852						
AL4820-033	-45.01347	13.76705	3852	49.89	1.00	15.46	10.18	0.15	8.08
AL4820-034	-45.01242	13.76689	3846	49.24	1.04	15.24	10.25	0.16	7.87
AL4820-035	-45.01085	13.76686	3753	50.15	1.86	14.89	10.01	0.15	7.44
AL4820-036	-45.01041	13.76691	3718	49.86	1.86	14.85	9.96	0.15	7.39
AL4820-037	-45.00810	13.76754	3773	50.44	1.88	14.99	9.91	0.16	6.99
AL4820-038	-45.00498	13.76847	3735	50.05	1.80	15.07	9.81	0.18	7.49
AL4820-039	-45.00506	13.76857	3724	50.06	1.81	14.90	9.89	0.15	7.46
AL4820-040	-45.00408	13.76924	3657	49.71	1.80	15.07	9.76	0.15	7.42
AL4820-041	-45.00256	13.76954	3645	49.84	1.82	15.16	9.69	0.16	7.21
AL4820-042	-45.00250	13.76956	3645	50.71	1.81	15.18	9.74	0.17	7.23
AL4820-043	-45.00076	13.76982	3619	49.88	1.81	14.88	9.83	0.16	7.35
AL4820-044	-45.00011	13.76951	3603	50.27	1.40	15.15	9.85	0.15	8.23
AL4820-045	-44.99823	13.76875	3492	50.54	1.41	15.03	9.93	0.15	8.43
AL4820-046	-44.99723	13.76883	3457	51.47	1.39	15.07	9.92	0.17	8.33
AL4820-047	-44.99818	13.77091	3583	51.05	1.37	15.15	9.79	0.17	8.33
AL4821-048	-45.01198	13.78163	3884	50.29	1.85	14.79	9.89	0.15	7.56
AL4821-049	-45.01195	13.77962	3821	49.97	1.84	14.93	9.99	0.18	7.61
AL4821-050	-45.01167	13.77635	3741	50.46	1.85	14.88	9.97	0.15	7.40
AL4821-051	-45.01143	13.77512	3711	50.22	1.84	14.89	9.95	0.15	7.40
AL4821-053	-45.01104	13.77387	3669	50.41	1.85	14.91	10.01	0.15	7.38
AL4821-054	-45.01102	13.77385	3669	50.55	1.84	14.93	10.01	0.18	7.37
AL4821-055	-45.01042	13.77357	3666	50.17	1.87	14.88	10.02	0.15	7.42
AL4821-056	-45.01041	13.77363	3667	50.29	1.84	14.91	9.97	0.16	7.37
AL4821-057	-45.00905	13.77377	3684	50.12	1.82	14.97	10.03	0.18	7.31
AL4821-058	-45.00908	13.77378	3684	50.60	1.85	14.88	9.97	0.16	7.32
AL4821-059	-45.00897	13.77101	3706	50.01	1.82	14.94	10.00	0.18	7.42

Table S.4.1 (cont.)

Sample	CaO	Na2O	K2O	P2O5	Total Majors	Li	Li (stdev)	Sc	Sc (stdev)
	(wt. %)	(wt. %)	(wt. %)	(wt. %)	(wt. %)	(ppm)	(ppm)	(ppm)	(ppm)
AL4818-001	10.84	2.85	0.60	0.32	98.84	6.16	0.357	34.35	1.637
AL4818-002	10.71	2.70	0.60	0.35	98.79	6.33	0.297	34.98	1.296
AL4818-003	10.78	2.73	0.61	0.34	99.26	6.32	0.404	35.93	2.078
AL4818-004	11.79	2.32	0.30	0.19	99.05	4.71	0.197	39.32	1.578
AL4818-005	12.25	2.32	0.30	0.15	99.39	4.35	0.236	41.24	1.435
AL4818-006	11.99	2.28	0.29	0.18	98.82	4.17	0.441	39.34	3.49
AL4818-007	11.99	2.36	0.29	0.15	99.40	4.66	0.376	38.26	3.387
AL4818-008	12.41	2.27	0.28	0.12	99.60	3.93	0.387	43.06	4.061
AL4818-009	12.42	2.18	0.29	0.16	99.88	3.05	0.302	44.57	2.173
AL4818-010	12.09	2.27	0.30	0.17	98.58	4.55	0.102	42.87	0.95
AL4818-011	11.30	2.70	0.55	0.25	98.74	4.70	0.441	40.26	2.539
AL4818-012	11.42	2.67	0.55	0.21	99.20	5.42	0.275	41.19	1.083
AL4819-014	11.45	2.68	0.55	0.27	99.29	5.30	0.547	39.55	3.712
AL4819-015	11.24	2.69	0.58	0.30	99.18	5.31	0.499	39.82	2.84
AL4819-016	11.44	2.58	0.52	0.23	97.96	5.12	0.46	39.93	3.639
AL4819-017	11.55	2.61	0.53	0.25	98.96	5.10	0.601	39.86	3.874
AL4819-018	11.34	2.77	0.76	0.27	98.92	5.33	0.508	36.40	2.917
AL4819-019	11.03	2.76	0.79	0.33	98.29	4.22	0.348	33.09	2.264
AL4819-020	11.19	2.85	0.81	0.27	98.69	5.43	0.399	36.16	2.811
AL4819-021	11.05	2.80	0.82	0.33	99.01	5.27	0.393	36.15	2.446
AL4819-022	11.29	2.71	0.57	0.22	98.55	5.36	0.481	36.37	2.87
AL4819-023	11.11	2.69	0.58	0.28	98.98	5.27	0.52	36.59	3.056
AL4819-024	11.21	2.74	0.57	0.23	99.25	5.29	0.345	37.81	2.222
AL4819-025	11.63	2.59	0.54	0.27	99.10	5.02	0.368	39.43	2.051
AL4819-026	11.04	2.73	0.59	0.27	98.49	5.11	0.423	39.41	2.721
AL4819-027	10.93	2.77	0.59	0.30	98.52	5.37	0.303	39.06	2.48
AL4819-028	10.81	2.77	0.60	0.28	98.14	5.19	0.507	37.00	2.902
AL4819-029	11.93	2.28	0.47	0.23	99.06	4.49	0.284	36.13	1.233
AL4819-030	11.95	2.29	0.28	0.13	99.78	4.06	0.41	40.52	3.331
AL4819-031	12.16	2.43	0.36	0.16	99.01	4.38	0.333	39.56	2.949
AL4819-032						3.53	0.414	43.57	3.665
AL4820-033	12.64	2.22	0.22	0.13	99.96	4.25	0.3	41.35	2.235
AL4820-034	12.62	2.27	0.24	0.11	99.04	3.69	0.274	44.69	2.874
AL4820-035	10.84	2.78	0.61	0.29	98.99	6.09	0.375	35.56	2.335
AL4820-036	10.70	2.77	0.61	0.29	98.44	6.12	0.463	35.58	2.026
AL4820-037	10.97	2.77	0.61	0.31	99.03	6.26	0.423	38.02	2.477
AL4820-038	11.08	2.72	0.63	0.32	99.14	6.14	0.469	37.35	2.422
AL4820-039	10.93	2.76	0.63	0.29	98.88	6.39	0.585	37.16	2.959
AL4820-040	11.09	2.79	0.62	0.28	98.69	6.20	0.45	36.25	2.687
AL4820-041	11.12	2.72	0.63	0.28	98.64	6.14	0.476	37.32	2.559
AL4820-042	11.23	2.79	0.65	0.34	99.85	6.09	0.505	36.69	2.601
AL4820-043	10.89	2.78	0.61	0.29	98.48	6.17	0.494	36.24	3.033
AL4820-044	11.23	2.51	0.25	0.17	99.22	4.46	0.271	25.41	1.103
AL4820-045	11.19	2.50	0.25	0.18	99.61	5.62	0.563	37.68	3.121
AL4820-046	11.17	2.44	0.26	0.22	100.43	5.72	0.524	37.83	3
AL4820-047	11.27	2.44	0.25	0.19	100.00	5.65	0.422	36.89	1.641
AL4821-048	10.76	2.73	0.59	0.27	98.89	6.09	0.237	35.96	1.469
AL4821-049	10.81	2.69	0.60	0.33	98.94	6.22	0.372	36.08	1.483
AL4821-050	10.88	2.73	0.60	0.30	99.22	6.41	0.441	35.96	2.088
AL4821-051	10.90	2.75	0.61	0.30	99.01	6.32	0.487	36.57	1.762
AL4821-053	10.75	2.73	0.60	0.28	99.06	6.52	0.185	36.35	1.175
AL4821-054	10.84	2.74	0.61	0.33	99.39	6.25	0.329	35.89	1.243
AL4821-055	10.87	2.80	0.59	0.30	99.06	6.46	0.407	36.53	2.131
AL4821-056	10.79	2.75	0.60	0.30	98.97	6.26	0.401	35.47	1.784
AL4821-057	10.77	2.73	0.61	0.33	98.86	6.34	0.374	36.33	1.397
AL4821-058	10.79	2.77	0.60	0.29	99.22	6.36	0.34	35.71	1.694
AL4821-059	10.89	2.70	0.61	0.32	98.90	6.31	0.301	35.73	1.43

Table S.4.1 (cont.)

Sample	V	V (stdev)	Cr	Cr (stdev)	Co	Co (stdev)	Ni	Ni (stdev)	Cu
	(ppm)	(ppm)	(ppm)	(ppm)	(ppm)	(ppm)	(ppm)	(ppm)	(ppm)
AL4818-001	250.39	12.36	244.00	12.75	41.85	2.037	116.75	6.507	71.09
AL4818-002	254.61	10.3	248.10	9.246	43.75	1.579	135.67	5.684	71.50
AL4818-003	260.15	15.06	239.83	13.48	41.66	2.493	105.70	6.592	75.53
AL4818-004	224.42	10.46	291.28	13.37	42.74	2.239	103.83	5.63	91.43
AL4818-005	219.18	7.67	308.92	10.8	44.29	1.365	106.97	4.63	98.95
AL4818-006	205.54	19.67	331.30	28.69	41.17	3.557	102.99	9.219	96.98
AL4818-007	214.01	21.89	315.76	27.42	40.94	3.557	103.87	9.246	88.68
AL4818-008	197.59	20.91	352.01	32.45	43.76	3.882	102.71	10.7	110.38
AL4818-009	212.16	12.41	282.97	20.08	45.95	2.813	101.76	5.858	124.81
AL4818-010	228.76	4.475	320.05	8.352	45.62	1.132	104.91	2.393	105.66
AL4818-011	254.20	14.28	169.43	11.46	41.88	2.547	78.25	4.685	102.26
AL4818-012	265.66	7.018	132.97	3.342	41.75	1.171	64.66	1.686	92.17
AL4819-014	247.44	25.67	168.24	15.68	39.44	3.773	70.09	6.443	87.93
AL4819-015	252.99	21.43	141.19	8.63	38.95	3.086	62.04	4.844	90.52
AL4819-016	241.24	25.13	166.12	14.61	39.78	3.446	67.86	6.797	91.10
AL4819-017	245.43	26.58	169.12	16.69	40.01	3.632	64.23	6.341	87.39
AL4819-018	239.60	21.37	148.03	12.21	37.59	3.078	53.86	4.821	75.28
AL4819-019	199.44	17.27	35.11	2.402	37.96	2.748	44.18	2.655	76.67
AL4819-020	239.91	20.48	51.19	3.687	41.22	3.021	45.29	3.645	86.99
AL4819-021	236.44	19.6	75.23	5.044	41.70	2.728	53.95	3.799	95.55
AL4819-022	241.93	20.85	132.39	10.69	37.15	2.934	50.25	4.5	75.80
AL4819-023	235.49	23.99	47.99	3.89	41.32	3.296	44.49	4.41	92.72
AL4819-024	240.21	18.9	157.40	10.46	38.82	2.592	62.57	4.533	79.62
AL4819-025	244.34	13.32	153.66	7.256	40.13	2.283	56.03	2.922	86.94
AL4819-026	245.92	19.66	153.52	10.766	40.70	2.874	60.74	4.812	84.41
AL4819-027	252.87	18.2	140.11	8.727	39.97	2.779	56.83	4.063	84.09
AL4819-028	239.79	20.14	161.91	12.46	37.64	2.764	58.49	5.023	84.22
AL4819-029	227.77	8.887	317.66	11.38	39.19	1.453	110.73	4.016	77.33
AL4819-030	199.21	20.52	388.40	31.22	42.68	3.483	104.00	9.838	114.02
AL4819-031	210.51	17.65	344.87	27.44	40.13	3.099	88.89	7.184	108.22
AL4819-032	188.16	17.7	355.77	27.12	46.58	4.198	123.57	11.36	116.47
AL4820-033	204.06	13.26	330.72	17.74	44.25	2.308	113.36	6.875	103.02
AL4820-034	194.71	14.45	353.63	20.9	44.47	2.634	99.77	6.242	119.84
AL4820-035	241.72	18.52	265.39	16.92	40.25	3.001	111.13	7.647	73.11
AL4820-036	242.48	16.64	265.47	14.38	40.79	2.601	116.13	7.137	66.11
AL4820-037	251.95	17.83	261.84	16.57	42.34	2.886	122.17	7.289	67.77
AL4820-038	252.49	19.74	273.18	19.87	42.03	2.805	127.63	8.234	71.24
AL4820-039	259.26	23.58	263.03	21.21	41.71	3.224	116.76	9.234	68.51
AL4820-040	247.39	22.13	287.49	22.63	41.65	3.167	124.39	10.03	65.28
AL4820-041	257.78	20.36	285.23	21.02	40.85	2.864	107.62	8.048	72.39
AL4820-042	249.55	22.57	287.46	21.73	41.47	3.051	117.76	9.63	70.43
AL4820-043	252.21	24.05	267.77	20.85	42.21	3.396	125.48	10.88	64.22
AL4820-044	247.95	9.919	348.27	16.12	45.49	1.947	167.52	7.562	71.63
AL4820-045	245.56	24.63	384.94	35	43.90	3.873	152.69	13.16	71.93
AL4820-046	244.47	24.54	388.12	31.56	44.60	3.79	157.89	14.39	73.63
AL4820-047	252.40	12.09	361.57	17.22	44.80	2.424	159.47	8.338	70.82
AL4821-048	252.72	10.36	247.21	10.49	41.88	1.985	117.82	4.929	64.57
AL4821-049	249.58	11.5	255.81	11.71	42.41	2.183	126.21	5.378	60.54
AL4821-050	259.70	14.67	242.78	15.16	41.96	2.65	109.41	7.251	61.52
AL4821-051	259.28	14.41	248.98	14.16	41.86	2.127	107.64	5.639	60.49
AL4821-053	259.40	9.251	245.21	9.244	42.69	1.495	117.13	3.88	59.08
AL4821-054	255.32	9.525	243.96	9.11	41.42	1.561	109.31	4.22	56.12
AL4821-055	258.96	14.96	243.93	16.13	41.77	2.622	108.50	5.024	56.62
AL4821-056	255.53	14.55	239.19	13.04	40.59	2.422	103.13	6.747	58.80
AL4821-057	261.18	10.32	246.72	9.531	41.89	1.838	109.89	5.167	61.98
AL4821-058	252.17	13.17	242.02	11.68	41.70	1.729	112.06	5.239	55.32
AL4821-059	256.43	9.149	247.80	9.332	41.89	1.735	113.42	4.403	56.86

Table S.4.1 (cont.)

Sample	Cu (stdev)	Zn	Zn (stdev)	Ga	Ga (stdev)	Rb	Rb (stdev)	Sr	Sr (stdev)
	(ppm)	(ppm)	(ppm)	(ppm)	(ppm)	(ppm)	(ppm)	(ppm)	(ppm)
AL4818-001	4.812	81.65	4.487	14.83	0.676	12.90	0.712	274.90	13.46
AL4818-002	4.184	85.54	4.512	14.88	0.665	13.21	0.71	275.45	12.82
AL4818-003	5.464	83.87	5.367	14.95	0.902	13.18	0.815	252.66	15.64
AL4818-004	6.241	65.04	4.525	11.28	0.815	6.66	0.428	159.20	10.41
AL4818-005	4.942	65.18	2.608	11.39	0.532	6.54	0.324	166.32	8.073
AL4818-006	7.995	65.00	6.117	10.05	0.878	6.21	0.498	163.56	13.27
AL4818-007	7.895	67.81	6.073	10.21	0.95	6.26	0.535	159.69	13.78
AL4818-008	9.812	64.80	5.95	9.81	0.968	6.02	0.567	160.64	13.7
AL4818-009	6.985	70.28	2.76	11.32	0.861	6.44	0.357	164.06	8.218
AL4818-010	3.925	66.66	1.978	11.76	0.364	6.82	0.237	171.64	6.32
AL4818-011	6.243	80.61	5.236	14.48	0.948	11.80	0.776	218.31	12.08
AL4818-012	2.926	79.05	2.819	14.77	0.576	12.69	0.537	217.35	8.426
AL4819-014	8.494	77.87	8.22	13.18	1.419	12.02	1.145	216.86	19.79
AL4819-015	7.056	79.72	7.062	13.30	1.184	12.53	0.953	220.67	17.45
AL4819-016	8.679	77.25	7.203	12.71	1.231	11.40	0.977	211.78	17.55
AL4819-017	8.707	77.92	7.437	13.02	1.392	11.72	1.025	217.39	18.6
AL4819-018	5.895	78.70	6.65	13.75	1.358	13.39	1.073	225.91	18.41
AL4819-019	5.273	74.01	5.825	14.16	1.146	16.46	1.041	228.07	18.47
AL4819-020	6.361	79.95	5.948	16.29	1.348	16.90	1.136	264.13	20.8
AL4819-021	6.257	80.54	6.032	16.16	1.345	16.77	1.251	261.63	19.84
AL4819-022	6.089	79.92	7.064	13.72	1.296	13.59	1.124	222.39	18.01
AL4819-023	8.319	80.36	6.711	16.22	1.602	17.01	1.461	265.85	22.99
AL4819-024	5.516	80.31	6.181	14.15	1.04	13.32	0.967	219.70	15.81
AL4819-025	4.984	79.44	3.91	14.82	0.674	12.96	0.526	224.57	9.357
AL4819-026	6.607	76.50	6.053	14.86	1.16	13.15	0.971	226.73	17.088
AL4819-027	5.421	84.39	6.004	15.51	1.098	14.03	0.97	228.49	17.14
AL4819-028	6.971	79.50	6.475	14.11	1.193	13.14	0.994	220.12	17.03
AL4819-029	4.251	64.32	3.204	12.93	0.576	10.12	0.494	201.99	10.65
AL4819-030	9.773	70.69	6.093	10.66	0.943	6.45	0.552	174.10	14.57
AL4819-031	8.105	71.93	5.825	11.41	1.027	8.02	0.614	191.13	15.7
AL4819-032	9.597	64.28	5.746	9.30	0.969	4.43	0.421	139.68	13.35
AL4820-033	5.423	69.94	4.345	10.66	0.587	6.77	0.417	171.36	10.4
AL4820-034	7.011	65.65	3.956	9.50	0.632	4.65	0.279	139.38	7.755
AL4820-035	5.373	86.43	5.915	13.85	0.907	12.72	0.773	247.77	17.88
AL4820-036	3.889	87.18	5.96	13.88	0.864	12.64	0.763	247.59	15.11
AL4820-037	4.26	89.09	6.062	14.66	0.983	13.19	0.746	259.04	16.15
AL4820-038	5.036	85.80	6.754	15.15	1.175	14.29	1.101	257.22	19.55
AL4820-039	5.246	90.72	7.488	15.28	1.42	14.62	1.169	256.55	20.9
AL4820-040	5.078	86.51	6.534	14.52	1.218	14.56	1.099	258.03	21.11
AL4820-041	5.479	87.85	7.162	15.72	1.217	14.70	1.101	268.91	19.92
AL4820-042	4.753	86.19	5.782	15.10	1.291	14.51	1.176	260.72	21.77
AL4820-043	5.407	86.64	7.683	14.84	1.403	14.18	1.163	250.02	22.17
AL4820-044	4.178	76.35	3.8	10.64	0.525	4.34	0.197	122.00	6.323
AL4820-045	6.953	79.49	7.414	10.66	1.082	5.50	0.533	138.18	12.93
AL4820-046	5.569	80.31	7.476	10.52	1.096	5.46	0.446	137.52	13.39
AL4820-047	4.87	75.42	4.38	11.38	0.674	5.53	0.299	139.46	7.831
AL4821-048	2.682	82.05	3.434	14.77	0.727	12.35	0.655	268.12	11.68
AL4821-049	4.547	83.23	4.168	14.91	0.784	12.77	0.639	278.86	14.94
AL4821-050	5.076	82.44	5.807	14.88	0.994	13.29	0.918	261.03	16.92
AL4821-051	4.12	83.16	5.15	15.10	1.044	13.26	0.893	259.31	17.91
AL4821-053	3.391	82.54	4.185	14.90	0.701	13.24	0.751	260.78	11.23
AL4821-054	3.277	81.47	3.782	14.76	0.705	13.14	0.423	258.63	9.312
AL4821-055	4.615	89.52	5.753	15.15	0.794	13.24	0.857	262.26	15.51
AL4821-056	5.306	80.92	5.962	14.85	1.043	12.94	0.929	255.13	17.75
AL4821-057	4.483	82.47	4.288	14.98	0.79	13.24	0.686	261.84	13.47
AL4821-058	4.553	80.63	4.962	14.70	0.822	13.08	0.593	258.25	13.57
AL4821-059	2.82	85.36	3.668	15.02	0.601	13.24	0.689	263.56	12.78

Table S.4.1 (cont.)

Sample	Y	Y (stdev)	Zr	Zr (stdev)	Nb	Nb (stdev)	Cs	Cs (stdev)	Ba
	(ppm)	(ppm)	(ppm)	(ppm)	(ppm)	(ppm)	(ppm)	(ppm)	(ppm)
AL4818-001	29.19	1.508	150.68	8.459	24.71	1.2	0.12	0.007	146.64
AL4818-002	29.83	1.479	153.94	7.664	24.86	1.105	0.13	0.005	149.69
AL4818-003	30.33	1.783	151.81	9.403	24.34	1.486	0.13	0.008	149.61
AL4818-004	22.31	1.256	82.29	4.128	11.48	0.678	0.07	0.002	79.02
AL4818-005	21.54	0.867	77.05	3.465	11.09	0.585	0.06	0.001	77.94
AL4818-006	20.22	1.737	74.20	5.835	10.94	1.00	0.07	0.004	72.53
AL4818-007	21.84	1.72	79.72	5.803	11.23	0.92	0.06	0.008	73.33
AL4818-008	20.01	1.726	66.86	6.085	10.43	0.98	0.07	0.004	70.12
AL4818-009	20.99	1.133	69.17	3.403	10.76	0.60	0.07	0.008	75.83
AL4818-010	21.85	0.859	79.41	2.727	11.53	0.333	0.07	0.004	82.02
AL4818-011	25.68	1.447	111.59	6.838	19.64	1.27	0.13	0.008	140.73
AL4818-012	26.95	0.772	117.40	4.355	20.68	0.884	0.13	0.005	150.46
AL4819-014	25.23	2.358	114.42	9.242	20.61	1.83	0.13	0.009	139.51
AL4819-015	25.84	2.124	118.23	9.353	21.00	1.90	0.13	0.014	145.49
AL4819-016	24.69	1.953	107.19	8.648	19.26	1.72	0.12	0.009	133.80
AL4819-017	25.28	2.067	109.69	9.196	19.70	1.83	0.12	0.011	137.63
AL4819-018	24.75	1.956	119.07	8.678	20.70	1.72	0.14	0.008	154.37
AL4819-019	22.47	1.387	127.19	8.018	27.34	1.93	0.16	0.015	176.92
AL4819-020	23.98	1.777	121.96	9.004	25.85	1.96	0.17	0.011	186.69
AL4819-021	23.62	1.609	122.95	8.294	25.69	1.83	0.17	0.015	184.72
AL4819-022	24.90	1.95	119.96	9.9	21.10	1.72	0.14	0.011	156.23
AL4819-023	23.53	1.957	121.68	9.886	25.99	2.31	0.17	0.019	188.07
AL4819-024	24.58	1.567	116.73	7.458	20.37	1.46	0.12	0.01	151.63
AL4819-025	23.95	1.159	109.68	5.519	19.69	0.994	0.12	0.005	151.85
AL4819-026	24.18	1.687	113.02	8.009	20.31	1.597	0.13	0.01	154.48
AL4819-027	25.85	1.745	120.49	8.396	21.02	1.57	0.14	0.005	161.27
AL4819-028	24.36	1.833	115.44	8.282	20.36	1.58	0.12	0.013	152.74
AL4819-029	20.20	1.078	97.06	4.986	17.07	0.722	0.10	0.002	119.17
AL4819-030	19.49	1.584	71.33	5.856	11.23	1.03	0.06	0.002	76.49
AL4819-031	20.79	1.701	86.54	6	14.20	1.06	0.06	0.008	92.98
AL4819-032	19.06	1.701	54.39	5.058	8.05	0.72	0.02	0.004	53.65
AL4820-033	21.90	1.23	81.41	4.604	12.69	0.70	0.04	0.003	78.67
AL4820-034	19.80	1.086	58.39	3.018	8.69	0.54	0.02	0.002	56.93
AL4820-035	28.78	1.873	145.92	10.04	24.05	1.70	0.09	0.006	141.06
AL4820-036	28.98	1.823	147.69	9.83	24.21	1.74	0.08	0.012	139.43
AL4820-037	29.59	1.607	147.74	8.44	24.16	1.49	0.13	0.007	145.61
AL4820-038	29.87	2.034	144.93	8.989	24.46	1.77	0.13	0.012	161.49
AL4820-039	31.12	2.291	148.44	12.04	24.98	1.91	0.14	0.007	163.49
AL4820-040	29.84	2.304	146.11	10.83	24.68	1.99	0.13	0.007	167.84
AL4820-041	30.27	2.065	146.53	10.27	24.79	1.97	0.14	0.014	168.67
AL4820-042	29.88	2.051	143.26	10.49	24.67	1.85	0.13	0.007	163.29
AL4820-043	30.63	2.608	145.71	11.39	24.10	2.20	0.13	0.007	159.02
AL4820-044	19.48	0.82	95.36	4.646	10.68	0.499	0.04	0.003	59.37
AL4820-045	28.03	2.421	101.72	7.577	10.78	0.95	0.04	0.006	59.40
AL4820-046	28.15	2.345	101.31	7.918	10.76	0.93	0.03	0.007	58.69
AL4820-047	27.49	1.411	99.72	5.825	10.13	0.472	0.05	0.004	64.46
AL4821-048	29.05	1.33	144.10	5.962	23.62	0.948	0.12	0.005	141.81
AL4821-049	29.17	1.455	149.40	6.704	24.53	1.073	0.11	0.006	141.45
AL4821-050	30.62	2.111	151.89	10.49	24.53	1.467	0.13	0.007	148.37
AL4821-051	30.49	1.929	151.79	8.974	24.65	1.42	0.13	0.009	149.88
AL4821-053	30.24	1.416	151.99	7.865	24.41	1.159	0.13	0.005	149.18
AL4821-054	30.12	1.387	151.44	5.562	24.37	1.004	0.11	0.006	144.38
AL4821-055	30.73	1.921	151.76	9.492	24.49	1.522	0.12	0.008	147.36
AL4821-056	30.01	1.849	149.74	7.905	24.20	1.344	0.13	0.009	147.24
AL4821-057	30.37	1.269	151.32	6.114	24.38	1.012	0.13	0.006	148.27
AL4821-058	30.10	1.363	148.30	8.938	24.21	1.336	0.11	0.01	143.32
AL4821-059	30.26	1.307	153.22	6.598	24.80	1.116	0.12	0.008	146.70

Table S.4.1 (cont.)

Sample	Ba (stdev)	La	La (stdev)	Ce	Ce (stdev)	Pr	Pr (stdev)	Nd	Nd (stdev)
	(ppm)	(ppm)	(ppm)	(ppm)	(ppm)	(ppm)	(ppm)	(ppm)	(ppm)
AL4818-001	8.809	13.01	0.664	29.81	1.676	4.06	0.228	17.79	1.034
AL4818-002	7.063	13.24	0.572	30.08	1.101	4.17	0.224	18.18	0.772
AL4818-003	8.817	12.97	0.964	29.57	1.929	4.06	0.269	17.96	1.197
AL4818-004	4.173	6.61	0.34	15.52	0.844	2.18	0.126	9.86	0.628
AL4818-005	3.524	6.45	0.283	14.95	0.718	2.07	0.096	9.43	0.498
AL4818-006	6.577	6.17	0.47	14.12	1.163	2.01	0.17	8.85	0.734
AL4818-007	6.005	6.31	0.539	14.78	1.209	2.13	0.181	9.44	0.748
AL4818-008	5.917	5.74	0.5	13.21	1.143	1.85	0.163	8.06	0.724
AL4818-009	4.305	6.12	0.309	14.11	0.718	1.96	0.1	8.99	0.455
AL4818-010	2.747	6.74	0.209	15.61	0.574	2.17	0.09	9.95	0.388
AL4818-011	7.008	10.94	0.705	24.35	1.586	3.26	0.207	14.04	0.986
AL4818-012	5.059	11.53	0.335	25.92	0.88	3.41	0.179	15.04	0.563
AL4819-014	12.57	11.05	0.904	24.58	2.114	3.35	0.306	13.99	1.204
AL4819-015	10.62	11.44	0.936	25.63	1.928	3.50	0.256	14.58	1.244
AL4819-016	11.24	10.27	0.983	23.04	2.191	3.13	0.3	13.35	1.144
AL4819-017	11.23	10.60	0.931	23.67	2.062	3.23	0.293	13.43	1.274
AL4819-018	12.13	11.33	0.892	25.26	2.006	3.45	0.279	14.43	1.075
AL4819-019	13.2	14.11	0.954	29.41	1.916	3.66	0.252	15.38	1.126
AL4819-020	13.45	13.93	1.087	29.76	2.348	3.85	0.285	15.99	1.174
AL4819-021	12.52	14.06	0.973	29.83	2.03	3.86	0.259	16.14	1.24
AL4819-022	13.31	11.46	0.986	25.70	2.053	3.52	0.281	14.54	1.303
AL4819-023	14.57	14.04	1.142	30.01	2.573	3.85	0.292	16.13	1.157
AL4819-024	11.92	11.20	0.782	25.05	1.564	3.45	0.189	14.70	0.803
AL4819-025	7.546	11.08	0.54	24.50	1.236	3.26	0.142	14.22	0.885
AL4819-026	11.155	11.14	0.842	24.84	1.84	3.33	0.241	14.28	1.04
AL4819-027	11.69	11.84	0.847	26.26	1.923	3.50	0.247	15.35	0.953
AL4819-028	11.33	11.25	0.746	25.06	1.684	3.42	0.236	14.55	1.068
AL4819-029	5.307	9.52	0.363	21.36	0.918	2.86	0.135	12.53	0.501
AL4819-030	6.72	6.28	0.555	14.34	1.256	2.02	0.18	9.04	0.85
AL4819-031	6.759	7.83	0.574	17.60	1.396	2.47	0.184	10.84	0.794
AL4819-032	5.027	4.52	0.414	10.24	1.004	1.47	0.147	6.83	0.638
AL4820-033	5.224	6.91	0.391	15.60	0.914	2.19	0.155	9.85	0.557
AL4820-034	3.061	4.85	0.272	11.06	0.595	1.58	0.105	7.27	0.439
AL4820-035	9.277	12.76	0.829	28.83	1.837	4.01	0.232	17.35	1.177
AL4820-036	10.14	12.78	0.859	28.75	1.906	3.99	0.293	17.48	1.07
AL4820-037	9.709	12.92	0.797	29.64	1.568	4.08	0.242	17.55	1.141
AL4820-038	11.78	12.86	0.899	29.30	1.868	4.02	0.216	17.41	1.068
AL4820-039	12.72	13.31	1.03	30.02	2.342	4.13	0.281	17.83	1.221
AL4820-040	12.02	13.07	1.021	29.53	2.177	4.05	0.305	17.60	1.367
AL4820-041	13.06	13.13	1.036	29.58	2.244	4.00	0.317	17.47	1.528
AL4820-042	13.1	12.99	0.988	29.27	2.279	4.00	0.335	17.45	1.261
AL4820-043	13.44	12.96	1.016	29.18	2.336	4.02	0.278	17.41	1.257
AL4820-044	2.539	4.91	0.25	13.45	0.607	1.79	0.085	8.59	0.381
AL4820-045	5.618	6.62	0.591	16.56	1.416	2.46	0.184	11.08	1.027
AL4820-046	5.996	6.63	0.576	16.47	1.304	2.41	0.205	10.93	1.098
AL4820-047	4.085	6.44	0.335	16.01	0.869	2.32	0.123	11.10	0.684
AL4821-048	7.794	12.75	0.715	28.91	1.719	3.91	0.197	17.13	0.991
AL4821-049	8.346	12.85	0.721	29.11	1.425	3.95	0.211	17.47	1.039
AL4821-050	9.917	13.09	0.804	29.99	1.993	4.12	0.261	18.19	1.195
AL4821-051	9.029	13.22	0.768	30.24	1.518	4.18	0.225	18.28	0.989
AL4821-053	5.721	13.10	0.685	29.86	1.477	4.10	0.178	17.91	0.979
AL4821-054	6.29	13.00	0.553	29.45	0.96	3.99	0.155	17.68	0.76
AL4821-055	9.836	13.09	0.834	29.99	1.626	4.08	0.26	18.01	1.031
AL4821-056	8.869	12.95	0.649	29.70	1.632	4.05	0.24	17.61	1.067
AL4821-057	6.832	13.08	0.609	29.92	1.397	4.14	0.176	18.25	0.553
AL4821-058	5.62	12.86	0.637	28.81	1.635	3.96	0.226	17.53	1.02
AL4821-059	7.786	13.18	0.676	29.75	1.651	4.08	0.169	18.08	0.778

Table S.4.1 (cont.)

Sample	Sm	Sm (stdev)	Eu	Eu (stdev)	Gd	Gd (stdev)	Tb	Tb (stdev)	Dy
	(ppm)	(ppm)	(ppm)	(ppm)	(ppm)	(ppm)	(ppm)	(ppm)	(ppm)
AL4818-001	4.52	0.262	1.53	0.095	5.08	0.243	0.89	0.053	5.13
AL4818-002	4.61	0.203	1.57	0.066	5.33	0.241	0.92	0.05	5.23
AL4818-003	4.55	0.323	1.56	0.098	5.35	0.357	0.92	0.047	5.20
AL4818-004	2.74	0.165	1.02	0.052	3.64	0.19	0.62	0.034	3.80
AL4818-005	2.66	0.117	0.98	0.058	3.50	0.151	0.60	0.032	3.62
AL4818-006	2.46	0.175	0.91	0.065	3.04	0.314	0.55	0.053	3.37
AL4818-007	2.61	0.274	0.96	0.084	3.30	0.304	0.59	0.054	3.71
AL4818-008	2.32	0.191	0.86	0.09	2.94	0.284	0.54	0.055	3.33
AL4818-009	2.47	0.147	0.91	0.049	3.18	0.198	0.58	0.029	3.60
AL4818-010	2.74	0.125	1.02	0.041	3.60	0.14	0.62	0.021	3.71
AL4818-011	3.66	0.164	1.26	0.057	4.21	0.281	0.74	0.053	4.37
AL4818-012	3.75	0.153	1.32	0.065	4.55	0.17	0.80	0.032	4.61
AL4819-014	3.56	0.344	1.25	0.099	4.14	0.382	0.73	0.062	4.32
AL4819-015	3.73	0.276	1.27	0.113	4.26	0.346	0.75	0.058	4.49
AL4819-016	3.42	0.304	1.19	0.105	4.00	0.325	0.70	0.069	4.17
AL4819-017	3.49	0.298	1.23	0.113	4.04	0.402	0.71	0.072	4.29
AL4819-018	3.65	0.32	1.27	0.106	4.14	0.367	0.73	0.063	4.24
AL4819-019	3.41	0.292	1.26	0.08	3.71	0.297	0.64	0.056	4.00
AL4819-020	3.74	0.291	1.28	0.106	4.20	0.318	0.72	0.057	4.17
AL4819-021	3.76	0.26	1.31	0.074	4.20	0.267	0.72	0.046	4.20
AL4819-022	3.72	0.315	1.28	0.108	4.28	0.342	0.75	0.055	4.31
AL4819-023	3.68	0.339	1.29	0.118	4.19	0.345	0.71	0.063	4.15
AL4819-024	3.70	0.234	1.26	0.106	4.25	0.274	0.74	0.047	4.34
AL4819-025	3.56	0.202	1.25	0.076	4.14	0.177	0.72	0.04	4.25
AL4819-026	3.56	0.263	1.25	0.094	4.20	0.299	0.70	0.053	4.23
AL4819-027	3.85	0.217	1.35	0.094	4.45	0.34	0.78	0.051	4.57
AL4819-028	3.62	0.262	1.26	0.098	4.20	0.329	0.74	0.053	4.31
AL4819-029	3.08	0.14	1.07	0.057	3.58	0.156	0.65	0.031	3.54
AL4819-030	2.46	0.201	0.93	0.071	3.08	0.245	0.55	0.043	3.40
AL4819-031	2.83	0.221	1.02	0.076	3.42	0.233	0.60	0.047	3.65
AL4819-032	1.97	0.212	0.78	0.074	2.68	0.256	0.50	0.053	3.22
AL4820-033	2.69	0.18	0.99	0.064	3.33	0.254	0.60	0.034	3.75
AL4820-034	2.13	0.098	0.82	0.049	2.87	0.132	0.52	0.034	3.35
AL4820-035	4.33	0.349	1.45	0.095	4.98	0.34	0.87	0.063	5.10
AL4820-036	4.41	0.207	1.47	0.085	5.06	0.327	0.86	0.053	5.13
AL4820-037	4.44	0.304	1.50	0.094	5.14	0.355	0.88	0.053	5.16
AL4820-038	4.44	0.265	1.49	0.102	5.24	0.315	0.90	0.048	5.30
AL4820-039	4.57	0.383	1.51	0.113	5.37	0.425	0.92	0.072	5.48
AL4820-040	4.56	0.31	1.50	0.098	5.20	0.397	0.90	0.065	5.24
AL4820-041	4.48	0.401	1.49	0.134	5.26	0.397	0.91	0.069	5.32
AL4820-042	4.49	0.31	1.49	0.109	5.21	0.381	0.89	0.059	5.30
AL4820-043	4.43	0.386	1.46	0.124	5.21	0.413	0.90	0.071	5.30
AL4820-044	2.39	0.129	0.86	0.049	3.24	0.126	0.58	0.03	3.38
AL4820-045	3.31	0.27	1.12	0.097	4.32	0.328	0.77	0.07	4.72
AL4820-046	3.21	0.339	1.13	0.113	4.23	0.347	0.77	0.067	4.75
AL4820-047	3.24	0.142	1.15	0.07	4.37	0.284	0.78	0.052	4.62
AL4821-048	4.38	0.247	1.49	0.077	5.11	0.307	0.86	0.048	5.05
AL4821-049	4.45	0.326	1.52	0.084	5.27	0.297	0.81	0.044	5.08
AL4821-050	4.64	0.252	1.53	0.115	5.36	0.378	0.90	0.059	5.39
AL4821-051	4.64	0.165	1.55	0.044	5.39	0.275	0.91	0.054	5.39
AL4821-053	4.61	0.2	1.54	0.071	5.38	0.329	0.87	0.055	5.32
AL4821-054	4.51	0.217	1.51	0.041	5.29	0.257	0.80	0.036	5.41
AL4821-055	4.55	0.367	1.52	0.11	5.39	0.344	0.85	0.06	5.40
AL4821-056	4.49	0.256	1.49	0.088	5.24	0.301	0.88	0.051	5.23
AL4821-057	4.59	0.153	1.51	0.08	5.36	0.261	0.91	0.035	5.32
AL4821-058	4.49	0.224	1.48	0.076	5.29	0.248	0.80	0.048	5.33
AL4821-059	4.60	0.208	1.52	0.065	5.27	0.205	0.83	0.039	5.41

Table S.4.1 (cont.)

Sample	Dy (stdev)	Ho	Ho (stdev)	Er	Er (stdev)	Tm	Tm (stdev	Yb	Yb (stdev)
	(ppm)	(ppm)	(ppm)	(ppm)	(ppm)	(ppm)	(ppm)	(ppm)	(ppm)
AL4818-001	0.25	1.05	0.066	2.83	0.135	0.43	0.025	2.59	0.162
AL4818-002	0.247	1.09	0.052	2.91	0.139	0.45	0.023	2.74	0.153
AL4818-003	0.331	1.12	0.055	2.99	0.185	0.46	0.027	2.77	0.166
AL4818-004	0.211	0.83	0.041	2.28	0.115	0.35	0.018	2.15	0.121
AL4818-005	0.179	0.80	0.029	2.18	0.082	0.33	0.014	2.06	0.1
AL4818-006	0.296	0.72	0.054	1.98	0.171	0.33	0.026	1.88	0.188
AL4818-007	0.295	0.79	0.065	2.14	0.182	0.35	0.031	2.06	0.177
AL4818-008	0.301	0.71	0.069	1.95	0.194	0.33	0.032	1.91	0.174
AL4818-009	0.155	0.76	0.047	2.15	0.094	0.34	0.014	2.02	0.14
AL4818-010	0.172	0.80	0.033	2.22	0.085	0.34	0.008	2.11	0.09
AL4818-011	0.325	0.93	0.06	2.62	0.129	0.41	0.028	2.42	0.176
AL4818-012	0.172	0.98	0.037	2.68	0.106	0.40	0.024	2.53	0.116
AL4819-014	0.412	0.91	0.076	2.48	0.223	0.41	0.038	2.36	0.204
AL4819-015	0.335	0.94	0.073	2.53	0.215	0.42	0.034	2.41	0.191
AL4819-016	0.415	0.87	0.075	2.43	0.221	0.40	0.031	2.31	0.199
AL4819-017	0.417	0.90	0.089	2.47	0.242	0.41	0.035	2.32	0.252
AL4819-018	0.332	0.87	0.068	2.34	0.173	0.39	0.024	2.18	0.184
AL4819-019	0.266	0.92	0.056	2.21	0.142	0.33	0.022	1.91	0.129
AL4819-020	0.307	0.87	0.063	2.36	0.163	0.36	0.028	2.19	0.178
AL4819-021	0.264	0.86	0.062	2.33	0.159	0.36	0.026	2.20	0.174
AL4819-022	0.352	0.90	0.063	2.39	0.194	0.39	0.032	2.22	0.157
AL4819-023	0.34	0.86	0.072	2.32	0.21	0.36	0.034	2.16	0.208
AL4819-024	0.265	0.89	0.053	2.38	0.166	0.38	0.022	2.25	0.184
AL4819-025	0.247	0.88	0.05	2.37	0.147	0.36	0.02	2.20	0.126
AL4819-026	0.304	0.88	0.062	2.40	0.171	0.37	0.026	2.22	0.168
AL4819-027	0.316	0.96	0.06	2.57	0.158	0.39	0.021	2.37	0.148
AL4819-028	0.321	0.88	0.063	2.42	0.193	0.38	0.03	2.24	0.176
AL4819-029	0.134	0.75	0.037	2.07	0.054	0.30	0.01	1.88	0.085
AL4819-030	0.276	0.72	0.056	1.98	0.169	0.31	0.031	1.91	0.157
AL4819-031	0.24	0.76	0.05	2.09	0.148	0.34	0.02	2.01	0.125
AL4819-032	0.269	0.69	0.05	1.90	0.189	0.31	0.029	1.91	0.171
AL4820-033	0.256	0.80	0.045	2.22	0.149	0.36	0.018	2.12	0.144
AL4820-034	0.205	0.73	0.042	2.03	0.145	0.34	0.016	2.02	0.103
AL4820-035	0.314	1.04	0.067	2.88	0.168	0.45	0.028	2.66	0.16
AL4820-036	0.364	1.04	0.076	2.84	0.227	0.45	0.027	2.65	0.22
AL4820-037	0.31	1.05	0.078	2.90	0.179	0.46	0.027	2.70	0.201
AL4820-038	0.321	1.09	0.073	2.98	0.205	0.47	0.029	2.78	0.149
AL4820-039	0.403	1.12	0.088	3.10	0.194	0.48	0.037	2.93	0.214
AL4820-040	0.423	1.10	0.073	2.99	0.19	0.48	0.028	2.84	0.155
AL4820-041	0.429	1.09	0.098	2.99	0.246	0.46	0.041	2.80	0.213
AL4820-042	0.331	1.08	0.077	2.96	0.198	0.46	0.037	2.76	0.197
AL4820-043	0.466	1.09	0.096	3.04	0.214	0.47	0.039	2.81	0.238
AL4820-044	0.173	0.73	0.042	2.02	0.121	0.30	0.015	1.88	0.095
AL4820-045	0.41	1.00	0.077	2.79	0.263	0.45	0.034	2.70	0.216
AL4820-046	0.354	0.98	0.089	2.80	0.239	0.45	0.034	2.72	0.212
AL4820-047	0.283	1.02	0.042	2.76	0.155	0.42	0.024	2.60	0.178
AL4821-048	0.263	1.04	0.036	2.86	0.117	0.44	0.019	2.61	0.127
AL4821-049	0.407	1.06	0.056	2.92	0.162	0.45	0.03	2.66	0.148
AL4821-050	0.398	1.11	0.077	3.00	0.226	0.47	0.037	2.81	0.213
AL4821-051	0.31	1.11	0.072	3.00	0.186	0.48	0.028	2.82	0.145
AL4821-053	0.294	1.11	0.055	3.04	0.11	0.46	0.023	2.81	0.12
AL4821-054	0.194	1.11	0.047	3.03	0.123	0.46	0.016	2.76	0.147
AL4821-055	0.326	1.11	0.071	3.09	0.173	0.47	0.028	2.78	0.195
AL4821-056	0.242	1.08	0.041	2.95	0.161	0.47	0.02	2.73	0.153
AL4821-057	0.269	1.09	0.056	3.01	0.151	0.48	0.019	2.77	0.15
AL4821-058	0.191	1.08	0.057	3.00	0.149	0.46	0.024	2.74	0.133
AL4821-059	0.217	1.10	0.055	3.01	0.11	0.47	0.015	2.78	0.14

Table S.4.1 (cont.)

Sample	Lu	Lu (stdev)	Hf	Hf (stdev)	Ta	Ta (stdev)	Pb	Pb (stdev)	Th
	(ppm)	(ppm)	(ppm)	(ppm)	(ppm)	(ppm)	(ppm)	(ppm)	(ppm)
AL4818-001	0.40	0.023	3.58	0.157	1.49	0.076	0.83	0.036	1.33
AL4818-002	0.42	0.02	3.68	0.171	1.53	0.079	0.83	0.034	1.35
AL4818-003	0.44	0.031	3.62	0.26	1.47	0.095	0.88	0.069	1.32
AL4818-004	0.35	0.018	2.15	0.099	0.71	0.043	0.50	0.031	0.66
AL4818-005	0.33	0.018	1.97	0.095	0.68	0.036	0.49	0.024	0.63
AL4818-006	0.31	0.033	1.82	0.16	0.53	0.057	0.42	0.041	0.59
AL4818-007	0.34	0.035	1.96	0.176	0.55	0.05	0.44	0.041	0.61
AL4818-008	0.31	0.035	1.66	0.15	0.51	0.054	0.38	0.031	0.55
AL4818-009	0.32	0.017	1.74	0.135	0.67	0.034	0.49	0.014	0.62
AL4818-010	0.35	0.007	2.11	0.019	0.72	0.021	0.55	0.004	0.67
AL4818-011	0.37	0.03	2.61	0.175	1.23	0.068	0.74	0.063	1.16
AL4818-012	0.41	0.013	2.86	0.12	1.26	0.052	0.81	0.04	1.21
AL4819-014	0.39	0.031	2.67	0.263	1.00	0.111	0.72	0.077	1.13
AL4819-015	0.39	0.028	2.75	0.242	1.04	0.1	0.72	0.068	1.18
AL4819-016	0.37	0.039	2.52	0.213	0.94	0.097	0.63	0.058	1.07
AL4819-017	0.38	0.044	2.56	0.259	0.97	0.129	0.65	0.085	1.08
AL4819-018	0.36	0.028	2.79	0.194	0.99	0.107	0.69	0.061	1.14
AL4819-019	0.29	0.023	2.75	0.161	1.30	0.084	1.10	0.063	1.60
AL4819-020	0.33	0.032	2.82	0.232	1.23	0.128	1.03	0.072	1.56
AL4819-021	0.32	0.033	2.92	0.147	1.25	0.085	1.04	0.07	1.53
AL4819-022	0.36	0.035	2.83	0.23	1.03	0.093	0.70	0.072	1.16
AL4819-023	0.32	0.027	2.80	0.261	1.26	0.136	1.08	0.095	1.56
AL4819-024	0.36	0.024	2.76	0.21	1.01	0.067	0.81	0.049	1.17
AL4819-025	0.32	0.021	2.66	0.168	0.95	0.082	0.78	0.051	1.12
AL4819-026	0.34	0.028	2.68	0.195	1.23	0.092	0.74	0.063	1.14
AL4819-027	0.36	0.021	2.90	0.196	1.02	0.061	0.87	0.058	1.23
AL4819-028	0.36	0.028	2.76	0.201	0.99	0.105	0.79	0.061	1.16
AL4819-029	0.30	0.013	2.42	0.135	1.03	0.05	0.64	0.045	0.95
AL4819-030	0.29	0.029	1.78	0.129	0.56	0.06	0.46	0.048	0.65
AL4819-031	0.32	0.02	2.11	0.151	0.71	0.047	0.55	0.033	0.83
AL4819-032	0.31	0.025	1.41	0.142	0.40	0.043	0.31	0.042	0.45
AL4820-033	0.34	0.021	2.00	0.135	0.63	0.042	0.43	0.023	0.71
AL4820-034	0.32	0.02	1.50	0.097	0.44	0.032	0.30	0.028	0.49
AL4820-035	0.42	0.026	3.42	0.253	1.17	0.098	0.74	0.049	1.31
AL4820-036	0.42	0.029	3.43	0.239	1.18	0.11	0.74	0.053	1.31
AL4820-037	0.41	0.036	3.53	0.216	1.18	0.088	0.83	0.069	1.35
AL4820-038	0.43	0.027	3.48	0.246	1.18	0.099	0.82	0.036	1.40
AL4820-039	0.44	0.039	3.62	0.243	1.22	0.107	0.88	0.064	1.42
AL4820-040	0.45	0.025	3.48	0.275	1.18	0.084	0.98	0.057	1.44
AL4820-041	0.42	0.033	3.53	0.26	1.18	0.117	0.96	0.069	1.42
AL4820-042	0.43	0.029	3.46	0.249	1.19	0.105	0.80	0.05	1.39
AL4820-043	0.43	0.038	3.50	0.247	1.17	0.122	0.81	0.072	1.36
AL4820-044	0.31	0.017	2.46	0.113	0.64	0.04	0.52	0.03	0.41
AL4820-045	0.42	0.038	2.54	0.198	0.52	0.046	0.42	0.028	0.59
AL4820-046	0.42	0.031	2.52	0.191	0.52	0.06	0.39	0.035	0.59
AL4820-047	0.41	0.027	2.54	0.169	0.61	0.049	0.60	0.06	0.57
AL4821-048	0.41	0.012	3.42	0.144	1.42	0.058	0.85	0.03	1.29
AL4821-049	0.40	0.025	3.49	0.239	1.47	0.075	0.72	0.049	1.29
AL4821-050	0.44	0.023	3.64	0.263	1.48	0.109	0.85	0.062	1.34
AL4821-051	0.43	0.022	3.60	0.193	1.49	0.07	0.93	0.051	1.38
AL4821-053	0.43	0.019	3.58	0.188	1.47	0.091	0.79	0.049	1.36
AL4821-054	0.42	0.028	3.46	0.226	1.46	0.084	0.73	0.045	1.32
AL4821-055	0.44	0.025	3.62	0.223	1.49	0.096	0.79	0.073	1.34
AL4821-056	0.42	0.022	3.55	0.188	1.44	0.081	0.87	0.039	1.32
AL4821-057	0.43	0.022	3.55	0.172	1.47	0.065	0.86	0.054	1.34
AL4821-058	0.43	0.018	3.50	0.204	1.45	0.071	0.74	0.043	1.31
AL4821-059	0.43	0.018	3.60	0.145	1.49	0.077	0.77	0.045	1.36

Table S.4.1 (cont.)

Sample	Th (stdev)	U	U (stdev)
	(ppm)	(ppm)	(ppm)
AL4818-001	0.071	0.43	0.021
AL4818-002	0.079	0.44	0.017
AL4818-003	0.102	0.43	0.026
AL4818-004	0.034	0.21	0.009
AL4818-005	0.038	0.19	0.01
AL4818-006	0.049	0.18	0.018
AL4818-007	0.055	0.19	0.014
AL4818-008	0.057	0.17	0.016
AL4818-009	0.036	0.21	0.009
AL4818-010	0.028	0.21	0.008
AL4818-011	0.093	0.38	0.026
AL4818-012	0.032	0.36	0.012
AL4819-014	0.121	0.35	0.034
AL4819-015	0.106	0.36	0.035
AL4819-016	0.102	0.32	0.032
AL4819-017	0.12	0.33	0.028
AL4819-018	0.112	0.35	0.029
AL4819-019	0.12	0.54	0.033
AL4819-020	0.118	0.47	0.034
AL4819-021	0.13	0.48	0.028
AL4819-022	0.101	0.36	0.028
AL4819-023	0.134	0.49	0.04
AL4819-024	0.083	0.36	0.017
AL4819-025	0.085	0.35	0.026
AL4819-026	0.099	0.34	0.027
AL4819-027	0.075	0.39	0.024
AL4819-028	0.089	0.38	0.027
AL4819-029	0.058	0.29	0.015
AL4819-030	0.064	0.21	0.015
AL4819-031	0.058	0.25	0.017
AL4819-032	0.04	0.15	0.015
AL4820-033	0.037	0.23	0.003
AL4820-034	0.034	0.15	0.011
AL4820-035	0.083	0.43	0.024
AL4820-036	0.103	0.45	0.025
AL4820-037	0.078	0.44	0.016
AL4820-038	0.101	0.44	0.026
AL4820-039	0.119	0.44	0.033
AL4820-040	0.084	0.45	0.032
AL4820-041	0.115	0.45	0.025
AL4820-042	0.117	0.44	0.03
AL4820-043	0.122	0.43	0.03
AL4820-044	0.026	0.18	0.013
AL4820-045	0.068	0.18	0.012
AL4820-046	0.049	0.18	0.008
AL4820-047	0.029	0.18	0.013
AL4821-048	0.052	0.42	0.016
AL4821-049	0.091	0.43	0.022
AL4821-050	0.132	0.44	0.04
AL4821-051	0.051	0.44	0.026
AL4821-053	0.063	0.44	0.022
AL4821-054	0.061	0.42	0.022
AL4821-055	0.121	0.43	0.036
AL4821-056	0.105	0.43	0.024
AL4821-057	0.085	0.43	0.014
AL4821-058	0.097	0.42	0.025
AL4821-059	0.075	0.44	0.015

Table S.4.2 Volatile concentrations and vesicularity characteristics

Sample	Category	CO_2	H_2O	F	Cl	S	Vesicularity (2D)	Total CO_2	Vesicularity (3D)
		(ppm)	(wt. %)	(ppm)	(ppm)	(wt. %)	(%)	(ppm)	(%)
AL4818-001	Non-popping	253	0.49	390	254	0.10			
AL4818-002	Non-popping	279	0.53	403	263	0.10	2.3	1410	
AL4818-003	Popping	177	0.48	411	253	0.09	13.3	7633	13.6
AL4818-004	Non-popping	164	0.33	209	144	0.10			
AL4818-005	Non-popping	174	0.30	188	111	0.09	1.4	878	
AL4818-006	Non-popping	176	0.31	194	110	0.10	0.5	397	
AL4818-007	Non-popping	156	0.28	198	104	0.09			
AL4818-008	Non-popping	189	0.26	172	99	0.10	1.8	1071	
AL4818-009	Non-popping	202	0.28	177	102	0.10	0.1	238	
AL4818-010	Non-popping	187	0.30	193	106	0.09	0.7	533	
AL4818-011	Non-popping	179	0.55	339	242	0.11	1.4	895	
AL4818-012	Non-popping	170	0.52	333	234	0.11	1.0	666	
AL4819-014	Non-popping	172	0.53	349	247	0.11	0.9	595	
AL4819-015	Non-popping	157	0.57	353	254	0.11	0.7	508	
AL4819-016	Non-popping	252	0.52	314	226	0.11	1.0	769	
AL4819-017	Non-popping	169	0.53	319	230	0.11	1.7	1022	
AL4819-018	Non-popping	196	0.63	411	296	0.12	1.1	725	
AL4819-019	Non-popping	213	0.65	420	298	0.12	1.5	952	
AL4819-020	Non-popping	168	0.67	438	314	0.12	1.2	762	
AL4819-021	Non-popping	167	0.64	435	301	0.12	1.4	873	
AL4819-022	Non-popping	158	0.58	374	273	0.11	0.8	575	
AL4819-023	Non-popping	157	0.59	374	283	0.11			
AL4819-024	Non-popping	188	0.58	373	274	0.11			
AL4819-025	Non-popping	195	0.51	337	229	0.11			
AL4819-026	Non-popping	153	0.60	380	285	0.12			
AL4819-027	Non-popping	159	0.59	379	276	0.11			
AL4819-028	Non-popping	154	0.77	405	468	0.11			
AL4819-029	Non-popping	273	0.41	288	133	0.09	2.0	1273	
AL4819-030	Non-popping	257	0.31	184	125	0.09			
AL4819-031	Non-popping	199	0.36	221	169	0.09			
AL4819-032	Non-popping	197	0.22	139	87	0.09			
AL4820-033	Non-popping	199	0.23	135	85	0.09			
AL4820-034	Non-popping	208	0.24	146	93	0.10			
AL4820-035	Popping	166	0.51	421	270	0.09			
AL4820-036	Popping	171	0.50	413	269	0.09	13.3	7663	13.2
AL4820-037	Popping	175	0.50	412	265	0.09	20.0	12368	19.7
AL4820-038	Non-popping	170	0.49	412	263	0.09			
AL4820-039	Popping	165	0.49	425	272	0.09	14.1	8178	
AL4820-040	Non-popping	167	0.50	424	273	0.09	8.2	4550	
AL4820-041	Non-popping	166	0.50	429	274	0.09	4.4	2392	
AL4820-042	Non-popping	173	0.50	419	269	0.09	7.0	3817	
AL4820-043	Non-popping	165	0.50	423	270	0.09	6.7	3663	
AL4820-044	Non-popping	198	0.30	238	114	0.10	1.0	699	
AL4820-045	Non-popping	184	0.30	239	113	0.10			
AL4820-046	Non-popping	210	0.29	237	109	0.10			

Table S.4.2 (cont.)

AL4820-047	Non-popping	183	0.29	231	106	0.10			
AL4821-048	Non-popping	255	0.51	399	255	0.10	0.3	382	
AL4821-049	Non-popping	269	0.51	393	244	0.10	0.2	356	
AL4821-050	Popping	164	0.48	395	253	0.09	5.7	3112	5.2
AL4821-051	Popping	171	0.46	400	246	0.09	11.9	6731	9.1
AL4821-053	Popping	174	0.48	405	253	0.09	14.2	8270	12.9
AL4821-054	Popping	176	0.49	405	259	0.09	11.2	6345	7.1
AL4821-055	Popping	169	0.48	401	254	0.09	17.9	10823	15.6
AL4821-056	Popping	164	0.49	406	260	0.09	13.8	7993	12.8
AL4821-057	Popping	168	0.50	406	259	0.09	13.4	7731	9.8
AL4821-058	Popping	164	0.49	406	267	0.09	11.7	6643	11.3
AL4821-059	Popping	165	0.48	403	256	0.09	24.8	16231	20.1

Table S.4.3 Helium and argon isotopic compositions. Ra is the air $^{3}He/^{4}He$ ratio (1.384×10^{-6}). $^{40}Ar^{*}$ is the radiogenic ^{40}Ar. Reported values are averages from step crushing measurements; standard deviations of step crushing measurements are given in parentheses.

Sample	$^{3}He/^{4}He$	$C/^{3}He$	$^{4}He/^{40}Ar^{*}$
	(R/Ra)		
AL4818-003	8.09 (1.78)	2.97E+09 (4.39E+08)	1.05 (0.09)
AL4818-005	7.87 (0.15)	1.88E+09 (5.21E+08)	13.80 (2.57)
AL4819-029	7.63 (0.10)	1.79E+09 (2.41E+08)	32.42 (3.62)
AL4820-041	8.33 (0.12)	2.53E+09 (2.12E+08)	1.32 (0.07)
AL4821-055	8.07 (0.10)	3.01E+09 (2.91E+08)	1.09 (0.07)
AL4821-058	8.30 (0.14)	3.11E+09 (2.57E+08)	1.07 (0.14)

Table S.4.4 CO_2 density in bubbles determined by Raman spectroscopy.

Sample	CO_2 density
	(g/cm^3)
AL4818-003	0.12
AL4818-003	0.18
AL4818-003	0.11
AL4818-003	0.09
AL4820-036	0.15
AL4820-036	0.12
AL4820-036	0.14
AL4820-036	0.20
AL4820-037	0.10
AL4821-055	0.17
AL4821-055	0.09
AL4821-055	0.10